RESEARCH

IN

THE SPACE SCIENCES

Collected Publications

for the First Quarter of 1972

Volume I

Space Sciences Laboratory

University of California

Professor K. A. Anderson, Director

(NASA-CR-155665) RESEARCH IN THE SPACE SCIENCES. COLLECTED PUBLICATIONS FOR THE FIRST QUARTER OF 1972, VOLUME 1 Quarterly Report, 1972 (California Univ.) 290 p

N78-73049 THRU N78-73054

Unclas

00/99 03680

This research was supported by contracts and grants from the National Aeronautics and Space Administration, the National Science Foundation the Atomic Energy Commission, the Office of Naval Research and others, awarded to the University of California, Berkeley

REPRODUCTION RESTRICTIONS OVERRIDDEN

NASA Scientific and Technical Information Facility

PREFACE

This publication is a compilation of articles and reports produced generally during the First Quarter of 1972. We attempt to present here a broad overview of the many faceted areas of research in the space sciences currently in progress at the Space Sciences Laboratory, University of California, Berkeley.

It is our hope that by such a quarterly publication we will be able to provide those interested with a technical summary detailing the fields of current research being carried out by those investigators affiliated with this Laboratory.

TABLE OF CONTENTS

1. Alvarez, H., Haddock, F., and Lin, R. P., Evidence for Electron Excitation of Type III Radio Burst Emission.

2. Buffington, A., Smith, L. H., Smoot, G. F., Alvarez, L. W., and Wahlig, M. A., A Search for Antimatter in the Primary Cosmic Rays.

3. Eberhard, Philippe H., Ross, Ronald R., Alvarez, Luis W., and Watt, Robert D., Search for Magnetic Monopoles in Lunar Material.

4. Henderson, W.,and Steel, G., Isolation and Characterization of a Triterpenoid Alcohol from the Green River Shale.

5. Henderson, William, Reed, Walter E., Steel, Gordon, and Calvin, Melvin. Isolation and Identification of Sterols from a Pleistocene Sediment.

6. Holland, P. T., Simoneit, B. R., Wszolek, P. C., McFadden, W. H., and Burlingame, A. L. Carbon Chemistry of Apollo 14 Size-Fractionated Fines.

7. Hurley, K. C., Search for X-Rays from the Planet Jupiter.

8. Kane, S. R., Kahler, S. W., and Kurfess, J. D., The Impulsive X-Ray Burst of October 10, 1970.

9. Lin, R. P., Comments on Brief Report by T. E. Graedel and L. J. Lanzerotti 'Interplantetary-Particle Associations with Type III Solar Bursts'.

10. Margon, Bruce, Bowyer, Stuart, Lampton, Michael, and Cruddace, Ray. Evidence for a Highly Compact X-Ray Source.

11. Margon, Bruce, Lampton, Michael, Bowyer, Stuart, and Cruddace, Ray. A Pulsing X-Ray Source in Circinus.

12. Mason, Richard O., An Earth Resource Debate.

13. Meng, C.-I., and Mihalov, J. D., On the Diamagnetic Effect of the Plasma Sheet Near 60 R_E.

14. Mozer, F. S., On the Relationship Between DP-1, DP-2, the Growth and Expansion Phases of Substorms, and Ionospheric Electric Fields.

15. Mozer, F. S., Simultaneous Electric Field Measurements on Nearby Balloons.

16. Mozer, F. S., Bogott, F. H., and Tsurutani, B., Relations Between Ionospheric Electric Fields and Energetic Trapped and Precipitating Electrons.

17. Nicholls, J., Carmichael, I. S. E., Stormer, Jr., J. C., Silica Activity and P_{total} in Igneous Rocks.

18. Paresce, F., Kumar, S., and Bowyer, C. S. Continuous Discharge Line Source for the Extreme Ultraviolet.

19. Richter, W. J., Tesarek, J. M., and Burlingame, A. L., Ring Contraction in Molecular Ions of Acylated Alicyclic Amines as a Function of Ring Size.

20. Richter, W. J., Bursey, J. M., and Burlingame, A. L., Ring Contraction Upon Electron-Impact as a Function of Ring Size: The Mass Spectrometric Fragmentation of Acylated Cyclic Amines.

21. Simoneit, Bernd R., and Burlingame, A. L., Organic Analyses of Selected Areas of Surveyor III Recovered on the Apollo 12 Mission.

22. Smoot, G. F., Buffington, A., and Smith, L. H., Spatial Spark Jitter Measurements of Highly Charged Nuclei for Optical Spark Chambers.

23. Tsurutani, B., and Bogott, F., The Onset of Magnetospheric Substorms.

SPACE SCIENCES LABORATORY

EVIDENCE FOR ELECTRON EXCITATION OF TYPE III RADIO BURST EMISSION

H. Alvarez, F. Haddock, and R.P. Lin

N76-75197

April 21, 1972

UNIVERSITY OF CALIFORNIA, BERKELEY

EVIDENCE FOR ELECTRON EXCITATION OF TYPE III RADIO BURST EMISSION

H. Alvarez and F. Haddock

Radio Astronomy Observatory
University of Michigan, Ann Arbor 48104 U.S.A.

and

R. P. Lin

Space Sciences Laboratory
University of California, Berkeley 94720 U.S.A.

April 21, 1972

ABSTRACT

Type III radio bursts observed at kilometric wavelengths (≤ 0.35 MHz) by the OGO-5 spacecraft are compared with > 45 keV solar electron events observed near 1 A.U. by the IMP-5 and Explorer 35 spacecraft for the period March 1968-November 1969.

Fifty-six distinct type III bursts extending to ≤ 0.35 MHz (≥ 50 $R_\odot$ equivalent height above the photosphere) were observed above the threshold of the OGO-5 detector; all but two were associated with solar flares. Twenty-six of the bursts were followed ≤ 40 minutes later by > 45 keV solar electron events observed at 1 A.U. All of these 26 bursts were identified with flares located west of W09 solar longitude. Of the bursts not associated with electron events only three were identified with flares west of W09, 18 were located east of W09 and 7 occurred during times when electron events would be obscured by high background particle fluxes.

Thus almost all type III bursts from the western half of the solar disk observed by OGO-5 above a detection flux density threshold of the order of 10^{-13} wm^{-2} Hz^{-1} at 0.35 MHz are followed by > 45 keV electrons at 1 A.U. with a maximum flux of ≥ 10 cm^{-2} sec^{-1} $ster^{-1}$. If particle propagation effects are taken into account it is possible to account for lack of electron events with the type III bursts from flares east of the central meridian. We conclude that streams of $\sim$10-100 keV electrons are the exciting agent for type III bursts and that these same electrons escape into the interplanetary medium where they are observed at 1 A.U. The total number of > 45 keV electrons emitted in association with a strong kilometer wavelength type III burst is estimated to be $\geq 5 \times 10^{32}$.

INTRODUCTION

Of the various forms of radio burst emissions from the sun, type III bursts are most likely to be indicative of the escape of energetic particles from the sun. These radio bursts exhibit a rapid frequency drift ($\sim$80 MHz/second at 100 MHz) from high to low frequencies and have been shown to be due to disturbances propagating outward in the solar corona at speeds of $\sim c/3$ (Wild et al., 1954; 1959). Radio observations have identified these bursts over a frequency range from $\sim$500 MHz (Maxwell et al., 1960) to 0.05 MHz (Haddock and Alvarez, 1969) corresponding to a height range of $\sim$20,000 km to $\sim$100-200 $R_\odot$ above the photosphere. It is clear therefore that at least for the type III bursts extending to low frequencies the exciting agent escapes from the sun. The nature of the exciting agent has been hypothesized to be particles, both proton (Wild et al., 1954; Friedman and Hamberger, 1969) and electron streams (Wild et al., 1959), and magnetohydrodynamic shock waves (Westfold, 1957; Zirin, 1966). The latter appears unlikely in view of the large coronal magnetic fields required ($\sim$100 gauss at 3×10^5 km height).

There are theoretical grounds for the choice of proton streams as the excitation agent (Smith, 1970). However, protons of the requisite energy ($\sim$50 MeV) are rarely observed to be emitted by the sun, and when they are emitted, they are not necessarily accompanied by type III radio emission but rather by type IV and type II (Lin, 1970). Smith (1970) raises the possibility that the proton flux from a type III burst is too small to be observed above galactic cosmic ray background by current spacecraft experiments, due to the diffusive nature of the

propagation of these particles in the interplanetary medium. However, protons responsible for type III bursts would have velocities near c/3 and thus would contribute to the background galactic cosmic ray spectrum in a limited energy interval about 50 MeV. That portion of the cosmic ray spectrum has been studied extensively for solar source and modulation effects (Kinsey, 1970) and there is no evidence for a long term solar component above ~20 MeV.

On the other hand, solar electrons of the ~c/3 velocity (~32 keV energy) are frequently observed in the interplanetary medium, although not nearly as frequently as metric and decametric wavelength type III bursts. Furthermore, almost every solar electron event of ~40 keV is accompanied by such type III burst emission (Lin, 1970). The main objections to the electron stream hypothesis for type III burst generation are (1) the relatively small number of electron events compared to type III bursts and (2) the difficulty of providing a theoretical explanation for the stabilization of the electron streams.

Type III bursts do not always drift down to very low frequencies. On many occasions bursts observed at metric wavelengths are not observed at decametric wavelengths, and similarly many bursts are not observed at hectometric and kilometric wavelengths which are seen by ground based observations which extend to decametric wavelengths (Hartz, 1969). Occasionally the reverse is also true. The reasons for these cutoffs are not understood at the present time. One possibility is that the exciting agent is impeded or dispersed in its progress outward through the corona.

In order to bypass the problem of interpretation of these cutoffs we have tabulated only type III bursts which extend to kilometric

wavelengths (frequencies ≤ 0.350 MHz at height ≥ 50 $R_\odot$) and compared them with > 45 keV electron events observed at 1 A.U.

EXPERIMENTS

The radio data is from the instrument that the University of Michigan has aboard the OGO-5 spacecraft (launched March 4, 1968). The electron data is provided by the University of California experiments aboard the Explorer 35 (AIMP-2) and Explorer 41 (IMP-5) spacecraft. The orbits of both spacecraft lie predominantly in the interplanetary medium. A detailed description of the Explorer 35 and OGO-5 instrumentation has been given elsewhere by Lin (1970) and MacRae (1968), respectively. Here it suffices to note that in Explorer 35, electron fluxes are unambiguously identified and are measured in two integral energy ranges, > 22 keV and > 45 keV. IMP-5 provides comparable measurements in four integral electron energy ranges; > 18, > 45 and > 120 keV. The events studied here are those with a maximum 45 keV electron flux of ≥ 10 cm^{-2} sec^{-1} $ster^{-1}$. The OGO-5 radio-astronomy receiver steps in 9.2 sec through the following frequencies: 3.5, 1.8, 0.9, 0.6, 0.35, 0.2, 0.1 and 0.05 MHz.

OBSERVATIONS

From the OGO-5 observations in March 1968 through November 1969 those type III bursts which clearly extend from 3.5 MHz to 0.35 MHz and down to 0.05 MHz were tabulated. For each of these bursts the IMP and Explorer 35 data were examined for evidence of an electron event commencing within ≤ 40 minutes after the type III burst onset time (observed at 1 A.U.) at 3.5 MHz.

To obtain the location of the type III emission region, each type III burst was identified with a solar flare under the criterion that the burst must occur within ± 3 minutes of the period from flare start to flare maximum. We find that almost every one of the type III bursts observed by OGO-5 in the kilometric wavelength range was associated with a flare. This high correlation may be due to the high intensity of the type III burst necessary for detection by OGO-5. For four type III bursts, although no flare was found, an electron event was observed which had been attributed to an over-the-limb flare. A total of 26 of 56 distinct kilometric wavelength type III bursts located west of central meridian were followed by electrons observed at 1 A.U. at an average of 25 minutes later.

Figure 1 shows an example of a type III burst followed by a solar electron event. There is a gap in the radio data between 0928 and 0932 UT and in the electron data between 0938 and 0948 UT. There was no flare associated with this event but the radio data give evidence that this burst was one in a sequence that originated in the McMath plage no. 10109 before and after it disappeared behind the west limb. We have estimated that the flare longitude was approximately between W120 and W130. Analysis of the radio event shown in Figure 1 (Haddock and Alvarez, 1971) indicated that the 0.1 MHz burst was emitted as second harmonic at a heliocentric distance of $\geq 120\ R_{\odot}$ and arrived at the Earth not earlier than 0927 UT. If we assume that burst exciters or electron streams followed an Archimedes spiral that started 120° west of the central meridian and passed through the earth then the radio data arrival times at the earth are consistent with exciters streams having a constant velocity with a value between

0.28c and 0.38c. With these velocities the exciter particles were expected to arrive at the earth at 0939 and 0951 UT, respectively. The observations show that the 45 keV solar electrons did not arrive earlier than 0936 UT but were already present at 0948 when the data gap was terminated. We conclude that the radio and particle data are consistent with a velocity $\sim$0.38c.

The locations of the type III emission are plotted in Figure 2. None of the observed electron events come from type III bursts located at longitudes east of W09; only three type III bursts out of 26 from flares located west of W09 did not give rise to electrons at 1 A.U. The correlation to events originating in the western hemisphere of the sun is consistent with the propagation characteristics of these electrons in the interplanetary medium. The Archimedean spiral field structure of the interplanetary field implies that field lines at the earth connect back to the vicinity of $\sim$W50 solar longitude. Electrons do not propagate transverse to the interplanetary magnetic field lines (Lin et al., 1968) and the angular extent of the observed events from W09 to the west limb should be interpreted as due to an extended emission region (of ≥ 50-60° solar longitude) at or near the sun.

We conclude that essentially every kilometric type III burst above the OGO-5 detection threshold and associated with a flare on the western hemisphere produces an electron event at 1 A.U. with a maximum >45 keV flux of ≥ 10 cm^{-2} sec^{-1} $ster^{-1}$.

Graedel and Lanzerotti (1971) have questioned the association of solar electron events with type III bursts. Their result, however, does not consider the relevance of the associated flare position to the degree of solar electrons-radio burst correlations, as revealed in this

study. It also does not consider the influence of the associated flare importance, as indicated by Sakurai (1971). Finally about 25% of the electron data they use (> 300 keV) corresponds to electron velocities ($\beta > 0.77$) out of the range of most type III exciters. Further discussion of Gradel and Lanzerotti's paper is contained in Lin (1972).

The maximum particle flux observed at 1 A.U. may be used to derive the total number of electrons per burst emitted from the sun, under some crude assumptions about the propagation of these particles on the interplanetary medium. Following the method of Lin and Hudson (1971), we find that the particle flux threshold of ~ 10 cm^{-2} sec^{-1} ster^{-1} corresponds to $\geq 5 \times 10^{32}$ electrons released at the sun.

SUMMARY

Earlier studies of $\sim$40 keV solar electron events have established that such events are almost always accompanied by type III bursts at the time of particle injection into the interplanetary medium. Here we have presented evidence that essentially a one-to-one correspondence exists between kilometric wavelength type III bursts above a threshold of approximately 10^{-13} wm^{-2} Hz^{-1} and > 45 keV electrons observed at 1 A.U. We conclude that streams of $\sim$10-100 keV electrons are the exciting agent for type III bursts, and that $\geq 5 \times 10^{32}$ electrons with energy > 45 keV are emitted in a strong type III burst. A problem which remains is to explain the cutoff of many type III bursts before they reach kilometric wavelengths. The present correlation suggests that such cutoffs may be due to the stopping or dispersion of the electron stream before it reaches 1 A.U.

ACKNOWLEDGMENTS

We acknowledge the contributions of the staff of the University of Michigan radio astronomy space program responsible for the success of the OGO-5 experiment. The OGO-5 research was funded by the NASA under contract NAS 5-9099 (University of Michigan). The Explorer 35 and IMP-5 research was supported in part by the NASA under contract NAS 5-9091 and grant NGL 05-003-017 (University of California).

REFERENCES

Friedman, M., Hamberger, S.M.: 1969, Solar Phys., 8, 398

Graedel, T.E., Lanzerotti, L.J.: 1971, J. Geophys. Res., 76, 6932

Haddock, F.T., Alvarez, H.: 1970, Bulletin AAS, 2, 196 (Abstract)

Haddock, F.T., Alvarez, H.: 1971, Bulletin AAS, 3(1), 6 (Abstract)

Hartz, T.R.: 1969, Planet. Space Sci., 17, 267

Kinsey, J.H.: 1960, Phys. Rev. Letters, 24, 246

Lin, R.P.: 1970, Solar Phys., 12, 266

Lin, R.P.: 1972, Comments on a brief report by T.E. Graedel and L.J. Lanzerotti, 'Interplanetary particle associations with type III solar bursts,' submitted to J. Geophys. Res.

Lin, R.P., Kahler, S.W. and Roelof, E.C.: 1968, Solar Phys., 4, 338

Lin, R.P., Hudson, H.S.: 1971, Solar Phys., 17, 412

MacRae, B.D.: 1968, University of Michigan, Radio Astronomy Observatory Technical Report, September

Maxwell, A., Howard, W.E., III, and Garmire, G.: 1960, J. Geophys. Res., 65, 3581

Sakurai, K.: 1971, Solar Phys., 16, 125

Smith, D.F.: 1970, Solar Phys., 15, 202

Westfold, K.C.: 1957, Phil. Mag., 2, 1287

Wild, J.P., Murray, J.D., and Rowe, W.C.: 1954, Australian J. Phys., 7, 439

Wild, J.P., Sheridan, K.V. and Neylan, A.A.: 1959, Australian J. Phys., 12, 369

Zirin, H.: 1966, Nature, 212, 909

FIGURE CAPTIONS

1. Type III bursts observed at kilometric wavelengths by the OGO-5 spacecraft followed by > 45 keV solar electrons observed by IMP-5 near 1 A.U. The event occurred on 2 June 1969. The gaps in the radio data correspond to telemetry gaps.

2. Displayed here are the locations of the flares associated with each type III burst extending below 0.35 MHz. The bursts followed by solar electron events at 1 A.U. are grouped in the west as expected from propagation considerations.

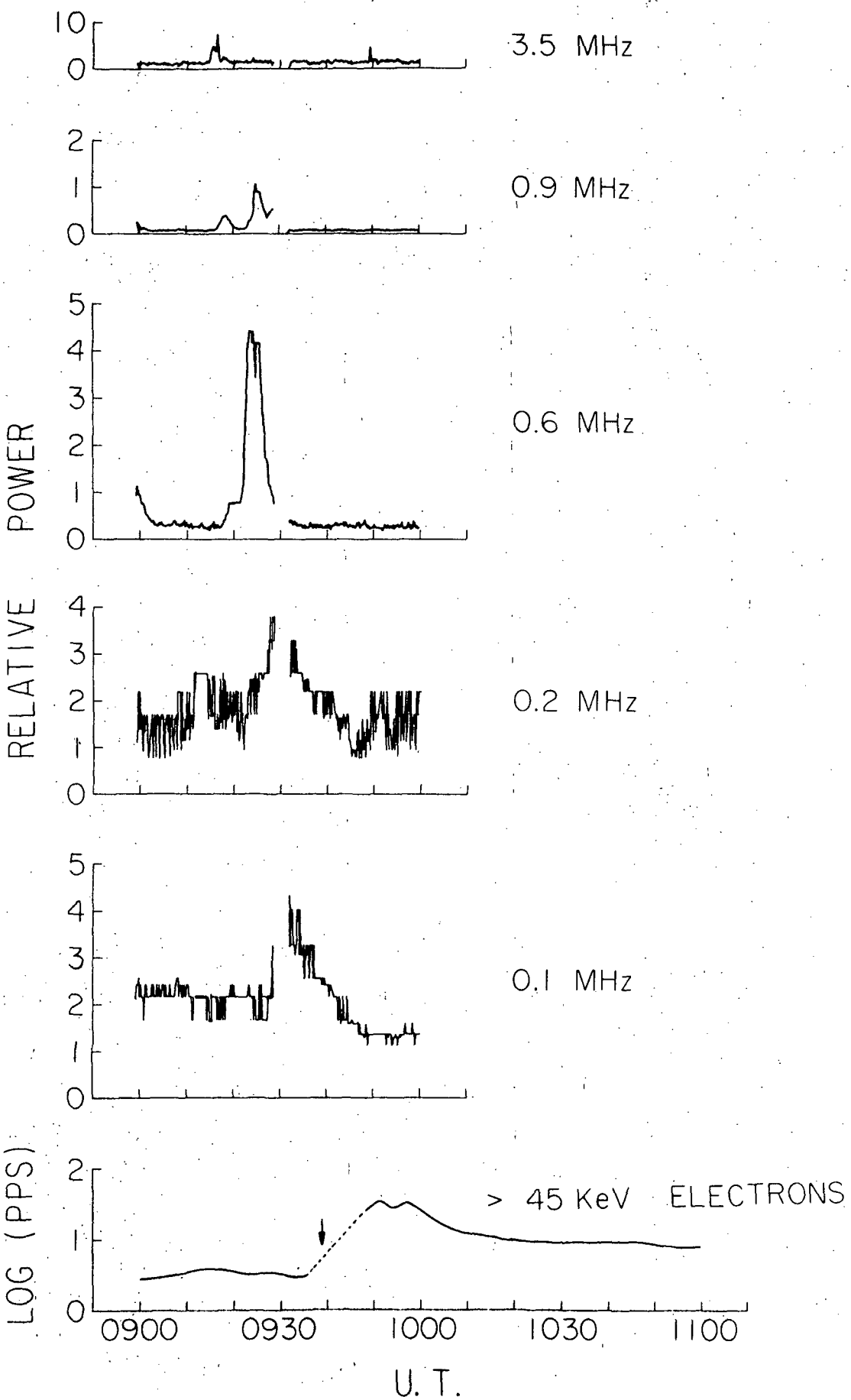
TYPE III SOLAR BURST & > 45 KeV ELECTRONS OBSERVED ON 2 JUNE 1969
RELATIVE POWER
3.5 MHz
0.9 MHz
0.6 MHz
0.2 MHz
0.1 MHz
LOG (PPS)
> 45 KeV ELECTRONS
0900
0930
1000
1030
1100
U. T.

Figure 1

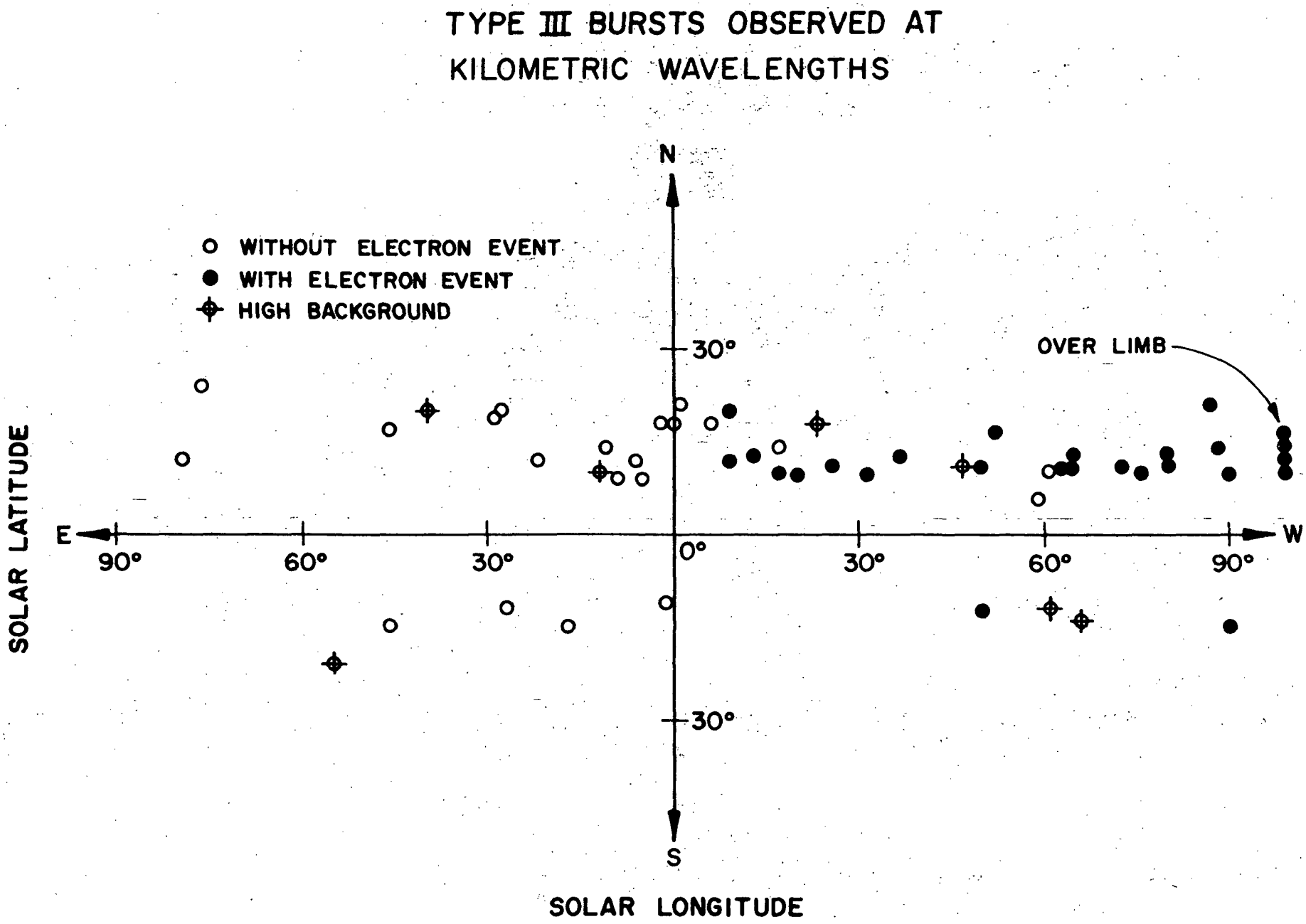
TYPE III BURSTS OBSERVED AT
KILOMETRIC WAVELENGTHS
WITHOUT ELECTRON EVENT
WITH ELECTRON EVENT
HIGH BACKGROUND
N
S
E
W
30°
OVER LIMB
90°
60°
30°
0°
30°
60°
90°
30°
SOLAR LATITUDE
SOLAR LONGITUDE

Figure 2

SPACE SCIENCES LABORATORY

A73-26474
A73-27416

A SEARCH FOR ANTIMATTER IN THE PRIMARY COSMIC RAYS

A. Buffington, L. H. Smith,
G. F. Smoot, and L. W. Alvarez

Space Sciences Laboratory
University of California, Berkeley

and

M. A. Wahlig

Lawrence Berkeley Laboratory
University of California, Berkeley

Principal Investigator: Prof. L. W. Alvarez

November 1971

Work performed under
NASA Contract NAS 9-7801

Space Sciences Laboratory Series 12 Issue 96

UNIVERSITY OF CALIFORNIA, BERKELEY

Space Sciences Laboratory
University of California
Berkeley, California 94720

A SEARCH FOR ANTIMATTER IN THE PRIMARY COSMIC RAYS

A. Buffington, L. H. Smith, G. F. Smoot, and L. W. Alvarez
Space Sciences Laboratory, University of California, Berkeley

and

M. A. Wahlig
Lawrence Berkeley Laboratory, University of California

Submitted to *Nature (Letters)* for publication.

Work supported by NASA Contract NAS 9-7801

Space Sciences Laboratory Series 12 Issue 96

A Search for Antimatter in the Primary Cosmic Rays

A. Buffington, L. H. Smith, G. F. Smoot, and L. W. Alvarez
Space Sciences Laboratory, University of California, Berkeley*

and

M. A. Wahlig
Lawrence Berkeley Laboratory, University of California

The symmetry between matter and antimatter observed at accelerators has led many astrophysicists[1] to speculate that a similar balance exists in the universe. However, if matter and antimatter were allowed to mix, considerable annihilation reactions would occur. Gamma-ray measurements[2] set a stringent upper limit on any mixing of matter and antimatter within our galaxy. Alfvén[3] has advanced a mechanism which might permit regions of matter and of antimatter to coexist within our galaxy without appreciable mixing. On the other hand, matter and antimatter may be concentrated in whole galaxies, with the non-mixing requirement thus automatically satisfied. However, if the early state of the universe were homogeneous, a mechanism would have to be devised capable of separating galaxy-sized groups of matter and antimatter.

Whichever is the case, one way we would be certain that regions of antimatter exist elsewhere in the universe would be the unambiguous detection of antimatter nuclei in the primary cosmic rays. A small flux of antiprotons, expected to be about 10^{-5} of the proton flux,[4] should come

---

* Research performed under the auspices of the National Aeronautics and Space Administration under Contract No. NAS 9-7801.

from reaction products of cosmic-ray interactions with the interstellar gas. Such reactions should produce negligible fluxes of anti-helium and the more complex anti-elements. Therefore, observation of complex anti-nuclei such as helium, carbon, or oxygen would almost certainly imply the existence of antimatter stars capable of nucleosynthesis.

A number of authors have already reported searches for antimatter.[5-9] The most stringent experimental upper limits for antimatter flux have been set by searches in large emulsion blocks that have been exposed at high altitudes to the incident cosmic rays. Examination of several thousand stopping cosmic-ray nuclei of charge greater than 2 showed no events with the characteristic annihilation products at the termination of the track. However, as Greenhill et al.[7] have pointed out, these measurements apply only to low-energy antimatter flux, and there is reason to expect that antimatter might become more plentiful at higher energy. Observation of just one or two well-verified, unambiguous anti-nuclei in the incident cosmic-ray flux would have profound astrophysical significance, since most present-day cosmologies do not take account of significant amounts of antimatter.

In this letter we report the first data from two flights of a new superconducting magnetic spectrometer which was capable of a direct matter-antimatter separation in the cosmic rays. Antimatter events would appear in the spectrometer as trajectories which curve opposite to common matter, because of their negative charge. A detailed description of our equipment will appear soon.[10] Figure 1 presents a schematic diagram and Table 1 summarizes some of the properties of the instrument.

The spark locations and scintillator pulse height data were recorded on photographic film. All sparks were automatically measured on a

cathode-ray tube encoding machine, and all pictures were scanned by hand. Events showing occasional delta-ray activity in the spark chambers were re-displayed on a cathode-ray tube, and a scanner rejected the spurious tracks. Multiprong interactions in the apparatus and other background events were rejected after measurement. Then each good event was fitted to a curved trajectory through the magnetic field, and its specific curvature $\underline{K}$ (= 1/rigidity) and goodness of fit χ were calculated. Poorly fitting events were eliminated using a χ-cut, which should reject only 3 per cent of the good data. Figure 2 shows a specific curvature distribution for a sample of the fitted data. The maximum detectable rigidity with the automatic measuring machine was about 50 GV/c. A large body of common matter events starts at $\underline{K} = 0$ and extends beyond the end of the graph to geomagnetic cutoff at $K \approx 0.25$ (c/GV). Any potential antimatter signal might be masked by some of the common matter events near $\underline{K} = 0$ spilling over into the region of negative $\underline{K}$. Spillover could be due to measurement error or to occasional misinterpretation of the event by our automatic measuring and analysis sequence. Therefore, all events which had $\underline{K}$ less than zero were remeasured by hand on a machine which had three times the accuracy of the automatic machine. Upon remeasurement, most of these gave a positive specific curvature, but some remained with negative $\underline{K}$ and thus were regarded as antimatter candidate events in our data.

Table 2 presents a list of possible explanations for these events. We are able to rule out source 2 as an explanation, since we observed no albedo time-of-flight (a difference in timing of about 10 nsec) on any of the antimatter candidates. To calculate sources 1 and 3 we made a Monte Carlo calculation which included the optical error, multiple coulomb scattering, and nuclear scattering for our instrument. The optical error

was obtained by a detailed study of several hundred "straight-through" events which were taken for each flight with the superconducting magnet turned off. Figure 3 shows the K-distribution for straight-throughs in the second flight. The smooth curve is the Monte Carlo fit to these data. For the nuclear scattering, we used a diffraction shape for the angular distribution with a cutoff in total momentum transfer of ΔP_{max} = 300 MeV/c. Any greater momentum transfer in a collision than this ΔP_{max} would be expected to fragment the incident nucleus. Usually this would cause it to fail our spark chamber topology requirement and to give a much smaller pulse height reading in the bottom scintillator of the apparatus. Nuclear scattering should have contributed several antimatter candidates in the helium portion of our data, but the cutoff on momentum transfer becomes such a stringent limit for higher-Z elements (whose total momentum is Z times the rigidity) that in our $Z \geq 3$ data there are no appreciable antimatter candidates expected from this source.

Table 3 presents the antimatter candidates and Monte Carlo predictions for all of our data. We have presented helium (with about 9% admixture of higher-Z data) separately from our $Z \geq 3$ data, since the nuclear scattering mechanism is unimportant for the latter. For the distribution of common matter events that could contribute in our Monte Carlo predictions we used a power law distribution in rigidity, $dN/dR \propto R^{-j}$ where the value for j = 2.6 was determined by a fit to all our data. A more detailed analysis of the rigidity spectra of our data is now being prepared for publication. In terms of specific curvature, the power law becomes $dN/dK \propto K^{j-2}$. The Monte Carlo predictions of Table 3 are quite sensitive to the value chosen for j. Uncertainty in j causes the overall scale of the values to have an uncertainty of about ±20 per cent. No significant

enhancement is seen in any of the bins. For R below 33 GV/c in the high-Z data no events are seen. This limit, plus the one set by statistics in the rigidity range between 33 and 100 GV/c is shown in Figure 4. This figure also presents results of previous experiments, all limits shown having 95 per cent confidence level.

Realizing that the antimatter candidates of Table 3 were potentially a greatly enriched sample, we carefully inspected the spark chamber and pulse height records for each event. All of these had a normal appearance, except for a single oxygen event which had interacted halfway through the last spark chamber and then deposited 202 MeV of energy in the bottom scintillator instead of the usual 124 MeV. The spark chambers showed that the interaction had at least three prongs at wide angles to the incident trajectory. Such a violent interaction must surely have fragmented the incident nucleus thoroughly, making it difficult for the event to have as much as the normal pulse height in the bottom counter, let alone the abnormally large pulse we saw. The rigidity of this event was 40 GV/c, two standard deviations from a straight trajectory in our apparatus.

Common matter might occasionally make up this large an energy deposition in the scintillator below, through the combined energy deposition of cascade protons from the struck nucleus and of inelastically produced mesons. The material of the spark chamber was sufficient to stop any evaporation products from the struck nucleus. Antimatter, of course, would have all of the energy deposition capability of common matter plus that of the extra mesons resulting from plentiful annihilation processes. To evaluate the relative probabilities of these two processes, we made a Monte Carlo study that included cascade protons[11] from the struck

nucleus in the spark chamber (taken to be aluminum), inelastic pion production,[12] and the relativistic fragments of the incident nucleus. For the antimatter case, we added extra mesons to take account of annihilation processes. Averaged over all our data we found that only 1 per cent of the time could an oxygen nucleus interact in the fourth spark chamber and then make as large a pulse as the one we saw in the counter below. On the other hand, we found a 40 GV/c antimatter nucleus could make as large a pulse 20 to 50 per cent of the time. The difference between these two numbers (with even greater disparity with our original estimates) led us to make a detailed study of large pulse height probabilities for this event. We found that the chance of common matter making the large pulse height is an increasing function of incident rigidity. Furthermore, only high-rigidity events could in turn have a chance to appear as antimatter due to the optical distortions of our spectrometer. Integrating over our known rigidity spectrum, we found that the chances were about 12 per cent that this oxygen event was high-energy common matter that appeared as antimatter in the spectrometer due to optical distortion and made up the large pulse height by producing many inelastic mesons. Therefore, it finally appears only an insignificant three times easier to explain this event as true antimatter than it does as common matter spillover.

The limits set on antimatter flux by our experiment are considerably lower than for any previous experiment. We feel we have done the best job possible on a search for antimatter events among helium with our present equipment, because of the contributions to antimatter candidates from nuclear scattering within the detector. A new apparatus, with much less material in the detector, could perhaps carry the helium search further. However, for a magnetic field integral of 3 kG-M the momentum transfer

necessary to scatter a common matter event to negative curvature is greater than 90 Z MeV/c. As we noted before, greater than 300 MeV/c total momentum transfer is likely to fragment an incident nucleus. Therefore, on the higher charged elements, nuclear scattering becomes unimportant and our experiment is limited only by optics reconstruction error and statistics. We are planning to fly a second-generation magnetic spectrometer with improved optics, which will also have a thick Cerenkov counter following the momentum measurement. Antimatter candidates should interact in this counter about 50 per cent of the time, and the Cerenkov threshold will diminish the response of the counter to the troublesome nonrelativistic cascade products which characterize interactions of common matter. With this innovation and multiple balloon flights, it should be possible to push the upper limit down by another decade or so, or hopefully to make the first positive unambiguous identification of complex anti-nuclei in the primary cosmic rays!

We would like to thank the National Center for Atmospheric Research balloon launch crew at Palestine, Texas, for the kind hospitality they extended to us during our field operations. We also thank Dr. Charles Orth of the Manned Space Flight Center at Houston, Texas, who provided valuable help in getting us started in the Monte Carlo program to calculate the pulse height probabilities, and Dr. John Naugle of NASA, who called our attention to the possibility that our very small sample of very high-energy ordinary matter events had to be considered seriously as a cause for the one apparent anti-oxygen event.

References

[1]Alfvén, H. and Elvins, A., *Science* 164, 911 (1969); Hoyle, F., and Burbidge, G. R., *Nuovo Cimento* 4, 558 (1956); Morrison, P., *Nuovo Cimento* 7, 858 (1958).

[2]Kraushaar, W., Clark, G. W., Garmire, G., Helmken, H., Higbie, P., and Agogino, M., *Ap. J.* 141, 845 (1965).

[3]Alfvén, H., *Rev. Mod. Phys.* 37, 652 (1965).

[4]Rosen, S., *Phys. Rev.* 158, 1227 (1967).

[5]Greenhill, J. G., Clarke, A. R., and Elliot, H., *Nature* 230, 170 (1971).

[6]AppaRao, M. K. V., *Canad. J. Phys.* 46, S654 (1968); Aizu, H., Fujimoto, Y. H., Hasegawa, S., Koshiba, M., Mito, I., Nishimura, J., and Yokoi, K., *Phys. Rev.* 121, 1206 (1961).

[7]Evanson, P., and Meyer, P., Paper OG-41, *12th International Conference on Cosmic Rays*, Hobart, 1971, Conference Papers 1, 138; Golden, Robert, private communication.

[8]Bogomolov, E. A., Lubyanaya, N. D., and Romanov, V. A., Paper OG-42, *12th International Conference on Cosmic Rays*, Hobart, 1971, Conference Papers 1, 144.

[9]Brooke, G., and Wolfendale, A. W., *Nature* 202, 480 (1964).

[10]Smith, L. H., Buffington, A., Wahlig, M. A., and Dauber, P., "A Superconducting Magnetic Spectrometer," to be published in *Rev. Sci. Inst.*

[11]Metropolis, N., Bivins, R., Storm, M., Turkevich, A., Miller, J. M., and Friedlander, G., *Phys. Rev.* 110, 185 (1958).

[12]Multiparticle production parameters were taken from Barashenkov, V. S., Maltsev, V. M., Patera, I., and Toneev, V. D., *Forschritte der Physik* 14, 372 (1966).

Table 1. SPECIFICATIONS OF THE MAGNETIC SPECTROMETER

Flight dates	18 September, 1970, and 8 May, 1971
Mean magnetic field integral	3.8 kG meters (first flight) 4.3 kG meters (second flight)
Spatial detectors	Four optically viewed spark chambers, four 1-cm gaps each
Optical reconstruction error	±0.14 mm per spark chamber
Maximum detectable rigidity (set by optics and field integral)	75 GV/c (first flight) 90 GV/c (second flight)
Scattering material within the spectrometer	4.12 g/cm^2, 0.25 radiation lengths (first flight) 2.04 g/cm^2, 0.055 radiation lengths (second flight)
Geometry factor	660 cm^2 ster
Trigger counters	Pilot B and Y plastic scintillators
Time-of-flight measurement	With helium incident, timing error = ±4 nsec giving rejection of > 95% against albedo events With Z > 2 incident, timing error = ±2½ nsec giving rejection of > 99% against albedo events
Charge resolution (helium through oxygen)	±0.15 charge, by recording light levels in the three trigger scintillators
Trigger threshold	Selectable to gather data with charge Z greater than or equal to 1, 2, or 3
Residual atmosphere for flights	About 5 g/cm^2 of air left above the instrument
Data-taking times	2½ hours with Z ≥ 2 and 13 hours with Z ≥ 3

Table 2. SOURCES OF ANTIMATTER CANDIDATES

(1)	Optical reconstruction error moves an event over from K > 0 region.
(2)	High-energy albedo nucleus simulates negative charge because it is incident from below.
(3)	Nuclear scattering in the material of the instrument caused an apparent negative curvature for a common matter event.
(4)	An actual antimatter signal.

Table 3. ANTIMATTER SEARCH STATISTICS AND MONTE CARLO PREDICTIONS

Data sample	Rigidity range (c/GV)	Observed Antimatter candidates	Monte Carlo predicted spillover
Flight 1	R < 33	5	2.6
Helium	33 < R < 100	7	6
(6131 events)	R > 100	12	11
Flight 2	R < 33	0	1
Helium	33 < R < 100	0	4
(3838 events)	R >100	8	7
Flight 1	R < 33	0	0.4
Charge $Z \geq 3$	33 < R < 100	1	4
(3152 events)	R > 100	5	7
Flight 2	R < 33	0	0.2
Charge $Z \geq 3$	33 < R < 100	4	9
(10445 events)	R > 100	8	18
All data	R < 33	5	4
combined	33 < R < 100	12	23
(23566 events)	R > 100	33	43

Figure Captions

Fig. 1. Schematic SSCM detectors and cryogenics.

Fig. 2. A plot of specific curvature $\underline{K}$ distribution for a sample of data from second flight measured automatically. All events with $K < 0$ to be remeasured on a more accurate machine.

Fig. 3. 377 events (2nd flight) straight-through (magnet off) data fit to curved trajectory.

Fig. 4. Summary of present information on upper limits for antiparticles in the cosmic rays at 95% confidence limits.

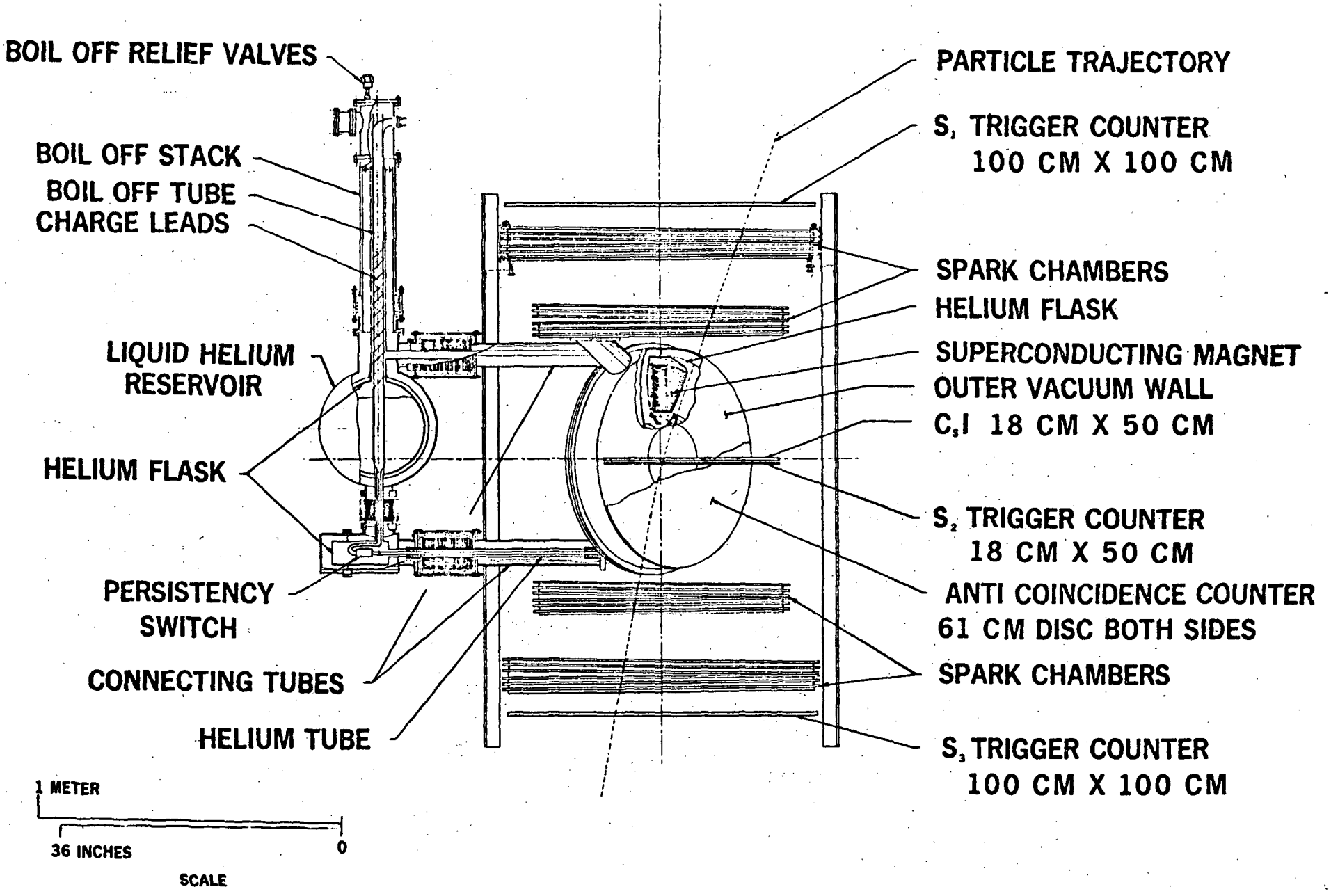

XBL 714-676

Fig. 1. Buffington et al.

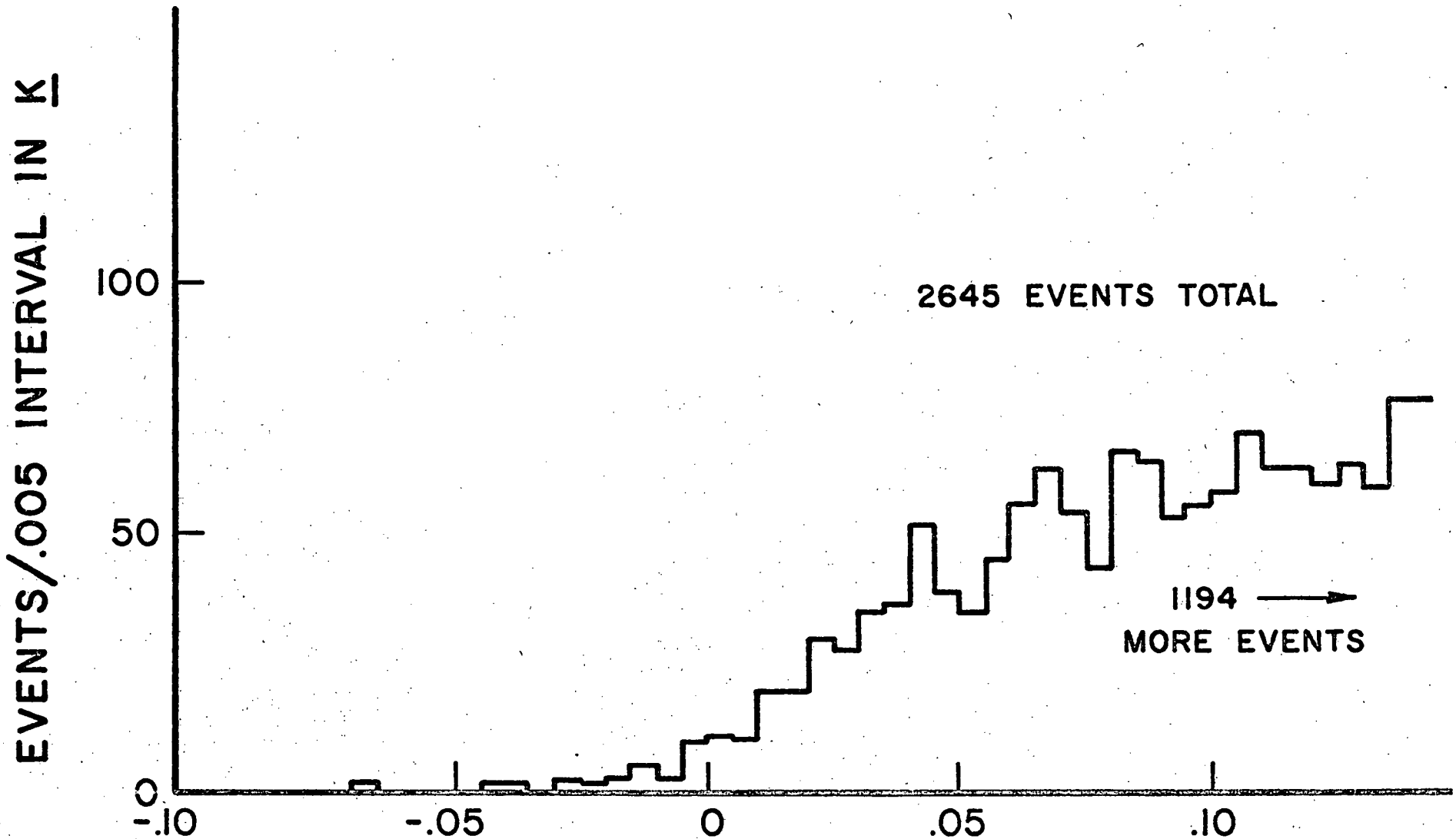

Fig. 2. Buffington et al.

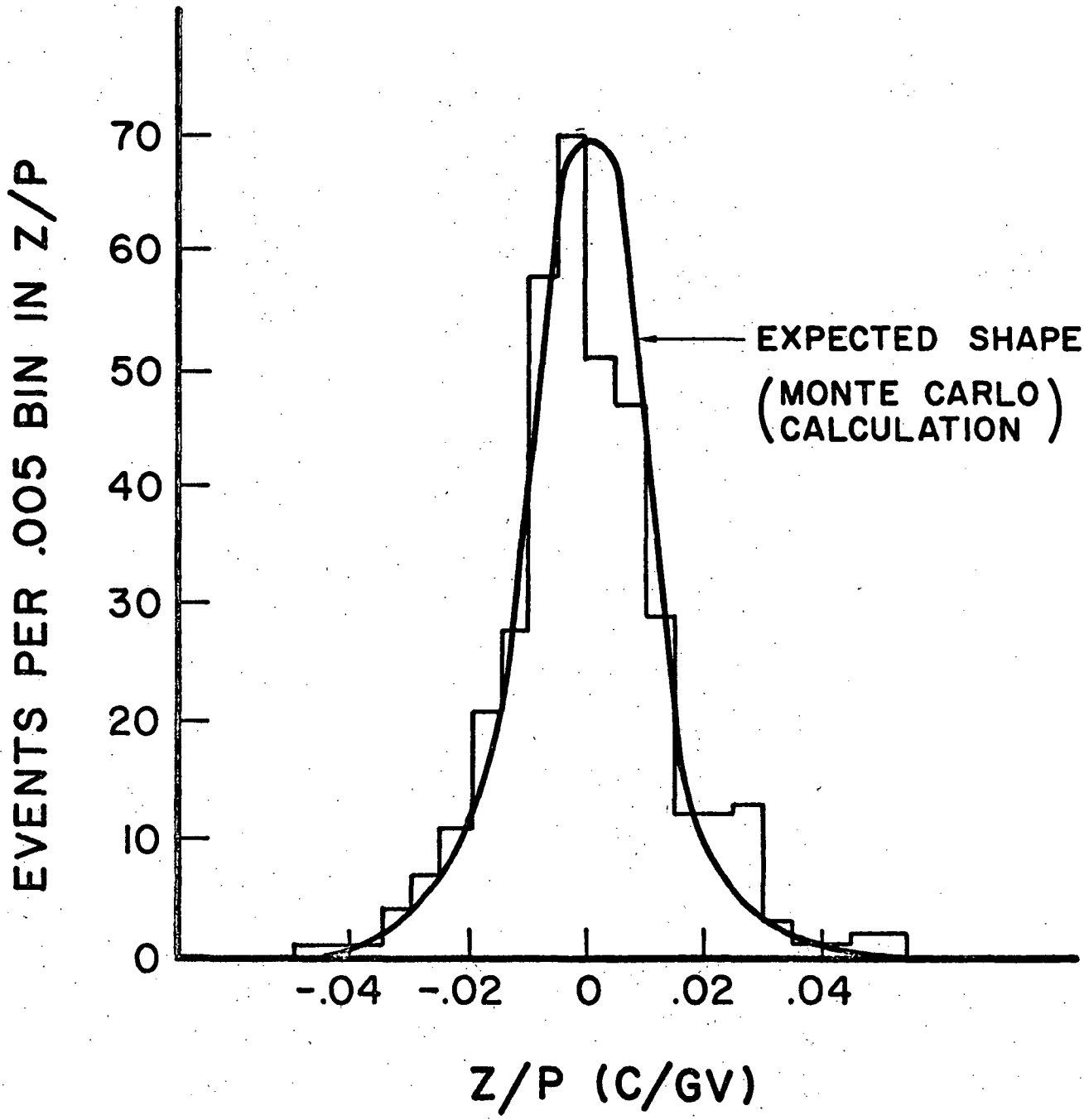

Fig. 3. Buffington et al.

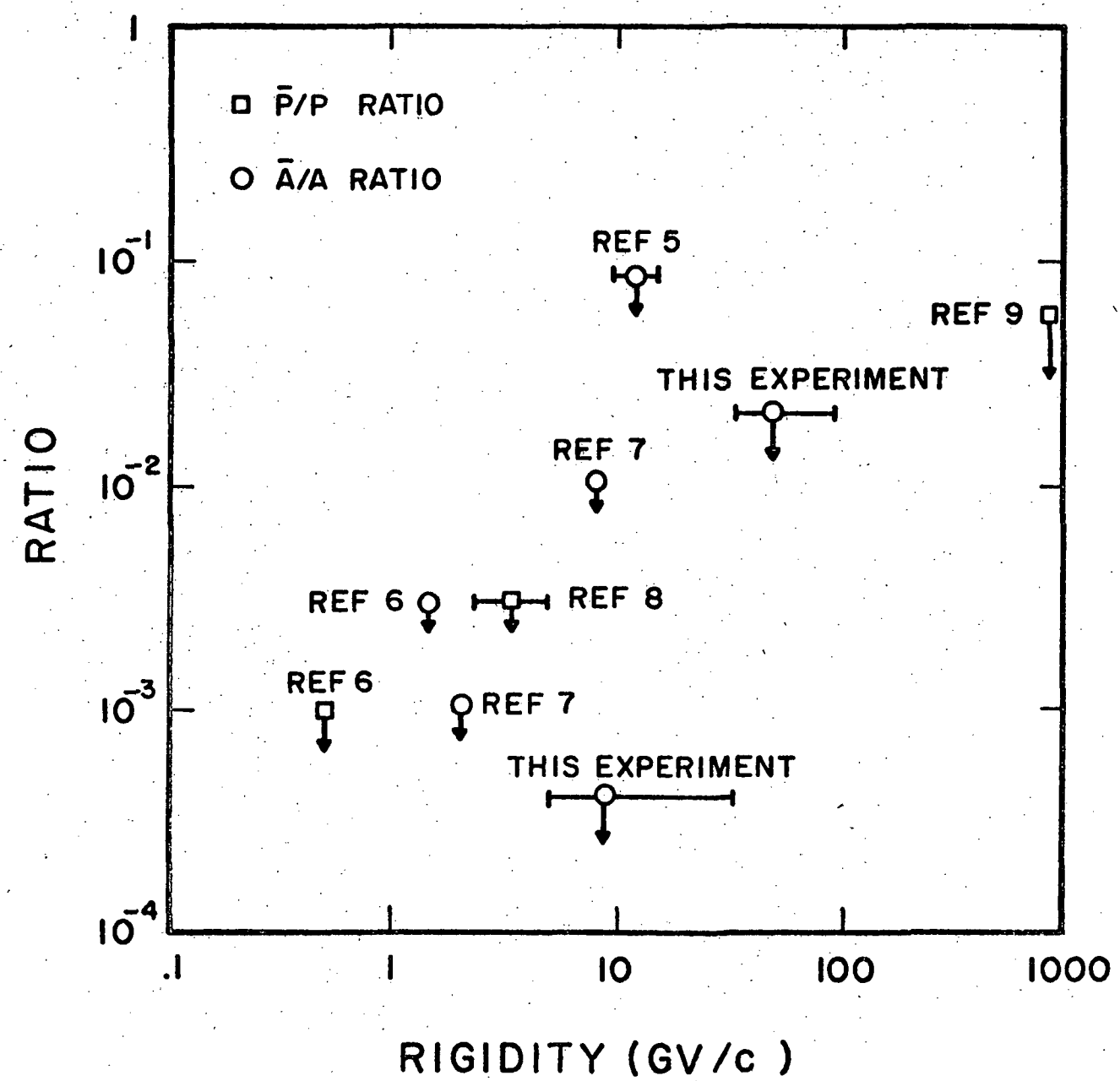

Fig. 4. Buffington et al.

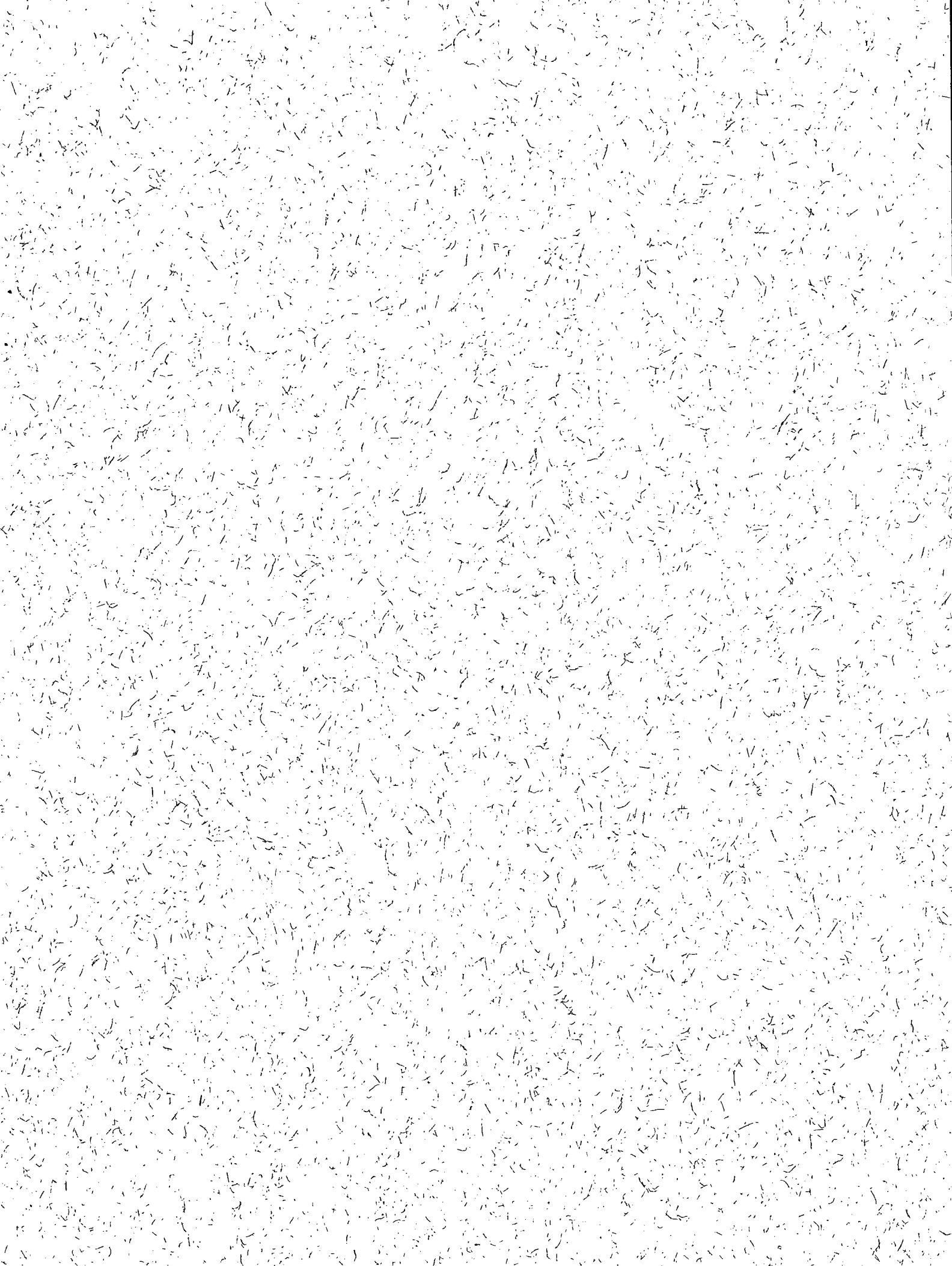

AT-3849

Reprinted from:

PHYSICAL REVIEW D VOLUME 4, NUMBER 11 1 DECEMBER 1971

Search for Magnetic Monopoles in Lunar Material*

Philippe H. Eberhard, Ronald R. Ross, and Luis W. Alvarez
Lawrence Radiation Laboratory, University of California, Berkeley, California 94720

and

Robert D. Watt
Stanford Linear Accelerator Center, Stanford, California 94305

(Received 6 July 1971)

A search for magnetic monopoles in lunar material has been performed by the electromagnetic measurement of the magnetic charge of samples. All measurements were found consistent with zero charge for all samples and inconsistent with any other value allowed by the Dirac theory. Upper limits are determined for the monopole flux in cosmic radiation and for the pair-production cross section in proton-nucleon collisions.

I. INTRODUCTION

An electromagnetic monopole detector has been used to measure the magnetic charge of samples of lunar material returned by the Apollo 11 mission. The null result and a preliminary interpretation have been reported.[1] This paper gives a more complete analysis of the experiment.

The discovery of magnetic monopoles would have far-reaching consequences. Their existence has been invoked in the explanation of the phenomenon of electric charge quantization,[2,3] a phenomenon which has been verified to the limit of experimental accuracy.[4] According to a recent theory,[5] the elementary particles would be made of electrically charged monopoles, i.e., particles having both an electric and a magnetic charge.

All searches for monopoles rely on some physical properties attributed to those particles. The failure to discover them in a given experiment calls for careful documentation of the monopole properties that were assumed and for an assessment of their likelihood. A "legalistic" point of view may be appropriate to judge the proofs of absence of monopoles in such an experiment. All the properties assumed in our detection technique stem from long-range interactions, i.e., the only interactions for which reliable predictions can be computed when the coupling constant is as large as the one expected for magnetic monopoles.

In Sec. II we describe the basic properties of the monopole, and in Sec. III we discuss some experimental consequences based on them. In Sec. IV we describe our measurements of the magnetic charge of 28 samples of lunar material. Interpretation of our negative result in terms of limits for the cosmic-ray flux and the production cross sections depends on the history of the lunar surface, for which reasonable hypotheses are advanced; that history justifies the search for monopoles in the lunar material. These hypotheses cannot be paralleled to the properties assumed for the detection technique. They are described and used to interpret our data in Secs. V, VI, and VII. Some measurements performed on different material with the same equipment and the limit we have obtained for the monopole density in ordinary matter are reported in Sec. VIII. Some remarks about the present experimental situation are given in Secs. IX and X.

II. BASIC PROPERTIES OF MONOPOLES

In classical electrodynamics, a magnetic monopole is a particle that possesses a magnetic charge

g, i.e., a source of a flux of magnetic induction $\vec{B}$,

$$4\pi g = \oiint_S \vec{B}\cdot d\vec{A}, \tag{1}$$

where S is a surface surrounding the monopole and $d\vec{A}$ an element of that surface, and all quantities are measured in Gaussian units. If a monopole is in motion, it generates an electric field E around its path in a way similar to that in which an electric charge generates a magnetic field (see Fig. 1),

$$\vec{\nabla}\times\vec{E} = -\frac{1}{c}\frac{\partial\vec{B}}{\partial t} - \frac{4\pi}{c}\vec{j}_m, \tag{2}$$

where $\vec{j}_m$ is the current density of magnetic charges. From Eqs. (1) and (2) one can derive a continuity equation for magnetic current density. Therefore, just as electric charge is conserved, magnetic charge is conserved, so a monopole cannot decay into magnetically neutral particles only. If monopoles exist, there must be at least one kind of them that is stable.

When the general principles of quantum theory are brought into the picture, a study of the scattering of an electron by a magnetically charged particle, even at large distances, shows[3] that the magnetic charge must be quantized if the basic principles on which quantum mechanics is founded are to be retained:

$$g = \nu g_0, \tag{3}$$

where ν is an integer and g_0 is the unit of quantization. In the Gaussian system of units

$$g_0 = \frac{e}{2}\frac{\hbar c}{e^2} = \frac{e}{2}\frac{1}{\alpha}, \tag{4}$$

where $\alpha \approx \frac{1}{137}$ is the fine-structure constant and e is the electron charge. Therefore, g_0, in emu, is about 68.5 times the value of e in esu, a condition originally derived by Dirac[2] and referred to as the Dirac quantization condition.

Other theories[5,6] have been hypothesized which require that Eq. (3) be valid but that ν in Eq. (3) be a multiple of 2 or 4. References to possible violations of Eq. (3) can be found in the literature,[7] and searches for such violations have been made.[8,9] But the demonstration that yields (3) and (4) is the same as the one that quantizes electric charge; therefore, only if monopoles satisfy (3) can they be invoked in the explanation of electric charge quantization we have referred to.

We assume quantization of magnetic charge according to Eqs. (3) and (4) as a basic property of the monopoles we are looking for, except when explicitly mentioned otherwise.

The minimum nonzero magnetic charge is g_0. Even if a monopole had the minimum charge, its coupling constant to the electromagnetic field would be much stronger than the strong-interaction coupling constant. It follows that computations of short-range interactions will be at least as unreliable for monopoles as they are for hadrons. However, monopoles have long-range interactions due to the electromagnetic field. For them, the corrections to the $1/r$ Born approximation vary as $1/r^5$ and, for large enough r, should be negligible.[10] For large r the first approximation is reliable, and the properties derived from it are very well established.

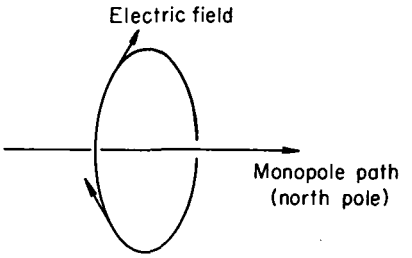

FIG. 1. Electric field surrounding the path of a moving monopole.

III. EXPERIMENTAL CONSEQUENCES

A. Induction in a Coil

Using long-range interactions only, one can deduce the property used in our detection technique. If a monopole travels along the axis of a coil (as in Fig. 2) it will induce an electric field that will contribute to the electromotive force in the coil,[11]

$$-\mathcal{E} = n\frac{4\pi g}{c}\frac{dN}{dt} + \frac{1}{c}\frac{dF}{dt}, \tag{5}$$

where n is the number of turns of the coil and dN/dt is the number of monopoles of charge g passing per unit of time; F is the flux of B in the coil.

If the coil is a superconducting coil shorted by a superconducting switch, $\mathcal{E}$ is forced to be zero. The flux F is increased at each pass of the monopole by the value ΔF_1 (Ref. 12):

$$-\Delta F_1 = n4\pi g. \tag{6}$$

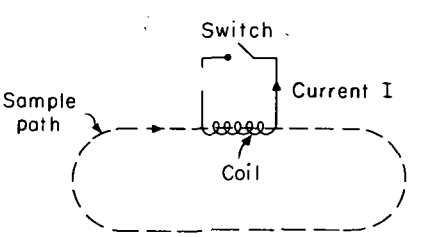

FIG. 2. Sample path through the superconducting loop used for magnetic-charge measurement.

If one arranges to have a sample containing charge g make N_p passes along the path of Fig. 2 and the total change, ΔF, is measured, the magnetic charge of the sample can be determined from

$$g = \frac{-\Delta F_1}{4\pi n} = \frac{-\Delta F}{4\pi n N_p} . \quad (7)$$

B. Binding to Ferromagnetic Crystals

Of course, the above technique detects monopoles that are attached to the sample analyzed, i.e., that are bound to it.

Once a magnetic monopole is in the neighborhood of a ferromagnetic crystal, it will be attracted by its image charge in the crystal. One can show that the binding energy in the ferromagnetic material is greater than ≈30 eV by using the classical laws for interaction at distances greater than 1000 Å. A monopole can escape a magnetic trap formed of ferromagnetic material only if exposed to a very strong magnetic field.[13] Of course, it is probable that monopoles would be tightly bound to atoms or to nuclei with a magnetic moment,[14,15] but, in ferromagnetic material, the binding is established with more certainty because it depends only on long-range interactions. The presence of ferromagnetic material in a sample would insure trapping of the monopoles that would have been thermalized in it, even if all other binding mechanisms did fail.[13] That is the case of the lunar sample.[16]

C. Energy Loss

Monopoles are bound to lose energy by energy transfer to atoms of the material they traverse. Unless pathological characteristics are attributed to monopoles (like a zero mass, for instance),[7] they will, because of this energy loss, slow down and be thermalized if there is no magnetic field to accelerate them. However, the rate of energy loss and therefore the range depend on different processes. Some of them, the nuclear interactions for instance, involve short-range interactions and therefore cannot be predicted.

Energy loss by ionization is, however, well understood. When quantum effects are taken into account,[17] one finds that the process involves atoms at distances up to more than 1000 Å from the path of the monopole. Therefore, computation of ionization effects may be considered as trustworthy even for large coupling constants. Moreover, it can be checked by studying the energy loss of high-Z nuclei. Such computation for monopoles predicts an energy loss rather uniform as a function of energy,[18]

$$-\frac{dE}{dx} \approx \nu^2\, 10\ \text{GeV cm}^2/\text{g}, \quad (8)$$

where ν is the constant appearing in Eq. (3). To take the uncomputable effects into account, we introduce a new constant N defined by

$$N^2 = \frac{\langle -dE/dx \rangle_{\text{real}}}{10\ \text{GeV cm}^2/\text{g}} . \quad (9)$$

N is defined for a given monopole of a given energy E in such a way that Eq. (9) is satisfied for $\langle -dE/dx \rangle$, the average of the energy loss over the entire range R of the particle. Therefore,

$$R(\text{g/cm}^2) = \frac{E\ (\text{GeV})}{N^2 10} . \quad (10)$$

N is an effective charge, that of a monopole that would have an energy loss by ionization equal to the $\langle -dE/dx \rangle_{\text{real}}$ of the monopole considered. N does not have to be an integer, but the real energy loss must be at least equal to the energy loss by ionization. Therefore,

$$N \gtrsim \nu . \quad (11)$$

IV. THE MEASUREMENT OF MAGNETIC CHARGE

A. Technique

Our detector has been described elsewhere.[19] It is essentially a superconducting coil shorted by a superconducting switch as shown in Fig. 2. The sample is attached to a cart moving along a closed path that traverses the coil in a tunnel at room temperature, so that the sample need not be cooled below ambient temperature. A superconducting shield protects the coil against induction of current due to changes in the ambient magnetic field.

In order to run the equipment with samples not containing a monopole and still have observable results, a measurable current, i_0, is stored before the sample is run. This current is generated by feeding a current into an auxiliary coil while the superconductiong switch is open, closing the superconducting switch, and then de-energizing the auxiliary coil. Next, the sample is circulated 400 times through the coil. Finally, the switch is opened and the signal resulting from opening the switch is recorded. A magnetically neutral sample gives a standard signal whose amplitude would be exactly the value expected for the current i_0 if it were not for the noise in the electronics. This method of operation provides a test of the apparatus during each measurement even when no monopole is detected.

The magnetic charge of a sample is proportional to the difference between the amplitude of the signal obtained upon opening the switch after running the sample and the standard amplitude. The equipment is calibrated by using a very long solenoid carrying a known flux uniformly along the path of

the sample in the coil. The north pole and the south pole of the solenoid protude out opposite ends of the coil and superconducting shielding in order that the passage of a monopole be properly simulated. The long solenoid is itself calibrated in flux versus current by use of a copper coil of a known number of turns, outside the superconducting shielding.

The current i_0 is equal to the current that a monopole of charge g_0 circulated 1000 times would have produced. Therefore, when circulated 400 times, the minimum charge g_0 would have produced a change of $\pm 40\%$ in the signal recorded on the scope. A bigger charge would have induced an even bigger change.

A study of the noise shows that the standard deviation is roughly equal to the signal produced by a charge g_0 circulated 50 times and was independent of the number of passes N_p actually performed by the sample. When $N_p = 400$ passes, as for most of our measurements, the magnetic charge is measured with an error

$$\delta g = \tfrac{1}{8} g_0 . \tag{12}$$

If, on a measurement, the signal is not consistent with a zero magnetic charge, it is either because the equipment is not functioning correctly or because a nonzero charge has been found. In the latter case, the effect should be found again and again when the measurement is repeated, because our measurement does not in any way alter the sample analyzed. Whenever g is found not zero by a measurement, the sample is rerun, but just before rerunning, the equipment is tested for malfunctions. In all such cases so far, evidence of malfunction was found.

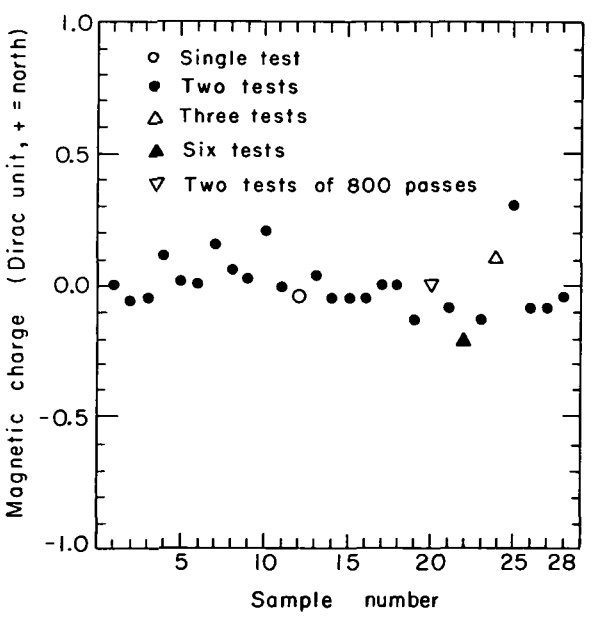

FIG. 3. Magnetic-charge measurements of samples 1 through 28 of Table I.

TABLE I. Apollo 11 samples used in this experiment.

Sample number	NASA number	Weight (g)	Sample number	NASA number	Weight (g)
1	10002,94	298.0	15	10002,107	303.0
2	10002,87	285.0	16	10002,106	296.5
3	10002,86	286.8	17	10002,108	294.0
4	10002,92	293.2	18	10002,109	319.0
5	10002,93	286.2	19	10002,A	301.5
6	10002,89	300.6	20	10002,7A	304.5
7	10002,90	261.5	21	10002,7B	298.5
	{10022,1}		22	10002,4B	318.0
8	{10023,1}	213.0	23	10002,4C	297.5
	{10024,3}		24	{10002,5C} {10002,4A}	356.0
9	10002,88	312.5			
10	10002,85	325.8	25	10002,8B	272.0
11	10002,91	300.4	26	10002,5A	312.0
12	10002,96	304.8	27	10002,5B	316.5
13	10002,95	325.8	28	10002,8A	296.5
14	10002,97	288.8			

B. Results

The lunar material analyzed in this experiment was divided into 28 samples of approximately equal weight whose magnetic charges were measured independently. Figure 3 shows the measurement of those charges in a sequence that is approximately chronological. Table I lists the samples by their NASA reference number and by the number as they appear in Fig. 3. Sample 8 was composed of three rocks. Samples 25 and 28 were chips between 1 mm and 1 cm, and samples 22 and 23 were unsieved fines. The remaining samples were sieved fines less than 1 mm from the "Bulk Sample" of material returned, weighing 7.0 kg altogether.

Each of the samples 1 to 11, 13 to 19, and 26 to 28 was run twice, and the value of the magnetic charge reported on Fig. 3 is the average of the two measurements. For the average, the error should be about $0.1 g_0$. During that period, for only one sample (sample 10) did the measured magnetic charge differ from zero by more than 2 standard deviations, but for this sample as well as for all others of this category, the measurement represents still more than 8 standard deviations from $\pm g_0$, the nearest possible value for g.

Sample 12 was run twice, but after the experiment was over, we discovered that the shape of the signal for one of the tests gave clear evidence of switch bouncing; the corresponding measurement ($-0.3 g_0$) was considered unreliable, and thus disregarded. The value corresponding to the other test is plotted in Fig. 3. It is still 7 standard devi-

ations away from any allowed quantized charge.

When we were running sample 20, and until we ran sample 26, the superconducting switch showed signs of fatigue. The noise on the signal was obviously increased by a factor of about 2. To overcome that difficulty, we increased the number of passes from 400 to 800 per run, or performed more than two runs, to make the average more accurate. Later on, we could disregard some of those measurements because we discovered the symptom of switch bouncing in the shapes of their signals. We plotted the average of the remaining measurements on Fig. 3. They are all consistent with a magnetic charge of zero. However, the error is difficult to estimate because the noise did not appear to stay constant and no standard deviation can be given to it reliably. This remark applies to samples 20 to 25 only.

At the time we were running sample 26, a spare switch was adjusted and substituted for the original one. The noise level was again about $\frac{1}{8}$ of g_0 per measurement and constant. For sample 26, Fig. 3 shows only the value of the magnetic charge obtained from the measurement with the good switch.

The measured magnetic charges are all compatible with zero and incompatible with a value $\pm g_0$. If fractional charges were considered as a possibility, then we can state that the charges more than $0.3g_0$ cannot have been present in more than one sample or two.

V. DENSITY OF MONOPOLES IN LUNAR SAMPLE

Once we accept the idea that magnetic charges are all multiples of g_0, our experiment demonstrates that in all 28 samples, no monopoles were present, or the numbers of north poles and of south poles were equal. We want to use this result to set an upper limit on the total density of monopoles in the lunar sample. We choose to quote the upper limit at 95% confidence, i.e., the density for which the probability of getting our zero-magnetic-charge result is 5%.

If the density of north poles and the density of south poles are not correlated statistically and if the expectation values for both densities are known, the probability that the magnetic charges of N_s equal samples are all zero can be computed. For $N_s \geq 23$, it is less than 5% if the density of north poles and the density of south poles are the same and if the expected sum of both is more than 3.3 for the whole volume explored. Therefore, for the processes that involve statistically independent densities of north and south poles, we state that the expectation value for the density of north and south monopoles in our sample is less than 3.3 with 95% confidence. This number would have been between 3.0 and 3.3 for unequal north- and south-pole densities and would have been 3.0 if we had not taken into account the possibility of having nonzero equal numbers of south and north poles in the sample.

We consider two main sources of monopoles in the lunar material and treat them separately, since each may have a different density limit due to the different natures of the sources. During all the time the samples have been exposed near the moon's surface at different depths, (a) monopoles of the primary cosmic radiation would have been slowed down and some of them would have ended trapped in the samples, and (b) protons of the cosmic rays could have produced pairs of monopoles in collisions with nucleons of the lunar sample. For process (a) the densities of north and south poles have obviously been statistically independent. The maximum density due to that source of monopole is obtained by dividing 3.3 by the weight of all samples, 8.3 kg. It is 4×10^{-4} monopoles/g.

For process (b) the creation in pairs causes a potential strong correlation between both densities. However, once the poles of a pair were sufficiently separated, it is unlikely that the mutual attraction between them would have played much of a role, because each of them would rather have been immediately trapped by an atom or a nucleus,[14,15] or, in any event, been attracted by its magnetic image in a ferromagnetic crystal[16] closer to it than the other pole is. Each monopole would have been trapped in the grain where it had stopped. If a grain were small, it would have captured only one of the monopoles of the pair and left the other pole to another grain. There is a typical grain size, d, below which a grain would have trapped only one monopole. It is of the order of the distance between the two poles at rest. It depends on the angle between monopoles at production, the range of each of them, etc. It is hard to estimate reliably. However, the contribution to it from multiple scattering can be computed,[20] and it represents a minimum for the value of d. It should be of the order of 1 mm in lunar material, for instance, for a pair of monopoles of mass 20 GeV created near threshold.

We consider that the densities of north and of south poles from this process are not correlated statistically if the poles of the pair have been trapped in different grains, because it is believed[21] that the lunar material has, several times in its existence, been thrown out by meteoritic impact and transported over distances of up to 100 km. In such displacements the mixing should have been so thorough that neighboring grains would find them-

selves far apart. There is indeed plenty of evidence that a thorough mixing actually did occur, from analysis of solar-wind particles,[22] from fossil tracks in dielectric crystals,[23] and from measurement of the neutron exposure.[24]

To compute the limit for the monopole density due to pair production by incident cosmic-ray protons, we used only the 7.0 kg of material called "sieved fines" and considered the densities of south poles and north poles to be uncorrelated. That selection corresponds to an arbitrary size limit d of less than 1 mm for the particles in the material used; therefore, of the lunar samples run, samples 8, 22, 23, 25, and 28 are disregarded. The maximum density is then 4.7×10^{-4} monopoles/g for a 95% confidence level.

If north and south poles are believed, after production and thermalization, to have been separated by a typical distance d less than 1 mm, only the fraction of material smaller than d mm should be used in this analysis. The curve of Fig. 4 represents the percentage by weight of the fine sample with grain size greater than a given dimension.[25] It can be read to find what fraction f of our sample did not meet the requirements, and therefore the fraction $1-f$ by which the above density (and consequently our cross-section limits on Figs. 6 and 8) should be divided.

VI. RADIATION HISTORY OF THE LUNAR SAMPLE

The relations between density and primary monopole cosmic flux on the one hand or between density and pole pair-production cross section on the other hand depend on the history of the samples,[21] i.e., at what depths they have been over the years. We use the same approximation as do the geologists studying the radiation history of the lunar soil,[24,26] i.e., we imagine that its surface has been mixed completely and uniformly down to a depth L during its existence as a solid.

We consider only the time for which the sample has been a solid because – even if monopoles were bound to nuclei[15] – there is no insurance that monopoles stopping in a liquid medium would not have drifted and spread into the bulk of the moon. It is safer to count only on the trapping inside solid material. The age of crystallization we use is 3.6×10^{9} years.[27–29]

In the simple model of uniform mixing, the depth L determines the amount of exposure of the sample to cosmic radiation and is estimated by matching the measured exposure age deduced from spallation products. These products are believed to be produced mostly by high-energy cosmic-ray protons of 1 GeV or so. Among all the possible measures

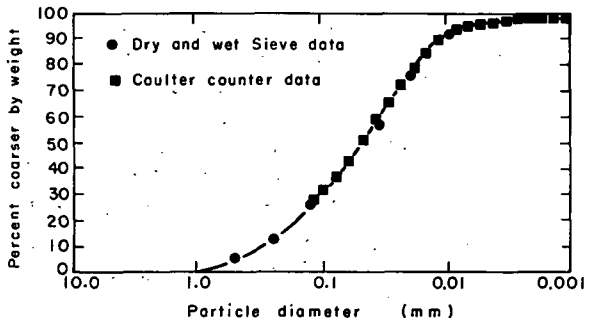

FIG. 4. Submillimeter-fines size distribution according to Ref. 25.

of radiation exposure time, spallation products seem the most appropriate for representing exposure of the sample to the high-energy primary cosmic-ray flux. The exposure ages are deduced from the measured amount of a given stable spallation product and an estimate of its rate of production based either on the measured amount of a radioactive spallation product of the same element or other auxilliary measurements on the sample. Exposure ages measured on small samples of Apollo 11 fines range from 100 million to 1300 million years with an average of about 500 million years.[30] This large spread in measured ages can be attributed to different histories of burial for the different samples. For our sample, which is large, the average exposure age of 500 million years should be quite accurate compared to the spread in measured ages of milligram-size samples.

Our estimate of the mixing depth L involves (1) estimating the rate of nuclear interactions as a function of depth below the lunar surface due to the incident isotropic cosmic radiation, (2) calculating from these interaction rates the average density of interactions expected after a time equal to the age of crystallization, T_c, if the soil was uniformly mixed to a depth L, and (3) equating this density to the density of interactions expected for a sample exposed at the surface of the moon for a time equal to the average exposure age, T_e.[31]

The following assumptions are made:

(a) The collision mean free path is 85.5 g/cm^2 in lunar material.

(b) The isotropic cosmic-ray flux of protons above an energy E has been constant in time and is given by[32]

$$\phi(E)=1.4E^{-1.67}\ \text{particles/cm}^2\,\text{sec}\,\text{sr}\,, \qquad (13)$$

where E is the kinetic energy in GeV.

(c) At each interaction the incident particle retained 60% of its original energy and continued on in the same direction.[32]

(d) The interaction of primary cosmic rays gave

rise to a secondary flux capable of producing spallation products. (This flux is normalized to give 0.8 interaction per primary interaction at large depths to match the experimental results for a thick lead target in the atmosphere.[33])

(e) The sample resided on the surface of the moon for a period of time prior to collection which was long compared to the half-life of the radioactive spallation product used to determine the production rate of the stable product. (This time is ~0.2 million years for ^{81}Kr, one of the main isotopes used in determining production rates.)

The resulting estimate of the mixing depth is proportional to T_c/T_e and amounts to 1000 g/cm^2.[31] Since both the flux limits and cross-section limits of Sec. VII are proportional to L/T_c, it is clear that the errors in these limits are not very sensitive to the model of uniform mixing but depend more heavily on the measured average exposure age. Our 95% confidence limits do not take into account any uncertainty in the radiation history of the lunar sample; this uncertainty, however, may well decrease as more measurements are made.

VII. UPPER LIMITS DEDUCED FROM DENSITIES

A. Cosmic Monopole Flux

The efficiency of trapping monopoles depends on how deeply they penetrated the surface, i.e., on their range R, i.e., on their energy and on the constant N defined by Eq. (9). If north and south monopoles present in the primary cosmic radiation are isotropically distributed and monoenergetic with energy E, the sum of their fluxes per cm^2 sec sr is given by

$$\phi(E) = \frac{(\text{density of monopoles}) \times L}{\pi \times \epsilon(E) \times (T \text{ crystallization})}, \tag{14}$$

where $\epsilon(E)$ corrects for solid-angle effects for large ranges R;

$$\epsilon(E) = \begin{cases} 1 & \text{for } R < L \\ L^2/R^2 & \text{for } R > L. \end{cases} \tag{15}$$

Using the value[31] for L and the 95% confidence limit for the density, we get the upper limit for the flux of monopoles in the cosmic rays as a function of E,

$$\phi(E) < \frac{1.1 \times 10^{-18}}{\epsilon(E)}. \tag{16}$$

In reality, E in Eq. (16) is an average energy of the cosmic monopole, such that $\epsilon(E)$ is the average of the collection efficiencies of the monopoles over their energy spectrum. The result is plotted in Fig. 5 for different values of N.

B. Pair-Production Cross Section

The limit for the production cross sections, by collision of an incident cosmic-ray proton with a nucleon of the lunar surface, is proportional to the

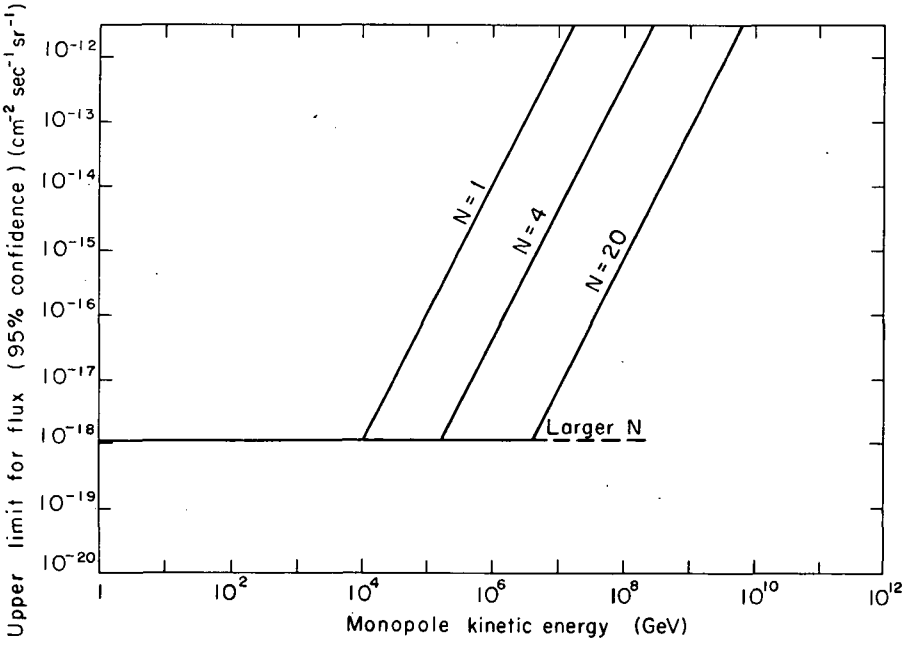

FIG. 5. Upper limit (95% confidence level) on the flux of cosmic monopoles of a given energy as a function of that energy. The dependence on the parameter N defined by Eq. (9) of the text is illustrated by the curves for $N = 1$, 4, and 20.

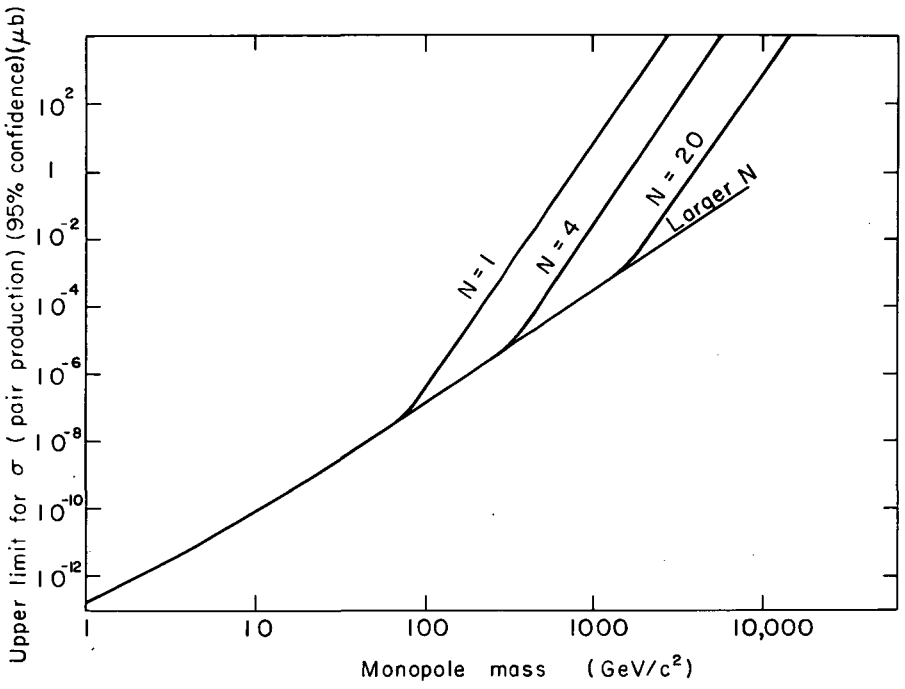

FIG. 6. Upper limit (95% confidence level) on monopole pair-production cross section in proton-nucleon collisions as a function of assumed monopole mass. The dependence on the parameter N defined by Eq. (9) of the text is illustrated by the curves for $N = 1$, 4, and 20.

limit for the density of monopoles in the sample, with a factor of proportionality that we derive from a Monte Carlo computation.[34] Much of this computation depends on the same parameters as the mixing depth L in such a way that, because of cancellation effects, much of the error in their determination has little influence on the final result.

In that computation, proton interactions are simulated with the properties listed from (a) to (c) in Sec. VII A. We neglect monopole production by the secondary flux [condition (d) in Sec. VII A], therefore we compute an upper limit slightly greater than the real one. In addition, we assume (a) the cross section σ for each mass M assumed for the monopoles of a pair is constant above threshold and zero below it; (b) the produced monopoles were emitted in the same direction as the incident proton, with the same velocity as the original nucleon-nucleon system, and with range given by Eq. (10).

The limit for the cross section σ for 95% confidence level is plotted on Fig. 6 as a function of the mass M, for different values of the constant N of Eq. (10). If the distance between two monopoles of a pair is believed to have been typically equal to a value d less than 0.1 cm, then the cross sections should be increased by the factor $1/(1-f)$, where f is the factor read on Fig. 4 for the abscissa equal to d.

Because of our accuracy in the measurement of the magnetic charge, our flux and our cross-section limits are valid for any monopole of charge equal to or larger than g_0. Those limits are still of the same order of magnitude if the monopole charge is smaller than g_0 but not lower than $0.3g_0$.

VIII. RESULTS OBTAINED WITH OTHER MATERIALS

Our monopole detector was used also to measure the magnetic charge of other materials. The total mass of materials measured in our detector, including the containers used for lunar material, weighed about 28 kg. Our negative result sets an upper limit of 2×10^{-28} monopoles/nucleon with 95% confidence for the average density of monopoles in all those samples, i.e., for the average density of monopoles in matter.

The nonlunar materials were measured with a number of passes N_p greater than 2000, therefore with an accuracy

$$\delta g < g_0/40 . \tag{17}$$

The goal was to detect possible monopoles of charge $g_0/3$, following reports that there could be charges of that magnitude (see Ref. 35, for instance).

2.4 kg of ocean sediment of the kind analyzed in an earlier experiment[35] and an emulsion containing a suspect track, exposed in the same experiment, were available. The ocean sediment was run as eight different samples with $N_p = 2000$, and the emulsion with $N_p = 4000$. All magnetic charges were found consistent with zero and inconsistent with charge $g_0/3$ by more than 10 standard deviations. It should be pointed out, however, that the ocean sediment and the emulsion had been exposed to the very high magnetic fields used in the previous experiment, and our measurement is meaningful only if monopoles are supposed to be bound so strongly to the material that they would have escaped extraction in the strong field.

Portions of various meteorites[36] were also available and were run through our detector, with $N_p = 2000$. Again the magnetic charges were found compatible with zero and incompatible with charge $g_0/3$ by more than 10 standard deviations. The total weight analyzed was about 2 kg.

Various materials such as targets exposed to the Brookhaven AGS accelerator and some geological samples were measured with $N_p = 2000$; the same zero results were obtained. A permanent magnet with a north and a south pole of charge 10^3 emu and its keeper were run with $N_p = 100$. The measurement shows that the north and the south pole of that magnet were equal, at least to 1 part in 5×10^{10}.

IX. STATUS OF MONOPOLE SEARCH

Our search has not identified a magnetic monopole, and no other experiment has found one either. All measurements thus give only upper limits for monopole density in various locations. Figure 7 shows some 95% confidence limits for the sum of the primary fluxes of north and south monopoles in cosmic radiation as a function of the monopole kinetic energy as they are determined by some of the monopole searches.[35,37-41] Figure 8 shows some 95% confidence limits obtained for production cross section in proton-nucleon collisions as a function of the mass of the assumed monopole.[35,37-39,42-45] More results about monopoles have been reported than are shown on Figs. 7 and 8. Some former work can be found in a recent review article.[46] Limits for pole pair-production cross sections by neutrinos[47] and γ rays[9,37,38] have been published. Mass- and charge-dependent upper limits for cosmic monopole flux more restrictive than those of Fig. 7 have been estimated from reasonable assumptions concerning the behavior of monopoles in space.[41] Monopoles have been searched for by studying Čerenkov light emitted by sea-level minimum-ionizing cosmic-ray particles.[48]

In different experiments different properties have been assumed for the monopole. They must be believed if the resulting upper limit is to be be-

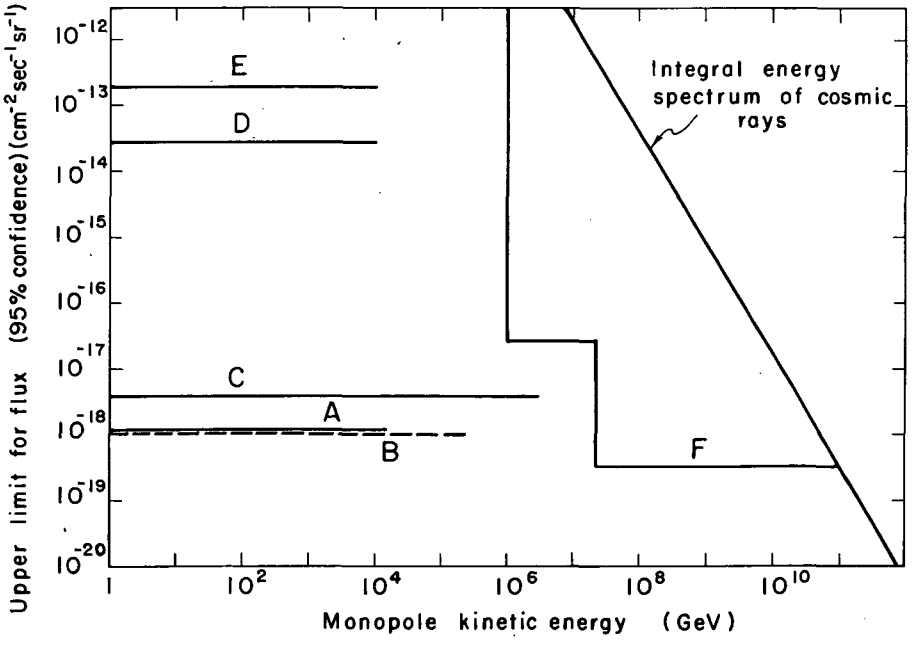

FIG. 7. Upper limit (95% confidence level) on the flux of cosmic monopoles as determined in various monopole searches. *A* from this work; *B* from Ref. 35; *C* from Ref. 39; *D* from Ref. 38; *E* from Ref. 37; *F* from Ref. 40. The flux of cosmic-ray protons above an energy E as given by Eq. (13) of the text is shown for comparison; for this curve the cosmic-ray kinetic energy E is read on the monopole kinetic-energy scale.

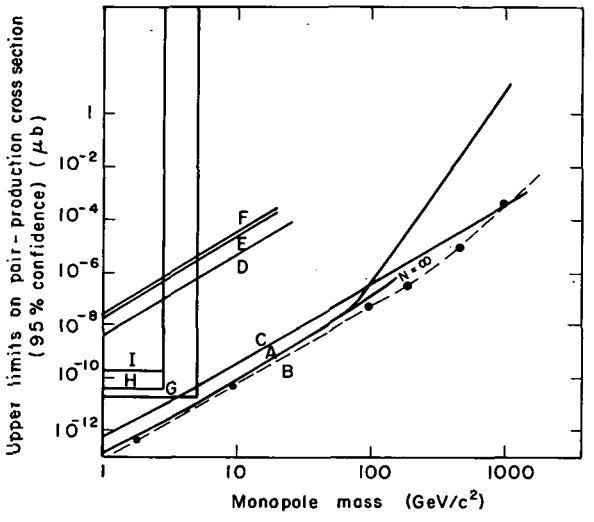

FIG. 8. Upper limit (95% confidence level) on monopole pair-production cross section in proton-nucleon collisions as determined in various monopole searches. *A* from this work; *B* from Ref. 35; *C* from Ref. 39; *D* from Ref. 38; *E* from Ref. 45; *F* from Ref. 37; *G* from Ref. 44; *H* from Ref. 42; *I* from Ref. 43.

lieved. In order to illustrate the different kinds of experiments that have been done, some of the assumptions involved are listed below. (The list is not claimed to be exhaustive.)

1. *Electromagnetic induction and source of magnetic field.* The two phenomena are bound together by Lorentz invariance. They constitute a definition of the monopole.

2. *Acceleration in magnetic fields.* There is a force on the monopole proportional to the value of the magnetic field. That property could be considered as an alternative definition of the monopole.

3. *Thermalization.* Monopoles are supposed to lose energy in matter by some mechanism such as ionization and be slowed from high velocity down to very low velocities.

4. *Migration.* After thermalization the monopoles are supposed to move from the point of thermalization through gases or liquids to a collector by some mechanism such as following magnetic field lines.

5. *Trapping.* After slowing down and perhaps migrating somewhere, the monopoles are supposed to be trapped in ferromagnetic or paramagnetic materials by a magnetic binding energy.

6. *No binding to atoms or nuclei.* Monopoles are supposed not to be bound to atoms or nuclei in nonferromagnetic material.

7. *Extraction.* Monopoles trapped in a material are supposed to be wrenched out of the material by large magnetic fields.

8. *Track signature.* Monopoles are supposed to leave characteristic tracks in emulsion or crystals due to their high rate of energy loss; they would not have been detected unless they produced a very heavy track.

9. *Scintillation signature.* Large light pulses are required from monopoles traversing scintillators in order for the monopoles to be detected.

10. *North-pole–south-pole separation.* North and south poles are supposed to be substantially separated for kinematical reasons after pair production and after slowing down in matter, without the influence of an external magnetic field.

11. *Incident cosmic-ray nucleon flux.* Whenever pair production by cosmic-ray nucleons is involved, some assumptions have been made on their power spectrum. These assumptions may concern longer or shorter periods of time, depend-

TABLE II. Experiments determining limits for cosmic monopole flux.

Assumed property	Reference 35	37	38	39	40	41	This work
Electromagnetic induction or source of magnetic flux							x
Acceleration in magnetic field	x	x	x	x		x	
Thermalization	x	x	x	x			x
Migration	x	x	x	x			
Trapping	x	x		x			x
No binding to atoms or nuclei	x						
Extraction	x	x		x			
Track signature		x	v	x	x		
Scintillation signature	x		v				
Interstellar environment						x	
Charge range (Dirac units)	0.16–27		1–3	1–30	≥2	≥1	≥0.3

ing on the experiment.

12. Interstellar environment. Some consequences rely on assumptions concerning the configuration and the magnitude of the magnetic field in space and the ambient thermal radiation.

13. The asymmetry of magnetic charge. Monopoles are supposed to be mainly of a given sign.

The question of which experiment depends on which property can be answered by reading the original papers. A partial answer is given, to the best of our objectivity, in Tables II to IV: in Table II for some experiments[35,37-41] determining limits on the cosmic-ray monopole flux, in Table III for experiments determining pair-production cross-section limits,[35,37-39,42-46] and in Table IV, for experiments[8,35,39,49] that set limits on density of magnetic monopoles in ordinary matter. The limit obtained per nucleon, with the Dirac charge assumed for the monopole, appears in Table IV. In each table, there is a column corresponding to each experiment (identified by the reference reporting it). An *x* in the row corresponding to an assumed property indicates that it was used in that experiment; a *v* indicates that the assumption concerns only part of the experiment. Also indicated is the range of monopole charge covered (when specified by the authors). The assumptions quoted for each experiment are the ones that have been quoted by the authors themselves.

The main feature of our experiment is that the only properties assumed for the monopoles, aside from their production, stem from their electromagnetic interactions at ranges of 1000 Å or more. The other assumptions necessary for the interpretation concern essentially the radiation history of the moon and are independent of the monopole theory itself.

X. CONCLUSION

Monopoles may not exist. The monopole theory as expressed in Refs. 2, 4, 5, and 7 could actually be disproved experimentally if a small difference were found between the magnitude of the electron and the proton electric charges, because it would require an enormous increase in the unit of magnetic charge quantization according to those theories. Since experiment[4] limits that difference to less than 10^{-20} times the electron charge, any possible difference would correspond to minimum magnetic charges' experiencing forces of more than 3000 tons in a magnetic field of 1 G. If such a difference were ever found, it would certainly be interpreted as a violation of charge quantization and hence as a disproof of the theories referred to above.

However, monopoles may just have been tricky enough to elude all searches to date. According to a recent analysis,[50] the cross section might be very low for producing pairs of monopoles that would remain separated. It would be necessary to have longer exposure to high-energy particles to be able to isolate a magnetic monopole.

ACKNOWLEDGMENTS

We gratefully acknowledge informative discussions with G. Wasserburg and J. Arnold concerning the history of our lunar samples. We thank H. H. Kolm for providing some of the ocean sediment and an emulsion used in the experiment of Ref. 35, and E. A. King and B. R. Simoneit for supplying our meteorite samples.

TABLE III. Experiments determining limits for cross section for pair production by protons.

Assumed property	Reference 35	37	38	39	42	43	44	45	This work
Electromagnetic induction or source of magnetic flux									*x*
Acceleration in magnetic field	*x*	*x*	*x*	*x*	*x*	*x*	*x*	*x*	
Thermalization	*x*	*x*	*x*	*x*		*x*	*x*	*x*	*x*
Migration	*x*	*x*	*x*	*x*		*x*			
Trapping	*x*	*x*		*x*			*x*	*x*	*x*
No binding to atoms or nuclei	*x*								
Extraction	*x*	*x*		*x*		*x*	*x*		
Track signature		*x*	*v*	*x*	*x*	*v*	*x*		
Scintillation signature	*x*		*v*			*v*		*x*	
North–South separation									*x*
Cosmic-ray flux	*x*	*x*	*x*	*x*				*x*	*x*
Charge range (Dirac units)	0.16–27		1–3	1–30	1–2	1			≥0.3

TABLE IV. Experiments determining limits for density in ordinary matter.

Assumed property	Reference 8	35[a]	39	49	This work
Electromagnetic induction or source of magnetic flux	x			x	x
Acceleration in magnetic field		x	x		
No binding to atoms or nuclei		x			
Extraction		x	x		
Track signature			x		
Scintillation signature		x			
Asymmetry of charge				x	
Charge range (Dirac units)	$>10^{-2}$	0.16–27		unlimited	>0.3
Limit found in monopole/nucleon	10^{-24}	2×10^{-30}	5×10^{-28}	7×10^{-32}	2×10^{-28}

[a] For the value of the density we have used the largest mass mentioned in this paper.

For excellent technical support of the experiment we especially thank John Taylor, Maurilio Antuna, Jr., Roscoe Byrns, Glenn Eckman, Leo Foley, Robert Gilmer, Egon Hoyer, and Hans Stellrecht. For support from the Lunar Receiving Laboratory we thank in particular Bryan Erb, Richard Wright, and William Greenwood.

This experiment would not have been possible without the support of J. Naugle, W. N. Hess of NASA, and, of course, of the astronauts N. Armstrong and B. Aldrin who collected our samples.

*Work done under auspices of U. S. Atomic Energy Commission and NASA Contract No. NASA9-8806.

[1]L. Alvarez, P. Eberhard, R. Ross, and R. Watt, Science 167, 701 (1970); Geochim. Cosmochim. Acta 3, 1953 (1970), Suppl. I.

[2]P. A. M. Dirac, Proc. Roy. Soc. (London) A133, 60 (1931); Phys. Rev. 74, 817 (1948).

[3]A. Goldhaber, Phys. Rev. 140, B1407 (1965).

[4]J. G. King, Phys. Rev. Letters 5, 562 (1960); L. J. Fraser, E. R. Carlson, and V. W. Hughes, Bull. Am. Phys. Soc. 13, 636 (1968).

[5]J. Schwinger, Phys. Rev. 173, 1536 (1968); Science 165, 757 (1969).

[6]L. W. Alvarez, Lawrence Radiation Laboratory Physics Note 479, 1963 (unpublished); J. Schwinger, Phys. Rev. 144, 1087 (1965); D. Zwanziger, Phys. Rev. D 3, 880 (1971).

[7]A. Salam, Phys. Letters 22, 683 (1966).

[8]L. Vant-Hull, Phys. Rev. 173, 1412 (1968).

[9]M. I. Blagov, V. A. Murashova, T. I. Syreitshikova, Yu. Ya. Tel'nov, Yu. D. Usachov, and M. N. Yakimenko, in *Proceedings of the Fifteenth International Conference on High Energy Physics, Kiev, 1970* (Atomizdat, Moscow, 1971).

[10]R. Omnès (private communication); E. Wichmann (private communication).

[11]L. W. Alvarez, Lawrence Radiation Laboratory Physics Note 470, 1963 (unpublished).

[12]P. Eberhard, Lawrence Radiation Laboratory Physics Note 506, 1964 (unpublished); L. J. Tassie, Nuovo Cimento 38, 1935 (1965).

[13]E. Goto, J. Phys. Soc. Japan 13, 1413 (1958).

[14]W. V. R. Malkus, Phys. Rev. 83, 899 (1951).

[15]D. Sivers, Phys. Rev. D 2, 2048 (1970).

[16]See, for instance, D. W. Strangway, E. E. Larson, and G. W. Pearce, Science 167, 691 (1970); G. E. Helsley, *ibid.* 167, 693 (1970); R. R. Doell, C. S. Gromme, A. N. Thorpe, and F. E. Senftle, *ibid.* 167, 696 (1970); C. L. Herzenberg and D. L. Riley, *ibid.* 167, 683 (1970).

[17]J. D. Jackson, *Classical Electrodynamics* (Wiley, New York, 1962), p. 438.

[18]E. Bauer, Proc. Cambridge Phil. Soc. 47, 777 (1951); H. J. D. Cole, *ibid.* 47, 196 (1951).

[19]L. Alvarez, M. Antuna, Jr., R. Byrns, P. Eberhard, R. Gilmer, E. Hoyer, R. Ross, H. Stellrecht, J. Taylor, and R. Watt, Rev. Sci. Instr. 42, 326 (1971).

[20]P. Eberhard, Lawrence Radiation Laboratory Physics Note 715, 1970 (unpublished).

[21]E. M. Shoemaker, M. H. Hait, G. A. Swann, D. L. Schleicher, G. G. Schaber, R. L.Sutton, D. H. Dahlem, E. N. Goddard, and A. C. Waters, Geochim. Cosmochim. Acta 3, 2399 (1970), Suppl. I.

[22]S. H. R.E. L. L. D. A. L. F. F., Geochim. Cosmochim. Acta 2, 1503 (1970), Suppl. I.

[23]R. L. Fleischer, E. L. Haines, H. R. Hart, Jr., R. T. Woods, and G. M. Comstock, Geochim. Cosmochim. Acta 3, 2103 (1970), Suppl. I.

[24]O. Eugster, F. Tera, D. S. Burnett, and G. J. Wasser-

burg, Earth Planet. Sci. Letters 8, 20 (1970); A. L. Albee, D. S. Burnett, A. A. Chodos, O. J. Eugster, J. C. Huneke, D. A. Papanastassiou, F. A. Podosek, G. Price Russ II, H. G. Sanz, F. Tera, and G. J. Wasserburg, Science 167, 463 (1970).

[25]M. B. Duke, C. C. Woo, G. A. Sellers, M. L. Bird, and R. B. Finkelman, Geochim. Cosmochim. Acta 1, 347 (1970), Suppl. I.

[26]G. J. Wasserburg (private communication).

[27]The age of crystallization of the Apollo 11 fine materials has been somewhat of a puzzle. Estimates on the basis of U-Pb or Th-Pb decay chains have all given ages between 4.6×10^9 and 4.7×10^9 years. (See, for instance, Ref. 28.) However, there are more recent arguments indicating that the age is about 3.6×10^9 years (see Ref. 29).

[28]For instance, K. Goplan, S. Kaushal, C. Lee-Hu, and G. W. Wetherill, Geochim. Cosmochim. Acta 2, 1195 (1970), Suppl. I; M. Tatsumoto, *ibid.* 2, 1595 (1970), Suppl. I; R. K. Wanless, W. D. Loveridge, and R. D. Stevens, *ibid.* 2, 1729 (1970), Suppl. I.

[29]D. A. Papanastassiou, G. J. Wasserburg, and D. S. Burnett, Earth Planet. Sci. Letters 8, 1 (1970); also G. J. Wasserburg (private communication).

[30]P. Eberhardt, J. Geiss, H. Graff, N. Grögler, U. Krähenbühl, H. Schwaller, J. Schwarzmüller, and A. Stettler, Geochim. Cosmochim. Acta 2, 1037 (1970), Suppl. I; D. Heymann and A. Yaniv, *ibid.* 2, 1247 (1970), Suppl. I; C. M. Hohenberg, P. K. Davis, W. A. Kaiser, R. S. Lewis, and J. H. Reynolds, *ibid.* 2, 1283 (1970), Suppl. I; T. Kirsten, O. Müller, F. Steinbrunn, and J. Zähringer, *ibid.* 2, 1331 (1970), Suppl. I; K. Marti, G. W. Lugmair, and H. C. Urey, *ibid.* 2, 1357 (1970), Suppl. I.

[31]R. Ross, Lawrence Radiation Laboratory Physics Note 730, 1971 (unpublished).

[32]We use essentially the approximations of Carithers *et al.*, Ref. 38, p. 1075.

[33]M. M. Shapiro, B. Stiller, M. Birnbaum, and F. W. O'Dell, Phys. Rev. 83, 445 (1951).

[34]R. Ross, Lawrence Radiation Laboratory Physics Note 733, 1971 (unpublished).

[35]Henry H. Kolm, Francesco Villa, and Allen Odian, Phys. Rev. D 4, 1285 (1971).

[36]The meteorite samples were from the Odessa, M3, Nordheim, Tulia, and Pueblo de Allende Meteorites, Dr. E. A. King (private communication), and Dr. B. R. Simoneit (private communication).

[37]E. Goto, H. H. Kolm, and K. W. Ford, Phys. Rev. 132, 387 (1963).

[38]W. C. Carithers, R. Stefanski, and R. K. Adair, Phys. Rev. 149, 1070 (1966).

[39]R. L. Fleischer, H. R. Hart, Jr., I. S. Jacobs, P. B. Price, W. M. Schartz, and F. Aumento, Phys. Rev. 184, 1393 (1969).

[40]R. L. Fleischer, P. B. Price, and R. T. Woods, Phys. Rev. 184, 1398 (1969); R. L. Fleischer, H. R. Hart, Jr., I. S. Jacobs, P. B. Price, W. M. Schwarz, and R. T. Woods, J. Appl. Phys. 41, 958 (1970).

[41]W. Z. Osborne, Phys. Rev. Letters 24, 1441 (1970).

[42]E. Amaldi, G. Baroni, A. Manfredini, and H. Bradner, Nuovo Cimento 28, 773 (1963).

[43]E. M. Purcell, G. B. Collins, T. Fujii, J. Hornbostel, and F. Turkot, Phys. Rev. 129, 2326 (1963).

[44]I. I. Gurevich, S. Kh. Khakimov, V. P. Martemianov, A. P. Mishakova, V. V. Ogurtzov, V. G. Tarasenkov, L. M. Barkov, and N. M. Tarakanov, Phys. Letters 31B, 394 (1970).

[45]V. A. Petukhov and M. N. Yakimenko, Nucl. Phys. 49, 87 (1963). We have used the interpretation according to Ref. 46 of this work in quoting the limit in Fig. 8.

[46]E. Amaldi, in *Old and New Problems in Elementary Particles*, edited by G. Puppi (Academic, New York, 1968), pp. 20–61.

[47]R. A. Carrigan, Jr. and F. A. Nezrick, Phys. Rev. D 3, 56 (1971).

[48]P. J. Green, D. R. Tompkins, and R. E. Williams, Bull. Am. Phys. Soc. 12, 190 (1967).

[49]K. H. Schatten, Phys. Rev. D 1, 2245 (1970).

[50]M. A. Ruderman and D. Zwanziger, Phys. Rev. Letters 22, 146 (1969).

N77-16319

Isolation and Characterization of a Triterpenoid Alcohol from the Green River Shale

By W. HENDERSON* and G. STEEL
(Department of Chemistry, University of California, Berkeley, California 94720)

Reprinted from

Chemical Communications 1971

The Chemical Society, Burlington House, London W1V OBN

Isolation and Characterization of a Triterpenoid Alcohol from the Green River Shale

By W. HENDERSON* and G. STEEL
(*Department of Chemistry, University of California, Berkeley, California* 94720)

Summary A triterpenoid alcohol (tetrahymanol) has been isolated from the Green River Shale (60 million years).

SEVERAL publications have shown the presence of fully reduced steroids and triterpenoids (steranes and triterpanes) in the Green River Shale (Eocene, 60×10^6 years old).[1-3] The identities of many of these compounds have been established by capillary g.l.c., capillary g.c.–m.s.,[3] and by *X*-ray crystallography.[2] Although absolute stereochemistries in most cases have not been established, the following structural identifications have been made: cholestane, ergostane, stigmastane, gammacerane, and a hopane-type structure. The presence of these compounds in the Green River Shale has been taken as substantial proof that the original source of the organic content of the sediment was biological and probably dominantly algal.[4] It has been suggested that these molecules were derived from naturally occurring phytosterols, and higher plant and micro-organism triterpenoids which, through the processes of deposition, consolidation and maturation of the sediment, were reduced to the cycloalkanes described above. No evidence has been produced which would confirm this postulate by identifying the precursors of the cycloalkanes, *i.e.*, sterols and triterpenoid alcohols, from this sediment. However, it has been reported that the Messel Oil Shale (Eocene; with a milder geological history than the Green River Formation) does contain triterpenoid alcohols although the authors found no evidence for triterpenoid alcohols in the Green River Shale.[5,6] We now report the isolation and identification of a triterpenoid alcohol from the Green River Shale.

The sediment (350 g) from the Mahogany Ledge was broken into small pieces, pulverized in a disc mill (Angstrom Inc., Chicago, Illinois) and the powder extracted with a mixture of benzene–methanol (3:1 v/v) with ultrasonication. After centrifugation the supernatant solution was separated, evaporated to dryness, and the total extract chromatographed on a silica gel column eluting successively with n-heptane, mixtures of 5—40% diethyl ether in n-heptane, diethyl ether, and finally ethyl acetate. The fractions collected were monitored by analytical t.l.c. using a solvent mixture of n-heptane, diethyl ether, and methanol (18:6:1 v/v). By comparison of the extract fractions with the mobilities of reference compounds some of the fractions obtained using 40% diethyl ether in n-heptane showed constituents with the correct mobilities to be sterol or triterpenoid in character. The hydroxylated compounds were selectively removed from extraneous materials by preparative t.l.c. (n-heptane:benzene 1:1 v/v as mobile phase) in the form of trimethylsilyl ethers. After purification, fractions as trimethylsilyl ethers were examined by g.l.c. on two different liquid phases (*viz.* JXR and OV-17) and finally by g.c.–m.s.[7]

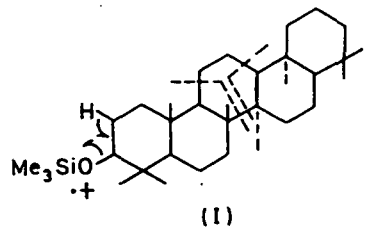

(I)

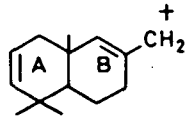

m/e 189

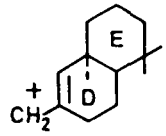

m/e 191

The mass spectra obtained showed that one of the main derivatives had a molecular ion (M) at m/e 500 and showed other ions at m/e 410 ($M - 90$), 395 ($M - 105$), and 73 characteristic of the trimethylsilyl ether of an alcohol. The two most abundant ions in the spectrum were found at m/e 191 and m/e 189, respectively, which were deduced to result from a fragmentation of a symmetrical nucleus such as is found in the pentacyclic triterpenoid alcohol tetrahymanol (I; shown here as the trimethylsilyl ether).

TABLE

G.l.c. retention data for extracts and reference compounds as trimethylsilyl ethers

Parent compound	I(JXR)[a]	I(OV-17)[b]
Alcohol from Green River Shale ..	3520	3725
Alcohol from *Tetrahymena pyriformis*	3520	3725
Authentic tetrahymanol	3520	3730

[a] 10 ft × ⅛ in stainless-steel column packed with 3% JXR on 60–80 mesh Gas Chrom Q at 265°.
[b] 6 ft × ¼ in stainless-steel column packed with 3% OV-17 on 60–80 mesh Gas Chrom Q at 270°.

In order to confirm this tentative identification a sample of the protozoan, *Tetrahymena pyriformis* (from which tetrahymanol had previously been isolated and identified[8]) was obtained and cultured in this laboratory. Extraction and liquid–solid chromatography followed by t.l.c. of the trimethylsilyl ether fraction yielded a mixture of components dominated by tetrahymanol trimethylsilyl ether. Comparison of the g.l.c. retention indices of this component with those of the alcohol isolated from the Green River Shale showed them to be identical. Further confirmation was achieved by comparison of the retention data (Table) and mass spectrum of an authenticated sample of tetrahymanol trimethylsilyl ether with those of the compounds obtained from *Tetrahymena pyriformis* and the Green River Shale.

The triterpane gammacerane has already been identified in the hydrocarbon fraction from Green River Shale,[2,3] and this new evidence showing the presence of the corresponding saturated alcohol indicates that hydroxylated triterpenoids can exist intact over a significant period of geological time and provides information on the mechanisms of diagenesis and maturation of organic natural products in a sedimentary environment. Qualitative evidence indicates the presence of other, as yet unidentified, possible triterpenoid alcohols in the Green River Shale.

We acknowledge a gift of pure tetrahymanol from Dr. F. B. Mallory, Dept. of Chemistry, Bryn Mawr College, Penn. This work was supported by a grant from NASA.

(*Received, September 2nd*, 1971; *Com.* 1538.)

[1] G. Eglinton, P. M. Scott, T. Belsky, A. L. Burlingame, and M. Calvin, *Science*, 1964, **145**, 263.
[2] I. R. Hills, E. V. Whitehead, D. E. Anders, J. J. Cummings, and W. E. Robinson, *Chem. Comm.*, 1966, 752.
[3] W. Henderson, V. Wollrab, and G. Eglinton, *Adv. Org. Geochem.*, 1968, **31**, 181.
[4] W. H. Bradley, *Geol. Soc. Amer. Bull.*, 1966, **77**, 1333.
[5] P. Albrecht and G. Ourisson, *Science*, 1969, **163**, 1192.
[6] G. Mattern, P. Albrecht, and G. Ourisson, *Chem. Comm.*, 1970, 1570.
[7] W. Henderson, W. E. Reed, G. Steel, and M. Calvin, *Nature*, 1971, **231**, 308.
[8] F. B. Mallory, J. T. Gordon, and R. L. Conner, *J. Amer. Chem. Soc.*, 1963, **85**, 1362.

(*Reprinted from Nature, Vol. 231, No. 5301, pp. 308–309, June 4, 1971*)

A71-31367

Isolation and Identification of Sterols from a Pleistocene Sediment

BECAUSE of their chemical stability, alkanes and fatty acids have been widely used as indicators of biological origin in studies of sediments[1–4], but their formation may often be attributable to abiogenic syntheses and transformations[5] so that their distribution patterns should be approached with caution. Little effort has been expended on analysis of sediments for relatively unaltered molecules which are biologically more significant, such as sterols which are present in sea water[6], bottom muds (both marine and non-marine)[7,8], surface soils[9], and an Eocene shale[10]. If such molecules are present in sediments representing a wide period of geological time, their significance with regard to depositional environment and contributory organisms would exceed any other biological marker in common use. We report some organic geochemical studies of a Pleistocene basin and a contemporary lake where we are attempting to correlate alkane, fatty acid, steroid, amino-acid and sugar distribution patterns with stratigraphy and biological environment.

Mono Lake is one of the strongly alkaline desert lakes of eastern California, and has a combination of high organic productivity with almost no scavengers. It is situated in a structural downwarp and has been continuously in existence for ~3 m.y. (refs. 11, 12). Sediments deposited in this lake show no clearly freshwater fauna but contain an abundance of algal debris, diatoms, ostracods and, locally, gastropods.

The sediment analysed contained alternate bands of algal silt and diatomite. It resides within a complete Pleistocene lacustrine sequence and its position within that sequence (that is, 80 m below the top of the Wilson Creek Formation, which is the latest Pleistocene sediment exposed in the Mono Basin) suggests an age ~130,000 yr.

We have isolated and identified the components of a complex mixture of steroids by gas-liquid chromatography (GLC) and combined gas chromatography–mass spectrometry (GCMS). Powdered sediment (9.95 g) was extracted using a mixture of benzene, acetone and methanol (2 : 1 : 1 v/v). The concentrated extract (6.75% w/w of sediment) was chromatographed on a silica gel column eluting successively with heptane, benzene and methanol. The methanol fraction was saponified with 5% NaOH and the non-saponifiables were dissolved in ether, chromatographed on a modified McCarthy-Duthie column[13] and the ether collected. The presence of sterols in this fraction was established on analytical thin-layer chromatographic plates (silica gel; 0.25 mm, using ceric sulphate and sulphuric acid spray reagent) by comparison with authentic sterols. Isolation of the sterol fraction was carried out by preparative thin-layer chromatography on silica gel with chloroform and ethyl acetate (3 : 1 v/v) as the mobile phase. The total fraction in pyridine solution was treated with *bis*-(trimethylsilyl) fluoroacetamide and trimethylchlorosilane (5 : 1 v/v). The resultant sterol trimethylsilyl ethers were analysed by GLC on a Perkin–Elmer Model 900 instrument using JXR, OV-17 and OV-210 as liquid phases. High and low voltage (70 and 16 eV) mass spectrometry (GEC-AEI MS-12) using a direct introduction solid probe yielded molecular ion data for the principal components of the complex mixtures. Single component identifications were achieved by GCMS using an Aerograph 204 gas chromatograph (flame ionization detector) coupled directly to a Dupont 492–1 mass spectrometer without a molecular separator or effluent splitting device.

Table 1 Identities of Sterols found in a Mono Lake Sediment

Peak	Retention index * (JXR)	Identity
1	3,120	
2	3,155	Cholesterol † TMS and cholestanol ‡ TMS
3	3,195	Brassicasterol † TMS
4	3,250	*Campesterol* † TMS
5	3,285	Stigmasterol † TMS and compound ‡ molecular weight 486
6	3,340	Stigmastanol † TMS and β-sitosterol TMS †
7	3,410	Compound of molecular weight 502 thought to be lanostanol ‡ TMS

* GLC retention indices from a 10 foot × 1/8 inch stainless steel column containing 3% JXR on 60–80 mesh (gas Chrom Q) at 265° C.

† These identifications made by GLC and GCMS analyses.

‡ These identifications made by GCMS alone.

The results of the analysis of the purified sterol fraction in the form of trimethylsilyl ethers (TMS) by GLC is shown in Fig. 1. Comparison of the retention data obtained on two liquid phases (JXR, OV-17) with those of reference sterol derivatives suggested the following assignment of peak 2 to cholesterol TMS, peak 3 to brassicasterol TMS, peak 4 to campesterol TMS, peak 5 to stigmasterol TMS and peak 6 to β-sitosterol TMS. But analysis by GCMS indicated that some of the peaks contained more than one component. Peak 2 was shown to contain the TMS ethers of cholesterol and cholestanol, peak 5 contained a derivative of molecular weight 486 as well as stigmasterol TMS and peak 6 was chiefly stigmastanol TMS with a little β-sitosterol TMS. The assignments given to the chief peaks in Fig. 1 are also shown in Table 1. Further analyses by GLC on a more polar liquid phase (OV-210) confirmed the multicomponent nature of peaks 5 and 6 (Fig. 1).

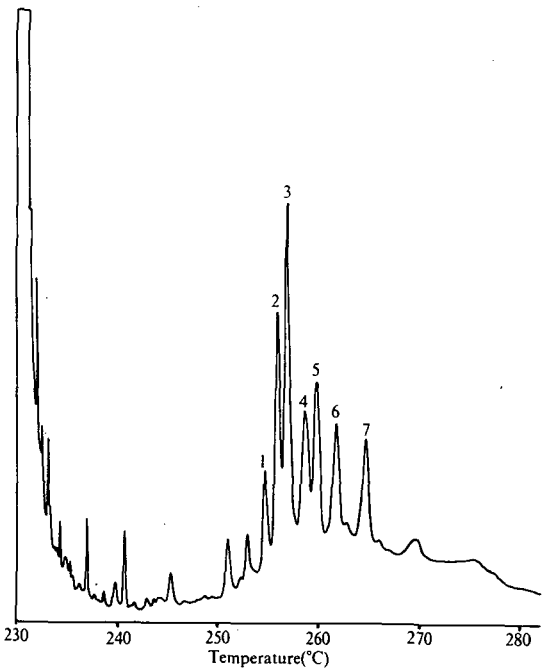

Fig. 1 Gas chromatogram of sterol trimethylsilyl ethers from a Mono Lake sediment obtained using a 10 foot × 1/8 inch stainless steel column packed with 3% JXR on 60–80 mesh ('Gas Chrom Q'). The column was programmed between 230° C and 280° C at 2° C min^{-1}

The types of sterol found in the sediment examined strongly suggest that they had an algal origin and underwent a certain amount of reduction during sedimentation and the initial stages of lithification. Indeed, cholesterol, stigmasterol and β-sitosterol are known components of fresh water algae[14,15] and cholesterol, brassicasterol, campesterol and β-sitosterol have been found in marine algae[16]. It may, therefore, not be possible to use sterol distribution patterns for identification of the deposition environment of a sediment (compare ref. 8).

Analyses of *in vitro* cultures of Mono Lake wild algae so far confirm the algal origin of the unsaturated sterols isolated from the sediment. There is no evidence for the presence of fully saturated sterols in the algae.

The identification of fully saturated counterparts of algal sterols, together with the unaltered compounds, is good evidence that at least partial reduction of naturally occurring molecules has taken place within the 130,000 yr since deposition. Simulated diagenesis experiments (using pressure, relatively mild temperatures and reducing conditions) seem to generate significant quantities of the fully reduced steroid hydrocarbons (steranes). Further work may not only allow chemotaxonomic correlations of organic compositions (alkanes, fatty acids, sterols, amino-acids and sugars) of sediments and contemporary organisms, but may also yield more specific information about the rates of the alteration of organic material in a geological environment and other parameters involved.

This work was supported by NASA.

WILLIAM HENDERSON
WALTER E. REED
GORDON STEEL
MELVIN CALVIN *

Department of Chemistry,
University of California,
Berkeley, California 94720

Received April 6, 1971.

* Present address: Laboratory of Chemical Biodynamics, University of California, Berkeley, California 94720.

[1] Eglinton, G., in *Advances in Organic Geochemistry* (edit. by Schenck, P. A., and Havenaar, I.), 1 (Pergamon Press, Oxford, 1968).
[2] Blumer, M., and Cooper, W. J., *Science*, **158**, 1463 (1967).
[3] Oró, J., Nooner, D. W., Zlatkis, A., Wikström, S. A., and Barghoorn, E. S., *Science*, **148**, 77 (1965).
[4] Henderson, W., Wollrab, V., and Eglinton, D., in *Advances in Organic Geochemistry* (edit. by Schenck, P. A., and Havenaar, I.), 181 (Pergamon Press, Oxford, 1968).
[5] Studier, M. H., Hayatsu, R., and Anders, E., *Geochim. Cosmochim. Acta*, **32**, 151 (1968).

[6] Matthews, W. S., and Smith, L. L., *Lipids*, **3**, 239 (1968).
[7] Schwendinger, R. B., and Erdman, J. G., *Science*, **144**, 1575 (1964).
[8] Attaway, D., and Parker, P. L., *Science*, **169**, 674 (1970).
[9] Meinschein, W. G., and Kenny, G. S., *Anal. Chem.*, **29**, 1153 (1957).
[10] Mattern, G., Albrecht, P., and Ourisson, G., *Chem. Commun.*, 1570 (1970).
[11] Gilbert, C. M., Christensen, M. N., Al-Rawi, Y., and Lajoie, K. R., in *Studies in Volcanology* (edit. by Coats, R. R., Hay, R. L., and Anderson, C. A.), Memoir 116 (Geological Society of America, 1968).
[12] Lajoie, K. R., thesis, Univ. California, Berkeley (1968).
[13] McCarthy, R. D., and Duthie, A. H., *J. Lipid Res.*, **3**, 117 (1962).
[14] Reitz, R. C., and Hamilton, J. G., *Biochem. Physiol.*, **25**, 401 (1968).
[15] de Souza, N. J., and Nes, W. R., *Science*, **162**, 363 (1968).
[16] Ikekawa, N., Morisaki, N., Tsuda, K., and Yoshida, T., *Steroids*, **12**, 41 (1968).

Printed in Great Britain by Flarepath Printers Limited, Watling Street, Colney Street, St Albans, Herts.

A72-20290

LETTERS TO NATURE

Carbon Chemistry of Apollo 14 Size-fractionated Fines

TOTAL carbon measurements of crystalline lunar rocks returned by the Apollo missions have revealed only low concentrations of carbon (10–50 p.p.m.)[1–3]. The breccias and fines, however, have, in general, higher carbon concentrations (up to 200 p.p.m.). This carbon is more concentrated in the finer fractions[1] and is correlated with the noble gas content of the solar wind[2]. It has been postulated that most of the carbon associated with the fines and breccia originated in the solar wind[1,4]. The dissolution of lunar material in mineral acids and direct pyrolysis have been the principal techniques used to reveal the nature of this lunar carbon; in particular, experiments[5–8] on Apollo 12 samples using deuterated reagents have shown the presence of indigenous CH_4 and C_2H_6. The CD_4, C_2D_4 and C_2D_6 also released are evidence for the presence of hydrolysable carbides in the samples. The yields of these gases from several samples have been shown[6,7] to correlate with various parameters related to exposure to the solar wind. Shallow etching of fines with NaOD released more than 60% of the CH_4 found by complete dissolution[7], indicating that most of the CH_4 is in the surface of the grains and may therefore be connected with implantation by the solar wind[5].

We have conducted experiments on several Apollo 12 and 14 samples that confirm the identification of CH_4 and C_2H_6 in lunar fines and breccias. In particular, we report data in this communication for various size fractions of sample 14240,5 which show that the concentrations of these species are dependent on particle size. This effect is expected if the CH_4 and C_2H_6 are located in the surface of the grains. The trapped fraction of the noble gases has been shown convincingly[9,10] to be associated with implantation by the solar wind by this size fractionation technique, and our results strongly support proposals[5,8] that solar wind activity is a source of CH_4 in lunar samples. Sample 14240,5 is from the Special Environmental Sample Container (SESC) and consists of fines from the bottom of the 30 cm trench at station G. This sample was sealed on the Moon and was not opened until distribution from the University of California ultra clean facility[11,12]. Results are also reported on other samples from the same trench (14149, 14148, 14156 all sieved to sizes of less than 1 mm).

All handling of the samples before dissolution or pyrolysis took place in the controlled atmosphere of a glove box flushed with dry nitrogen (H_2O, 20 p.p.m.; CO_2, CH_4, <0.1 p.p.m.)[11]. The handling included sieving into five size fractions, the cumulative weight percentages of which (not including fragments larger than 5 mm) were as shown in Table 1.

This size distribution agrees with that reported for the trench sample 14149 (ref. 3) and indicates that these two adjacent samples are indeed similar. Dissolutions were carried out in a glass system using 30 to 40% DF for 1 to 2 h with subsequent fractionation and concentration of the evolved gases by traps and mercury pumps. Identification and quantitative estimation of the gases were accomplished by high resolution mass spectrometry. A fraction of the gases was also passed into a high sensitivity helium ionization gas chromatograph (Varian-Aerograph, model 1732). Pyrolysis was carried out directly into the ion source of an AEI MS-902 mass spectrometer with LOGOS computer data acquisition[13]. A resolution of 6,000 was used to enable the separation and identification of many important multiplets in the mass spectra such as $O/NH_2/CH_4$, $^{20}Ne/H_2{}^{18}O$ and $CO/N_2/C_2H_4$ (see also ref. 14).

Table 1 Cumulative Weight Percentages of the Five Size Fractions

>420 μm	46.0%
420–106 μm	60.5%
106–53 μm	70.0%
53–37 μm	77.5%
<37 μm	100.0%

Table 2 Yields of Some Gases released by DF Etch of Apollo 14 Samples (nmole g^{-1})

Apollo 14 samples	CD_4	CH_4	^{20}Ne	^{36}Ar	C_2H_6	DCN	D_2S	CS_2
14240,5 >420 μm	57	15	7	1.3	ND	ND	ND	ND
14240,5 420–106 μm	130	24	10	2.9	1.0	0.5	2.0	15
14240,5 106–53 μm	450	110	20	8.0	10	60	7,200	10
14240,5 53–37 μm	380	120	23	12	13	62	1,900	2.6
14240,5 <37 μm	770	300	72	21	140	24	12,200	47
14148,3 surface <1 mm	810	290	40	25	3.5	50	760	110
14156,6 middle <1 mm	580	160	31	15	10	20	4,700	7.6
14149,25 bottom <1 mm	370	150	38	12	1.2	13	3,700	4.0

ND, Not determined.

Table 2 summarizes the amounts of some of the gases evolved on DF dissolution. Besides CD_4, higher deuterocarbons, up to C_5D_{10}, were detected but the yields were 10 to 100 times lower. The yields of ^{20}Ne and ^{36}Ar, derived from the solar wind, provide a measure of influence of the solar wind on the soil, although an exposure age is not directly calculable from the concentrations of these gases, because of saturation, diffusive loss, and impact heating effects[9,10]. Fig. 1 shows the yields of CH_4, CD_4, ^{20}Ne and ^{36}Ar from the SESC fractions. There is a linear correlation of the surface area parameter, $1/r$, with the contents of CH_4, ^{20}Ne and ^{36}Ar, showing that these components are associated with the surface of the grains. This type of correlation has been observed for noble gases in the solar wind that were released on pyrolysis of Apollo 11 and 12 fines[9,10]. The reaction of protons in the solar wind with carbon in the fines has been suggested as a source of the CH_4 (ref. 5) and this model is supported by the surface area dependence of this product. The SESC sample was exposed to very low moisture levels; thus hydrolysis of lunar carbides by terrestrial water adsorbed during handling is not likely to have occurred to any significant extent[15]. This view is supported by our pyrolysis experiments on the size fractions where CH_4, ^{20}Ne, C_2H_6 and ^{36}Ar are released in the 500° to 800° C temperature range in amounts equivalent to those observed on dissolution. The similar temperature release patterns for these gases support association of the CH_4 and C_2H_6 with the gases implanted by the solar wind in the outer few microns of the grains, where they can be released at temperatures below melting-point. If a substantial proportion of this methane arose from hydrolysis of carbides

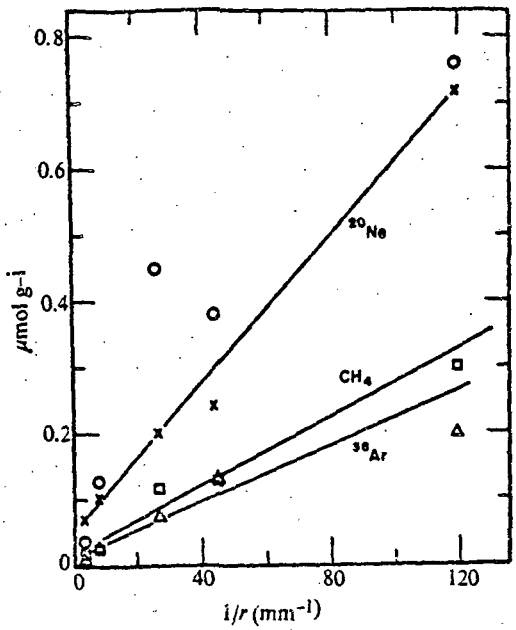

Fig. 1 Correlation plot of the gases released by DF etch with grain size for sample 14240,5. ○, CD_4; □, CH_4; ×, ^{20}Ne (×10); △, ^{36}Ar (×10).

by contaminating water, it is unlikely that it would be bound as strongly as gases arising from implantation by the solar wind.

The 0.14 μmol g^{-1} of C_2H_6 that was released on dissolution of the size fraction <37 μm is the highest that has been observed, and, when related to the low yields obtained from the coarser fractions, a higher dependence on grain radius than r^{-1} is indicated for this component. An r^{-2} dependence would be expected if the C_2H_6 is formed in the surfaces of the fines by bimolecular processes involving single carbon species. Two plausible mechanisms are, first, the formation of C_2 species when carbon in the solar wind reacts with C atoms already present and the building up of these species into C_2H_6 by reaction with protons in the solar wind; second, photolytic, radiolytic or thermal decomposition of the methane in the fines to yield methyl radicals which could then combine to give ethane. The harsh radiation environment means that the probability of survival for organic molecules on the lunar surface must be considered. The half-life, before ionization by protons in the solar wind, of methane molecules in the outer 0.5 μm of the grains can be estimated to be of the order of 10 yr by assuming four ionizations per 100 eV dissipated in the surface layer by each 1 keV proton at a flux of 2×10^8 cm^{-2} s^{-1} and using the measured CH_4 concentration of 2×10^{14} molecules cm^{-2} (ref. 16). When isolated in an inorganic lattice, methane molecules may be relatively stable to ionization and subsequent neutralization. Destruction times longer than $\sim10^2$ yr do not, however, seem likely. Therefore, to maintain significant concentrations of methane or other organic molecules in the layer accessible to protons in the solar wind, production rates must be sufficient to produce the required concentration in the same time period, 2×10^{12} molecules cm^{-2} yr^{-1} for CH_4, for example. This production rate is probably too high because the proton flux, which is presumed also to play a part in the methane production as well as destruction, is only a factor of 3×10^3 higher, and methane formation cannot be a very favoured process. A steady state mechanism would predict that the CH_4 concentration should become constant after an exposure time of the order of 100 yr, whereas there is good evidence for increasing CH_4 content with exposure time[6,7,14]. A more plausible mechanism may involve a much lower production rate combined with diffusion of some of the CH_4 deeper into grains where it would be protected from solar radiation. The distribution of gases induced by the solar wind in lunar samples has been explained by this process and the diffusion may be activated by wind-

particles[10] but cannot be sufficient to alter significantly the surface correlated character of the gases. Neon has a mean penetration depth of ~2 μm (ref. 10), a factor of 10 more than expected from direct penetration of particles in the solar wind. This is a plausible depth for most of the methane and ethane and would result in a surface area dependence of the type reported here, while not requiring as high a production rate as is necessary if the molecules were in the outer sub-micron layer of the grains. Solar flare particles and cosmic rays will still be able to cause destruction, but their fluxes are at least six orders of magnitude lower than that of the solar wind.

The pattern of deuterocarbon release from the samples is similar to that produced by Fe_3C (refs. 8, 14) or meteoritic cohenite $(Fe,Ni)_3C$ (ref. 7). Solar wind implantation or meteoritic material have been suggested as possible sources for carbide material in lunar samples[1,4,7,17]. As the yields of CD_4 from the sieved fractions also exhibit a rough inverse correlation with grain size (Fig. 1), the solar wind would seem a plausible source. A concentration of meteoritic material in the finer fractions is another possibility in view of the explosive impact expected for meteorites striking the lunar surface. Previous arguments[1,2] for loss of meteoritic carbon on impact do not seem conclusive. The high ratio of ^{13}C to ^{12}C for carbon in the fines compared with meteoritic carbide[4,17] has been postulated as due to "hydrogen-stripping" by protons in the solar wind[4]. The direct observation of carbide grains in lunar fines[18–20], and a recent calculation that the solar wind may only contribute as little as 50 p.p.m. carbon to the fines[21], could mean that meteoritic material plays a more important part in lunar carbon chemistry than has been previously assumed[1,2]. Metal particles and inclusions in Apollo 11 and 12 samples have been identified as predominantly of meteoritic origin[22]. Carbides would be expected to be found in association with the Fe, Ni and Co phases. No grain size distribution for these particles is, however, available at present.

The DCN, D_2S and CS_2 released during the DF hydrolysis of these samples are of some interest. The yields listed in Table 2 correspond to roughly 150 p.p.m. S as D_2S and 0.1 to 0.5 p.p.m. each as DCN and CS_2. HCN, H_2S, SO_2 and CS_2 were also observed on pyrolysis of these samples. Solar wind interactions may introduce the protobiologically important C–N and C–S bonds into the surface of the lunar fines. CS_2 is also a prominent pyrolysis product of carbonaceous chondrites[14]. The D_2S is the hydrolysis product of FeS, which is known to be present in lunar samples as the mineral troilite[23]. Difficulty was experienced, however, in reproducing the yields of D_2S, DCN and CS_2 and their variation, listed in Table 2, probably cannot be taken as differences due to grain size or sample location. It seems that only variable portions of these gases (of relatively low volatility) are recovered from our dissolution system.

The trench samples exhibited rather similar yields of gases to those from the SESC sample (taking a weighted average for the sieved fractions), as would be expected because of the common site for this set of samples and their similar total carbon contents[2] (14148, 160 p.p.m.; 14156, 180 p.p.m.; 14149, 145 p.p.m.). There is a slight trend to lower yields with depth in the trench for the gases released on dissolution. This may be due to the coarser nature of the bottom trench sample[3] rather than any gross difference in history.

It should be noted that dissolution releases less than 10% of the carbon content of these samples as has also been noted for Apollo 11 and 12 samples[7,8]. Pyrolysis of these Apollo 14 samples also showed that most of the carbon is released as CO at temperatures between 900° and 1,300° C. Carbides are known to exhibit this type of pyrolysis behaviour[8,24] and only to release a fraction of their carbon as hydrocarbons on acid hydrolysis[7,14]. Other nonvolatile and nonhydrolysable carbon phases such as amorphous carbon and SiC may, however, also be present.

We thank Dr J. Chang, Miss R. Jackson, Mr H. Melling, Mr J. Wilder and Mrs E. Yang for

We also thank Admiral A. Shepard for filling the SESC in trying conditions on the Moon and returning it. Financial support from NASA is gratefully acknowledged.

P. T. HOLLAND
B. R. SIMONEIT
P. C. WSZOLEK
W. H. MCFADDEN
A. L. BURLINGAME*

Space Sciences Laboratory, University of California, Berkeley, California 94720

Received December 13, 1971.

* John Simon Guggenheim Memorial Fellow, 1970–1971.

1 Moore, C. B., Gibson, E. K., Larimer, J. W., Lewis, C. F., and Nichiporuk, W., *Proc. Apollo 11 Lunar Sci. Conf.*, **2**, 1375 (Pergamon, London, 1970).
2 Moore, C. B., Lewis, C. F., Larimer, J. W., Delles, F. M., Gooley, R. C., and Nichiporuk, W., *Proc. Second Lunar Sci. Conf.*, **2**, 1343 (MIT, Cambridge, 1971).
3 LSPET Apollo 14 report, *Science*, **173**, 681 (1971).
4 Kaplan, I. R., Smith, J. W., and Ruth, E., *Proc. Apollo 11 Lunar Sci. Conf.*, **2**, 1317 (Pergamon, London, 1970).
5 Abell, P. I., Eglinton, G., Maxwell, J. R., Pillinger, C. T., and Hayes, J. M., *Nature*, **226**, 251 (1970).
6 Cadogan P. H., Eglinton, G., Maxwell, J. R., and Pillinger, C. T., *Nature*, **231**, 29 (1971).
7 Abell, P. I., Cadogan, P. H., Eglinton, G., Maxwell, J. R., and Pillinger, C. T., *Proc. Second Lunar Sci. Conf.*, **2**, 1843 (MIT, Cambridge, 1971).
8 Chang, S., Kvenvolden, K. A., Lawless, J., Ponnamperuma, C. A., and Kaplan, I. R., *Science*, **171**, 474 (1971).
9 Eberhardt, P., Geiss, J., Graf, H., Grögler, N., Krähenbühl, U., Schwaller, H., Schwarzmüller, J., and Stettler, A., *Proc. Apollo 11 Lunar Sci. Conf.*, **2**, 1037 (Pergamon, London, 1970).
10 Kirsten, T., Steinbrunn, F., and Zähringer, J., *Proc. Second Lunar Sci. Conf.*, **2**, 1651 (MIT, Cambridge, 1971).
11 Burlingame, A. L., Holland, P., McFadden, W. H., Simoneit, B. R., Wilder, J. T., and Wszolek, P. C., *UCB Space Sciences Laboratory Organic Clean Room and Lunar Material Transfer Facilities* (University of California, Space Sciences Laboratory Report, Berkeley, May 1971).
12 Burlingame, A. L., Holland, P., McFadden, W. H., Simoneit, B. R., Wilder, J. T., and Wszolek, P. C., *UCB Space Sciences Laboratory Simulation 3 Sand Transfer and Transfer of Apollo 14 SESC Lunar Material* (University of California, Space Sciences Laboratory Report, Berkeley, June 1971).
13 Smith, D. H., Olsen, R. W., Walls, F. C., and Burlingame, A. L., *Anal. Chem.*, 43, 1796 (1971).
14 Holland, P. T., Simoneit, B. R., Wszolek, P. C., and Burlingame, A. L., *Intern. J. Space Biol. Med.* (in the press).
15 Oró, J., Flory, D. A., Gibert, J. M., McReynolds, J., Lichtenstein, H. A., and Wikstrom, S., *Proc. Second Lunar Sci. Conf.*, **2**, 1913 (MIT, Cambridge, 1971).
16 Tilles, D., *Science*, **148**, 1085 (1965).
17 Epstein, S., and Taylor, H. P., *Proc. Second Lunar Sci. Conf.*, **2**, 1421 (MIT, Cambridge, 1971).
18 Frondel, C., Klein, C., Ito, J., and Drake, J. E., *Proc. Apollo 11 Lunar Sci. Conf.*, **1**, 445 (Pergamon, London, 1970).
19 Carter, J. L., and MacGregor, I. D., *Proc. Apollo 11 Lunar Sci. Conf.*, **1**, 247 (Pergamon, London, 1970).
20 Anderson, A. T., Crew, A. V., Goldsmith, J. R., Moore, P. B., Newton, J. C., Olsen, E. J., Smith, J. V., and Wyllie, P. J., *Science*, **167**, 587 (1970).
21 Hayes, J. M., *Intern. J. Space Biol. Med.* (in the press).
22 Goldstein, J. I., and Yakowitz, H., *Proc. Second Lunar Sci. Conf.*, **1**, 177 (MIT, Cambridge, 1971).
23 Evans, T. E., *Proc. Apollo 11 Lunar Sci. Conf.*, **1**, 399 (Pergamon, London, 1970).
24 Gibson, jun., E. K., and Johnson, S. M., *Proc. Second Lunar Sci. Conf.*, **2**, 1351 (MIT, Cambridge, 1971).

Simulation Study of Lunar Carbon Chemistry

LUNAR fines are a source of information about surface phenomena on the Moon, including solar wind implantation, the rate and extent of meteorite bombardment, the effects of solar flares and cosmic rays, and the formation of and reimplantation from the lunar atmosphere.

It is now clear that total carbon[1,2], "carbides" and hydrocarbon gases, principally CH_4 (refs. 3, 4 and P. H. C., G. E., J. M. N. F., J. R. M., B. J. M. and C. T. P., to be published), can be correlated with the surface areas of the particles in lunar fines. Indeed, the concentrations of CD_4 (from the "carbides") and of CH_4 released by DCl treatment of Apollo 11 fines increase linearly with the inverse of particle size in the range 48 to 152 μm. They can also be correlated with several parameters relating to lunar surface exposure of the fines. The data suggest that solar wind implantation plays a significant role in the synthesis of endogenous hydrocarbons. Also, a dual extra-lunar origin (solar wind implantation and meteoritic impact) seems likely for the "carbides"[5,6]. There are several laboratory processes by which hydrocarbons[7–11] and iron–carbon alloys[12] can be produced from reactive species of carbon and hydrogen; these include the reaction of protons generated from hydrogen by microwave discharge[7,8] or dissociation at a hot filament[9], with elemental carbon (lampblack, graphite or diamond) to produce hydrocarbons; the generation of C–H or C–D bonds in diamond irradiated with protons or deuterons (0.7 to 1.5 MeV) from a Van de Graaff generator[10,11]; and the formation of alloys with the structure of martensite in iron implanted with carbon[12].

Ion implantation into crystalline solids can result in the formation of amorphous outer layers accompanied by a reduction in the albedo, the precipitation of gases (for example, Ar) into voids and of compounds from solid solutions, thermal and radiation enhanced diffusion of the implanted species, preferential erosion effects, and in some cases increased solubility of the material in mineral acids[13,14]. Effects of this type have an obvious relevance to the implantation of ionized species (solar wind, solar flares and cosmic rays) into the lunar surface. In fact, several have been reported for lunar fines (amorphous coatings and variations in albedo in micron sized particles[15], increased mineral solubilities in DCl (P. H. C., G. E., J. M. N. F., J. R. M., B. J. M. and C. T. P., to be published), and preferential erosion of FeS relative to metallic iron on the surfaces of glass particles[16]. Such observations are consistent with ion bombardment at the energy and flux estimated for the solar wind.

We have attempted to test the above hypothesis about the origin of lunar hydrocarbons and "carbides" by implanting carbon and hydrogen ionized species ($^{13}C^+$, D_2^+) into several targets (Table 1), including lunar fines. Target disks (1.3 cm in diameter) were prepared by compression of the fine material with KBr (about 30% by weight). Iron films were vacuum deposited onto glass (10^{-4} torr, filament temperature > 1,100° C). Both sides of the targets were then irradiated in an isotope separator[17]. Doses of $^{13}C^+$ and D_2^+ (more than 99% pure and generated from CO and D_2 respectively) were 5×10^{15} atoms cm^{-2} and 1×10^{18} molecules cm^{-2}, at fluxes of 3×10^{12} atoms s^{-1} and 1.4×10^{14} molecules s^{-1} respectively. The labeled products released by acid dissolution or pyrolysis of the implanted targets were measured by low resolution mass spectrometry. Beam energies ($^{13}C^+$, 13 keV per atom; D_2^+, 10 keV per molecule) were similar to those estimated for the solar wind (1 keV per nucleon); both species would be expected to penetrate the targets to depths between 300 and 700 Å. The simulation is only approximate in that species were implanted consecutively and high fluxes were used to shorten the time scale, D_2^+ being used instead of D^+ (although D_2^+ might be expected to dissociate on impact).

The results show, first, that methane was synthesized in the targets of fines either completely ($^{13}CD_4$) or partly ($^{12}CD_4$) from the irradiating species, and, second, that material reacting as carbide was synthesized in the metal targets (Al, Fe) and possibly also in the targets containing fines. Samples that were not irradiated did not contain ^{13}C and D species in quantities greater than expected from terrestrial abundances. The yields of $^{13}CD_4$ and $^{12}CD_4$ measured for one sample of fines by gas chromatography and mass spectrometry were about 2% and about 1% (% ^{13}C and D). The yields of labelled species from the fines targets were higher than from KBr alone. We had anticipated that irradiation with $^{13}C^+$

SEARCH FOR X RAYS FROM THE PLANET JUPITER

A72-17445

K. C. HURLEY

A Reprint from

JANUARY 1, 1972

Journal of Geophysical Research

VOLUME 77 NUMBER 1

PUBLISHED BY
THE AMERICAN GEOPHYSICAL UNION

Search for X Rays from the Planet Jupiter

K. C. HURLEY

Space Sciences Laboratory, University of California, Berkeley 94720

Actively collimated balloon-borne scintillation counters employing a special phoswich anticoincidence technique were flown a total of 5 times from Palestine, Texas. Jupiter was observed for a total of 133 min, and an upper limit to the flux of X rays present at the observation time is 1.6×10^{-2} X rays/cm^2 sec in the energy range 30–100 kev. Three separate calculations are made to estimate the flux of Jovian X rays at the earth; the first two calculations involve scaling up terrestrial precipitating electron fluxes by factors that depend on the energy intercepted by Jupiter's magnetosphere and the Jovian magnetic-field strength, whereas the third estimate is based on a model of Jovian decametric emission. These estimates range from 10^{-9} to 10^{-1} X rays/cm^2 sec in the energy range 30-100 kev. It is concluded that, since there was no decametric emission at the time of the flight and there had been no significant solar activity for several days prior to the flight, no X rays were being generated at the time of the observation.

The existence of a Jovian magnetosphere containing energetic electrons has been established from radio astronomical measurements. Thus Jupiter should be a source of bremsstrahlung X rays generated when electrons precipitate into the upper atmosphere from the radiation belts. Excluding the present work, three attempts were made to detect Jovian X rays [*Fisher et al.*, 1964; *Edwards and McCracken*, 1967; *Haymes et al.*, 1968]. All three of these attempts suffered from short observation times, and in all instances the results were negative.

X rays are produced sporadically in the earth's auroral zones, mainly in connection with magnetospheric substorms. Thus Jupiter, like the earth, might be X-ray 'quiet' for several days or more at a time; then, perhaps following a large solar flare, electron precipitation might occur for a period of several hours to a day, during which time X rays would be generated. Afterward Jupiter might lapse back into a quiet state, remain quiet for several days, and so on.

A correlation might also exist between Jovian decametric emission and X radiation. If decametric storms are caused by electron precipitation and if the fluxes are sufficiently high, X rays and gyroradiation might be generated simultaneously. This possibility will be considered in more detail in a following section.

Copyright © 1972 by the American Geophysical Union.

EXPERIMENTAL APPARATUS

A balloon-borne scintillation counter was employed as a directional X ray detector; this detector is illustrated in Figure 1. The heart of the detector is a NaI-CsI phosphor sandwich, or phoswich for short. Surrounding the phoswich, but optically separate from it, is a NaI(Tl) annulus viewed by 6 photomultipliers. Sitting on top of the phoswich and annulus, but optically separate from both, is a cylindrical CsI collimation crystal viewed by 4 photomultipliers; it contains an array of 99 holes leading to the phoswich.

The main crystal is operated in anticoincidence with the annulus and collimator. The only unobstructed path to the main crystal is through the array of holes in the CsI collimator, which defines a 5.7° viewing angle. In addition, pulse-shape discrimination on the phoswich output insures that most photons scattered in the NaI crystal are rejected; thus only photoelectric interactions in the NaI crystal are counted.

The detector is placed in a subframe that contains an equatorial mount and is motor-driven on the right ascension and declination axes. To maintain the right ascension axis parallel to the earth's axis as the balloon drifts north or south, the entire subframe may be rotated by a motor-drive and lead-screw arrangement. The right ascension and declination positions are read out to the nearest 0.35° by means of shaft

encoders; the subframe position is corrected to the nearest 0.5°. Also present on the subframe is a radioactive calibration source containing a mixture of Co 57 and Am 241; this source can be commanded in front of the collimation holes to accumulate a known spectrum.

The subframe is placed in a larger main frame; this frame is oriented by means of a magnetometer and torque motor. Since the separation between true and magnetic north varies considerably over the earth's surface, the magnetometer is attached to a motor drive, and thus it can be rotated while the balloon drifts. Accuracy of north-south alignment is maintained to 0.5° in this manner. The main frame contains a gyroscope used to detect oscillations or displacements from vertical.

The gondola was completely controlled from the ground by radio command; data was transmitted to the ground in 32 channels each 1 msec long by means of a pulse-duration modulation–frequency modulation system and was recorded on magnetic tape along with time signals from station WWV for later playback and analysis.

FLIGHT PROGRAM

Flights were made when Jupiter was in the night sky for two reasons. First, the earth is closest to Jupiter in this configuration, and therefore the flux is larger. Second, the solar activity on the side of the sun facing Jupiter can be observed at the earth. Thus, in principle, an observation of a solar flare and a subsequent geomagnetic disturbance can be used to estimate the travel time of flare particles out to Jupiter, and a flight time can be chosen for which there is a significant chance of X-ray emission.

One other method of choosing the flight time was used. Since the control that the Jovian satellite Io exerts over the decametric radiation

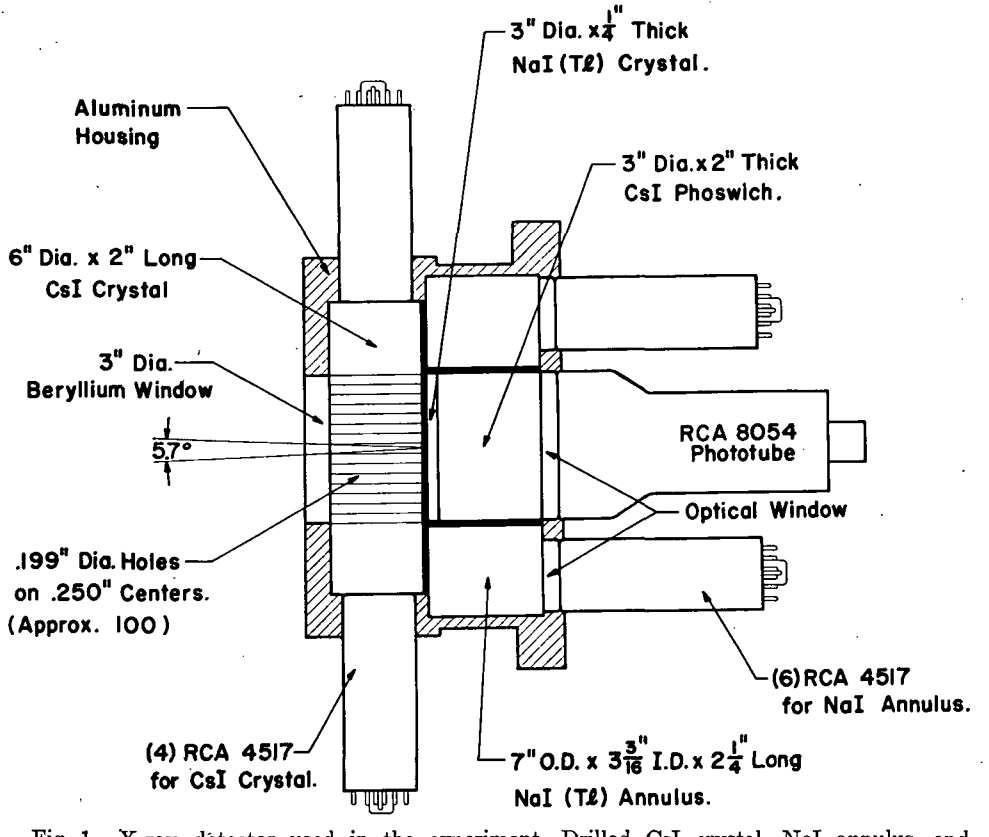

Fig. 1. X-ray detector used in the experiment. Drilled CsI crystal, NaI annulus, and NaI-CsI phoswich are optically separate from one another. The crystal effective area is 20.1 cm^2. The geometry factor is 0.156 cm^2 ster.

is virtually 100% at some frequencies, it is possible to predict the nights on which decametric radiation will occur. Although both of these methods were used for choosing most of the flight days, the one successful flight was made on a night when no decametric emission was present and there had been no significant solar activity for several days.

Once the balloon reached float altitude, the magnetometer servo system was turned on and the detector was oriented toward Jupiter. The right ascension drive was then set to the sidereal rate and Jupiter was tracked for 30 min. After 30 min, the calibration source was commanded in front of the detector for approximately 5 min, and the detector was swung backward in right ascension through an angle of 7.5° (corresponding to 30 min of the earth's rotation). The right ascension drive was then set to the sidereal rate, and a background spectrum was accumulated for 30 min. Then the detector was swung forward in right ascension to reacquire Jupiter, and Jupiter was tracked for another 30 min, and so on. Two purposes were served by this type of observing program. First, since Jupiter was expected to be a very weak X-ray source, the detector counting rate while looking at Jupiter would probably differ only slightly from the background counting rate. Thus, to make the best use of the total float time, equal statistics would be needed for Jupiter and background (i.e., equal observing times). Second, it would eliminate any anisotropy in the background counting rate, since the background spectra were acquired at the same altitude and azimuth angles as Jupiter. No known cosmic X-ray sources were in the field of view during these observations.

The course of the balloon was charted on a map and corrections were made by radio command for the changing latitude, magnetic-field direction, and local time.

RESULTS

Only one flight was successful enough to allow data analysis; it was launched on April 22, 1969, at 1629 CST (2229 UT) and floated at an average depth of 3.2 gm/cm^2 (128,200 feet) for 9 hours. Jupiter was observed between 0200 and 0630 UT.

Pulses from the main detector were later played back into a pulse-height analyzer. At the same time the channels containing the detector dead times were played back into a strip chart recorder and the record was examined for any abnormalities (for example, radio-frequency interference or telemetry dropouts) that might result either in spurious counts or in preventing counts from entering the data encoder. None of the sections of data containing such irregularities were used in the analysis that follows. The calibration spectra were played back and examined for possible malfunctions, such as drifts in the gain of the amplifier; no significant malfunctions were detected.

In this manner, count-rate data from the entire flight were played back, and the pulse-height analyzer was used to accumulate runs lasting from 2 to 5 min. After eliminating sections of data containing interference, a total of 133 min of time observing Jupiter and 78.8 min of time observing Jupiter-related background remained.

The background counting rate was then determined as follows. First, to improve statistics, the total number of counts between 30 and 100 kev was computed for each run; with this number designated B_i for the ith run, the counting rate can be written as

$$b_i = (B_i/T_i) \pm (B_i^{1/2}/T_i)$$

where T_i is the duration of the ith run. The weighted average of b_i was then determined by using the reciprocal of the square of the standard deviation, T_i^2/B_i, as the weighting function w_i; the weighted average was therefore

$$\langle b \rangle = \sum_i b_i w_i / \sum_i w_i$$

There was a total of 17 background runs, for which a χ-square analysis gave $\chi^2 = 31$; rejection of one of the background runs and recalculation of $\langle b \rangle$ gave $\chi^2 = 23$. The total background observation time then became 73.8 min, and the total number of counts accumulated was 1936; the counting rate was $\langle b \rangle = (2.166 \pm 0.049) \times 10^{-2}$ cm^{-2} sec^{-1}; $\sigma = 0.049 \times 10^{-2}$/cm^2 sec $= [1/(\Sigma_i w_i)]^{1/2}$.

The data are plotted in the form of an energy spectrum in Figure 2. The unweighted counting rate averages are plotted for both background and Jupiter plus background versus energy in 10 energy channels each 7 kev wide; the standard deviations are shown. No evidence of an

excess of counts from Jupiter is present in this raw data, where Jupiter X rays would be expected to be present in the lower-energy channels with a spectrum falling rapidly with energy.

The 3σ upper limits to the Jupiter X-ray fluxes, corrected for atmospheric absorption, detector pointing error, dead time, and detector efficiency, are also shown in Figure 2. The total flux in the energy range 30–100 kev is $\leq 1.6 \times 10^{-2}$/cm^2 sec; the total X-ray energy flux is thus $\lesssim 0.91$ kev/cm^2 sec at the earth, corresponding to $\lesssim 6.6 \times 10^{19}$ ergs/sec in X rays at Jupiter, 4 AU distant. At an energy of 100 kev, electrons passing through a $Z = 2$ atmosphere will have a ratio of radiative to ionization energy loss of 2.5×10^{-4}; thus a rough upper limit to the power in precipitating electron fluxes at the time of this observation is 2.6×10^{23} ergs/sec.

MODELS FOR JOVIAN X-RAY EMISSION

In the following analysis, the solar wind is assumed to have the same average velocity at Jupiter as at the earth, namely 350 km/sec. Conservation of flux requires that $nvR^2 =$ constant, where n is the particle density, v is the velocity, and R is the distance from the sun.

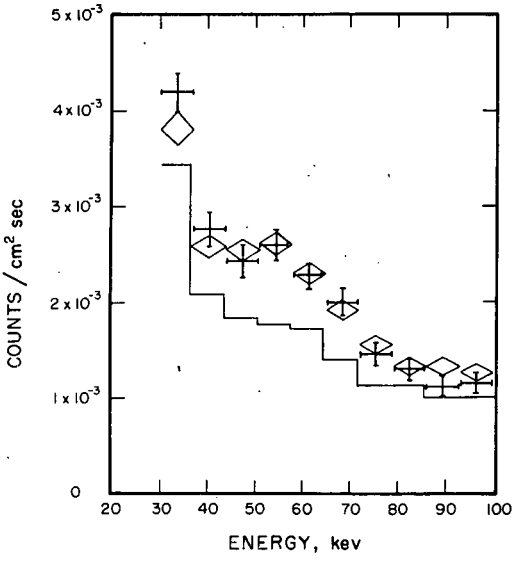

Fig. 2. Background and Jupiter plus background spectra; resulting upper limits to Jupiter fluxes at 3σ confidence. Crosses indicate the background; diamonds are Jupiter plus background; lines are the 3σ upper limit.

Thus the particle density must fall as R^{-2}, and n at Jupiter will be 1/25 of its value at the earth.

Two different methods will now be used to estimate Jovian X-ray fluxes; the first method involves the scaling up of terrestrial precipitating electron fluxes according to different features of the earth and of Jupiter. The second method relies on estimates of the Jovian precipitating fluxes based on theories of the decametric radiation. These methods will be described briefly in the three following sections, the detailed mathematics appearing in Appendix A. The detectability of the Jovian X-ray fluxes derived in Appendix A is discussed at the end of this section.

Model IA. The energy for all terrestrial auroral phenomena is generally assumed to be derived from the solar wind; if the fraction of Jupiter's energy input that goes into precipitating electron fluxes is the same as that fraction of the earth's energy input, the Jovian fluxes can be found by scaling the terrestrial fluxes by a factor that depends on the intercepted solar-wind energies.

Although electron precipitation shows different time structure on the earth's dayside and nightside, the total X-ray energy is approximately the same on both sides; thus the fact that only the dayside of Jupiter is visible from the earth should be unimportant.

The total power intercepted by the earth's magnetosphere is about 10^{20} ergs/sec, of which roughly 10^{18} ergs/sec is used to drive various magnetospheric phenomena. By using the numbers derived in Appendix A, it can be seen that Jupiter should intercept 1.5×10^{22} ergs/sec and, according to this model, use 1.5×10^{20} ergs/sec for its auroral phenomena. (For comparison, the average power dissipated in Jovian decimetric and decametric radiation is about 10^{16} ergs/sec.)

Model IB. There is good evidence that the magnetic-field lines in the earth's auroral zones connect to a highly diamagnetic sheet of plasma that stretches out in the antisolar direction behind the earth [*Anderson*, 1969; *Chase*, 1969]. Thus the electron energy density in this region is comparable to the magnetic-field energy density. If this represents an upper limit that holds for Jupiter as well as for the earth, the Jovian electron energy density may be

scaled by the ratio of the magnetic-field energy densities.

Model II. A theory of decametric emission developed by *Warwick* [1963] proposed that electron gyroradiation from a flux $F \lesssim 4 \times 10^{10}$ electrons/cm² sec of 10-kev electrons precipitating into an area $0.2\ R_J \times 0.3\ R_J = 3 \times 10^{18}$ cm² could explain the observed radio fluxes. By using this value for the electron flux and assuming an exponential spectrum (no particular spectral shape was used in Warwick's model), the flux of Jovian X rays is calculated in Appendix A. More recently, *Warwick* [1970] showed that F could be considerably smaller than the above value; thus the fluxes of model II represent an upper limit.

In general, the detectability of an X-ray source for this detector can be determined as follows. The background counting rate in the energy range 30–100 kev is approximately 0.5/sec. Thus in a time T, $0.5\ T \pm (0.5T)^{1/2}$ counts will be accumulated. An X-ray source producing n counts/sec in this same energy range can be considered to be detected with 95% confidence when the total number of counts accumulated from the source exceeds the background counts by 2 or more s.d.; that is, $nT \geq 2(0.5T)^{1/2}$, or $T(\text{hours}) \geq 5.5 \times 10^{-4}/n^2$. For two of the three models of Jovian X-ray emission discussed above, the quantity T(hours) is plotted versus the Jovian e-folding energy E_{oJ} in Figure 2. Also plotted in this figure is the total Jovian X-ray flux at the earth between the energy limits 30 and 100 kev. The X-ray fluxes of model IA (fluxes scaled as intercepted solar-wind energies) require observation times on the order of 10^{10} hours and are undetectable with this detector; model IB fluxes (scaled as the magnetic-field energy density) become detectable for sufficiently high e-folding energies, and model II fluxes (based on decametric emission) are detectable for e-folding energies slightly lower than those of model IB. Stated differently, these findings indicate that, with 133 min of Jupiter observation time, the fluxes of model IB would be detected if the e-folding energy were greater than about 60 kev, whereas the fluxes of model II would be detectable with $E_{oJ} \gtrsim 20$ kev.

Somewhat different treatments of the Jupiter data are implied by these models. The fluxes of model IA would contribute on the order of 10^{-4} counts in a 5-min interval, whereas the fluxes of model II might contribute as much as 50 counts (~4 s.d. over the background) in this same interval. Furthermore, the fluxes of model II might appear sporadically. Thus a weighted average of the counting rates, which would be appropriate for model IA (counting rates dominated by random background counts) would tend to suppress the large values in model II. A weighted average gives $(2.164 \pm 0.036) \times 10^{-2}$/cm² sec, a value that is slightly under the background rate, whereas an unweighted average gives $(2.200 \pm 0.037) \times 10^{-2}$/cm² sec; this latter value exceeds the background counting rate by approximately 1 s.d. and therefore cannot be considered statistically significant.

Owing to the lack of solar activity prior to the flight and the lack of decametric emission

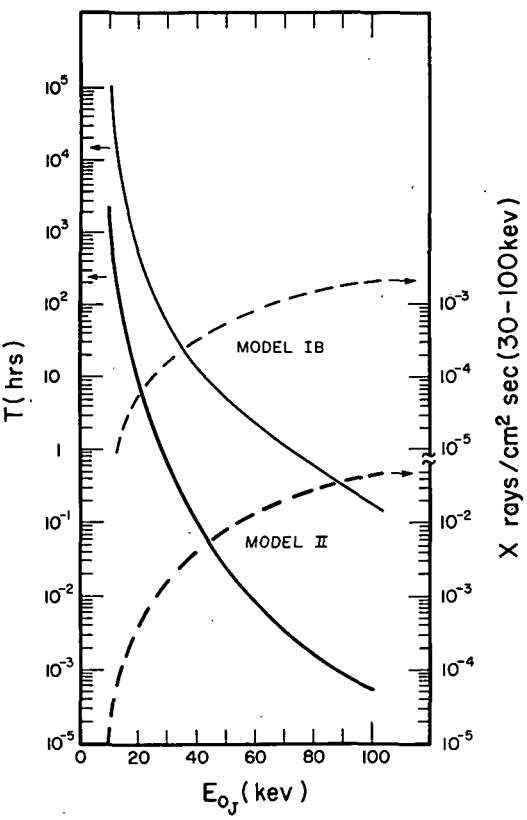

Fig. 3. Jovian X-ray fluxes (dashed lines, right-hand scale) and observing times required for their detection (solid lines, left-hand scale) as a function of e-folding energy for two of the models discussed in this paper.

during the flight, it seems rather unlikely that any X-ray emission was present; therefore the upper limit given in the previous section cannot be used to distinguish between the various models.

CONCLUSION

Large balloons may be launched only when local weather conditions are satisfactory, and observation times are rarely longer than 8 hours during a single flight. Even if one were fortunate enough to observe Jupiter during a decametric storm or a Jovian magnetospheric substorm, the fluxes would probably be quite weak and interpretation of the data would be rather limited. On the other hand, a significant amount of data could be gathered by an X-ray detector on a flyby spacecraft. Correlation of X rays with solar activity and decametric bursts are just two possible results of such an experiment where the long travel time could be used to collect large amounts of data. Although the Pioneer F and G missions will carry no X-ray detectors, the Grand Tour presents an excellent opportunity to study the magnetospheres of Jupiter and possibly of other outer planets. The possibility that magnetospheres are a universal astrophysical phenomenon makes it of great importance to learn as much as possible about radiation zones and auroral phenomena on as many planets as possible.

APPENDIX A

An electron passing through a thick target will lose part of its energy owing to the radiation of photons. It can be shown [*Evans*, 1955] that the initial electron energy E and the number of photons $dn(\hbar\omega)$ radiated in an infinitesimal energy interval about $\hbar\omega$ are related by

$$\frac{dn(\hbar\omega)}{d(\hbar\omega)} \propto \left(\frac{E}{\hbar\omega} - 1\right) \text{ photons/kev}$$

For Jupiter's atmosphere, the target may be taken to have an atomic number $Z = 2$, and the proportionality constant becomes 2.4×10^{-6}; thus

$$\frac{dn(\hbar\omega)}{d(\hbar\omega)} = 2.4 \times 10^{-6}\left(\frac{E}{\hbar\omega} - 1\right) \text{ photons/kev}$$

This result, known as the Kramers formula, holds for nonrelativistic electrons and has been applied to the problem of auroral zone X-ray production [*Hudson*, 1966].

An energy spectrum for precipitating electrons that is frequently observed in the earth's auroral zones is

$$\frac{dN}{dE} = C \exp\left[-(E/E_0)\right]$$

electrons/cm² sec kev

Typical values for the earth are $C = 7 \times 10^7$ electrons/cm² sec kev, $E_0 = 10$ kev. For the earth, functions other than exponentials can be used [*Hudson*, 1966]. For Jupiter, there is no experimental data that can be used to derive the spectrum of kiloelectron-volt electrons; the exponential spectrum will be used for the following calculations, with the understanding that it does not produce as many high-energy photons as, for example, a power law, and therefore it gives a lower limit to the fluxes of X rays.

With this spectrum for Jovian precipitating electrons, the number of photons produced per cm² sec kev is obtained by integration,

$$\int_{\hbar\omega}^{\infty} 2.4 \times 10^{-6}\left(\frac{E}{\hbar\omega} - 1\right) C \exp\left[-(E/E_0)\right] dE$$

$$= 2.4 \times 10^{-6} C E_0^{\,2} \frac{\exp\left(-\hbar\omega/E_0\right)}{\hbar\omega}$$

photons/cm² sec kev

(Although the upper limit of the integral is infinity, the contribution from relativistic energies will be negligible for the values of E_0 used here.)

A convenient measure of the X rays produced is the number per cm² sec with energies between 30 and 100 kev, or

$$n(30\text{–}100)$$

$$= \int_{30}^{100} 2.4 \times 10^{-6} C E_0^{\,2} \frac{\exp\left[-\hbar\omega/E_0\right]}{\hbar\omega} d(\hbar\omega)$$

$$= 2.4 \times 10^{-6} C E_0^{\,2}\left[E_1\left(\frac{30}{E_0}\right) - E_1\left(\frac{100}{E_0}\right)\right]$$

photons/cm² sec

where the function E_1 is the exponential integral, defined by

$$E_1(x) = \int_x^{\infty} (e^{-z}/z)\, dz$$

To get the number of X rays/sec received by a detector at the top of the earth's atmosphere, let A_J be the area of the region on Jupiter into which the electrons precipitate, D_{EJ} the distance between the earth and Jupiter, and A_D the area of the detector used; then the number n_e of photons/sec with energies between 30 and 100 kev reaching the detector is

$$n_E = (A_J A_D/4\pi D_{EJ}^2)n(30\text{–}100)$$

The assumption of isotropic X-ray emission implicit in the above expression is justified not by the radiation pattern from a single electron, which becomes strongly peaked in the forward direction at high energies, but rather by a consideration of the path taken by the electron as it traverses the atmosphere. A comparison of the range-energy relation with the expression for the mean-square scattering angle due to multiple small angle scattering shows that an initially directional electron beam is rendered isotropic after traveling at most one-fifth of its range for the energies involved here.

The detector area A_D equals 20 cm^2, and D_{EJ} equals 6×10^{13} cm, the value at opposition. A_J can be obtained by assuming that electron precipitation goes into the same fraction of Jupiter's total surface area as of the earth's; thus, with 3×10^{15} cm^2 as the area over one terrestrial hemisphere into which electron precipitation takes place at any given time,

$$A_J = (r_J^2/r_E^2) \times 3 \times 10^{15} \text{ cm}^2$$
$$= 3 \times 10^{17} \text{ cm}^2$$

where r is the planetary radius and the subscripts refer to Jupiter and the earth. This calculation gives

$$n_E = 3.2 \times 10^{-16} C E_0^2 \left[E_1\left(\frac{30}{E_0}\right) - E_1\left(\frac{100}{E_0}\right)\right]$$

photons/sec

Model IA. The radius of the magnetosphere at the subsolar point, obtained by balancing the solar-wind pressure against the magnetic field pressure, is

$$r_0 = (M^2/4\pi n m v^2)^{1/6}$$

where M is the planetary magnetic moment and n, m, and v are the solar-wind number density, particle mass, and velocity, respectively. The quantity of interest is the cross-sectional area presented to the solar wind, and this area will be proportional to r_0^2; thus the scaling factor relating Jovian to terrestrial intercepted energy becomes

$$\frac{\frac{1}{2} n_J m v^3 r_{0J}^2}{\frac{1}{2} n_E m v^3 r_{0E}^2} \cong 150$$

The energy flux in the assumed exponential electron spectrum is

$$\int_0^\infty E\, dN/dE\, dE = CE_0^2 \text{ kev/cm}^2 \text{ sec}$$

Thus the scaling equation becomes

$$A_J C_J E_{0J}^2 = 150 A_E C_E E_{0E}^2$$

and

$$n_E = 3.1 \times 10^{-6}\left[E_1\left(\frac{30}{E_{0J}}\right) - E_1\left(\frac{100}{E_{0J}}\right)\right]$$

photons/sec

Model IB. If u is the velocity of an electron with kinetic energy E, the total energy density in an exponential electron spectrum is

$$\int_0^\infty \frac{E}{u} C \exp\left[-(E/E_0)\right] dE$$
$$= \frac{C}{c}\left(\frac{\pi}{2}\right)^{1/2}(2E_0 mc^2)\Gamma\left(\frac{3}{2}\right)$$
$$\cdot\left[H_1\left(\frac{mc^2}{E_0}\right) - N_1\left(\frac{mc^2}{E_0}\right)\right]$$

where m is the electron mass, c is the speed of light, Γ is the gamma function, H_1 is the Struve function, and N_1 is the Neumann function (Bessel function of the second kind).

The scaling factor is B_J^2/B_E^2, where B_J and B_E are the magnetic-field strengths at corresponding points on Jupiter and the earth; if dipole fields are assumed, this value becomes

$$\left(\frac{M_J}{r_J^3}\frac{r_E^3}{M_E}\right)^2 \cong 2500$$

Thus

$$C_J E_{0J}\left[H_1\left(\frac{mc^2}{E_{0J}}\right) - N_1\left(\frac{mc^2}{E_{0J}}\right)\right]$$
$$= 2500 C_E E_{0E}\left[H_1\left(\frac{mc^2}{E_{0E}}\right) - N_1\left(\frac{mc^2}{E_{0E}}\right)\right]$$

and

$$n_E = 3.6 \times 10^{-4} E_{0J} \frac{E_1\left(\frac{30}{E_{0J}}\right) - E_1\left(\frac{100}{E_{0J}}\right)}{H_1\left(\frac{mc^2}{E_{0J}}\right) - N_1\left(\frac{mc^2}{E_{0J}}\right)}$$

(The denominator in this expression varies quite slowly; thus the main energy dependence is contained in the exponential integral terms and the factor of E_{0J}.)

Model II. If a flux $F = 4 \times 10^{10}$ electrons/cm² sec of 10-kev electrons is used, the constants C_J and E_{0J} are related by

$$C_J \exp(-10/E_{0J}) = 4 \times 10^{10} \text{ electrons/cm}^2 \text{ sec}$$

With the value $A_J = 3 \times 10^{18}$ cm²,

$$n_E = 1.3 \times 10^{-4} E_{0J}^2 \cdot \exp(10/E_{0J}) \left[E_1\left(\frac{30}{E_{0J}}\right) - E_1\left(\frac{100}{E_{0J}}\right) \right]$$

Acknowledgments. I am indebted to Professor K. A. Anderson for suggesting this project and for his help and encouragement throughout all phases of the research. Special thanks go to Mr. Henry Primbsch for his design of the gondola electronics and for many hours spent late at night in the laboratory. Mr. William Mahoney, Mr. Robert Steffen, and Mr. Paul Duffy gave valuable assistance in the laboratory and in the field; the staff of the National Center for Atmospheric Research Balloon Base assisted in the field operations.

This program was supported by the Atmospheric Sciences Section of the National Science Foundation under grant GA-1018 and by the National Aeronautics and Space Administration under grant NGL-05-003-017, K. A. Anderson, principal investigator.

* * *

The Editor thanks J. W. Warwick and another referee for their assistance in evaluating this paper.

REFERENCES

Anderson, K. A., Relation of energetic particles in the plasma sheet to the auroral zone, in *Atmospheric Emissions*, edited by B. M. McCormac and Anders Omholt, pp. 327–336, Van Nostrand Reinhold, New York, 1969.

Chase, L. M., Evidence that the plasma sheet is the source of auroral electrons, *J. Geophys. Res., 74,* 348, 1969.

Edwards, P. J., and K. G. McCracken, Upper limits to the hard X-ray flux from the quiet sun and Jupiter, *J. Geophys. Res., 72,* 1809, 1967.

Evans, R. D., *The Atomic Nucleus,* pp. 600–610, McGraw-Hill, New York, 1955.

Fisher, P. C., D. B. Clark, A. J. Meyerott, K. L. Smith, Upper limit to Jupiter's X-ray flux on September 30, 1962. *Nature, 204,* 982, 1964.

Haymes, R. C., D. V. Ellis, and G. J. Fishman, Upper limits to the hard X-ray fluxes from Mars, Venus, and Jupiter, *J. Geophys. Res., 73,* 867, 1968.

Hudson, H. S., Energy spectrum of auroral-zone electron precipitation, Ph.D. Thesis, Univ. of Calif., Berkeley, 1966.

Warwick, J. W., Dynamic spectra of Jupiter's decametric emission, 1961, *Astrophys. J., 137,* 41, 1963.

Warwick, J. W., Particles and fields near Jupiter, *NASA Rep. CR-1685,* 1970.

(Received April 20, 1971;
accepted September 14, 1971.)

SPACE SCIENCES LABORATORY

A73-13959

THE IMPULSIVE X-RAY BURST
OF OCTOBER 10, 1970

S.R. KANE
S.W. KAHLER
J.D. KURFESS

MARCH 7, 1972

UNIVERSITY OF CALIFORNIA, BERKELEY

THE IMPULSIVE X-RAY BURST OF OCTOBER 10, 1970

S. R. Kane

Space Sciences Laboratory
University of California, Berkeley 94720 U.S.A.

S.W. Kahler and J.D. Kurfess

E.O. Hulburt Center, Naval Research Laboratory
Washington, D.C. 20390 U.S.A.

March 7, 1972

Submitted for publication in SOLAR PHYSICS

ABSTRACT

An impulsive burst of 100-400 keV solar x-rays associated with a small solar flare was observed on October 10, 1970 with a large area scintillator aboard a balloon floating at an altitude of 4.2 g cm^{-2} above the earth's surface. The x-ray burst was also observed simultaneously in 10-80 keV range by the OGO-5 satellite and in 8-20Å range by the SOLRAD-9 satellite. The impulsive x-ray emission reached its maximum at ~1643 UT at which time the differential photon spectrum in 20-80 keV range was of the form $2.3 \times 10^{4}\ E^{-3.2}$ photons $cm^{-2}\ sec^{-1}\ keV^{-1}$ at 1 A.U. The event is attributed to a Hα-subflare located approximately at S13, E88 on the solar disc. The spectral characteristics of this event are examined in the light of the earlier x-ray observations of small solar flares.

INTRODUCTION

Since the early observations by Peterson and Winckler (1959) and Anderson and Winckler (1962) the measurements of solar flare x-rays with detectors flown aboard atmospheric balloons have contributed much to the understanding of the solar flare phenomena (see for example, Parks and Winckler, 1971). The balloon observations reported so far were associated with relatively large solar flares ($H\alpha$-importance >2). The purpose of this short paper is to report a balloon observation of a 100-400 keV x-ray burst which was apparently associated with a small solar flare ($H\alpha$-importance ≤ 1). These observations are compared with simultaneous measurements with detectors aboard the OGO-5 and SOLRAD-9 satellites and the spectrum of the impulsive solar x-ray burst in the 20-400 keV range has been deduced.

INSTRUMENTATION

A description of the balloon scintillator experiment has been given in Kurfess (1971). The detector used consisted of a NaI(Tl) crystal with an area of 855 cm^2 and a thickness of 15.2 cm. Charged particles were rejected by enclosing the NaI(Tl) crystal in two NE-102 well assemblies which were operated in anti-coincidence with the crystal. The experiment was designed primarily to measure x-ray emission from cosmic sources. The data presented here were obtained by a single-channel analyzer in the 100-400 keV region. At the time of the present observations the balloon floated at a level of 4.2 g cm^{-2} and the axis of the detector was pointed at the zenith throughout the flight. The sun was located at a zenith angle of 40°.

The University of California scintillator experiment on the OGO-5 spacecraft has been described by Kane and Anderson (1970). It consists of a NaI(Tl) crystal 0.5 cm thick and 9.5 cm^2 in area with a beryllium window 0.051 cm thick. Eight channels of pulse height analysis follow the output of the phototube. Seven differential channels cover the energy range 9.6-128 keV. The eighth channel is an integral channel for E > 128 keV. At the lowest telemetry bit rate a complete spectrum is read out every 2.3 seconds.

The 8 to 20Å ion chamber on SOLRAD 9 has been described by Kreplin and Horan (1969). The ion chamber window consists of 2.4×10^{-3} g cm^{-2} of aluminum and the fill gas is nitrogen at a pressure of 400 mm. Data from the spacecraft memory consists of one readout per minute.

OBSERVATIONS

The x-ray data for the October 10, 1970 solar flare event are shown in Figure 1. The 100-400 keV x-ray data show an impulsive burst at 1643 UT. This impulsive x-ray burst, which could also be clearly seen in the 19.2-80 keV x-ray channels, occurred simultaneously with an impulsive radio burst observed at 15400 MHz and 8800 MHz by the Sagamore Hill Radio Observatory (Geophysics and Space Data Bulletin, 1970).

Figure 2 shows, on an enlarged scale, the counting rates of 32-48 keV and 100-400 keV x-rays during the period 1642:44-1643:20 UT. It can be seen that the time-itensity profiles of the two x-ray channels are similar. Due to the relatively large statistical

uncertainties it is not possible to determine the rise and decay times accurately. For the 100-400 keV x-rays the exponential rise and decay times lie in the range 1.3-13 sec and 4-20 sec respectively. The rise and decay times for the 32-48 keV x-rays lie in the range 1.6-7.0 sec and 3.1-10.3 sec respectively. These may be compared with the rise and decay times of ~5 sec and ~17 sec respectively obtained for the 19.2-32 keV x-rays.

The spectrum of the x-ray emission at the time of peak flux as observed by the OGO-5 experiment is shown in Figure 3. It can be fitted by a power law of the form

$$\frac{dJ}{dE} = 2.3 \times 10^4 \, E^{-3.2} \text{ photons cm}^{-2} \text{ sec}^{-1} \text{ keV}^{-1} \qquad (1)$$

in the energy range 20 to 80 keV. The flux in the 9.6 to 19.2 keV range is substantially greater than would be expected by an extrapolation of equation (1) to the lower energy range. This steepening of the spectrum below 20 keV could be an intrinsic property of the impulsive burst or it might be due to the effects of a much steeper thermal spectrum in the low energy range (Kane and Anderson, 1970).

If equation (1) also holds at higher energies, then it can be integrated to give the total expected photon flux in the 100-400 keV range. This flux must then be corrected for atmospheric absorption and scattering to determine the expected rate in the balloon detector. Parks and Winckler (1971) and Makino (1970) have discussed the problem of correcting balloon data below 100 keV where the energy loss per Compton-scattering is small and the scattered radiation is nearly isotropic. Above 100 keV, the situation is more complicated since forward scattering dominates and the fractional energy loss in

a single scattering is higher. A detailed treatment of the atmospheric attenuation becomes very complicated. In addition to the minimum atmospheric path length of 5.5 g cm^{-2}, detector material contributes 1.6 g cm^{-2} of plastic and 1.1 g cm^{-2} of aluminum.

Neglecting atmospheric absorption or scattering, the expected 100-400 keV rate would be ~270 counts/sec. A lower limit on the expected rate of 90 counts/sec is obtained by assuming that no scattered photons are detected, and using a scattering cross-section of .13 cm^2 g^{-1} for the mean energy of 170 keV for an $E^{-3.2}$ spectrum (Evans, 1955). The effect of scattering would be to increase the 90 counts/sec by a factor of 1.5 to 2.0. This is in reasonable agreement with the observed increase of 150 ± 20 counts/sec. Therefore the 100-400 keV flux is consistent with the spectrum of equation (1), but does not preclude a steepening of the spectrum in the 100-400 keV region. Above 400 keV no increase is observed; however, the upper limit obtained is consistent with the 20-80 keV spectrum.

Hα-importance of the October 10, 1970 flare

The dynamic range of the OGO-5 detector limits the size of the impulsive bursts studied to those which are associated with Hα flares of importance ≤ 1. It is therefore of interest to study the Hα activity associated with the October 10 burst. No Hα flare or subflare was listed in the Solar Geophysical Data Reports (1970) for the time of the impulsive burst. Dr. Helen Dodson has kindly examined the Hα patrol films of the McMath-Hulbert Observatory and has reported (Dodson, 1971) that a small transient brightening occurred during the time of the x-ray burst. This brightening, which can be called a subflare, occurred during the time 1641-1659 UT

with a maximum at 1644 UT. Since the x-ray peak occurred at 1643 UT, the event is consistent with the observation of Kane and Anderson (1970) that the time of x-ray maximum precedes the time of Hα maximum by 0.5 to 3.0 minutes. The Hα event was observed near the limb at S13 E88 in plage region 10989. Since it was so close to the limb, it is difficult to decide what the intrinsic size of the event was. We shall advance two arguments to show that this Hα event was most probably a subflare, rather than a larger event seen in projection or lying partly over the limb.

The 8-20Å data in Figure 1 are expressed in units of ergs cm^{-2} sec^{-1}. These values are derived from the SOLRAD-9 ion chamber counting rates by assuming a 2×10^6 ^oK black body spectrum and folding it in with the measured detector response function to calculate the flux in the 8 to 20Å band as a function of the observed counting rate (Kreplin and Horan, 1968). When corrected for the background level, the peak 8-20Å flux for the October 10 event is 10^{-2} ergs cm^{-2} sec^{-1}. Thomas and Teske (1971) have examined the relation between the maximum 8-12Å flux and the Hα importance of 283 flares and subflares. They used an ion chamber (Teske, 1969) which is similar, but not identical to the SOLRAD 9 instrument. They also assume a 2×10^6 ^oK black body spectrum, so their OSO-3 flux values can be compared with the SOLRAD 9 data except that the SOLRAD 9 flux values refer to a larger energy bandwidth. For an 8-20Å flux of 10^{-2} ergs cm^{-2} sec^{-1} the 8-12Å flux is 2.6×10^{-3} ergs cm^{-2} sec^{-1}, or, assuming an isotropic x-ray source, the total radiative rate of the flare is 7×10^{24} ergs sec^{-1} in the 8-12Å band. From Figure 5 of Thomas and Teske (1971) it can be seen that this value is less than the average radiation rate of a

normal subflare or faint class 1 flare. Thus, on the basis of the low level of the 8-20Å x-ray emission it would appear that the October 10 event is an intrinsically small $H\alpha$ event, and would most likely be classified a faint or normal subflare if seen near the center of the disk.

Another reason for believing that the October 10 $H\alpha$ event was small is that the active region 10989 exhibited a low level of activity in its passage across the solar disk. The Solar-Geophysical Data Reports (1970) show only five confirmed subflares and no confirmed flares for region 10989. Again, it would appear that the October 10 $H\alpha$ event was most likely a subflare.

SUMMARY AND DISCUSSION

The October 10 solar x-ray event reported here has many similarities with the impulsive solar x-ray bursts studied earlier by Kane and Anderson (1970). For 13 impulsive bursts associated with flares of $H\alpha$-importance ≤ 1 they found that the spectra at the times of peak flux were consistent with a power law of the form

$$\frac{dJ}{dE} = kE^{-\gamma} \text{ photons cm}^{-2} \text{ sec}^{-1} \text{ keV}^{-1} \qquad (2)$$

in the range $10 \leq E \leq 70$ keV. Above ~70 keV the spectra were usually steeper, although the energy at which the spectrum steepened varied from event to event. This spectral steepening at higher energies was also observed by Frost (1969) and Frost and Dennis (1971) in the case of two impulsive bursts associated with flares of

$H\alpha$-importance >2. Since the problem of pulse pile-up (Kane and Hudson, 1970) limits the size of an event which can be studied in a scintillator experiment such as the one on the OGO-5 satellite, the $E \geq 100$ keV range had been relatively difficult to study for flares of $H\alpha$ importance ≤ 1 because of poor counting statistics. This difficulty did not occur in the present measurements because (i) a large area (855 cm^2) scintillator was used exclusively for measuring 100-400 keV x-rays; (ii) the lower energy x-ray flux was heavily attenuated by the earth's atmosphere between the sun and the detector.

The x-ray data for the present impulsive burst are consistent with a decrease in the rise and decay times with the increase in the photon energy, as was found in an earlier study (Kane and Anderson, 1970). However, in the 32-400 keV range the statistical uncertainties in the measured x-ray flux are large so that other types of energy dependence for the rise and decay times of 32-400 keV photons cannot be ruled out.

In the 20-80 keV range, the x-ray spectrum at the maximum of the October 10 event is consistent with the form (2) with $\gamma \approx 3.2$ and $k \approx 2.3 \times 10^4$. This value of γ is consistent with the upper limit on the hardness of the impulsive x-ray spectra ($\gamma_{min} \approx 2.3$) found earlier by Kane (1971).

In the 100-400 keV range a unique interpretation of the measurements is not possible. The measurements are consistent with the assumption that the same power law spectrum holds throughout the energy range 20-400 keV. However the measurements can also be reconciled with a spectrum which steepens in the 100-400 keV region.

This ambiguity in the interpretation of the balloon data is primarily due to the fact that only one detector channel covered the entire energy range 100-400 keV. It is suggested that in future experiments several energy channels be used so that a differential spectrum can be obtained for x-rays >100 keV.

ACKNOWLEDGMENTS

We are indebted to Dr. Helen Dodson of McMath-Hulburt Observatory for her prompt and careful attention to the Hα data. This research was supported by NASA Contract NAS 5-9094 at the University of California, Berkeley and NSF Grants GP 29794 and GP 27215 at the U.S. Naval Research Laboratory.

REFERENCES

Anderson, K.A. and Winckler, J.R.: 1962, J. Geophys. Res., 67, 4103

Dodson, H.W.: 1971, private communication

Evans, R.D.: 1955, The Atomic Nucleus, Chp. 25, McGraw-Hill, New York

Frost, K.J.: 1969, Ap. J., 158, L159

Frost, K.J. and Dennis, B.R.: 1971, Ap. J., 165, 655

Geophysics and Space Data Bulletin: 1970, Air Force Cambridge Research Laboratory, Bedford, Massachusetts

Kane, S.R.: 1969, Ap. J., 157, L139

Kane, S.R.: 1971, Ap. J., 170, 587

Kane, S.R. and Anderson, K.A.: 1970, Ap. J., 162, 1003

Kane, S.R. and Hudson, H.S.: 1970, Solar Phys., 14, 414

Kreplin, R.W. and Horan, D.M.: 1969, NRL Report 6800, Naval Research Laboratory, Washington, D.C.

Kurfess, J.D.: 1971, Ap. J., 168, L39

Makino, F.: 1970, Astrophys. and Space Sci., 8, 251

Parks, G.K. and Winckler, J.R.: 1971, Solar Phys., 16, 186

Peterson, L.E. and Winckler, J.R.: 1959, J. Geophys. Res., 64, 697

Solar-Geophysical Data: 1970, U.S. Department of Commerce, Washington, D.C.

Teske, R.G.: 1969, Solar Phys., 6, 193

Thomas, R.J. and Taske, R.G.: 1971, Solar Phys., 16, 431

FIGURE CAPTIONS

1. Counting rates of the SOLRAD 9, OGO-5 and balloon x-ray detectors during the October 10, 1970 solar flare event. The three detectors together cover the x-ray spectrum from 0.6 keV (20Å) to 400 keV. Note the impulsive x-ray burst at 1643 UT.

2. An expanded plot of the counting rates of the 32-48 keV and 100-400 keV x-ray channels observed during the October 10, 1970 solar x-ray burst. Note that the rate of the 100-400 keV channel is normalized to the peak value of the 32-48 keV channel rate.

3. The differential spectrum of 10-80 keV x-rays observed with the OGO-5 satellite at the maximum of the impulsive x-ray burst (1643:01 UT). The observations (open circles) are compared with the computed rates (dark rectangles) for an assumed spectrum of the form $\frac{dJ}{dE} = kE^{-\gamma}$ photons cm^{-2} $sec^{-1}keV^{-1}$ incident on the detector.

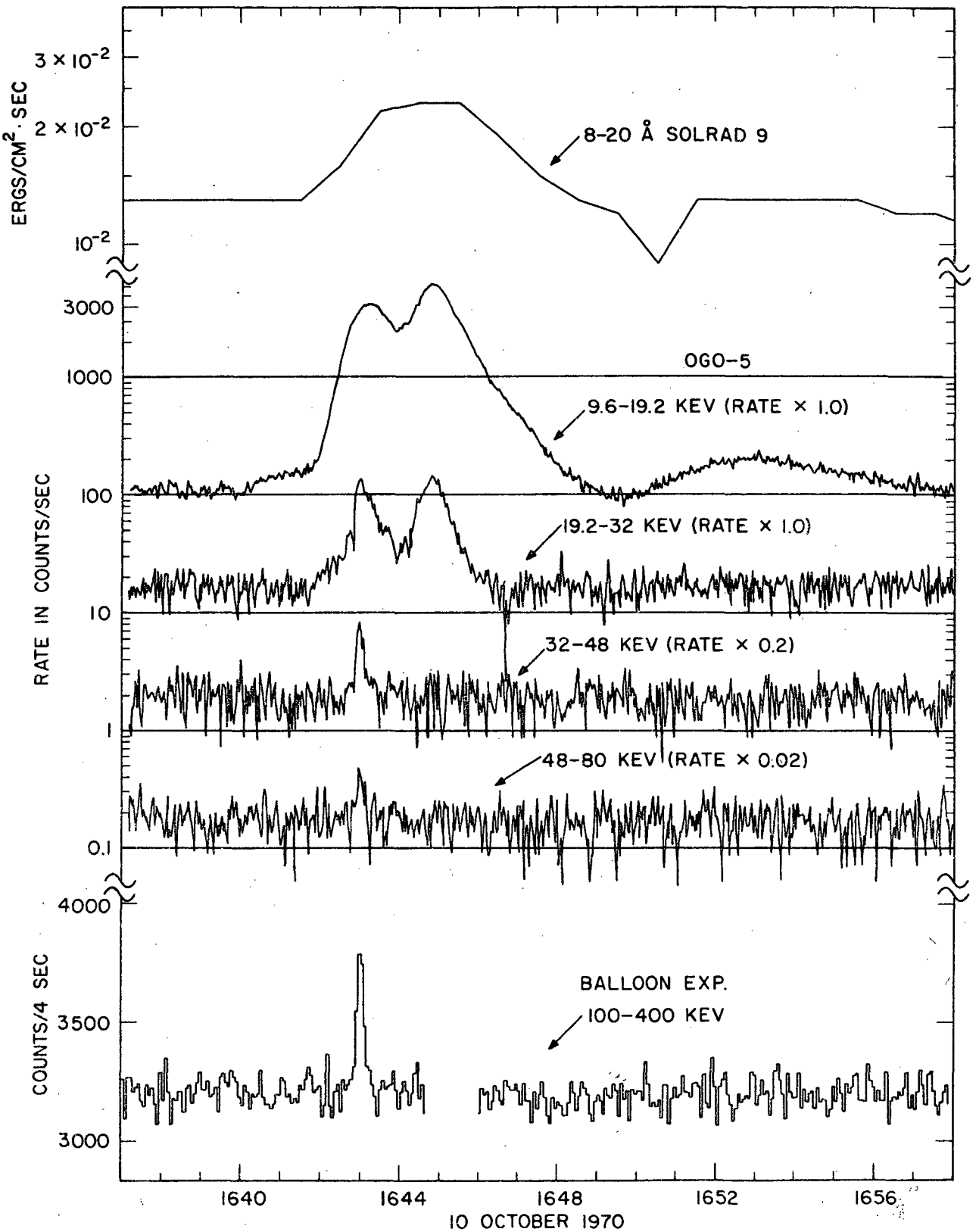
ERGS/CM^2·SEC
3×10^{-2}
2×10^{-2}
10^{-2}
8-20 Å SOLRAD 9
RATE IN COUNTS/SEC
3000
1000
100
10
1
0.1
OGO-5
9.6-19.2 KEV (RATE × 1.0)
19.2-32 KEV (RATE × 1.0)
32-48 KEV (RATE × 0.2)
48-80 KEV (RATE × 0.02)
COUNTS/4 SEC
4000
3500
3000
BALLOON EXP.
100-400 KEV
1640
1644
1648
1652
1656
10 OCTOBER 1970

Figure 1

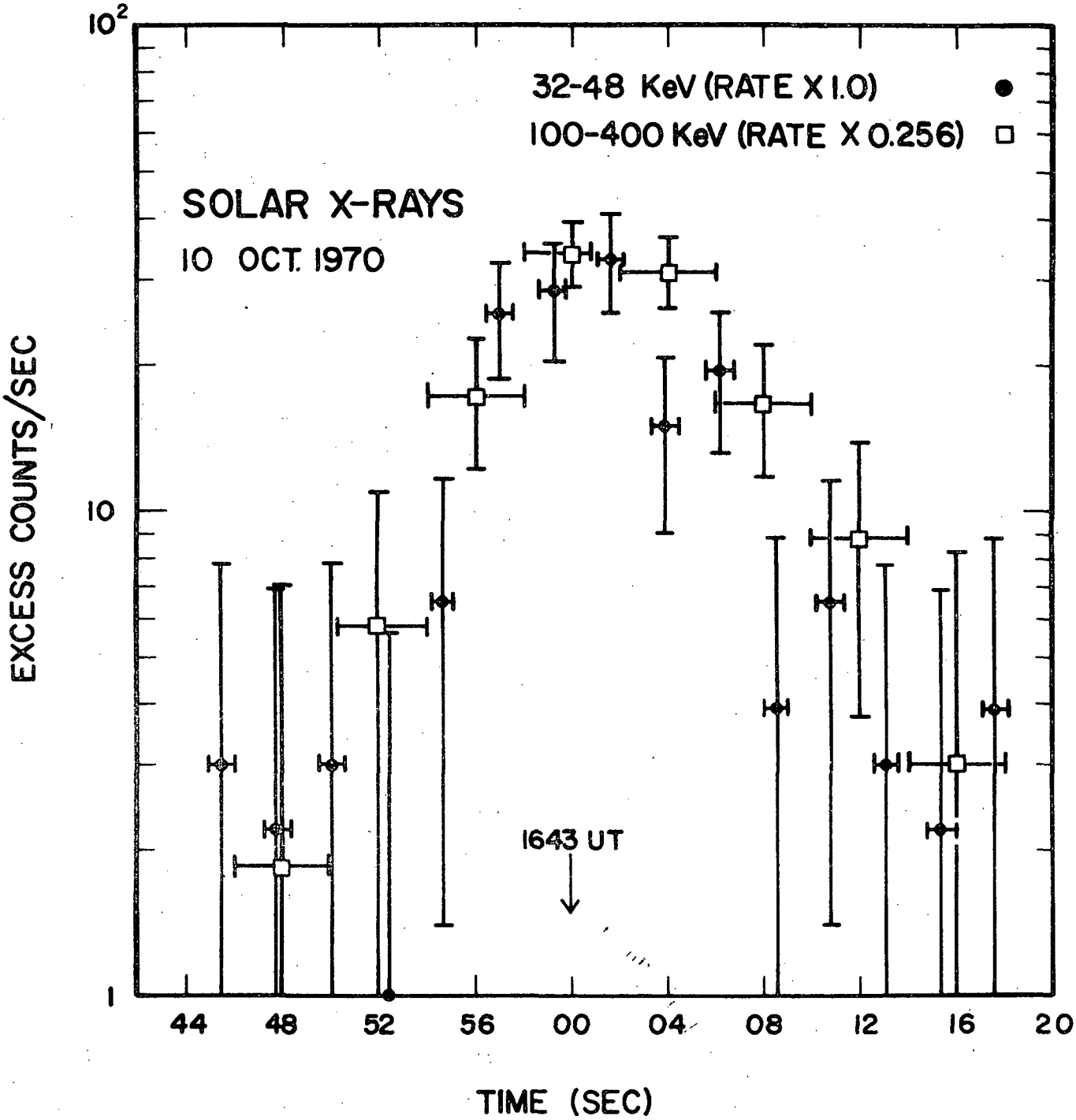
32-48 KeV (RATE X 1.0)
100-400 KeV (RATE X 0.256)
SOLAR X-RAYS
10 OCT. 1970
1643 UT
EXCESS COUNTS/SEC
TIME (SEC)
10²
10
1
44
48
52
56
00
04
08
12
16
20

Figure 2

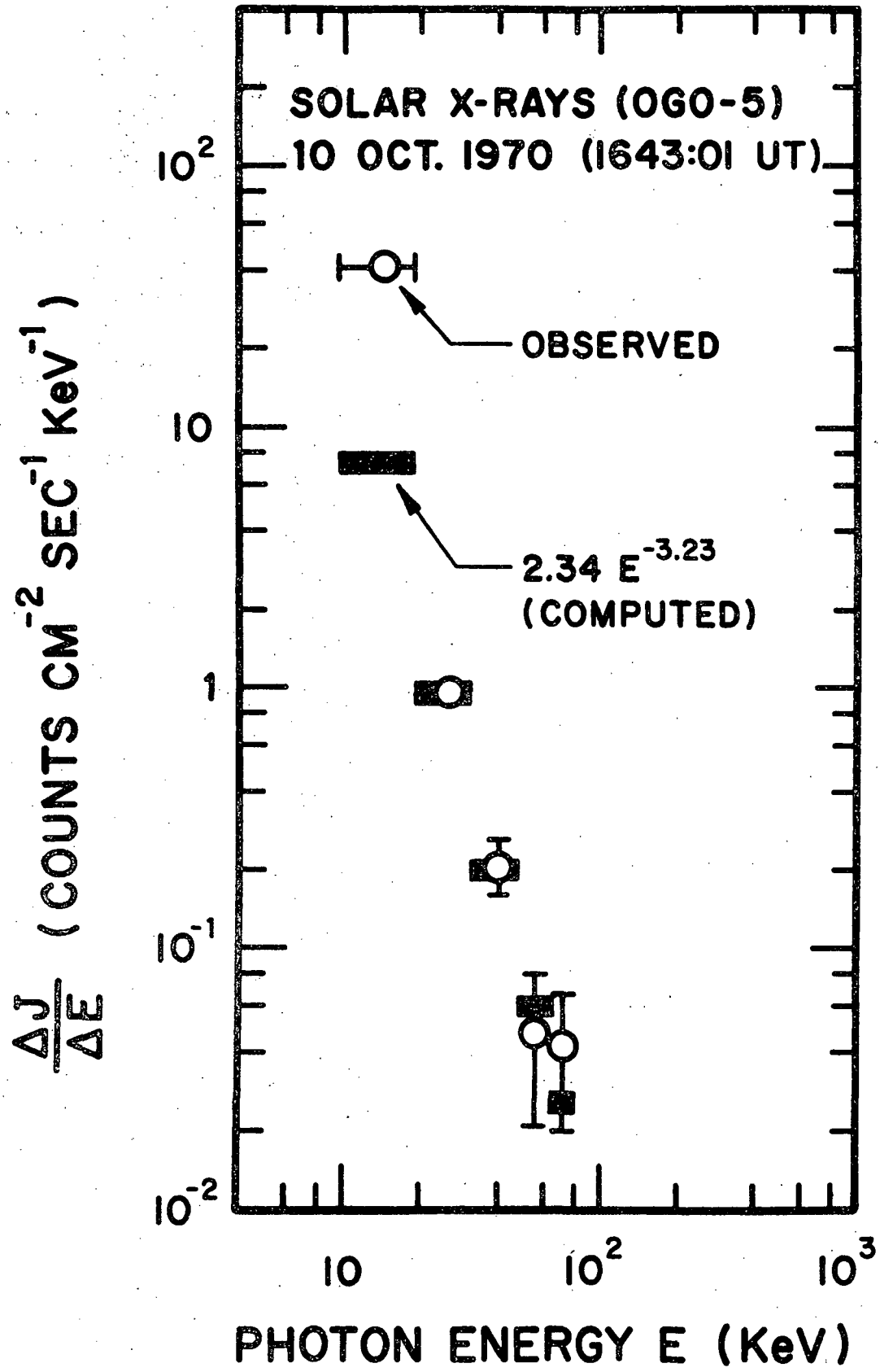
SOLAR X-RAYS (OGO-5)
10 OCT. 1970 (1643:01 UT)
OBSERVED
2.34 E^-3.23
(COMPUTED)
ΔJ/ΔE (COUNTS CM^-2 SEC^-1 KeV^-1)
PHOTON ENERGY E (KeV)
10^2
10
1
10^-1
10^-2
10
10^2
10^3

Figure 3

D1

COMMENTS ON BRIEF REPORT BY T.E. GRAEDEL AND L.J. LANZEROTTI 'INTERPLANETARY-PARTICLE ASSOCIATIONS WITH TYPE III SOLAR BURSTS'*

R. P. Lin

Space Sciences Laboratory
University of California, Berkeley 94720

November 30, 1971

(Revised March 16, 1972)

*This research supported in part by the National Aeronautics and Space Administration under grant NGL-05-003-017.

Graedel and Lanzerotti (1971) (herein referred to as G & L) claim that during the period from May 28 to November 30, 1967 the type III radio burst-interplanetary particle association "...do not support the common belief that interplanetary-particle observations confirm the association of electrons with type III radio bursts." They use three sets of particle data -- ~0.6 and ~1.2 MeV proton data, >300 keV electron data and >40 keV electron data -- in conjunction with decametric wavelength type III bursts reported in Solar-Geophysical Data (U.S. Dept. of Commerce, 1968) and the IAU Quarterly Bulletin on Solar Activity (1968) and satellite radio observations from OGO-5. The basis for their claim is that both the proton data and the >40 keV electron data can be associated with type III bursts, and therefore "The belief that interplanetary electron observations firmly support the electron and type III burst associations ...must be regarded as unproven."

I believe that their conclusion is unfounded for the following reasons:

1. Two (low energy protons and >300 keV electrons) of the three sets of particle data are inappropriate for correlation to type III bursts.
2. Their analysis and interpretation of the correlations are incorrect. The 65% correlation obtained between proton events and type III bursts is what would be expected from random choice of particle onset times under their correlation criteria. The >40 keV electron correlation to type III bursts of 55% is (a) incorrect and should be 58% ± 12%, and (b) is above the correlation of ~42% for randomly chosen onset times. Also the authors used

only part of the published >40 keV electron data; using a full sample and their criteria one would obtain 63% ± 9%.

3. G & L question the validity of the flare associations made for energetic particle events because of the large variation in transit times for the particles from the sun to the earth. I believe that the association of flares to >40 keV electron events are valid and that the variation (1.5 to 80 minutes) is explained by the criteria governing the choice of onset times and by the inherent inaccuracies of listed flare times.

I shall discuss each of these three points in turn.

Inappropriateness of the 0.6 and 1.2 MeV proton and >300 keV electron data

The observations of type III radio bursts from both terrestrial stations and spacecraft clearly indicate that the type III burst exciter speed stays essentially constant from close to the sun to 1 A.U. I quote from the abstract of Fainberg and Stone (1970), who examined 2500 type III burst drift rates by a method independent of a model for electron density along the path traveled by the exciter. "Based on this dependence, a least squares analysis of 2500 drift rates between frequencies in the 2.8 to 0.7 MHz range yields an average exciter speed of 0.38c for the height range from approximately 11 to 30 $R_\odot$. In conjunction with the available determinations of exciter speeds of 0.33c close to the sun, i.e. less than 3 $R_\odot$, and with in situ measurements of 40 keV solar electrons by space probes, the present results suggest that the exciters are electron packets which propagate with

little deceleration over distances of at least 1 AU." Hartz (1969) in a previous paper on hectometer wavelength observations also finds that "The average source drift velocities are found to be about 0.35c, in substantial agreement with results obtained at metric and decametric wavelengths."

Fainberg and Stone (1970) find a spread in frequency-drift rates which can be interpreted as a velocity spread of 0.2 to 0.6c for the exciter. However they believe that the spread is due to streamer density inhomogeneities. Although their analysis is carried out for a type III storm they indicate that preliminary analysis shows that such exciter velocities are also typical of isolated type III bursts.

In view of this evidence for velocities of $\sim$0.37c out to 30 $R_\odot$ (0.14 A.U.) it is clear that the >300 keV electrons ($v \sim 0.77c$) are inappropriate for this analysis.

The 0.6 and 1.2 MeV proton data are also completely irrelevant to the discussion since $v \sim 0.04c$. Presumably the proton data are applicable if, as G & L suggest, the exciter suffers substantial deceleration between the sun and 1 A.U. In fact Kaplan and Tsytovich (1968); Friedman and Hamberger (1969) and Smith (1970a, b) have suggested proton beams for just the reason that there is theoretical evidence indicating that protons will <u>not</u> lost much energy in their generation of plasma waves. Thus any proton observations should be directed at $\sim$50 MeV protons (Smith 1970a). It should also be mentioned here that since the observations are of the first arriving protons after the event at the sun little adiabatic deceleration will be suffered by the protons in their propagation out through the interplanetary medium.

Thus the only relevant data examined here is the >40 keV electron data.

Analysis and interpretation of the particle-type III correlation

G & L obtained a 65% correlation of 0.6 and 1.2 MeV protons with type III bursts using the criteria that the burst occurs 4 ± 1 hour or 5-8 hours before the onset of the event. They obtained a 55% correlation for >40 keV electron events under the criteria that the type III burst occurs with $\frac{1}{2}$ or 1 hour before the electron onset. In order to interpret their results one must ask that percent correlation would be obtained under these criteria for randomly chosen particle event onset times. To obtain this number I have taken the days when events occur and calculated what percent of the total observational time would be covered under the various criteria. Here I have used the IAU Quarterly Bulletin of Solar Activity (1968) listing of decametric bursts. Under the proton criteria, 4 ± 1 hour or 5-8 hours — equivalently 3-8 hours before the proton onset — a 62% correlation would be obtained for randomly chosen onset times compared with 65% obtained by G & L for the observed proton event onsets.

For the electron criteria, 0-1 hour before the electron onset, I obtain 42% for randomly chosen onset times compared to 55% obtained by G & L for actual electron event onsets. In addition, G & L used data from the Weissenau Observatory, which was the only one covering the ~0700-1200 period, to obtain negative correlations in several of the events. The negative correlation for those events is due to the fact that Weissenau does not report decametric bursts

since it only observes in the frequency range 46-540 mHz. Weissenau does report metric wavelength type III bursts for those events. Secondly G & L claim that the period 28 July-4 August 1967 should be treated separately because of the large probability of associating any interplanetary particles with a type III burst. The calculated probability for randomly chosen onset times is 65% for those days. The fact that all 14 electron events during 28 July-4 August are correlated to type III bursts is either a remarkable coincidence or highly significant.

If we throw out those events covered by Weissenau then we obtain 58% ± 12% correlation compared with 42% expected from randomly chosen onset times. This comparison indicates that the correlation is barely significant. However, G & L only used a part of the total published electron event listings (Lin and Anderson, 1970; Lin, 1970). Using all the events observed in 1964-1967, under their criteria I obtain, for 76 events with type III decametric coverage, 48 events with decametric type III bursts occurring within 1 hour before electron onset, 5 with metric type III, 8 with type III slightly longer than 1 hour after (up to 80 minutes) and 15 with none. Thus at least 48/76 = 63% ± 9% of all electron events are associated with type III decametric bursts. This is a very substantial correlation since perhaps on the order of 5-10 events would be expected to originate from flares well beyond the west limb where the accompanying type III radiation would be invisible.

Flare associations

In regard to flare associations for solar particle events, particularly >40 keV electron events, I would like to point out that:

1. It is quite clear that energetic particle events, both proton and electron, which can be identified from their time profile and velocity dispersion to be new impulsive injections of particles from the sun, are indeed produced by solar flares (with the possible exception of very small events).

2. G & L mention the complications in identifying the associated flare which arise from uncertainties in modes of particle propagation and diffusion in the interplanetary medium. These complications are <u>not</u> removed by correlation directly to type III bursts. This fact is implicitly recognized by the authors in their second proton association criteria.

3. Flare associations for >40 keV electron events have <u>not</u> been biased by the size of the flare; in fact Lin (1970) finds that one of the characteristics of electron flares is that they are predominantly importance 1 flares or subflares.

4. The time period between the flare and the >40 keV electron observed at 1 A.U. varies predominantly because the onset of the event is mechanically chosen as the time when the flux has risen above and stays above 1σ above background. If the background is high due to preceding events or if the rise of the event is slow, or if the event is weak the onset time will be chosen somewhat later. No extrapolation to zero flux has been used. In addition the onset time depends on the energy of the electrons. Furthermore

the timing accuracy of optical flare listings is on the order of ± 5 minutes — stations rarely agree among themselves to better than that. It is therefore quite reasonable to expect variations of 1.5 to 83 minutes (corresponding to 10 to 91 minutes travel time from the sun to the earth) between flare and electron onset at 1 A.U. The events which exhibit a rapid rise and for which accurate x-ray data exist always appear to have their onset within 40 minutes of the x-ray burst maximum.

5. Previous efforts to examine the question of type III burst correlation to >40 keV solar electron events have been based on the following criterion: "A radio or x-ray event was considered to be associated with the electron event if it occurred within ± 2 minutes of the period between the start and maximum of the electron flare event. The flare end time was not used because of its variability from one observatory to another and because, in many cases, the electron onset at 1 A.U. occurred before the end of the flare." (Lin, 1970) Using this same criteria and examining all flares from the Solar-Geophysical Data (U.S. Dept. of Commerce, 1968) and all type III bursts listed in the IAU Quarterly Bulletin on Solar Activity (1968), I find:

	Quiet Period April 1-20, 1967	Disturbed Period July 22-31, 1967
Total number of flares	394	555
Number of flares for which radio data is not available	124	92
Number of flares with type III burst	$\frac{51}{270} = 19\%$	$\frac{193}{463} = 40\%$

Number of electron event flares with type III burst (from Lin, 1970) $\frac{46}{56} = 82\%$

It is clear that the results are highly significant. Two points should be noted here: (a) contrary to G & L's claim, the association of particle events with flares does not automatically produce an association with type III bursts, even in highly disturbed times; and (b) the association of type III bursts with electron event flares is even higher than when the type III bursts were directly compared to electron events. This is partly because events which are not identified with a visible flare may be from flares over the limb whose type III emission is not observed.

In summary, I believe that G & L's conclusion is incorrect and that if the analysis is carried out correctly then the results actually support the association of type III bursts and >40 keV electron events.

One question which remains is that the number of type III radio bursts far exceeds the number of >40 keV electron events observed at 1 A.U. However, any correlations of the two phenomena must take into account:

1. the location of the type III burst at the sun,
2. the relative sensitivity for detection of type III bursts and electrons,
3. the possibility that type III burst particles are stopped high in the corona and do not escape.

Recently, Alvarez et al. (1972) have compared intense type III bursts observed by OGO-5 at 350 kHz (corresponding to a distance of ~50 $R_\odot$ away from the sun) to electron events observed at 1 A.U. They find

that essentially a one-to-one correlation (26/28) exists between these distant type III bursts and >40 keV electron events above detector threshold, for bursts from flares west of W10° solar longitude.

I would also like to correct one particular misquotation by G & L in their article: Lin (1970) did not suggest "...the possibility of similar behavior for >40 and >300 keV electrons." Quite the contrary the article clearly points out the difference between the relativistic electron component (which only accompany proton events) and the >40 keV electron component and notes (with reference to electrons) "...with the exception of a very few events not observed at 3-10 MeV energy all these 0.3-0.9 MeV events are observed only during proton events." (Lin, 1970)

REFERENCES

Alvarez, H., F.T. Haddock and R.P. Lin, Evidence for electron excitation of type III radio burst emission, submitted to Solar Phys., 1972

Fainberg, J. and R.G. Stone, Type III solar radio burst storms observed at low frequencies, 2, Average exciter speed, Solar Phys., 15, 433, 1970

Friedman, M. and S.M. Hamberger, On a possible proton origin for type III continuum radiation from a solar flare, Solar Phys., 8, 398, 1969

Graedel, T.E. and L.J. Lanzerotti, Interplanerary-particle associations with type III solar bursts, J. Geophys. Res., 76, 6932, 1971

Hartz, T.R., Type III solar radio noise bursts at hectometer wavelength, Planet. Space Sci., 17, 267, 1969

I.A.U. Quarterly Bulletin on Solar Activity, nos. 158, 159 and 160, Eidgen. Sternwarte, Zurich, 1968

Kaplan, S.A. and V.N. Tsytovich, Radio emission from beams of fast particles under cosmic conditions, Sov. Astron.-AJ, Engl. Transl. 11, 956, 1968

Lin, R.P., The emission and propagation of ~40-keV solar flare electrons, 1, The relationship of ~40-keV electrons to energetic proton and relativistic electron emission by the sun, Solar Phys., 12, 266, 1970

Lin, R.P. and K.A. Anderson, Electrons >40 keV and protons >500 keV of solar origin, Solar Phys., 1, 446, 1967

Smith, D.F., Towards a theory for type III solar radio bursts, 1, Nature of the exciting agency, Solar Phys., 15, 202, 1970a

Smith, D.F., Type III solar radio bursts, Advan. Astron. Astrophys., 7, 147, 1970b

EVIDENCE FOR A HIGHLY COMPACT X-RAY SOURCE

A71-43076

BRUCE MARGON, STUART BOWYER, MICHAEL LAMPTON,
AND RAY CRUDDACE

THE ASTROPHYSICAL JOURNAL, 169:L45–L48, 1971 October 15
© 1971. The University of Chicago. All rights reserved. Printed in U.S.A.

EVIDENCE FOR A HIGHLY COMPACT X-RAY SOURCE

BRUCE MARGON, STUART BOWYER, MICHAEL LAMPTON, AND RAY CRUDDACE
Department of Astronomy and Space Sciences Laboratory, University of California, Berkeley
Received 1971 August 26

ABSTRACT

A detailed spectrum of the X-ray source GX 340+0 is presented. The spectrum may be fitted from 1 to 10 keV by a blackbody model at $T = 1.5 \times 10^7$ ° K, subject to heavy photoelectric absorption. Unlike X-ray sources previously reported, the spectrum is not also compatible with power-law or thermal-bremsstrahlung models. If the source is a blackbody at the distance indicated by its X-ray absorption, its radius is 8 km and luminosity 3×10^{37} ergs s^{-1}. This source may provide direct evidence for the existence of a neutron star.

The observation reported in this Letter was made from an Aerobee 150 rocket launched from Natal, Brazil, on 1969 June 14. Data were obtained by two argon-methane proportional counters equipped with Mylar windows. The details of the instrumentation employed have been reported previously (Bowyer *et al.* 1970). During a scan of the galactic plane, a number of sources were detected. Sufficient counts were obtained from 10 of these sources to permit a comparison of the observed spectra with detailed models. The results for 9 of these sources will be reported separately (Cruddace *et al.* 1971); however, the spectrum of one source was found to be unique and is discussed herein.

The $3° \times 12°$ FWHM fan-beam detector observed this source at $l^{II} = 340°.0 \pm 0.5$, $b^{II} = 0° \pm 0.5$ ($\alpha = 16^h43^m$, $\delta = -45°\ 9'$, 1950.0) on the Ara-Scorpius boundary. We identify this source as GX 340+0, previously reported by several other groups and sometimes designated Ara XR-1. It was first reported by Friedman, Byram, and Chubb (1967) and located to an accuracy of 17′ by Bradt *et al.* (1971). In Figure 1 we present the X-ray spectrum of this source. The data employed were taken from 1.66 seconds of the record centered on the peak signal. The roll rate at the time was 1° per second. The contribution from other possible sources to these data due to possible source confusion was less than 16 percent of the total counts, based on comparison of our observations with those of the *Uhuru* satellite (Giacconi *et al.* 1971*a*). We have distinguished GX 340+0 from all other sources reported by *Uhuru* in this region. The experimental data have been corrected for counter efficiency, resolution, and background as previously described (Lampton *et al.* 1971). The data were fitted with three trial photon distributions: blackbody, thermal bremsstrahlung, and power law. Table 1 gives the results of this analysis. The blackbody model provides a good fit to the data, but the power-law and bremsstrahlung models do not.

The best-fit blackbody model is shown in Figure 1 by a solid line. The inset to Figure 1 presents a contour of constant probability for the blackbody model. The contour drawn is where the confidence of the χ^2 fit drops to $e^{-1/2} = 0.606$ of the best value. The small area enclosed by this contour indicates that the range of probable values of T and N_H is severely constrained.

Two other X-ray sources whose spectra are compatible with a blackbody distribution have been reported. However, in both of these sources the spectra are also compatible with thermal-bremsstrahlung emission mechanisms. The spectrum of Cen XR-3 (Giacconi *et al.* 1971*b*) has been reported in the 2–20-keV region, where bremsstrahlung and blackbody models are virtually indistinguishable at present levels of resolution. The

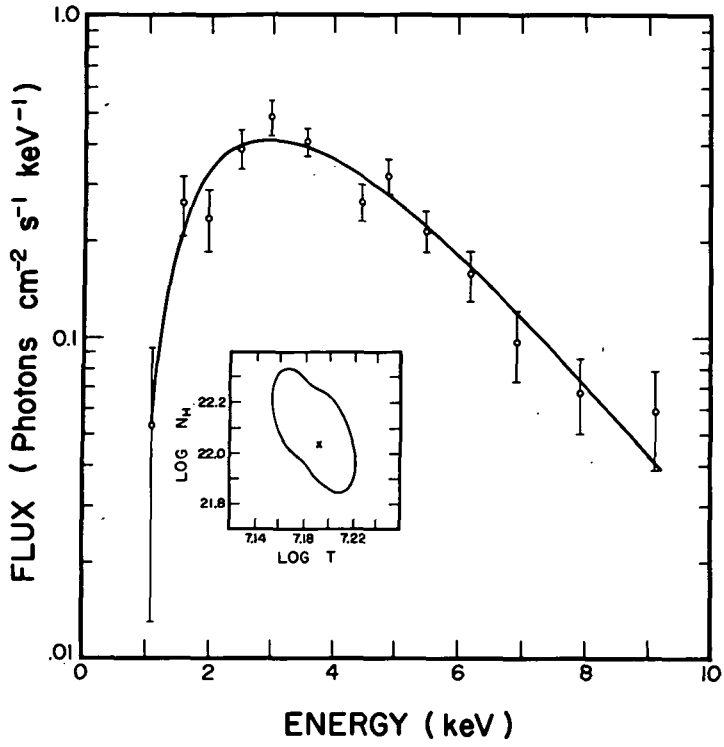

FIG. 1.—Spectrum of GX 340+0. Error bars are ± 1 σ statistical errors. Average background-corrected counting rate was 365 counts s^{-1}. *Solid line*, best blackbody fit. *Inset*, contour of constant probability for this fit.

TABLE 1

SPECTRAL ANALYSIS OF GX 340+0

Model	T or n*	N_H [cm^{-2}]	Intensity† 1–10 keV [keV cm^{-2} s^{-1}]	Confidence [percent]
Blackbody.....	1.55×10^{7}° K	1.20×10^{22}	8.29 ± 0.42	25.2
Power law.....	-2.25	5.01×10^{22}	9.76 ± 0.50	3.8
Bremsstrahlung.....	7.08×10^{7}° K	3.98×10^{22}	7.85 ± 0.40	8.3

* As used in this paper, n is the exponent describing the photon distribution. The power flux index is $n+1$.

† Errors quoted are statistical only.

spectrum of Cir XR-1 (Margon *et al.* 1971) has been reported in the 1–10-keV region; this spectrum may be fitted with either a bremsstrahlung or a blackbody model with acceptable confidence. Thus, GX 340+0 is the first X-ray source reported in which the blackbody spectral distribution is compatible with observations but bremsstrahlung and power-law distributions are not.

Since both Cen XR-3 and Cir XR-1 exhibit X-ray pulsation, a search for X-ray

pulsation in GX 340+0 was undertaken in the manner previously reported (Margon *et al.* 1971). The short observing time, combined with the 128-ms telemetry sample period, restricted this search to frequencies between 1 and 4 Hz. The power spectrum of GX 340+0 at these frequencies contained no peaks of equal significance to that reported for Cir XR-1.

Since the absolute intensity of blackbody radiation is fixed by its temperature, we can calculate the angular size of the radiating body. If $F(E)$ represents the flux observed and $I(E)$ represents the intensity of the blackbody source, then

$$\Omega = \frac{F(E)}{I(E)} = (1.43 \pm 0.46) \times 10^{-32} \text{ sterad} .$$

The corresponding linear radius R requires a determination of the distance to the source. This distance can be obtained from a comparison of the X-ray absorption data with 21-cm emission data. The present measurement yields an X-ray absorption fit of $N_{\rm H} = (1.2 \pm 0.6) \times 10^{22}$ cm^{-2}, based on the effective cross-section given by Brown and Gould (1970). Kerr (1969) has published a plot of 21-cm antenna temperature versus velocity at the position of this source. After correction for channel bandwidth and for random cloud velocities, this profile was combined with the Schmidt model of galactic rotation (Schmidt 1965) to provide a plot of distance versus $\int n_{\rm H} dl$. With an assumed cloud temperature of 100° K, we find that $N_{\rm H} = 1.2 \times 10^{22}$ cm^{-2} corresponds to a distance of 4 kpc. From these data, the linear radius of the source may be calculated:

$$R = D(\Omega/\pi)^{1/2} = 8 \pm 4 \text{ km} ,$$

where the uncertainty quoted reflects chiefly the uncertainty in our determination of $N_{\rm H}$ from the X-ray data. The corresponding total luminosity is 3×10^{37} ergs s^{-1}.

There exists a limited range of source models that could produce a blackbody spectral distribution peaked at X-ray wavelengths. Although a thermal-bremsstrahlung spectrum does not fit the observations, it might be argued that with the addition of recombination and line radiation the resultant spectrum could mimic a blackbody spectrum. Tucker and Koren (1971) have shown, however, that both recombination radiation and line emission are negligible at model temperatures appropriate for this case.

A high-temperature neutron star has been shown to emit a spectrum similar to that of a blackbody. Orszag (1965) computed neutron-star spectra including the possible effects of absorption edges. He found some deviations from a blackbody spectrum which were dependent upon the assumed composition and surface temperature. Most of the effects noted were washed out at a temperature of 10^7 ° K, however. In addition, Onyejuba and Gaustad (1967) showed that any absorption lines present in the atmosphere of a neutron star would be sufficiently Stark broadened that both the lines and any absorption edges present would be obliterated.

It has been proposed that a neutron star is formed, perhaps cataclysmically, at the endpoint of stellar evolution. Although it would initially be formed at a high temperature, it would cool rapidly. Arguments concerning cooling processes and time scales for these objects have been summarized by Cameron (1970), who shows that the cooling time for a 1 $M_\odot$ neutron star at $T = 10^7$ ° K is of the order of 1 year. The fact that this source was probably observed as early as 1965, coupled with the extremely rapid cooling rate for these objects, makes it unlikely that GX 340+0 is a recently formed neutron star.

Another possible model for a blackbody X-ray source involves accretion of interstellar matter on a neutron star (Ostriker, Rees, and Silk 1970). The spectrum of this process has been shown to resemble a blackbody within the energy range of our observations (Zel'dovich and Shakura 1969). Ostriker, Rees, and Silk (1970) suggest that a typical temperature for such a source is $T = 7.3 \times 10^5$ ° K. Thus, if this mechanism is respon-

sible for X-ray generation in GX 340+0, one or more parameters of the accretion process must be different from that suggested by these authors. One possibility is that the accretion rate of the object is increased by a factor of about 10^5 from the suggested value of 10^{12} g s^{-1}, which could be achieved if the velocity of the accretor relative to the interstellar medium were about 0.2 km s^{-1} rather than 10 km s^{-1}. The necessary accretion rate of 10^{17} g s^{-1} has in fact been suggested in connection with neutron-star accretion from a binary companion (Shklovskii 1967) and from a circumstellar shell of material (Zel'dovich and Shakura 1969). In the latter case, some models produce a 10–100-keV emission continuum in addition to the 1–10-keV thermal radiation. This predicted high-energy continuum may have already been observed in GX 340+0 by Lewin *et al.* (1969) and Davison *et al.* (1971).

The accretion rate onto a highly luminous star is diminished by the action of radiation pressure on the infalling plasma. The resulting effective stellar mass for accretion is

$$M_{\text{eff}} = M_* - \frac{R_*^2 \sigma T^4 \sigma_{\text{Thomson}}}{c(m_e + m_p)G},$$

where M_* and R_* are the star's mass and radius, respectively, and σT^4 gives its blackbody emittance. The maximum temperature at which accretion is possible occurs at $M_{\text{eff}} = 0$, or

$$T_{\max} = 2.05 \times 10^7 \left(\frac{M_*}{M_\odot}\right)^{1/4} \left(\frac{10\text{ km}}{R_*}\right)^{1/2} {}^\circ\text{K}.$$

The fact that our observed temperature approaches this limit may indicate that accretion of circumstellar plasma is occurring in a self-regulating manner.

In summary, we have observed a source which appears to be a blackbody radiator. If it is in fact a blackbody, then its radius is approximately 8 km. Our observations are consistent with a neutron star at a temperature of 1.5×10^7 ° K.

We are grateful to Dr. H. Weaver for interpretation of the 21-cm data, and acknowledge the assistance of Dr. J. E. Mack in payload preparation. This work has been supported by NASA grant NGR 05-003-278.

REFERENCES

Bowyer, C. S., Lampton, M., Mack, J., and deMendonca, F. 1970, *Ap. J. (Letters)*, **161**, L1.
Bradt, H., Burnett, B., Mayer, W., Rappaport, S., and Schnopper, H. 1971, *Nature*, **229**, 96.
Brown, R. L., and Gould, R. J. 1970, *Phys. Rev.*, **D1**, 2252.
Cameron, A. G. W. 1970, *Ann. Rev. Astr. and Ap.*, **8**, 179.
Cruddace, R. G., Mack, J. E., Lampton, M., Bowyer, S., and Margon, B. 1971 (in preparation).
Davison, P. J. N., Buselli, G., Clancy, M. C., and Thomas, R. M. 1971, *Ap. J.*, **167**, 479.
Friedman, H., Byram, E. T., and Chubb, T. A. 1967, *Science*, **156**, 374.
Giacconi, R., Kellogg, E., Gorenstein, P., Gursky, H., and Tananbaum, H. 1971*a*, *Ap. J. (Letters)*, **165**, L27.
Giacconi, R., Gursky, H., Kellogg, E., Schreier, E., and Tananbaum, H. 1971*b*, *Ap. J. (Letters)*, **167**, L67.
Kerr, F. J. 1969, *Australian J. Phys., Ap. Suppl.*, Vol. 9.
Lampton, M., Bowyer, S., Mack, J. E., and Margon, B. 1971, *Ap. J. (Letters)*, **168**, L1.
Lewin, W. H. G., Clark, G. W., Gerassimenko, M., and Smith, W. B. 1969, *Nature*, **223**, 1143.
Margon, B., Lampton, M., Bowyer, S., and Cruddace, R. 1971, *Ap. J. (Letters)*, **169**, L23.
Onyejuba, P. E., and Gaustad, J. E. 1967, *Ap. J.*, **147**, 806.
Orszag, S. A. 1965, *Ap. J.*, **142**, 473.
Ostriker, J. P., Rees, M. J., and Silk, J. 1970, *Ap. Letters*, **6**, 179.
Schmidt, M. 1965, in *Stars and Stellar Systems*, Vol. 5, ed. A. Blaauw and M. Schmidt (Chicago: University of Chicago Press).
Shklovskii, I. S. 1967, *Ap. J. (Letters)*, **148**, L1.
Tucker, W. H., and Koren, M. 1971, *Ap. J.*, **168**, 283.
Zel'dovich, Ya. B., and Shakura, N. I. 1969, *Soviet Astro.—AJ*, **13**, 175.

A PULSING X-RAY SOURCE IN CIRCINUS

BRUCE MARGON, MICHAEL LAMPTON, STUART BOWYER,
AND RAY CRUDDACE

THE ASTROPHYSICAL JOURNAL, 169:L23–L25, 1971 October 1
© 1971. The University of Chicago. All rights reserved. Printed in U.S.A.

A PULSING X-RAY SOURCE IN CIRCINUS

BRUCE MARGON, MICHAEL LAMPTON, STUART BOWYER, AND RAY CRUDDACE
Department of Astronomy and Space Sciences Laboratory,
University of California, Berkeley
Received 1971 August 4

ABSTRACT

A pulsing X-ray source with period 685 ± 30 ms has been observed in Circinus. Approximately 10 percent of the 1–10-keV X-ray emission of the source is contained in these pulses. A spectrum of the source is presented and may be fitted by a thermal bremsstrahlung emission mechanism with $T = 3.5 \times 10^{7}$ ° K, or by a blackbody at $T = 1.1 \times 10^{7}$ ° K, both subject to heavy absorption.

The observation reported in this Letter was made from an Aerobee 150 rocket launched from Natal, Brazil, on 1969 June 14. Data were obtained by two argon-methane proportional counters equipped with Mylar windows. Extragalactic observations from this flight, together with a description of the instrumentation and method of spectral-data analysis, have been reported previously (Bowyer *et al.* 1970; Lampton *et al.* 1971). A complete description of galactic-source observations made on the flight is in preparation (Cruddace *et al.* 1971).

During a scan of the Norma-Lupus-Circinus region, a well-isolated source was observed in both counters. The two detectors were collimated differently, one with a 3° × 12° full width at half-maximum (FWHM) fan beam, the other with a 1°.6 FWHM pencil beam. A comparison of the count rate of the source as observed by each detector in combination with the time lag between peak count rates permitted the source to be located with reference to the scan track to an accuracy of 0°.5. The location of the scan track was established by comparing our X-ray source observations with those of known sources. The source is located at $l^{II} = 321°.4 \pm 0°.9$, $b^{II} = -0°.5 \pm 2°$ ($\alpha = 15^{h}14^{m}$, $\delta = -57°49'$, 1950.0) within the constellation Circinus and is hereafter referred to as Circinus XR-1 (Cir XR-1).

The data presented here are taken from the fan-beam detector, whose average background-corrected count rate of 308 counts s^{-1} substantially exceeded that of the pencil-beam detector. The sampling period of our telemetry was 128 ms. The power spectrum of 64 successive count-rate accumulations, which represent the entire 8.2-s transit of Cir XR-1, was calculated by using the method described by Lampton, Bowyer, and Harrington (1970). Figure 1 is a plot of this power spectrum. The peak at 1.46 ± 0.06 Hz (685 ± 30 ms) is statistically significant. The probability of a random fluctuation reaching this power level anywhere in the observed spectrum is 8.36 percent. The fractional modulation, which we define as the ratio of half-amplitude to the mean background-corrected count rate, is 10 ± 2 percent. As a check against possible systematic error, we have similarly analyzed the count rate from four other galactic sources observed during this flight. No other obviously periodic variations were observed.

In Figure 2 we present the photon spectrum of Cir XR-1. These data represent 6.53 s of observation centered on the transit of the source through the fan-beam detector. Each point is corrected for counter efficiency, resolution, and background. Three different model photon distributions were fitted to the data in the manner described by Lampton *et al.* (1971). The results are shown in Table 1. It is clear that the bremsstrahlung and blackbody models are compatible with the observations, while the power law is not. The 1–10-keV intensity of the source is 9.46 ± 0.56 keV cm^{-2} s^{-1}, or 2.85 ± 0.17 photons cm^{-2} s^{-1} (errors quoted are statistical only). Figure 2 also presents contours of constant

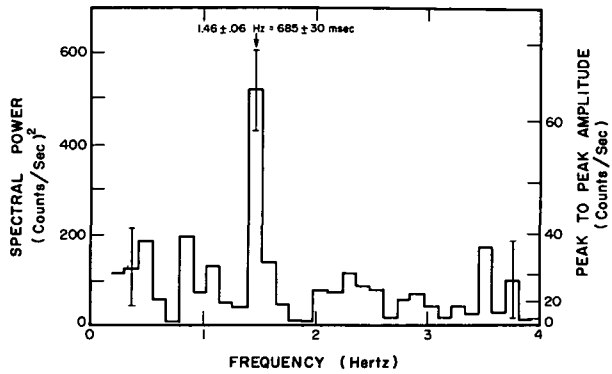

FIG. 1.—Power spectrum of Cir XR-1

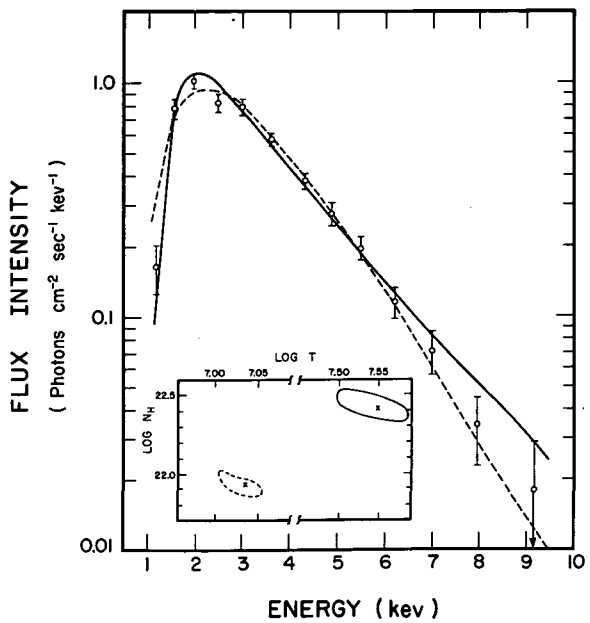

FIG. 2.—Photon spectrum of Cir XR-1. *Solid line*, best bremsstrahlung fit. *Broken line*, best blackbody fit. Error bars are $\pm 1\,\sigma$ statistical errors. *Inset:* contours of constant probability for the two models.

TABLE 1

SPECTRAL ANALYSIS OF CIRCINUS XR-1

Model	T or n	N_H (cm^{-2})	Confidence (%)
Bremsstrahlung.....	3.5×10^{7}° K	2.5×10^{22}	18.4
Blackbody.....	1.1×10^{7}° K	0.8×10^{22}	33.4
Power law.....	-2.925	3.5×10^{22}	0.1

probability for the bremsstrahlung and blackbody models. The contours shown are those where the confidence of the least-squares fit drops to $e^{-1/2} = 0.606$ of the peak value.

Circinus XR-1 resembles two previously reported pulsing X-ray sources, Tau XR-1 and Cyg XR-1, in that it has a fairly small fraction of the total counts in pulsed form; it is similar to the one other reported X-ray pulsar, Cen XR-3 (Giacconi *et al.* 1971*a*), in that Cir XR-1 has a thermal spectrum. All four objects thus far observed have extremely low galactic latitudes. Taurus XR-1 is known to be at a distance of 2 kpc and shows little photoelectric absorption. An upper limit of about 1 kpc can be placed on the distance to Cyg XR-1, based on the turnover in its spectrum (Gursky *et al.* 1971). Both Cen XR-3 and Cir XR-1 are heavily absorbed. For Cir XR-1, 21-cm emission measurements give a total column density $N_{\rm H} = 1.4 \times 10^{22}$ cm^{-2} (McGee, Milton, and Wolfe 1966). This is close to the number deduced from absorption in the X-ray spectrum and suggests that the source is quite distant.

The Milne catalog of galactic nonthermal radio sources (Milne 1970) lists three sources—designated MSH 15-52A, MSH 15-52B, and Kes 24—within the error box of Cir XR-1. Although the radio pulsar MP 1530 lies near Cir XR-1, its position falls 4°.9 from the center of our error box and is probably not associated with the source.

Due to uncertainties in latitude determinations of *Uhuru* satellite observations (Giacconi *et al.* 1971*b*), the source in Lupus tentatively reported by Giacconi *et al.* (1971*a*) as exhibiting X-ray pulsation may in fact be Cir XR-1, since the longitude of the two sources is virtually identical.

We wish to thank Dr. J. E. Mack for his assistance in payload preparation and data reduction. This work has been supported by NASA grant NGR 05-003-278.

REFERENCES

Bowyer, C. S., Lampton, M., Mack, J., and deMendonca, F. 1970, *Ap. J.* (*Letters*), **161**, L1.
Cruddace, R. G., Mack, J. E., Lampton, M., Bowyer, C. S., and Margon, B. 1971 (in preparation).
Giacconi, R., Gursky, H., Kellogg, E., Schreier, E., and Tananbaum, H. 1971*a*, *Ap. J.* (*Letters*), **167**, L67.
Giacconi, R., Kellogg, E., Gorenstein, P., Gursky, H., and Tananbaum, H. 1971*b*, *Ap. J.* (*Letters*), **165**, L27.
Gursky, H., Gorenstein, P., Kerr, F. J., and Grayzeck, E. J. 1971, *Ap. J.* (*Letters*), **167**, L15.
Lampton, M., Bowyer, C. S., and Harrington, S. 1970, *Ap. J.*, **162**, 181.
Lampton, M., Bowyer, S., Mack, J. E., and Margon, B. 1971, *Ap. J.* (*Letters*), **168**, L1.
McGee, R. X., Milton, J. A., and Wolfe, W. 1966, *Australian J. Phys.*, Suppl. No. 1.
Milne, D. K. 1970, *Australian J. Phys.*, **23**, 425.

SPACE SCIENCES LABORATORY

X72-17416

AN EARTH RESOURCE DEBATE

by
Richard O. Mason
University of California at Los Angeles

Internal Working Paper No. 11

February, 1972

UNIVERSITY OF CALIFORNIA, BERKELEY

AN EARTH RESOURCE DEBATE

by
Richard O. Mason
University of California at Los Angeles

Internal Working Paper No. 11

February, 1972

This research was supported in part by the National Aeronautics and Space Administration under General Grant #NGL 05-003-404 under the University of California.

Social Applications of Resource Information
Space Sciences Laboratory
University of California
Berkeley

AN EARTH RESOURCE DEBATE

by
Richard O. Mason

Introduction

Prologue

What is the true value of ERTS? There is no ultimate answer to this question but it is important to consider how one might go about answering it. Some would say that the answer is essentially simple but computationally insuperable. That is, in principle all one needs to do is to calculate the benefits or savings accruing from snowpack estimation, more efficient water management, blight detection, forest fire detection, new mineral discovery, improved cartography and land-use mapping, and so on for each application. Then, merely sum up the benefits from all applications and, by subtracting the actual and opportunity costs, obtain a figure representing ERTS' value.

But others, on reflection, find that the answer is more elusive and complex than that. Such a simple method raises some doubts. When one takes a broad view of resource and environmental problems (the problems which in the long run ERTS is to help us solve) one sees how fine these problems are interwoven with our governmental, industrial and cultural institutions.[1] The very way that we think and live and view the world is an integral part of the resource problem. If we can only find the right perspectives and institutions for nourishing the earth and insuring its survival then, in a most essential way, the resource problem will have been solved. A "solution" of

---

[1] See "Beyond Benefits and Costs" by R. O. Mason. Space Sciences Laboratory Social Sciences Group, Internal Working Paper #12, February, 1972

this type is not measurable in benefit-cost terms, since benefit-cost analysis must assume a certain institutional framework to make its procedures work. However, there is immense value to be gained if we can find the right perspectives and institutions to aid man in solving the earth resource management problem.

There are three fundamental components to the earth resource management problem. First, there is the physical nature of the earth itself. Second, are the institutions, that is the laws, customs, practices and organizations that man has devised for dealing with the earth. And, finally, there is the psychological outlook or perspective of the earth that each person, especially those in decision-making capacities, possesses. These components work together to determine the final dispensation and utilization of earth's resources. Disfunctional uses, such as pollution, result from breakdowns or misunderstandings in any of the three dimensions.

If the ERTS program is to achieve its ultimate goal of solving mankind's food, water and mineral resource problems, it must deal with all three components of the earth resource management problem. The NASA sponsored University of California Integrated study takes this perspective. While the bulk of the effort is directed toward determining how ERTS can provide better information about the physical nature of the earth, the social sciences group of the U. C. study is addressing the other two dimensions of the problem. Studies are currently underway which look at the questions of what kinds of organizations and institutions will be needed to deal with ERTS data and who should be involved in making earth-resource decisions. This study is concerned with the psychological perspective man uses as a guide in organizing ERTS data, developing institutions and carrying out decisions.

Perhaps the most intriguing thing about ERTS program is that it shows great potentiality for producing value in the sense of developing new perspectives about the earth. To be sure, there will be cost-effective "applications," but these will flow naturally from the creation of a more lasting impact--a sobering realization of man's place in this "fathomless universe." (Whitman - O Captain! My Captain!) The astronauts' descriptions and the awe-inspiring space photographs perhaps only herald a new world view to come. At least, there is some evidence of this. Take, for example, John Caffrey's letter to the editor in Science (March 20, 1970) in which he related the profound effect that the space photographs had on him. He then went on to say:

> Looking at the blackness beyond the sharp blue-green curve, trying to see even the place where the thin envelope of atmosphere and the solid Earth meet, the curious word "fragile" comes to mind. To be on Earth and think of it as fragile is ridiculous. But to see it from out there and to compare it with the deadness of the Moon! I suspect that the greatest lasting benefit of the Apollo missions may be, if my hunch is correct, this sudden rush of inspiration to try to save this fragile environment--the whole one--if we still can.

Such are the potential benefits of ERTS; but, more importantly, this fresh perspective sheds new light on our opening question. The "true value" of ERTS is not now of primary concern; rather, the question becomes "How can ERTS best be used to secure the value inherent in a more appropriate perspective toward the earth?" What follows is an initial response to this question.

A Method

ERTS imagery is only data--a set of basic observations of the world. Information is the "meaning" one derives from data. In order to produce information, data must be interpreted from some perspective or point of view. Data are inert; but, information becomes the basis for action. It is

information that determines what decisions will be made and what actions will be taken. Any notion of value must be based upon total short-and-long-range effects of these actions. Consequently, it is vital that we always consider whether the proper point of view was used to interpret the data, as well as the adequacy and completeness of the data-bank itself. This is the only way to evaluate the ERTS program in any ultimate sense. This kind of evaluation will require an approach which is different from that employed to review data-capturing and processing systems, because perspective is psychologically based.

NASA-sponsored research has led to the development of a new approach for exposing and examining points of view, or Weltanschauungen (world view). It is patterned after the dialectic. Using this approach the data are systematically and logically interpreted from two opposing points of view which are, in turn, debated for the manager. The manager, then, must reflect both on the data and on the point of view. The assumption is that, upon witnessing the thesis-antithesis debate, the manager forms a new, broader, more encompassing perspective from which to view the data and the situation--the synthesis. In the context of the ERTS program this synthesis may result in a "better" way of viewing earth, one that pressing environmental, resource and population problems seem so desperately to call for.

The dialectical method requires the determining of opposing positions, the writing of empathic scenarios for each, and the placing of these positions into conflict over the data and issues via debate. The next section represents the beginnings of such an Earth Resource Debate.

The Debate - An Illustration

Background

Our studies have shown that one of the early and perhaps most productive uses of ERTS will be to prepare comprehensive and comparable land-use data. These data will then be interpreted by policy makers to evaluate past usage and to make decisions about future usage. Their evaluations and decisions will depend principally on the perspective they take in interpreting the land-use data.

In order to expose these perspectives for conscious consideration, a debate has been prepared between policy makers possessing two different points of view. The sample data for this debate show land use trends in Los Angeles County from 1940 to the present and as projected through 1990.[2] In the future one might assume that the data would be produced from an analysis of ERTS imagery. Overlaying the photographic image would be a land-use map prepared by computer analysis of digitized data obtained from various sensors and augmented by inputs from trained human observers. However, for the present we will use the available data as the basis for the debate. The data are displayed in Table I.

---

[2] The source of these data is a short study prepared by Herbert Libow. The study revealed a definite lack of consistent, coherent and comparable land-use data for L.A. County over the last 30 years. Our other research suggests a similar lack of data for such important areas as the coastline. This is a problem that ERTS will help to correct.

TABLE I: LAND-USE TRENDS IN LOS ANGELES COUNTY, 1940-1970.

TABLE Ia

LAND USE (1,5,6)		1940	1970	1985-90
Urban used (4, 16)	southern county	25.1%	73.6%	82.0%
Urban vacant (3)	" "	10.1%	5.3	
Non urban used (4)	" "	45.3	7.3	
Non urban vacant (3)	" "	19.5	13.8	
		100.0%	100.0%	
Urban	southern county	35.2	78.9	
Non urban	" "	64.8	21.1	
		100.0%	100.0%	
Used (4)	southern county	70.4%	80.9	
Vacant (3)	" "	29.6	19.1	
		100.0%	100.0%	

TABLE Ib

LAND USE (2)	1940	1960	1970	1985-90
Recreation & parks (5, 7, 8)		** 0.83%	1.6%	2.3%
Agriculture (5, 9)		9.2 %	3.6%	
Crop acreage (5, 10, 11)	12.7%	5.8%	3.1%	2.3%
Range Land (5, 12)		7.9%	8.0%	
Freeway Mileage (13): in miles	6		405	1,045
Sand and gravel production (14, 15): in millions of tons	* 7.0		23.2	
Gold production (14, 15): in dollars	258,000	**7,200	**3,200	

*earliest available information indicates that production was 11.1 in 1947; however a trend line projection indicates that 1940 production was about 7 million tons.

**estimated from available data.

FOOTNOTES 1-16 on page 5b

FOOTNOTES FOR TABLE I

1. The figures represent the percentage of southern Los Angeles County acreage devoted to the particular land use.

2. The figures represent the percentage of Los Angeles County acreage devoted to the particular land use unless otherwise indicated.

3. "Vacant Land" has the possibilities of future development.

4. "Used Land" has minimal possibilities for future land development and may or may not have a current land use. Most land in this category is in use. Vacant land and used land are mutually exclusive categories.

5. Revised Land Use Acreages by Statistical Area, Los Angeles County Regional Planning Commission, April, 1971.

6. Land Use Survey, Los Angeles County Regional Planning Commission, July 1940.

7. Building for Tomorrow: The Community Improvement Program for Los Angeles County, Los Angeles County Department of Parks & Recreation, 1957.

8. Los Angeles County Regional Recreation Areas Plan, County of Los Angeles, 1965.

9. Land Uses, Los Angeles County Regional Planning Commission, 1960 (based upon Los Angeles Regional Transportation Study and U.S. Bureau of Census).

10. Southern California Agriculture: 1969 in Review, Los Angeles Regional Chamber of Commerce.

11. Southern California Agriculture: A Look Ahead to 1970 and 1980, Los Angeles Chamber of Commerce, 1961.

12. 1970 Crop & Livestock Report, Los Angeles County Agricultural Commissioner and County Veterinarian.

13. Verbal information obtained from Los Angeles Regional Planning Commission, Mr. Ron Mayhew, Sept. 1971.

14. Mineral Information Service, V21, 1968 and V6, 1953.

15. California Journal of Mines, V50, nos. 3 & 4, 1954.

16. 1990 Land Use, Los Angeles County Regional Planning Commission, Sept. 1971.

The Debate

Two policy makers--Adam and Bud--debate the "correctness" of the land use policy reflected in the above tables by interpreting the data from their respective points of view.

Adam begins.

Adam: Well, our land-use policy as reflected by these land-use data looks pretty good to me. From the standpoint of regional and national goals it demonstrates much of the great accomplishment of man. We have identified great new resources and have been able to employ them for the betterment of our ever-growing population. Just look at the extent to which we have been able to expand our cities as reflected in the increased urban usage. This means that more people may have their own private homes and their own place to work. There is smog, crime and some congestion, to be sure, but we are making progress and our agricultural land is still adequate to satisfy food needs for some time to come.

Contained here in this single table is a message of great inspiration. We have discovered our earth, subdued it and put it to work for us. Truly earth is now resting comfortably under the dominion of man.

Bud: Oh, the treachery of it all, Adam. The data show that our policy has obviously been to consume and destroy our land and its resources through too much urbanization. Man can never really be superior to his environment, he's a part of it. What the data show is that we are in the process of breaking the basic harmony which man must have with his world. Man is such a recent arrival here on earth--a few thousand years is nothing considering the billions of years that the earth has been around. Don't our predecessors, successors and partners have rights? Flora, Fauna and minerals have a rightful

place in a harmonious world, too. We are offending these rights and may not live to regret it.

Sure, we derive a lot of pleasure and comfort today from our expansive sprawling urban areas, the products of our mines, our transportation system and so forth; but, the cost of depleting our environment is very high. We must learn to "give and take" with nature, take a little "bitter with the sweet," if man and this earth are both to survive.

Maybe now is the time for man to start looking inward a little more to find himself and his place in the universe. Earth is not an object to be conquered, but a partner with which to live. If man could only understand this he would learn to understand himself. And, after all, that's the real purpose in life.

I believe that 73.6% of our land in urban use is far too much. The projections are for it to get worse. Let's cut it down to 20% and let's cut down on the transportation usage as well. Return the rest to wilderness where it belongs.

Adam: Come on now, Bud. We have to use our environment to our own advantage. Nature changes the environment every day of our lives, doesn't she? Why shouldn't we change it? Make it work for us? Besides, I'll never understand your concept of returning land to wilderness. Do you mean that you want us to take large sections of land and just set them aside, never to be touched evermore?

Bud: Certainly.

Adam: How ludicrous. I agree with you that we must plan the ways in which we use our land very carefully. We have made mistakes in the past and chopped

up wilderness areas much too fast and too rambunctiously. Certainly we aren't making the most efficient use of what we have. Some realignment and forethought are most assuredly needed. But to return to primitive times? Ridiculous!

In my view, the best land use principle is quite simple. Take a region of land. Survey it well and make a comprehensive plan for its use. Then make part of it accessible for man's use and part of it inaccessible. Don't touch the restricted portion until it's absolutely necessary. The 1990 projections seem consistent with this kind of planned land-use policy.

Bud: Would you preserve those restricted portions forever?

Adam: No, not forever. You can't take a large area of this country and keep it the way it was a thousand years ago. Nor can man afford to retreat from the most productive lands. We cannot continue to deny man's urgent needs by trying to create useless wilderness.

Bud: Wilderness is not useless. A wilderness area is worth saving or creating in its own right. Man has no business disturbing what lives there naturally. The pollution problem has shown that it doesn't take much to destroy ecological balance. In other areas our land use policy is literally driving some species prematurely into extinction. That's just not morally correct. They are partners in the universe. They have their rights, too. Only the forces of nature can sentence a species to extinction. It is not within man's moral purview to do so.

But, there is another reason for maintaining wilderness areas that perhaps you'll understand more quickly. Wilderness represents a bank for the genetic variability of the earth. It's our "gene pool," as it were.

We are depleting this reserve at a very alarming rate. Now is the time to stop. What is wild, leave wild. Then let's take the land we've unwisely developed in the past and start a genetic investment program by rebuilding our wilderness "capital." Wilderness is a place where natural forces keep working essentially uninterrupted by man. Man should not interfere constantly in the process of natural selection and adaptation; for, the long-range survival of earth depends upon it. Earth always seeks an ecological balance. Everything is connected with everything else. Once man materially disturbs the balance the whole thing can go out of control. Puff! No more earth. Let's protect man from his ignorance now, if its not already too late. As Pogo says, "We have met the enemy and he is us!" The wilderness reserve is our best policy for protection against ourselves and our ignorance.

Man has taken enough for himself already. He needs to start paying back his debt. We should pretend that these wilderness areas don't exist. Don't ever disturb them. They are there for a different purpose--one that will insure the ecological variety that will ultimately save man. But that's not the only point. The important point is that we must learn to be humble with our land and its creatures and pay them respect. That's the proper thing to do; it's part of our obligation to maintain a harmonious universe.

Adam: While you're maintaining harmony, what are we going to do about the people? Population pressures seem to be irresistible. This population growth simply will not permit the kind of policy you're proposing. During the next 20 years we can expect the earth's population to increase from 3.5 billion people to a low of 5.5 billion people, perhaps a high of 7.5 billion people. The Southern California region alone (6 counties) is expected to increase from a present 10 million people to nearly 16 million in 1990 and 22 million in the year 2020. That's a lot of people to feed, clothe, house--to provide

an acceptable standard of living. Where's it going to come from? Not from wilderness, that's for sure. It will have to come from the continued exploration and development of the land and eventually of the sea. We will have continually to discover and develop new resources in order to satisfy the demands of this ever-increasing population.

Bud: Just a minute, now. Those population figures are projections, not fact; I don't buy them. Indeed, the Washington Center for Metropolitan Studies suggests that there is a distinct possibility of achieving zero population growth within this century. We still have a choice in this matter. Population growth is not inevitable; in reality it's only an artifact of the extrapolations you make. But, if your crowd keeps talking that way, you'll come to believe it and then you'll go ahead and make it happen. Then we'll really be in trouble. The worst thing about all these population forecasts is that they tend to become self-fulfilling prophecies.

We have the knowledge and wherewithal today to control population growth and to level it off. It's naive merely to predict the population in the year 2020 and then plan how we are going to respond to it. The intelligent thing to do is to intervene now. We will have to intervene to re-establish the balance we have destroyed by excessive population growth. Within the limits of those already born, we can have any population we want in 2020. When we come to improve our understanding of the basic equilibrium of the universe, we will realize that this continued reproduction of man destroys the balance. Human population growth makes just too many of one resource-grubbing species.

Adam: Well I'm not as optimistic as you. History tells us that we just

cannot put our "head in the sand" on this population growth issue. Any way that you look at it the species is going to reproduce. Furthermore, we know that human wants are insatiable. Elementary economics tells us that we are going to require more resources to satisfy the wants of this ever-increasing population.

This means we need a plan for earth-resource and land-use development. Resources are where you find them and their quantities finite. Perhaps the most criminal thing in the world is to waste resources or to let them stand idle when people need them. Our standard of living depends upon them. The trouble with your wilderness policy is that it doesn't take into account some basic facts about resources. Their original source is fixed by nature. So man must go to them, seek them out and develop them, no matter where they are.

Bud: Do you include the beaches, the Santa Monica Mountains and Lake Arrowhead? The Sequoia's, the Saguaro's? Grand Canyon, Yellowstone, the Tetons, Yosemite? King's Canyon? Lassen? Shasta? Lake Tahoe?

Adam: Yes, if necessary. If that's where the vital resources are. You have to go to the resources. They don't come to you. But they are the ultimate basis of our standard of living. That's where we get our foodstuffs, houses, furniture, television, telephones, electric lights, autos, and airplanes. Everything.

If we need lumber we should cut down those trees that provide the greatest yield for the cost of procuring them, but never more than we need. If that's the Sequoias, O.K. If Mt. Shasta has an economical deposit of an ore that is needed mine it. That ore may improve the standard of living for a hundred years to come.

Bud: Adam, you're all costs and no aesthetics. In the long run you'll have to pay for this excessively economic view of things. You know, there isn't much natural world left now. What there is, is all men will ever have, and all their children will ever have, too. Somewhere, sometime, we must learn to revere our sanctuaries of beauty. The most impressive thing about ERTS space photographs is that the natural magnifience of earth comes radiating through what is at best a cumbersome technology. But even now we can see the flaws, man's defiling of the splendor that once was the earth.

No Adam, your concept of value has you trapped. What's the worth of Yosemite? Fifty billion dollars? No! There's no price on it. The price of beauty has never been evaluated. Look at El Capitan! What would it cost to replace it? If we destroy it what is the "cost" to those who will never thrill to it, who will never know its beauty?

Adam: Bud, modern society has developed a very good method of arriving at such prices. It's called the market system. In it everything has a price--each commodity and each service--and is available for free exchange. Everyone receives money for what he sells and uses this money to buy what he wishes. If you're short of a good the price goes up, if you're long it goes down. This way an equilibrium between supply and demand is maintained.

Now producers, such as the mining companies, continue to compare the prevailing price of their inputs, such as ore, with the cost of its extraction and the market price of its final product by means of a profitability calculus. As long as the enterprise is profitable they are interested.

So, the time may come when Yosemite becomes profitable for ore mining. El Capitan will go into ore production if the mining companies outbid the

other competitors for its use.

Bud: There's a limit to the utility of the market system when it comes to natural resources, a flaw which goes much deeper than just market imperfections or information lags. As you've defined it, only the producers bid, and only the living ones at that. We need to be sure that the aesthetic value, recreation value, peace-of-mind value, are cranked into these market decisions. In large measure these prices are beyond estimation.

But, it's not just the beauty, Adam, it's sustenance as well. The universe is infinite. We know nothing of its beginning or its end. There will (we hope) be many, many generations after ours. Where will they turn for the resources they need, when we have depleted them? And, there are the other creatures who inhabit and will inherit the earth. How does your market system take these other kinds of bids into account?

Adam: I am not going to penalize people today for the sake of future generations. Bud, my friend, "a bird in the hand, is worth two in the bush." Let me prove it to you. Suppose I offer you a choice between a dollar for certain today or a dollar a year, or say, a hundred years from now. Which would you take? The dollar today, wouldn't you? Why? Because the future is uncertain. Other things being equal, the longer we wait, the greater the possibility that conditions will change and the dollar will be worthless, or may never be paid back.

There is a second important reason why this is the right thing to do. The dollar received today can be invested to grow to more than a dollar a year from now, compounding as year builds upon year. The man who gets a dollar now and invests it wisely will have more money a year from now than the man who waits a year or more for his dollar.

Now, it's very much the same with resources. Their future value is less than their present value. An oil field, for example, is not worth very much a hundred years from now when we desperately need petroleum for energy today. For each year we fail to discover and develop new resources the world is losing some of this oil's value.

Bud: You're always thinking about just yourself, Adam, the all-powerful individual, the conquering hero. Never do you consider all of the others. You always place immediate needs ahead of those of the future generations and the other creatures. Remember that Noah took all species, not just man, on the Ark. He saw the need to preserve an ecological balance.

Consider, also, the needs of future generations. What's our obligation to them? Shouldn't the generations of the year 3000 "participate" in our resource decisions? 4000?

We should follow the advice of Theodore Roosevelt:

> The nation behaves well if it treats the natural resources as assets which it must turn over to the next generation increased and not impaired in value.

If we take him seriously then your idea of value is topsy-turvey. Resources are worth more in the future. We should at least be compounding forward rather than discounting backward. The future value of a resource is always higher than its present value. And, the "true value" of resources is very, very high. When we pump oil, mine ore or in any way spoil the beauty of nature, we change something forever. The recipient should at least pay a price equal to the cost of replacing the resource, of restoring nature to its original state; or he should pay the cost of depriving future generations of the resource.

Adam: Bud, those costs are unreasonable. They are astronomical.

Bud: Well, that's the true value. If you really need these resources, you'll be willing to borrow the money and amortize the debt over a few thousand years.

Adam, your version of the market system has made the cost of resources appear too cheap in the past. Consequently, we've become a society that is addicted to resource consumption. We had better "kick the habit" before it's too late.

Adam: Bud, you don't know what you are saying. If we place large amounts of land into wilderness and charge the fantastic prices you suggest, we'll be headed for an economic tailspin. Stagnation. Depression. Diaster.

The great accomplishment of the last 200 years has been our incredible ability to increase per capita real income despite an ever increasing population. This is, undoubtedly, Man's most singular achievement.

Bud: And, alas, it may be his very last!

Adam: Bud, economic development wasn't accomplished with the kind of mystical, religious, and fuzzy kind of thinking I've heard from you so far. No, it only was achieved through a rational, goods-centered concept of personal and social welfare. It was accomplished because we were dedicated to procedures for accumulating "factual data" and for measuring progress (such as the GNP). But, what a blessing the resulting economic growth has been for us. It has enabled the members of our society to look forward to an ever-rising standard of living. Economic growth, more-over is a great social solvent. When everyone can look forward to raising levels

of well-being, the pressure for redistributing the existing pie is reduced. Bud, not to be in favor of economic growth is as heinous a crime in our society as is hostility to dogs and little children.

Bud: I note that you don't include the buffalo or the bald eagle. Was what we did to them in the name of economic growth a crime?

Adam: That's not the point, Bud. Economic growth is the way we satisfy people's wants and needs. Demand for goods and services is the basic force that keeps the system running. People want better meals, new clothes, more comfortable living, automobiles, T.V.s, washers, dryers, stoves. This consumption is made possible by the productive output of capital stock and the labor force, and through technical progress. As long as we increase capital and the labor force at a propitious and proportionate rate, and as long as we continue technical progress, we'll achieve full employment. Thus we will enjoy steady per capita income growth.

Bud: The theory of economic growth is doomed. We live on a finite planet with an infinite time horizon. Earth resource management must now take this into account. The rate at which our natural resources are being ravaged in our present frantic attempt to keep growing is frightening. As Thoreau said, "What is the good of a house if you don't have a tolerable planet to put it on?"

The trouble with technical progress is that it leads us down Richard's "road to oblivion." It increasingly forces us to use our more marginal resources. Take the case of copper, for instance. Early in this century if an ore wouldn't yield 2%-3% copper it was bypassed. Today 0.7% ore is mined as a matter of course. Soon it will be 0.35%. Then what? Will

we dig huge open pit mines any place, anywhere an infinitesimal trace of copper is to be found?

This specter is only too clear today in the strip-mined hills of Kentucky. In the quest for coal to support our nation's growing need for energy we have literally denuded a good part of 11 counties of the state. Sure, strip-mining is less costly than deep mining and safer, in part because it employs fewer miners. But it has destroyed the terrain and led to erosion, land-slides, pollution and, alas, now that the coal is nearly gone, economic depression.

And, there seems to be no stopping. The U.S. Geological Survey says that 3,000 square miles in 26 states already have been "stripped," and that 71,000 more could profitably be gauged out in the future. But, it's not just the surface area that needs to be considered, it's the insides as well. Stripping has gone as deep as 700 feet in Germany. In the U.S. it could eventually go as deep as 2000 feet.

An alarming aspect of the L.A. County land-use data is that we are rapidly depleting our precious metal resources as shown by the decrease in tonnage. Meanwhile, our sand and gravel consumption goes up to construct our sprawling cities and expand our freeways. How much longer can we keep this up, Adam? When our mining resources and vacant land are gone, what then?

Adam: Of course, we must practice conservation to insure the maximum use of resources for the benefit of all people. But, stop exploration and development as you suggest? That's unthinkable.

There are some practical ways in which private enterprise can discharge its responsibility for conservation. Coal sells at about $7 to

$10 a ton. Why not spend 5 to 15 cents a ton for general conservation and restoration? These funds could be used for developing and financing new mining techniques in which topsoil would be stripped off and saved, the minerals would be extracted, "clean" atomic explosives would be used to level the land, the surplus earth would be distributed and compressed, and the topsoil would be redistributed on the surface and treated with fertilizer. This program would be backed up by additional conservation policy to ensure that the land was reclaimable, that the vegetation would grow, that proper drainage patterns were maintained and that the atomic blasting was not hazardous to the residents of the area. In the future we will have to follow these conservation policies more strictly.

Bud: Conservation is humanity caring for the future, Adam, not technology and cost/effectiveness. This must become the age of man's service to man. Personal service can continue to grow with a static population and without destroying nature. We don't have to continue to think in terms of increasing production and consumption, supply and demand. We must come to realize scarcity is the nature of the world now, and forevermore. All resources are limited; nothing is supperabundant. Man must cherish and live with his environment the way it is and not consume it excessively.

We must begin to take the "right view" of our world. All things are interconnected with everything else. Everything we do affects other things; everything goes somewhere. Pollution. DDT. They all go some place; affect something. In nature there are no "bottomless ponds." What is irrevocably destroyed or disturbed when we implement your plan, Adam? Are there not many unintended consequences from leveling the land, destroying habitats and valleys?

No, we must cease this craving for consumption. We must begin to live in a way that is least harmful to other living things, their habitat, their means of survival. In this way we will come to understand ourselves a little better, too, dispel some of our more evil thoughts, arouse and maintain some good ones. The alert mind of the future must pay close attention to every state of the body, feeling and mind and attempt to place them in eternal harmony with the environment. This will require reflection and concentration. But the rewards are worth it. It is in this way that we will find the infinity and pleasure we seek. Not an infinity of material resources, that doesn't exist; but, an infinity of freedom from excessive passion and desire.

Adam: Bud, it sounds like you are placing restrictions on man that even nature does not place on any carnivorous species. Man has a right to live, to eat, to shelter, to protect himself, and to grow.

Bud: Yes, but for the sake of harmony he should take only his share. These land use data indicate that he has gone too far. With the intelligence man has gained as a species there comes a moral obligation. He must strive to live in harmony with his environment. This means that our land-use policies must be changed.

Adam: Your plea is eloquent, Bud, but on the basis of the data and this debate I can only conclude that our past land-use policy has not been that bad. With intelligent planning for the future, and with the ERTS data, man will be able to make better use of earth resources and to continue his dominion over nature. The future of man is assured if he follows this approach.

Bud: No, Adam, from the debate one must conclude that our land-use policy has been disastrous. Man must stop thinking in terms of his dominion over the earth and begin to consider his moral obligation to all of creation. He must strive for harmony and ecological balance among all species and things. The hope of ERTS is that its imagery may provide some insights as to how to accomplish this. Man's survival hangs in the balance. The future of man is not assured. It is in great jeopardy. We must adopt a new approach.

SPACE SCIENCES LABORATORY

A72-42407

ON THE DIAMAGNETIC EFFECT OF THE PLASMA SHEET NEAR 60 R_E

C.-I. MENG AND J.D. MIHALOV

24 MARCH 1972

UNIVERSITY OF CALIFORNIA, BERKELEY

ON THE DIAMAGNETIC EFFECT OF THE PLASMA SHEET NEAR 60 R_E

C.-I. Meng

Space Sciences Laboratory
University of California, Berkeley 94720

J. D. Mihalov

Space Science Division, Ames Research Center NASA
Moffett Field, California 94035

24 March 1972

ABSTRACT

The two dimensional (YZ-plane) spatial distribution of magnetic field magnitudes in the geomagnetic tail at lunar distance is given in both solar magnetospheric and neutral sheet coordinate systems using three years of data from the Ames magnetometer on Explorer 35. The effect of changes in geomagnetic activity is also presented. In the magnetotail near 60 R_E, a broad region in which the magnetic field intensity is relatively weak compared with that in the other region of the tail is located adjacent to the solar magnetospheric equatorial plane and the calculated neutral sheet. This depression of the field due to the diamagnetic effect of the plasma sheet is more evident during times of minimum geomagnetic activity ($Kp \leq 1+$). Plasma energy densities of 200-300 eV/cm^3 in the plasma sheet are inferred by interpreting the field magnitude decrease as the effect of plasma diamagnetism.

INTRODUCTION

The plasma sheet constitutes a major feature of magnetotail structure, and plasma pressure must maintain the dynamical balance with the extended magnetotail. The configuration and characteristics of the plasma sheet in the near-earth region has been well studied by the Vela and OGO satellites (see for example, Bame, 1968; Hones, 1969; Vasyliunas, 1968a, b; Frank, 1971) and similar configurations are found at about 35 R_E (Fairfield and Ness, 1970; Hruska and Hruskova, 1970; Mihalov, 1970; Behannon, 1970; Meng and Anderson, 1971). A region of slightly depressed magnetic field magnitude was reported at the distance of the lunar orbit and a region of energetic electrons ($E_e \geq 20$ keV) distributed near the neutral sheet and the solar magnetospheric equator was also observed (Behannon, 1970; Meng, 1971). A region of magnetic field disturbance corresponding to the magnetotail plasma sheet has been observed at the lunar orbit with an average configuration similar to the plasma sheet at 18 R_E observed by Vela satellites (Meng and Mihalov, 1972).

Based on a quasi-static model of the magnetotail plasma sheet in which the plasma energy density is assumed to be the same order of magnitude as the magnetic energy density (Lazarus et al., 1968), some of the plasma sheet characteristics in the distant magnetotail can be inferred from the magnetic field observations. This paper presents a study of plasma sheet characteristics near 60 R_E. Spatial distributions of both the averaged magnetic field magnitude and the plasma energy density inferred from the field magnitude distributions are given on the basis of three years of Explorer 35 Ames magnetometer data. It is shown that there is a broad region in which the magnetic field

intensity is relatively weak compared with that in the other region of the tail. This depression of the field is identified with a diamagnetic effect of the plasma sheet, and the calculated plasma energy density within the plasma sheet near 60 R_E is about 200-300 eV/cm^3 using a quasi-static model.

ANALYSIS

The Explorer 35 satellite was launched on July 19, 1967 and injected into lunar orbit on July 22, 1967. This lunar anchored satellite moves across the magnetotail at a geocentric distance of about 60 R_E from the dusk to the dawn side with a time span of about four days once every synodic month, and its data have provided extensive mapping of the magnetotail at this distance.

The Explorer 35 Ames magnetometer is very similar to that on Explorer 33 (Mihalov et al., 1968; Sonett et al., 1968) which makes an individual triaxial sample of the magnetic field vector at intervals of approximately every 6.14 sec in the most sensitive range. The magnetic field magnitude averages used here are obtained over either 7 or 8 telemetry sequences (approximately every ten minutes) and are defined by

$$n\,B_j = \sum_{i=1}^{n} B_i \qquad \text{(the 10-minute average magnitude)}$$

$$B_i^2 = \sum_{k=1}^{3} B_k^2 \qquad \text{(each individual sample)}$$

where n is less than or equal to 107, depending on the number of telemetry sequences used and the percentage of missing data samples. A total of 34 magnetotail scans (including the initial orbit) made by Explorer 35 during the approximately three-year period from July 21, 1967 to March 24, 1970 are used in this study without any selection. The total observation time in the region ($-30\ R_E < Y_{sm} < 30\ R_E$) was more than 3000 hours and its distribution has been shown in Figures 2 and 3 of Meng and Mihalov (1972).

RESULTS

Two dimensional (YZ plane) spatial distributions of the magnetic field magnitude and calculated plasma energy density are presented in both the solar magnetospheric (SM) (Ness, 1965) and the neutral sheet (ZN) (Murayama, 1966) coordinate systems, ignoring the ellipticity of the moon's orbit and the size of the Explorer 35 orbit.

Average Magnetic Field Magnitude

The cross-section scanned by Explorer 35 at the distance of the lunar orbit from $Y = +30\ R_E$ to $Y = -30\ R_E$ and from $Z = +18\ R_E$ to $Z = -18\ R_E$ was divided into 240 square areal elements with a $3\ R_E \times 3\ R_E$ size. Within each areal element the average magnetic field magnitude was defined as the sample mean $\overline{B}$ of the 10-minute field magnitude B_j by

$$m\ \overline{B} = \sum_{j=1}^{m} B_j$$

where m is the number of 10-minute average field magnitudes, B_j, within each square element. Figure 1 shows such a spatial

distribution of the average magnetic field magnitude (in units of gammas, one gamma = 10^{-5} gauss) in the solar magnetospheric (SM) and the neutral sheet (ZN) coordinate systems. A blank square indicates either no satellite observation or insufficient sampling time, defined as less than 60 minutes (i.e., fewer than six 10-minute averages). Average magnetic field magnitudes observed here mostly range from 7γ to 12γ.

Scrutiny of Figure 1 reveals the following patterns of the magnetic field magnitude distribution in both coordinate systems:

1. Most of the high average magnetic field magnitudes (>11γ) are distributed along the upper and lower boundaries of the mosaic-like pattern, especially in the southern part (lower boundary) of the magnetotail.
2. The 3 R_E × 3 R_E regions with low average magnetic field magnitudes in the range 7 to 8.5γ are scattered adjoining to the solar magnetosphere equatorial plane and the neutral sheet but more in the northern part in the ZN coordinate system than in the SM coordinate system.
3. The magnetic field magnitudes lower than 7γ are observed at both the far right ($Y_{sm} < -20\ R_E$) and far left ($Y_{sm} > 24\ R_E$) regions corresponding to the magnetosheath.

The latitudinal changes near the midnight meridian generally display a minimum near the SM equator or the neutral sheet. For example, at $-6 < Y_{sm} < -3\ R_E$ in the solar magnetospheric coordinates, the average field diminishes from 13.0γ at $Z_{sm} \approx 8\ R_E$ to 8.0γ at $\sim 5\ R_E$ to 8.3γ at $\sim 2\ R_E$ and 7.4γ near the SM equator, then increase to 11.7γ at $\sim -5\ R_E$ and 14.6γ at $Z_{sm} \approx -7\ R_E$. In the neutral sheet coordinates along the same meridian, the field magnitude also gradually

decreases from 10.9γ at $Z_n \approx +10\ R_E$ to 9.2γ at ~8 R_E, 8.7γ at ~5 R_E and 6.8γ near the estimated neutral sheet and then similarly increases from 7.3γ to 9.6γ, 12.3γ and finally 14.4γ at $Z_n \approx -10\ R_E$. Such a spatial distribution of the magnetic field magnitude with a region of low field magnitude adjoining the solar magnetospheric equatorial plane in the SM coordinate and the estimated neutral sheet in the ZN coordinate suggests that the diamagnetic effect of the plasma sheet indeed exists in the distant magnetotail at the lunar orbit.

Besides the spatial distribution of the diamagnetic effect, the magnetic field magnitude in the distant (>50 R_E) magnetotail also has irregular temporal variations associated with continuous variations of the solar wind pressure (see for example, Mihalov et al., 1970a). A number of transient effects studied closer to Earth, e.g., the interplanetary magnetic field variation (Aubry and McPherron, 1970), the magnetic storm sudden commencement (SSC) (Behannon and Ness, 1966; Sugiura et al., 1968), the sudden impulse (SI) (Patel, 1968; 1971), and other geomagnetic fluctuations e.g., substorms (see Camidge and Rostoker, 1970; Fairfield and Ness, 1970; Russell et al., 1971; Rostoker and Camidge, 1971; Meng and Akasofu, 1971; Meng et al., 1971) also change the magnetic field magnitude. A sudden field magnitude increase in the distant magnetotail by a factor of two is not uncommon (see for example, Behannon, 1968). It is believed that the anomalous field magnitude values in these spatial distributions are, at least partly, due to such sudden large temporal variations. In order to reduce somewhat such effects, the spatial distribution of the field magnitude during low Kp values is also examined. Figure 2 gives the result for Kp ≤ 1+, consisting of about 1100 hours of magnetic field observations.

The pattern of the magnetic field distribution with the depressed field region adjacent to the SM equator and the estimated neutral sheet is found to be similar to that of Figure 1 and the diamagnetic effect of the plasma sheet is more evident here than in Figure 1, particularly in ZN coordinates. It is also noticeable that the magnetic field magnitude is generally weaker by about 3γ for low Kp observations over the entire cross-section of the tail.

The spread of the field magnitudes within each square areal element has also been computed by the standard deviation D from the following equation

$$(m - 1)\, D^2 = \sum_{j=1}^{m} (B_j - \bar{B})^2$$

where B_j represents each 10-minute field magnitude, m is the total number of B_js in each element and $\bar{B}$ is the average magnetic field magnitude shown in Figures 1 and 2. The standard deviation in the magnetotail is about 3 to 4γ for all observations in Figure 1 and about 2 to 3γ for low Kp observations in Figure 2. In the magnetosheath the scatter of the magnetic field magnitude is much smaller with the standard deviation value of about 2γ or less. It is found that the standard deviation of the magnetic field magnitude in the magnetotail for periods greater than 10 min does not show any systematic pattern in the spatial distribution such as the higher scatter near the boundaries of the depressed field region reported by Hruska and Hruskova (1970). Earlier we located and studied the plasma sheet configuration using field component deviations for periods less than 10 minutes (Meng and Mihalov, 1972).

Longitudinal and Latitudinal Distributions

The average magnetic field magnitudes are computed at each column and row of 2 R_E width within the region studied (-30 $R_E \leq Y_{sm} \leq 30\ R_E$ and $-20\ R_E \leq Z \leq 20\ R_E$). Figure 3 illustrates the distribution of the field magnitude with respect to the Y_{sm} coordinate during different geomagnetic activities indicated by 3-hour Kp indices. It is evident that the field magnitudes are about 3γ higher for higher Kp ($\geq$ 2-) values than for low Kp ($\leq$ 1+) values. For all Kp values, the average magnetic field magnitude is nearly constant (9.7γ) near the center of the tail ($-10\ R_E < Y_{sm} < 14\ R_E$) and gradually decreases to about 8γ toward both morning and evening sides at $Y_{sm} \approx -20\ R_E$ and $+26\ R_E$ where a sudden drop in magnitude occurs corresponding to the magnetopause locations (Behannon, 1970; Mihalov et al., 1970b; Meng, 1971; Meng and Mihalov, 1972). The longitudinal distribution of the average magnetic field magnitude is obscured here since the magnetopause location may change with changes of solar wind parameters, particularly the azimuthal flow direction, so that reduced field magnitudes from the magnetosheath are included in averages near the magnetopause. The field magnitude in the center of the longitudinal distribution is close to the earlier value from multiple correlation studies that excluded neutral sheet crossings (Mihalov and Sonett, 1968).

The latitudinal distributions of the average magnetic field magnitude in both the solar magnetospheric and the neutral sheet coordinates and for different geomagnetic activities are displayed in Figure 4. In the solar magnetospheric (SM) coordinate, there is no clear indication of the existence of a depressed field region associated with the plasma sheet at the expected location adjacent to the SM equatorial plane for

either unselected or high Kp conditions. Only a slight indication of the field depression between $Z_{sm} \approx -4\ R_E$ and $Z_{sm} \approx 6\ R_E$ is seen for low Kp ($\leq 1+$) values. However, in the neutral sheet coordinate, a broad depressed field region with the magnitude of about 6γ contiguous to the neutral sheet is quite evident for low Kp values. It suggests that the neutral sheet coordinate is a better one to organize the magnetic field data in the distant magnetotail. It is also interesting to note that in the neutral sheet coordinates an apparent higher average magnetic field magnitude occurs in the southern part of the tail regardless of the geomagnetic activity conditions which is also perceptible in the spatial distributions of Figures 1 and 2.

PLASMA SHEET ENERGY DENSITY

In a quasi-static magnetotail, constant total pressure is sustained by a balance between the tensor partial pressures of the magnetic field and the plasma. Thus, the approximate plasma energy density in the plasma sheet can be calculated from the observed diamagnetic effect by using the magnetohydrostatic equation

$$\rho \underline{F} - \text{grad } p + (1/4\pi\mu)\ (\text{curl } \underline{B}) \times \underline{B} = 0 \qquad (1)$$

when the plasma flow in the magnetotail is assumed to be subsonic. Here ρ, p and μ are the fluid mass density, isotropic pressure and permeability, respectively, and $\underline{B}$ is the magnetic field. After eliminating the non-magnetic forces, $\underline{F}$, and rewriting the magnetic force term, the pressure balance equation reduces to

$$\text{grad } [p + (B^2/8\pi\mu)] = (\underline{B} \cdot \text{grad})\ \underline{B}/4\pi\mu \qquad (2)$$

and its component along the z-axis is

$$\frac{\partial}{\partial z}\left(p + \frac{B^2}{8\pi\mu}\right) = \frac{B_x}{4\pi\mu}\frac{\partial B_z}{\partial x} + \frac{B_y}{4\pi\mu}\frac{\partial B_z}{\partial y} + \frac{B_z}{4\pi\mu}\frac{\partial B_z}{\partial z} \qquad (3)$$

At 60 R_E in the plasma sheet the average B_z is only about 0.6γ which is about one order of magnitude smaller than B_x (Behannon, 1970) and B_y is comparable to or smaller than 0.6γ (Mihalov et al., 1968; Behannon, 1968). Assuming B_z varies very slowly with respect to x, y, z which may be true in the plasma sheet but may not be at the neutral sheet (see Mihalov et al., 1970c), equation (3) in the plasma sheet is simplified to

$$\frac{\partial}{\partial z}\left(p + \frac{B^2}{8\pi\mu}\right) = \frac{B_x}{4\pi\mu}\frac{\partial B_z}{\partial x} \qquad (4)$$

or

$$\left(p + \frac{B^2}{8\pi\mu}\right)\Bigg|_Z^{Z_T} = \int_Z^{Z_T} dZ\, \frac{B_x}{4\pi\mu}\frac{\partial B_z}{\partial x}$$

where Z_T is located outside the plasma sheet in the high latitude part of the magnetotail.

The plasma pressure difference between the plasma sheet and the high latitude tail region (i.e., outside the plasma sheet) is

$$\Delta p = \frac{-\Delta (B^2)}{8\pi\mu} + \int_Z^{Z_T} dZ\, \frac{B_x}{4\pi\mu}\frac{\partial B_z}{\partial x} \qquad (5)$$

In the plasma sheet at 60 R_E, B_x is about 6γ and $\partial B_z/\partial x$ is taken as 0.15γ per 10 R_E (see Behannon, 1970); therefore, the ratio of $\frac{\Delta (B^2)}{8\pi\mu}$ and the finite integration on the right hand side of equation (5)

can be estimated as approximately 50 to 1 for a thick, homogeneous plasma sheet. Thus, the magnetic tension due to the field line curvature within the plasma sheet may be neglected in comparison with the magnetic pressure; the familiar equation $p + \frac{B^2}{8\pi\mu}$ = constant can be used.

In order to obtain the average plasma energy density w_p for an isotropic distribution from $w_p = 1.5 \times (B_o^2/8\pi\mu)$, the magnetic pressure $B^2/8\pi\mu$ is calculated at each 3 R_E × 3 R_E areal element from

$$\langle B^2 \rangle = \frac{1}{m} \sum_{j=1}^{m} B_j^2$$

where B_j is each 10-minute field magnitude and m is the number of B_js within each element and where μ is taken to be unity.

Figure 5 is the spatial distribution of the calculated average plasma energy density without taking into account different values of Kp. A field magnitude in the high latitude tail region outside the plasma sheet (B_o) of 12γ, equivalent to an isotropic plasma energy density of 540 eV/cm^3, is used. The blank square indicates insufficient (less than 60 minutes) or no observations and zero energy density means that $\langle B^2 \rangle$ is equal to or greater than B_o^2. It is noted that within the magnetotail (-21 $R_E < Y_{sm} < 24$ R_E) the plasma energy density is approximately 300 eV/cm^3 and high values are concentrated near the solar magnetospheric equatorial plane and the estimated neutral sheet; in the magnetosheath (-21 $R_E > Y_{sm} > 24$ R_E) the plasma energy density is about 400 eV/cm^3 which is consistent with the magnetosheath solar wind plasma thermal energy density obtained by the MIT Explorer 35 plasma measurement (Binsack, private communication).

During low Kp ($\leq$ 1+), the high latitude tail field B_o of 10γ corresponding to 375 eV/cm^3 isotropic plasma energy density is used and the enhancement of the plasma energy density adjacent to the solar magnetospheric equatorial plane and the estimated neutral sheet is more evident with an increase of the plasma energy density from about 50 eV/cm^3 or less in the high latitude tail to about 250 eV/cm^3 near the center of the plasma sheet (Figure 6).

It is concluded that the estimated average plasma energy density within the plasma sheet near 60 R_E is about 250 to 300 eV/cm^3. The spread of the calculated plasma energy density at each areal element is also computed by the standard deviation which is about 75 and 125 eV/cm^3 for low Kp ($\leq$ 1+) values and all Kp values, respectively.

CONCLUSION AND DISCUSSION

The spatial distribution of the average magnetic field in the magnetotail near 60 R_E is examined on the basis of the lunar orbiting Explorer 35 Ames magnetometer data taken during 34 magnetotail crossings. In the distant magnetotail near 60 R_E a broad depressed field region, with its magnitude less than those observed in the near earth region of the tail, is observed adjacent to the solar magnetospheric equatorial plane and the estimated neutral sheet. In the latitudinal profile the existence of this broad magnetic field depression region is most evident near $Z_n \approx 0$ during the geomagnetically quiet period (Kp $\leq$ 1+) in the neutral sheet coordinate, but not in the solar magnetospheric coordinate (Figure 4). This agrees with the finding of Mihalov (1970) that in the latitudinal distribution the diamagnetic effect adjacent to the solar magnetospheric equatorial plane exists only

within $-20\ R_E < X_{sm} < -50\ R_E$ but not further downstream along the tail from $-50\ R_E$ to $-81\ R_E$. An important distinction is that field orientations not near the solar-antisolar directions have been excluded in the earlier work but not here. From Figures 1 and 2 the plasma sheet region field magnitudes appear $\sim 1\text{-}2\gamma$ higher on the average than those in the magnetosheath. This is such a small difference that these two regions cannot easily be separated without using plasma measurements. The observed existence of the diamagnetic effect of the plasma sheet near $60\ R_E$ is in agreement with the earlier results of Behannon (1970).

The average magnetic field magnitude change with Kp was observed in the whole cross-section of the magnetotail and an increment during geomagnetically active periods ($Kp \geq 2-$) of about 3γ over the quiet time field ($Kp \leq 1+$) is similar to that observed by Behannon (1970) and to the increment from multiple correlation studies (Behannon, 1968; Mihalov and Sonett, 1968).

The calculated plasma energy density in the center of the average plasma sheet from the observed plasma diamagnetic effect is about 200 to 300 eV/cm^3 near $60\ R_E$. The spatial distribution of the averaged electron energy density during low Kp ($\leq 1-$) at the distance of the Vela satellites, $\sim 18\ R_E$ (Hones, 1969), showed that in the center of the plasma sheet it is approximately 200 eV/cm^3. The total plasma energy density is estimated to be 1300 eV/cm^3 by assuming that the proton energy density is five times greater than the electron energy density. Thus, the plasma energy density at $X_{sm} \approx -18\ R_E$ is about six times higher than that near $60\ R_E$. It has been suggested that the plasma energy density in the plasma sheet should decrease along the magnetotail

in the same manner as the magnetic field energy density in the high latitude part of the tail (Meng and Mihalov, 1972). The magnetic field outside the plasma sheet is about 22γ at 18 R_E and $\sim$9γ near 60 R_E for low Kp values; the corresponding magnetic field energy density decrease from 18 R_E to 60 R_E is by a factor of six. This agrees with the plasma energy density decrease from 18 R_E to 60 R_E by a factor of six shown above. The low plasma sheet energy density of about 200 to 300 eV/cm^3 near 60 R_E is supported by the recent plasma measurements from the Apollo 15 Particles and Fields Subsatellite (Chase, private communication) and the Apollo 14 Charged Particle Lunar Environment Experiment (CPLEE) on the lunar surface (Burke, private communication).

The spatial distributions of the average magnetic field magnitude in Figures 1, 2 and 4 show an appreciably higher magnetic field magnitude in the southern part of the magnetotail regardless of the geomagnetic activity. There is no prominent feature of this type in the more distant of the latitudinal distributions during low geomagnetic activity presented by Mihalov (1970) or Sonett et al. (1968), where magnetic field magnitudes without tail-like orientations are excluded. A likely explanation for these observations is that depressed field magnitudes characteristic of the plasma sheet or neutral sheet crossings are averaged together more often with solar directed tail fields in the northern part of the tail than with antisolar directed fields in the southern part. This is indicated by both the distribution of tail occurrence frequencies for these observations in Figure 3 of Meng and Mihalov (1972) and by the higher values ($\sim$9γ) for the distant tail field magnitudes in the extended latitudinal distribution in which neutral

sheet crossings are deleted (Mihalov, 1970). This effect could be associated with the reported northward displacement of the neutral sheet at lunar distance based on six months of Explorer 35 observations (Behannon, 1970) or with the neutral sheet movement related to the interplanetary field direction (Hruska, 1971); however, further study is required to clarify the problem.

ACKNOWLEDGMENTS

We would like to thank Professor K.A. Anderson for his support and helpful discussions and Dr. C.P. Sonett, the Principal Investigator of the Ames magnetic field experiment on Explorer 35, and Dr. D.S. Colburn for making the data available. Discussions with Professors S.I. Akasofu and V.M. Vasyliunas are also appreciated.

This work was supported by the National Aeronautics and Space Administration under grant NGL-05-003-017 and the Atmospheric Sciences Section of the National Science Foundation under grant GA-26582 to the Space Sciences Laboratory, University of California, Berkeley.

REFERENCES

Aubry, M.P. and R.L. McPherron, Magnetotail changes in relation to the solar wind magnetic field and magnetospheric substorms, J. Geophys. Res., 76, 4381, 1971

Bame, S.J., Plasma sheet and adjacent regions, in Earth's Particles and Fields, edited by B.M. McCormac, 373-383, Reinhold Book Corp., New York, 1968

Behannon, K.W., Mapping of the earth's bow shock and magnetic tail by Explorer 33, J. Geophys. Res., 73, 907, 1968

Behannon, K.W., Geometry of the geomagnetic tail, J. Geophys. Res., 75, 743, 1970

Behannon, K.W. and N.F. Ness, Magnetic storms in the earth's magnetic tail, J. Geophys. Res., 71, 2327, 1966

Camidge, F.P. and G. Rostoker, Magnetic field perturbations in the magnetotail associated with polar magnetic substorms, Canad. J. Phys., 48, 2002, 1970

Fairfield, D.H. and N.F. Ness, Configuration of the geomagnetic tail during substorms, J. Geophys. Res., 75, 7032, 1970

Frank, L.A., Relationship of the plasma sheet, ring current, trapping boundary, and plasmapause near the magnetic equator and local midnight, J. Geophys. Res., 76, 2265, 1971

Hones, E.W., Jr., Observations in the magnetotail and their interpretation, in Atmospheric Emissions, edited by B.M. McCormac and A. Omholt, 351-363, Van Nostrand Reinhold Co., New York, 1969

Hruska, A., Electric current system in the undisturbed magnetospheric tail, Radio Science, 6, 295, 1971

Hruska, A. and J. Hruskova, Transverse structure of the earth's magnetotail and fluctuations of the tail magnetic field, J. Geophys. Res., 75, 2449, 1970

Lazarus, A.J., G.L. Siscoe and N.F. Ness, Plasma and magnetic field observations during the magnetosphere passage of Pioneer 7, J. Geophys. Res., 73, 2399, 1968

Meng, C.-I., Energetic electrons in the magnetotail at 60 R_E, J. Geophys. Res., 76, 862, 1971

Meng, C.-I., and S.-I. Akasofu, Magnetospheric substorm observations near the neutral sheet, J. Geophys. Res., 76, 4679, 1971

Meng, C.-I. and K.A. Anderson, Energetic electrons in the plasma sheet out to 40 R_E, J. Geophys. Res., 76, 873, 1971

Meng, C.-I. and J.D. Mihalov, Average plasma sheet configuration near 60 R_E, J. Geophys. Res., 77, 1972 (in press)

Meng, C.-I., S.-I. Akasofu, E.W. Hones, Jr. and K. Kawasaki, Magnetospheric substorms in the distant magnetotail observed by IMP-3, J. Geophys. Res., 76, 7584, 1971

Mihalov, J.D., On geomagnetic tail structure near the null sheet, Planet. Space Sci., 18, 1845, 1970

Mihalov, J.D., D.S. Colburn, R.G. Currie and C.P. Sonett, Configuration and reconnection of the geomagnetic tail, J. Geophys. Res., 73, 943, 1968

Mihalov, J.D. and C.P. Sonett, The cislunar geomagnetic tail gradient in 1967, J. Geophys. Res., 73, 6837, 1968

Mihalov, J.D., W.C. Feldman, C.P. Sonett and J.H. Wolfe, Pressure balance across the distant magnetopause, Cosmic Electrodynamics, 1, 389, 1970a

Mihalov, J.D., D.S. Colburn and C.P. Sonett, Observations of magnetopause geometry and waves at the lunar distance, Planet. Space Sci., 18, 239, 1970b

Mihalov, J.D., C.P. Sonett and D.S. Colburn, Reconnection and noise in the geomagnetic tail, Cosmic Electrodynamics, 1, 178, 1970c

Murayama, T., Spatial distribution of energetic electrons in the geomagnetic tail, J. Geophys. Res., 71, 5547, 1966

Ness, N.F., The earth's magnetic tail, J. Geophys. Res., 70, 2989, 1965

Patel, V.L., Sudden impulses in the geomagnetotail, J. Geophys. Res., 73, 3407, 1968

Patel, V.L., Sudden impulses in the geomagnetotail and the vicinity (preprint), presented at the 15th General Assembly, IUGG, Moscow, USSR, August, 1971

Rostoker, G., and F.P. Camidge, Localized character of magnetotail magnetic fluctuations during polar magnetic substorms, J. Geophys. Res., 76, 6944, 1971

Russell, C.T., R.L. McPherron and P.J. Coleman, Jr., Magnetic field variations in the near geomagnetic tail associated with weak substorm activity, J. Geophys. Res., 76, 1823, 1971

Sonett, C.P., D.S. Colburn, R.G. Currie and J.D. Mihalov, The geomagnetic tail: topology, reconnection and interaction with the moon, in Physics of the Magnetosphere, edited by R.L. Carovillano, J.F. McClay and H.R. Radoski, 461-484, D. Reidel Publ. Co., Dordrecht, Holland, 1968

Sugiura, M., T.L. Skillman, B.G. Ledley and J.P. Heppner, Propagation of the sudden commencement of July 8, 1966 to the magnetotail, J. Geophys. Res., 73, 6699, 1968

Vasyliunas, V.M., A survey of low-energy electrons in the evening sector of the magnetosphere with OGO 1 and OGO 3, J. Geophys. Res., 73, 2839, 1968a

Vasyliunas, V.M., Low-energy electrons in the magnetosphere as observed by OGO 1 and OGO 3, in Physics of the Magnetosphere, edited by R.L. Carovillano, J.F. McClay and H.R. Radoski, 622-640, D. Reidel Publ. Co., Dordrecht, Holland, 1968b

FIGURE CAPTIONS

1. Two-dimensional (YZ plane) spatial distribution of the average magnetic field magnitudes in the geomagnetic tail at lunar distance in solar magnetospheric (SM) and neutral sheet (ZN) coordinates. Note a region of field depression adjacent to the SM equator and neutral sheet.
2. Same as Figure 1 but for low geomagnetic activity only ($Kp \leq 1+$).
3. Longitudinal distribution of the average magnetic field magnitude across the geomagnetic tail at the lunar distance, including the low ($Kp \leq 1+$) and high geomagnetic activity portions separately. The magnetic field magnitude during high Kp (≥ 2) is about 3γ higher than those during low Kp ($\leq 1+$).
4. Latitudinal distribution of the average magnetic field magnitude across the geomagnetic tail at the lunar distance in both neutral sheet (ZN) and solar magnetospheric (SM) coordinates.
5. The distribution of average plasma energy density in the geomagnetic tail at lunar distance inferred from the magnetic field magnitude distributions in Figure 1. Both solar magnetospheric (SM) and neutral sheet (ZN) coordinates are used. A field magnitude of 12γ or more (typical of the high latitude tail region on the average) is taken to correspond to zero plasma energy density.
6. Same as Figure 5 but for low geomagnetic activity only ($Kp \leq 1+$). A field magnitude of 10γ or more (typical of the high latitude tail region during times of minimum geomagnetic activity) is taken to correspond to zero plasma energy density.

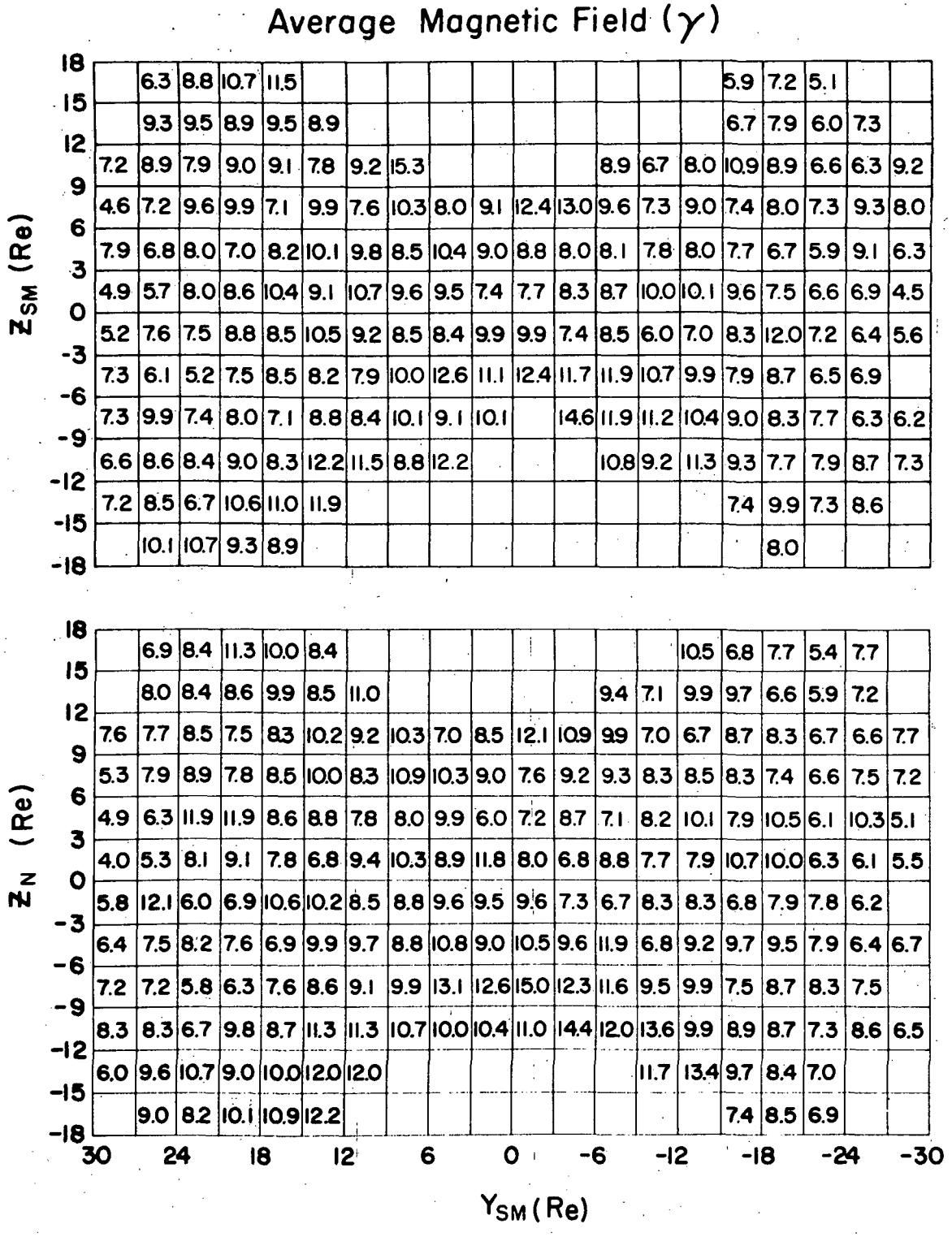
Average Magnetic Field (γ)
Z_{SM} (Re)
Z_N (Re)
Y_{SM} (Re)
18 15 12 9 6 3 0 -3 -6 -9 -12 -15 -18
30 24 18 12 6 0 -6 -12 -18 -24 -30

Figure 1

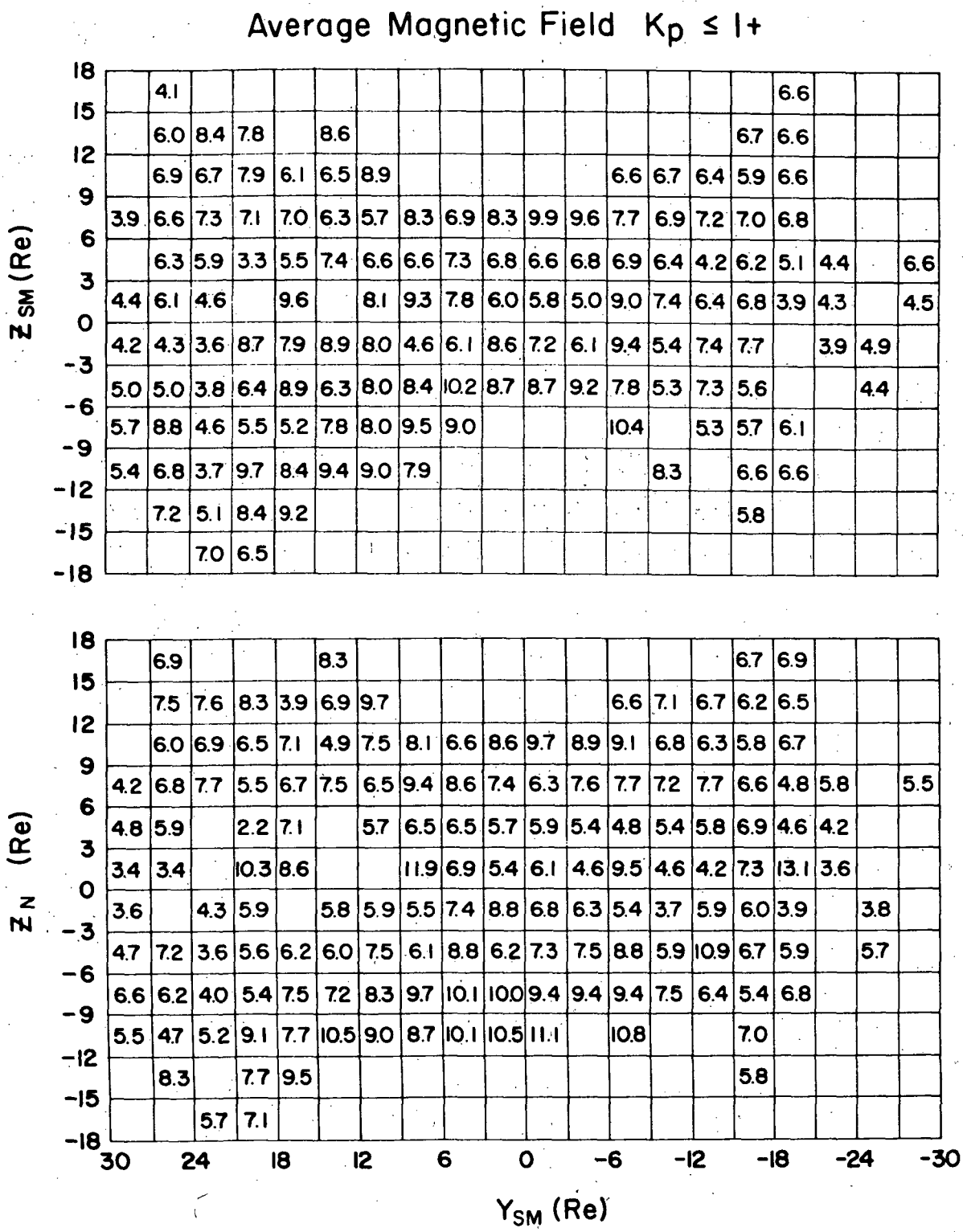
Average Magnetic Field $K_p \leq 1+$
Z_{SM} (Re)
18 15 12 9 6 3 0 -3 -6 -9 -12 -15 -18
4.1 6.6
6.0 8.4 7.8 8.6 6.7 6.6
6.9 6.7 7.9 6.1 6.5 8.9 6.6 6.7 6.4 5.9 6.6
3.9 6.6 7.3 7.1 7.0 6.3 5.7 8.3 6.9 8.3 9.9 9.6 7.7 6.9 7.2 7.0 6.8
6.3 5.9 3.3 5.5 7.4 6.6 6.6 7.3 6.8 6.6 6.8 6.9 6.4 4.2 6.2 5.1 4.4 6.6
4.4 6.1 4.6 9.6 8.1 9.3 7.8 6.0 5.8 5.0 9.0 7.4 6.4 6.8 3.9 4.3 4.5
4.2 4.3 3.6 8.7 7.9 8.9 8.0 4.6 6.1 8.6 7.2 6.1 9.4 5.4 7.4 7.7 3.9 4.9
5.0 5.0 3.8 6.4 8.9 6.3 8.0 8.4 10.2 8.7 8.7 9.2 7.8 5.3 7.3 5.6 4.4
5.7 8.8 4.6 5.5 5.2 7.8 8.0 9.5 9.0 10.4 5.3 5.7 6.1
5.4 6.8 3.7 9.7 8.4 9.4 9.0 7.9 8.3 6.6 6.6
7.2 5.1 8.4 9.2 5.8
7.0 6.5
Z_N (Re)
18 15 12 9 6 3 0 -3 -6 -9 -12 -15 -18
6.9 8.3 6.7 6.9
7.5 7.6 8.3 3.9 6.9 9.7 6.6 7.1 6.7 6.2 6.5
6.0 6.9 6.5 7.1 4.9 7.5 8.1 6.6 8.6 9.7 8.9 9.1 6.8 6.3 5.8 6.7
4.2 6.8 7.7 5.5 6.7 7.5 6.5 9.4 8.6 7.4 6.3 7.6 7.7 7.2 7.7 6.6 4.8 5.8 5.5
4.8 5.9 2.2 7.1 5.7 6.5 6.5 5.7 5.9 5.4 4.8 5.4 5.8 6.9 4.6 4.2
3.4 3.4 10.3 8.6 11.9 6.9 5.4 6.1 4.6 9.5 4.6 4.2 7.3 13.1 3.6
3.6 4.3 5.9 5.8 5.9 5.5 7.4 8.8 6.8 6.3 5.4 3.7 5.9 6.0 3.9 3.8
4.7 7.2 3.6 5.6 6.2 6.0 7.5 6.1 8.8 6.2 7.3 7.5 8.8 5.9 10.9 6.7 5.9 5.7
6.6 6.2 4.0 5.4 7.5 7.2 8.3 9.7 10.1 10.0 9.4 9.4 9.4 7.5 6.4 5.4 6.8
5.5 4.7 5.2 9.1 7.7 10.5 9.0 8.7 10.1 10.5 11.1 10.8 7.0
8.3 7.7 9.5 5.8
5.7 7.1
30 24 18 12 6 0 -6 -12 -18 -24 -30
Y_{SM} (Re)

Figure 2

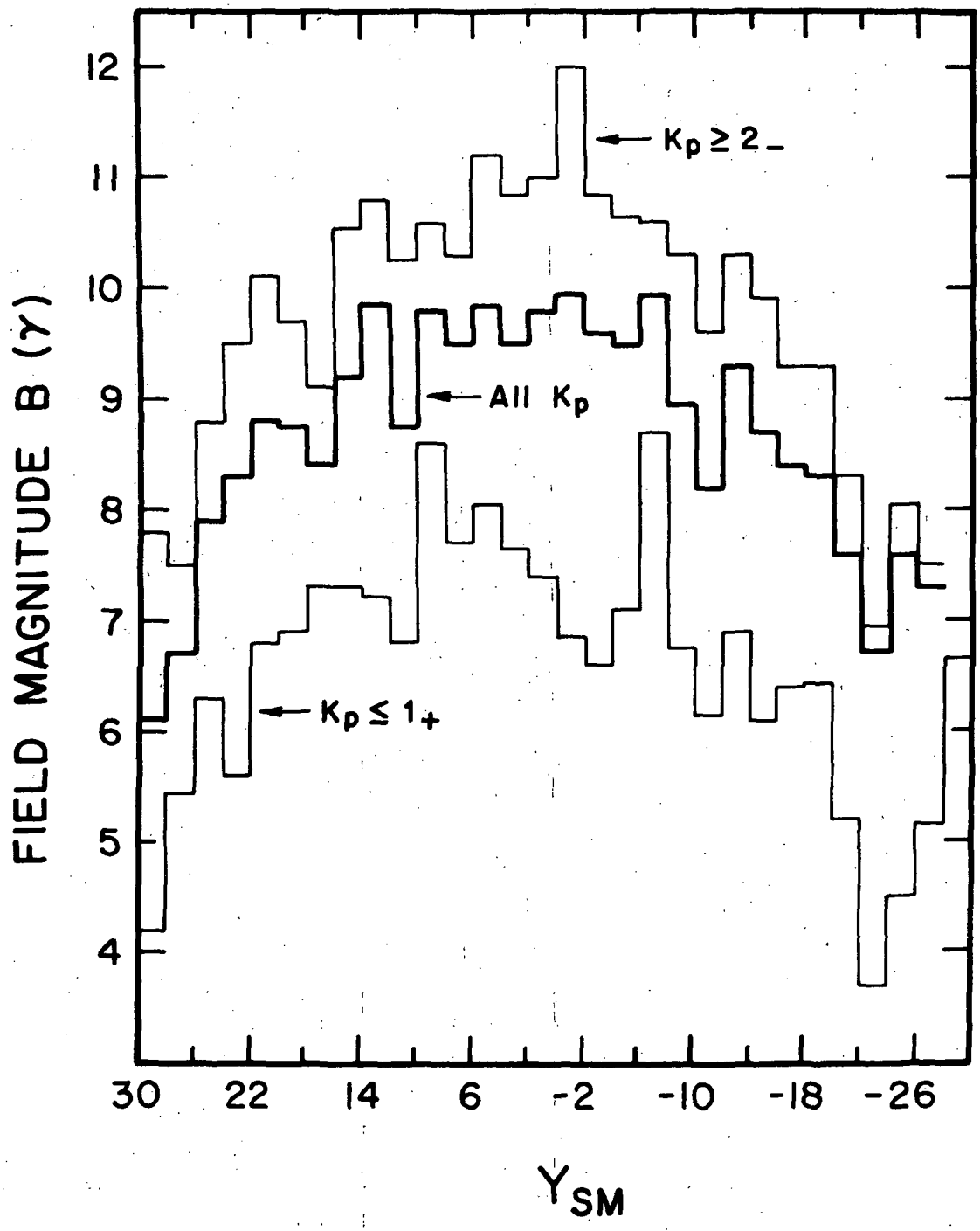
FIELD MAGNITUDE B (γ)
12
11
10
9
8
7
6
5
4
Kp ≥ 2₋
All Kp
Kp ≤ 1₊
30
22
14
6
-2
-10
-18
-26
YSM

Figure 3

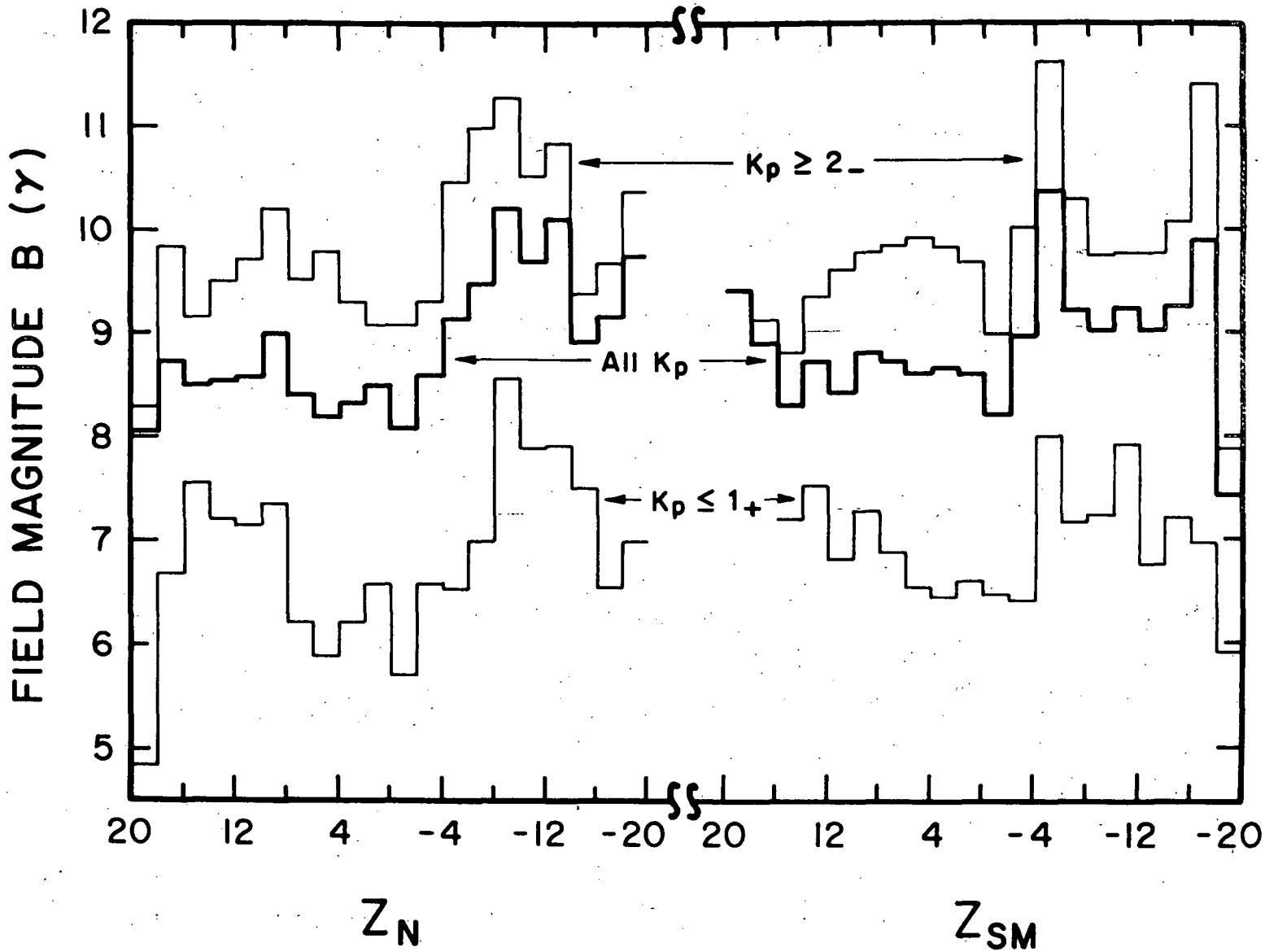
FIELD MAGNITUDE B (γ)
12
11
10
9
8
7
6
5
Kp ≥ 2_
All Kp
Kp ≤ 1+
20
12
4
-4
-12
-20
20
12
4
-4
-12
-20
ZN
ZSM

Figure 4

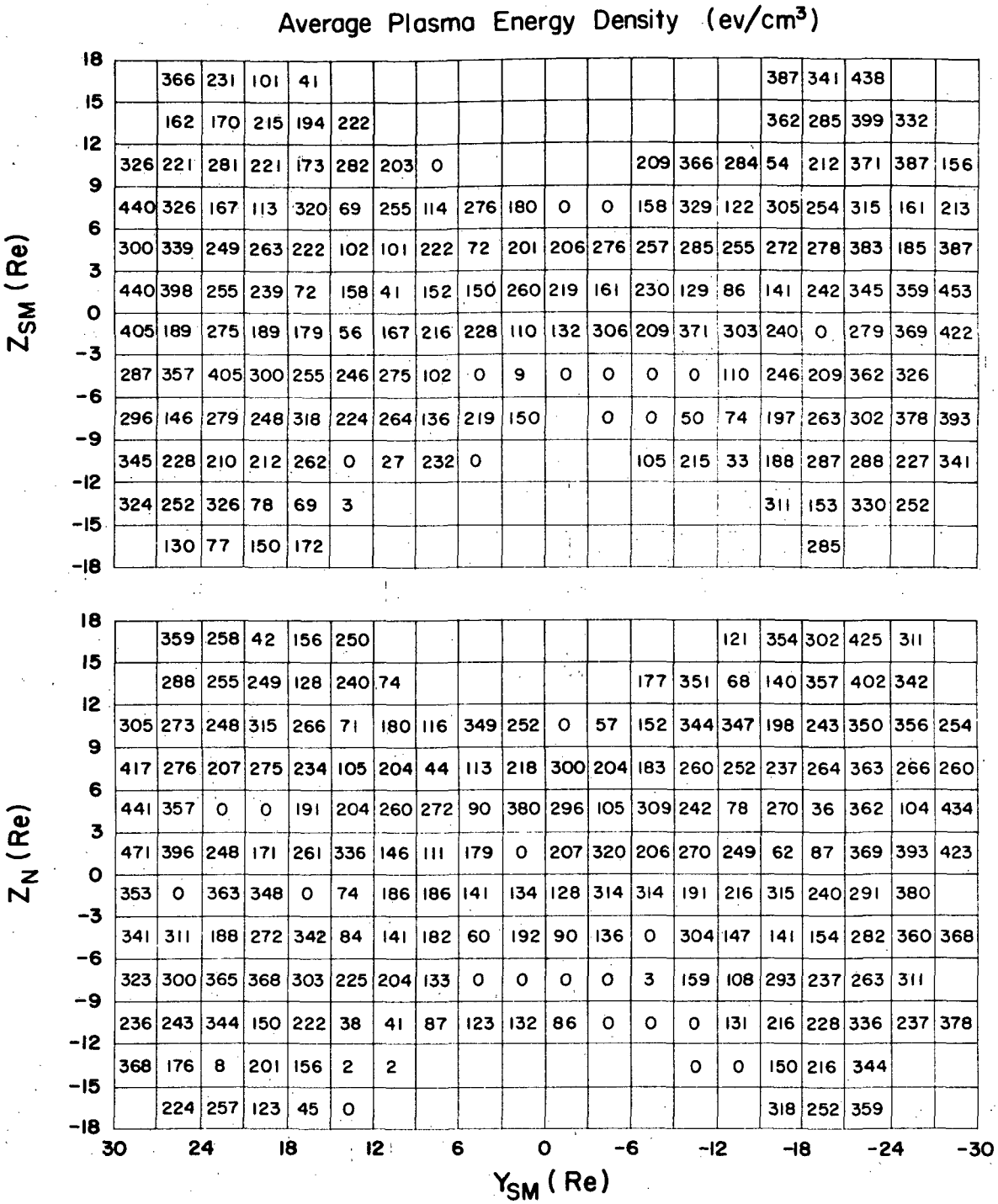
Average Plasma Energy Density (ev/cm³)
Z_SM (Re)
Z_N (Re)
Y_SM (Re)
18 15 12 9 6 3 0 -3 -6 -9 -12 -15 -18
30 24 18 12 6 0 -6 -12 -18 -24 -30

Figure 5

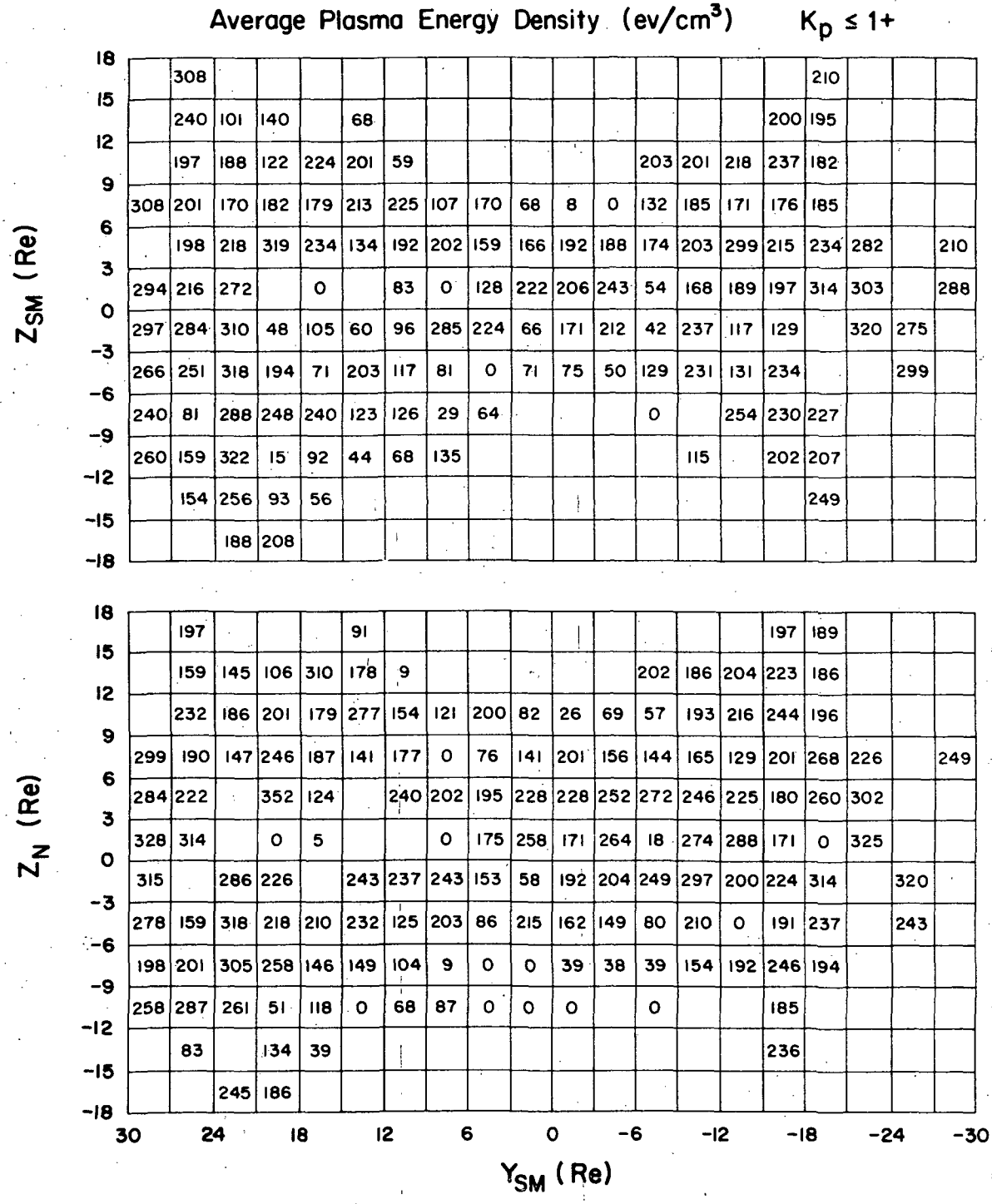
Average Plasma Energy Density (ev/cm³) Kp ≤ 1+
ZSM (Re)
ZN (Re)
YSM (Re)
18 15 12 9 6 3 0 -3 -6 -9 -12 -15 -18
30 24 18 12 6 0 -6 -12 -18 -24 -30

Figure 6

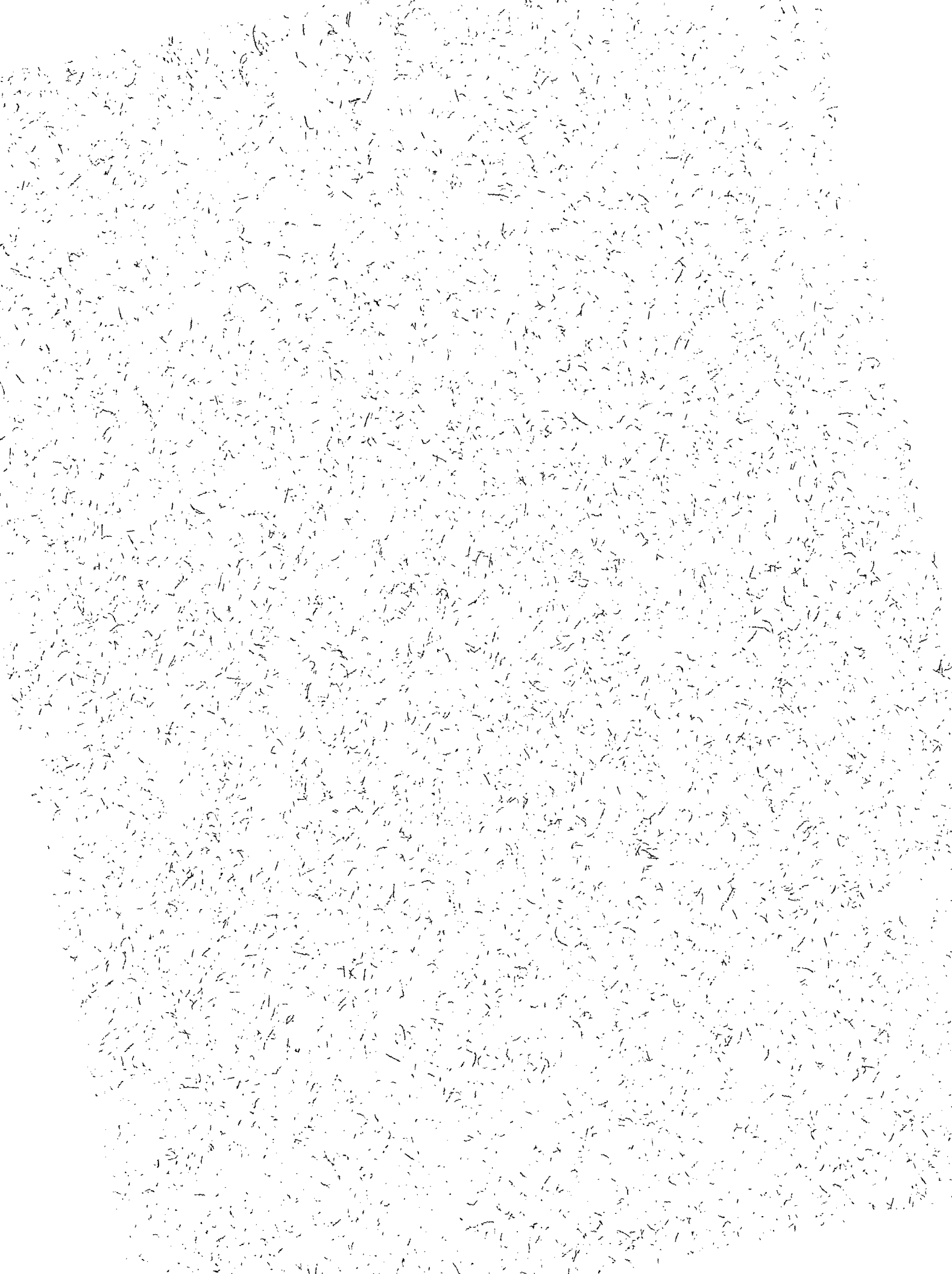

SPACE SCIENCES LABORATORY

A73-27005

ON THE RELATIONSHIP BETWEEN DP-1, DP-2, THE GROWTH AND EXPANSION PHASES OF SUBSTORMS, AND IONOSPHERIC ELECTRIC FIELDS

F. S. MOZER

SERIES 13, ISSUE 7

JANUARY 19, 1972

UNIVERSITY OF CALIFORNIA, BERKELEY

Space Sciences Laboratory Series 13, Issue 7

A73-27005

ON THE RELATIONSHIP BETWEEN DP-1, DP-2, THE GROWTH AND EXPANSION PHASES OF SUBSTORMS, AND IONOSPHERIC ELECTRIC FIELDS

F. S. Mozer

Physics Department and Space Sciences Laboratory
University of California, Berkeley 94720

Reproduction in whole or in part is permitted
for any purpose of the United States Government

Research supported in part by the Office of Naval Research under ONR Contract N00014-69-A-0200-1015; in part by the National Science Foundation under Grants GA-1317, GA-11259 and GA-17328; and in part by the National Aeronautics and Space Administration under Contract NAS 5-10362 and NAS-9-9052

January 19, 1972

*Submitted for publication in the Journal of Geophysical Research.

The problem of understanding the physical conditions preceding and causing the explosive or expansion phase of substorms has been studied for several years. In its most recent form this problem concerns questions of the existence of a growth phase prior to the explosive phase of a substorm and whether, if it exists, the growth phase current systems are fundamentally different from those during the expansion phase. The purpose of the present letter is to show that the resolution of different views on these questions may be achieved through examination of ionospheric electric field data obtained during isolated substorms.

Through examination of ground magnetometer records, Nagata and Kokobun (1962), Nishida, Iwasaki, and Nagata (1966), and Obayashi (1967) identified two types of high latitude equivalent ionospheric current systems, called DP2 and DP1. The high latitude, nighttime, DP2 currents flow poleward while those of DP1 flow as an intense westward electrojet (Nishida, 1971). DP2 currents are thought to be assoicated with southward turning interplanetary magnetic fields and are established about 15 minutes after such reorientations of the interplanetary magnetic field. DP1 currents are associated with substorms and develop explosively about an hour after DP2 appears (Nishida, 1971).

Through studies of typical signatures in ground magnetometer data, McPherron (1970) has proposed the existence of a growth phase of substorms lasting about an hour before the westward auroral electrojet develops explosively during the expansion phase of the substorm. Thus McPherron's growth and expansion phases might be associated with Nishida's DP2 and DP1 respectively, except that the current systems of DP2 and DP1 are in different directions, while currents during the growth phase are thought by McPherron (1970) to be similar in direction but smaller in magnitude than those during

the expansion. Thus, two major questions have arisen:

1. Is there a growth or DP2 phase to substorms occurring before the expansion or DP1 phase?

2. If so, is the current system during this precursor phase similar to or different from that during the explosive phase of the substorm?

The concepts of growth, expansion, DP2, and DP1, have arisen largely from analyses of ground magnetometer data. While such analyses have produced an important body of knowledge on magnetospheric processes, they may not be able to uniquely answer questions such as those above because:

1. Determining when and how a magnetometer trace deviates from the zero level involves definition of the zero level. Many workers feel that conclusions on the existence of DP2 and the growth phase depend critically on this choice of zero level.

2. Since negative bays are known to propagate in space at speeds of ~1 kilometer/second, time delays between observation of similar phenomena at different sites are the order of tens of minutes. Many workers feel that what appears as a precursor to the main negative bay can be explained in terms of these propagation effects without invoking a growth phase or DP2.

3. Since both the amplitude and direction of the north-south component of the interplanetary magnetic field are constantly changing, it is sometimes difficult to associate a feature of the interplanetary magnetic field with a feature in the substorm. Some workers find relations and time scales different from those of Nishida.

4. Because magnetometer deflections at a series of ground sites cannot be used to deduce uniquely the current pattern that produced them,

because of the possible importance of parallel currents in determining ground magnetic variations, and because the Hall and Pederson conductivities vary greatly during a substorm, different workers arrive at different interpretations of essentially the same initial magnetometer data. An example of this fact is the different current systems proposed by Nishida (1971) for DP2 and McPherron (1970) for the growth phase.

One may avoid all of the above difficulties by focussing attention on the ionospheric electric field variations driving the currents before and after the explosive phase of isolated substorms. Analyses of electric field variations during 19 such substorms have given the idealized picture reproduced in Figure 1 and described below (Mozer, 1971). Within a fraction of an hour after the interplanetary magnetic field turns southward, a large scale westward component of the ionospheric electric field develops on nightside auroral zone magnetic field lines. This component appears simultaneously within about 15 minutes at different auroral zone sites (Mozer and Manka, 1971; Mozer, 1971) where the time uncertainty results largely from the presence of turbulent variations of the ionospheric electric field. This westward field causes an inward motion and thinning of the plasma sheet, the equatorward motion of auroral arcs, the development of a tail-like magnetic field geometry deeper in the nightside magnetosphere, and the flow of currents in the ionosphere and along magnetic field lines. After about an hour, the magnetosphere drifts into an unstable condition in which a large equatorward component of ionospheric electric field develops. In each of the 19 substorms for which electric field data is available, the equatorward component developed after the westward component and, in those cases for which data from more than one site were available, the equatorward

components appeared simultaneously within ~15 minutes at different sites (Mozer and Manka, 1971; Mozer, 1971). This equatorward component drives a westward Hall auroral electrojet current that signals DP1 or the expansion phase in ground magnetometers.

From the electric field data there are thus two phases of a substorm corresponding respectively to the westward electric field and the equatorward field. The ~1 hour time scale for the duration of the westward field before the explosion corresponds well with time scales of both DP2 and the growth phase. The equatorward electric field component drives currents in different directions during DP1 or the expansion phase then were driven by the westward field during the growth or DP2 phase. The effects of these currents on ground magnetometers depend on how the Pederson and Hall conductivities vary during the substorm and how the different current systems close in the ionosphere or magnetosphere. The conclusions from analyses of ionospheric electric field data are thus that:

1. There is a ~1 hour initial phase to substorms that is associated with westward electric fields and the $\bar{E} \times \bar{B}$ drift of the magnetosphere into an unstable configuration. This interval of westward electric field probably corresponds to Nishida's DP2 or McPherron's growth phase.
2. The expansion or DP1 phase of substorms is associated with the development of an equatorward component of electric field in the nighttime magnetosphere. This field component combines with precipitation induced changes in the Hall and Pederson conductivities to change the previously existing current system. Since the ionospheric currents flowing before and after the appearance of the equatorward electric field component probably close by parallel currents having

different geometries (Mozer, 1971), there is a reorientation of the magnetospheric current system at the onset of the expansion phase. The details of this reorientation and its effects on ground magnetometers require further study.

ACKNOWLEDGMENTS

This work was supported in part by the Office of Naval Research under contract N00014-69-A-0200-1015; the National Aeronautics and Space Administration under contracts NAS 5-10362 and NAS 9-9502 and the Atmospheric Sciences Section of the National Science Foundation under grants GA-1317, GA-11259 and GA-17328.

REFERENCES

McPherron, R. L., Growth phase of magnetospheric substorms, J. Geophys. Res., 75, 5592, 1970

Mozer, F. S., Origin and effects of electric fields during isolated magnetospheric substorms, J. Geophys. Res., 76, 7595, 1971

Mozer, F. S., and R. H. Manka, Magnetospheric electric field properties deduced from simultaneous balloon flights, J. Geophys. Res., 76, 1697, 1971

Nagata, T., and S. Kokobun, An additional geomagnetic daily variation in the polar region on geomagnetically quiet days, Rept. Ionosphere Space Res. Japan, 16, 256, 1962

Nishida, A., Interplanetary origin of DP electric fields, review paper given at IAGA symposium, Moscow, August, 1971

Nishida, A., N. Iwasaki, and T. Nagata, The origin of fluctuations in the equatorial electrojet: A new type of geomagnetic variation, Ann. Geophys., 22, 478, 1966

Obayashi, T., The interaction of solar plasma with geomagnetic field, disturbed condition, in Solar Terrestrial Physics, 107 pp, edited by J. W. King and W. S. Newman, Academic Press, London and New York, 1967

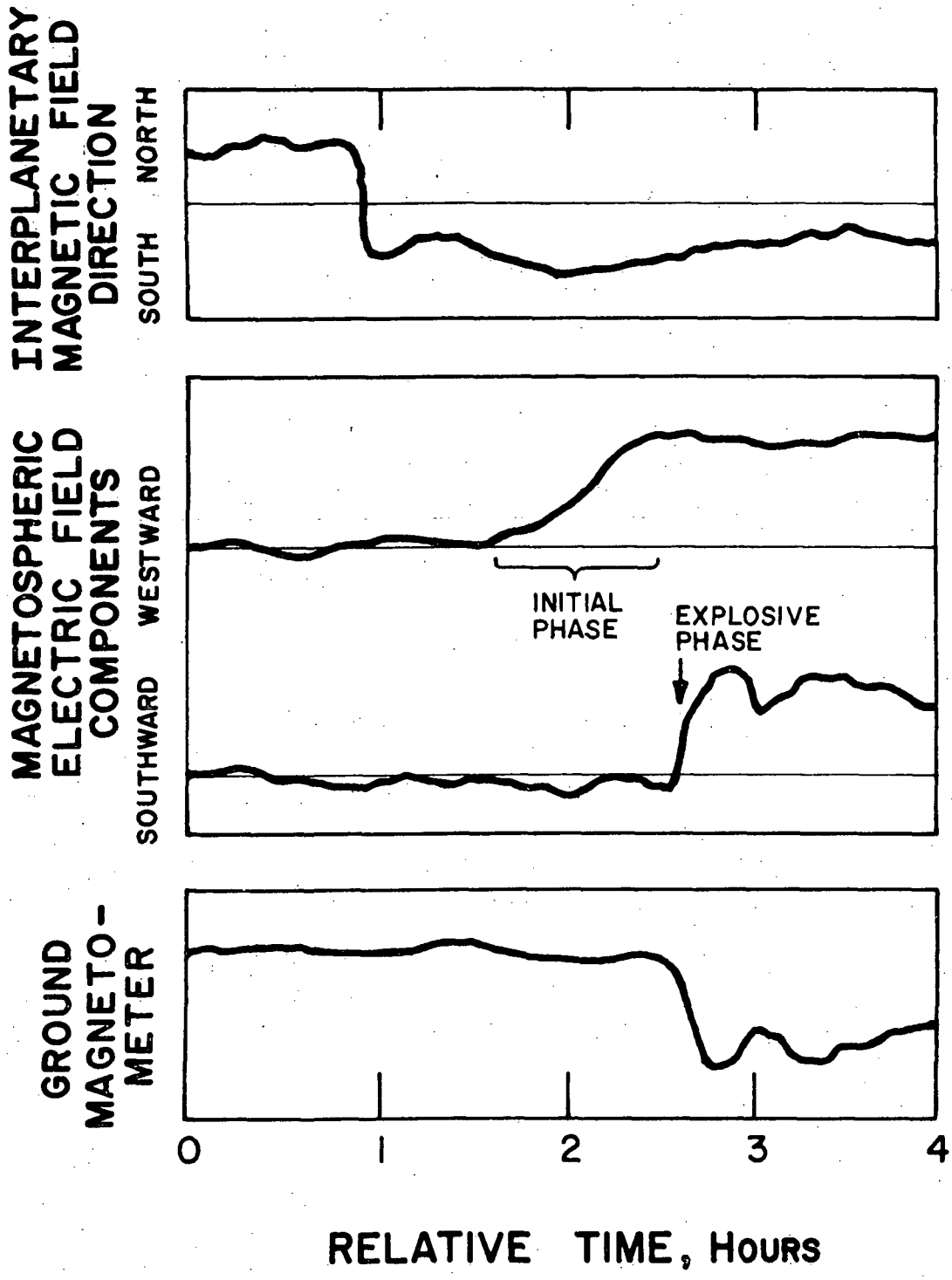

Figure 1 An idealized description of ionospheric electric field variations during an isolated magnetospheric substorm.

UNCLASSIFIED

Security Classification

DOCUMENT CONTROL DATA – R & D

(Security classification of title, body of abstract and indexing annotation must be entered when the overall report is classified)

1. ORIGINATING ACTIVITY (Corporate author)	2a. REPORT SECURITY CLASSIFICATION
Space Sciences Laboratory University of California Berkeley, California 94720	Unclassified
	2b. GROUP

3. REPORT TITLE

ON THE RELATIONSHIP BETWEEN DP-1, DP-2, THE GROWTH AND EXPANSION PHASES OF SUBSTORMS, AND IONOSPHERIC ELECTRIC FIELDS

4. DESCRIPTIVE NOTES (Type of report and inclusive dates)

Technical Report

5. AUTHOR(S) (First name, middle initial, last name)

Forrest S. Mozer

6. REPORT DATE	7a. TOTAL NO. OF PAGES	7b. NO. OF REFS
January 19, 1972	10	7

8a. CONTRACT OR GRANT NO.	9a. ORIGINATOR'S REPORT NUMBER(S)
N00014-69-A-0200-1015	Series 13, Issue 7
b. PROJECT NO. NR 021-213	
c. NASA Contracts NAS 5-10362 and NAS 9-9502	9b. OTHER REPORT NO(S) (Any other numbers that may be assigned this report)
d. NSF Grants GA 1317; GA 111259, GA 17328	

10. DISTRIBUTION STATEMENT

Distribution of this document is unlimited.

11. SUPPLEMENTARY NOTES	12. SPONSORING MILITARY ACTIVITY
	Nuclear Physics Branch Office of Naval Research

13. ABSTRACT

The problem of understanding the physical conditions preceding and causing the explosive or expansion phase of substorms has been studied for several years. In its most recent form this problem concerns questions of the existence of a growth phase prior to the explosive phase of a substorm and whether, if it exists, the growth phase current systems are fundamentally different from those during the expansion phase. The purpose of the present letter is to show that the resolution of different views on these questions may be achieved through examination of ionospheric electric field data obtained during isolated substorms.

DD FORM 1 NOV 65 1473

UNCLASSIFIED

Security Classification

14. KEY WORDS	LINK A		LINK B		LINK C	
	ROLE	WT	ROLE	WT	ROLE	WT
Substorms						
Growth phase						
Expansion phase						
Ionospheric electric fields						

A73-11736

SIMULTANEOUS ELECTRIC FIELD MEASUREMENTS ON NEARBY BALLOONS

F. S. Mozer

Physics Department and Space Sciences Laboratory
University of California, Berkeley 94720

March 3, 1972

ABSTRACT

Electric field payloads were flown simultaneously on two balloons from Great Whale River, Canada on September 21, 1971, to provide data at two points in the upper atmosphere that differed in altitude by more than one atmospheric density scale height and in horizontal position by 30 to 140 kilometers. The altitude dependences in the two sets of data prove conclusively that the vertical electric field at balloon altitudes stems from fair weather atmospheric electricity sources and that the horizontal fields are mapped down ionospheric fields since the weather associated horizontal fields were smaller than two millivolts/meter. The differences between the two sets of horizontal field data require the occasional appearance of spatially confined enhancements of the ionospheric electric field having enhancement factors of 10 to 50 and spatial scale sizes of 15 to 100 kilometers.

INTRODUCTION

On September 21, 1971, two balloons were flown from Great Whale River, Canada, to measure electric fields and x-rays during a magnetospheric barium cloud release. The goals of flying two balloons simultaneously from the same site were twofold:

1. To increase the probability of making ionospheric electric field measurements during the cloud release.
2. To obtain simultaneous data from nearby balloons at different altitudes and separation distances in order to test ideas of electric field mapping in the atmosphere and to measure the horizontal spatial structure of the ionospheric electric field.

Both balloons and payloads functioned nominally. It is the purpose of this paper to discuss the data and its interpretation in terms of the second of the above goals.

The volumes of the two balloons were 58,000 and 250,000 cubic feet, and they were launched at 0000 UT and 0105 UT on September 21, 1971. The larger balloon carried an x-ray detector as well as the electric field experiment and reached a ceiling altitude of about 112,000 feet at 0410 UT, while the smaller balloon reached a ceiling altitude near 85,000 feet at about 0130 UT. The difference in wind velocities at the two float altitudes caused the larger balloon to move eastward at a speed of about 30 kilometers/hour faster than the smaller balloon. Thus, about five hours of electric field data were obtained from two balloons that were separated in altitude by a little more than one atmospheric density scale height and that were separated horizontally by a distance that increased with time to a final value of

about 150 kilometers. Because of the changing horizontal separation of the two balloons with time, the two sets of data yield information on the scale sizes of horizontal ionospheric electric fields. Because of the vertical separation between the payloads, data on electric field mapping and the validity of the balloon technique for measurement of ionospheric fields was also obtained.

It has been shown (Mozer, 1971) that any large scale electric fields of low altitude atmospheric or weather origin vary with altitude, z , as

$$E_{\text{atmospheric}} = E_o \exp(-z/h) \qquad (1)$$

where h is the scale height of the neutral atmospheric density. Since the vertical separation between the balloons was greater than a scale height, equation (1) predicts that electric fields of atmospheric origin would be larger by a factor of about three near the lower altitude balloon than they were at the upper balloon. Large scale electric fields of ionospheric origin map down to the upper atmosphere (Mozer, 1971) as

$$E_{\text{ionospheric}} = E_1 \left[1 - \exp(-z/h) \right] \qquad (2)$$

Since $z \approx 5h$ at balloon altitudes, equation (2) predicts that fields of ionospheric origin have essentially the same magnitude at the two balloons. The first purpose in the examination of the experimental data will be to compare results with these predictions in order to determine the origin of the observed fields.

DISCUSSION OF THE EXPERIMENTAL DATA

In Figure 1, fifteen minute averages of the vertical and horizontal electric fields measured on the two balloons are presented with curves of the altitudes of each balloon as a function of time. During the first hour in the figure the larger balloon was ascending towards ceiling while the smaller balloon was at its float altitude because it was launched earliest. The vertical electric field measured on the larger balloon decreased as it rose with an altitude variation consistent with an exponential decrease having a scale height of 28,000 ± 6,000 feet. Since the average scale height of the neutral atmosphere at these altitudes is about 22,000 feet (Sagalyn and Fitzgerald, 1965) the time variation of the vertical electric field measured on the larger balloon is interpreted as an altitude variation of a vertical electric field that stems from atmospheric sources. This interpretation is verified by the fact that the higher altitude balloon always measured a smaller vertical field than did the lower balloon. The ratio of the vertical fields measured on the two balloons may be combined with their known vertical separation distance to obtain an independent estimate of the atmospheric scale height of 19,000 ± 4,000 feet. Additional evidence for the validity of the vertical field data and their interpretation is that the vertical fields measured by the balloons near 0320 UT were equal when the balloons were at the same altitude according to their altimeter readings. Also, the general increases of the vertical field with time in the latter part of both sets of data correlates well with those expected from the fact that the altitudes of both balloons decreased slowly with time. Thus, the data from the two balloons conclusively shows that vertical electric

fields at balloon altitudes stem from fair weather atmospheric processes, as has been deduced previously from less direct evidence (Mozer and Serlin, 1969; Mozer, 1971).

From the scale heights deduced above, atmospheric sources should produce horizontal fields at the two balloons whose average intensity ratio is about 3.6. The average ratio of the measured lower to upper horizontal field strengths was 0.97 and there is no time in Figure 1 where the ratio was as large as 3.6. Thus, the average horizontal field measured at the balloons both cannot come from atmospheric sources and is consistent with an ionospheric origin. These conclusions are strengthened by the fact that the upper balloon often measured the larger horizontal field, in complete disagreement with the altitude dependence expected from atmospheric sources. From comparison of the small, nearly equal horizontal fields measured between 0430 and 0545 with expectations from equation (1), it may be concluded that, at least during this time interval, the horizontal balloon field of atmospheric origin had a magnitude less than $\sim$2 millivolts/meter.

While the average horizontal fields of Figure 1 must result from the downward mapping of ionospheric fields, it might still be possible that discrepancies between the two measurements at times such as near 0338, 0352, 0422, and 0622 arise from atmospheric effects in the following way. The direction of the coordinate z of equation (1) is, by assumption, both vertical and normal to surfaces of constant atmospheric density. If the normals to the constant atmospheric density surfaces were inclined to the vertical at some point due to local dynamic processes, then the electric field of

atmospheric origin would have a horizontal component near that point. This is an extremely unlikely explanation of the large horizontal field observed at one balloon but not the other because the horizontal field was comparable to the vertical field during such events without the vertical field changing value, and because the required redistribution of neutral particle density would be unbelievably large.

A more reasonable interpretation of the differences between the horizontal fields measured on the two balloons is that such differences arose from horizontal spatial variations of the ionospheric electric fields like those that have been inferred from earlier data (Mozer and Manka, 1971). In order to test this interpretation, the 30 second averages of the components of the horizontal electric field in a geomagnetic, rotating frame of reference have been computed as in Figure 2, while the horizontal distance between the two balloons is given in Figure 3. The horizontal separation was determined from the pointing direction of the receiving antennas, the received signal strength, and the known atmospheric winds, to be mainly in an east-west direction with the larger balloon further east than the smaller one. The largest deviations between the two measurements occurred in the southward field component near 0350 and 0620 UT when the balloons were 45 ± 20 and 100 ± 40 kilometers apart. The largest ratio of southward field components observed on the two balloons was about 10. These results may be interpreted by computing the electric fields expected at balloon altitudes as a function of horizontal distance from an ionospheric region of width W in which the electric field is enhanced above the background level by a factor of K. In fitting the experimental data to this model, the factor, K, must be at least as large as the ratio of the observed field components and it

may be even larger since neither sensor probably measured the fully enhanced field. This factor cannot reasonably be larger than about 50 since the enhanced field would be bigger than the largest fields ever measured on rockets or satellites. Thus, $K \approx 10\text{-}50$. Atkinson et al. (1971) have computed the atmospheric electric field expected in the above model and have shown that, even for $K = 50$, the enhanced field maps to balloon altitudes with large enough amplitudes to agree with the experimental data only if W, the scale size of the enhanced field region, is greater than about 15 kilometers. If W were greater than the ~100 kilometer size of the ionospheric region over which the balloon measurement averages the ionospheric field (Mozer and Serlin, 1969), then the spatial region over which both balloons would measure large fields is greater than the boundary region over which one experiment would see a big field and the second, separated by ~50-100 kilometers, would measure a small field. Since the data of Figure 3 indicate that the balloons were most often in the boundary region, the scale size of the enhanced field region must have been less than ~100 kilometers. In summary, the differences between the two horizontal electric field measurements on the two separated balloons may be interpreted as due to 15 to 100 kilometer ionospheric regions within which the electric field was enhanced by a factor of 10 to 50.

ACKNOWLEDGMENTS

The author is indebted to the several balloon launch crews who sat through launch windows at Great Whale, and to the Project Skyhook Office of the Office of Naval Research for logistics support. This work was performed under NASA contract NAS-6-1922, and the author wishes to acknowledge the cooperation provided by the Langley Field group of NASA during the course of the experiment.

REFERENCES

Atkinson, W., S. Lundquist, and U.V. Fahleson, The electric field existing at stratospheric elevations, Pure and Appl. Geophys., 84, 46, 1971

Mozer, F.S., Balloon measurements of vertical and horizontal electric fields, Pure and Appl. Geophys., 84, 32, 1971

Mozer, F.S. and R.H. Manka, Magnetospheric electric field properties deduced from simultaneous balloon flights, J. Geophys. Res., 76, 1697, 1971

Mozer, F.S. and R. Serlin, Magnetospheric electric field measurements with balloons, J. Geophys. Res., 74, 4739, 1969

Sagalyn, R.C. and D.R. Fitzgerald, Atmospheric Electricity, in Handbook of Geophysics and Space Environments, Office of Aerospace Research, U.S. Air Force, 1965

FIGURE CAPTIONS

1. Fifteen minute averages of the horizontal and vertical electric fields measured on the two balloons along with the altitude profile of each balloon.
2. Electric field components in a rotating, geomagnetic frame of reference measured by the two balloons. Because of ground station malfunction, data were received alternately for about five minutes from each balloon. The spread in data points is real and arises from temporal and spatial variations of the measured ionospheric field. The solid dots represent data from the higher altitude balloon.
3. The horizontal separation distance between the two balloon payloads as a function of time. The shaded region delineates the uncertainty in the relative position of the balloons.

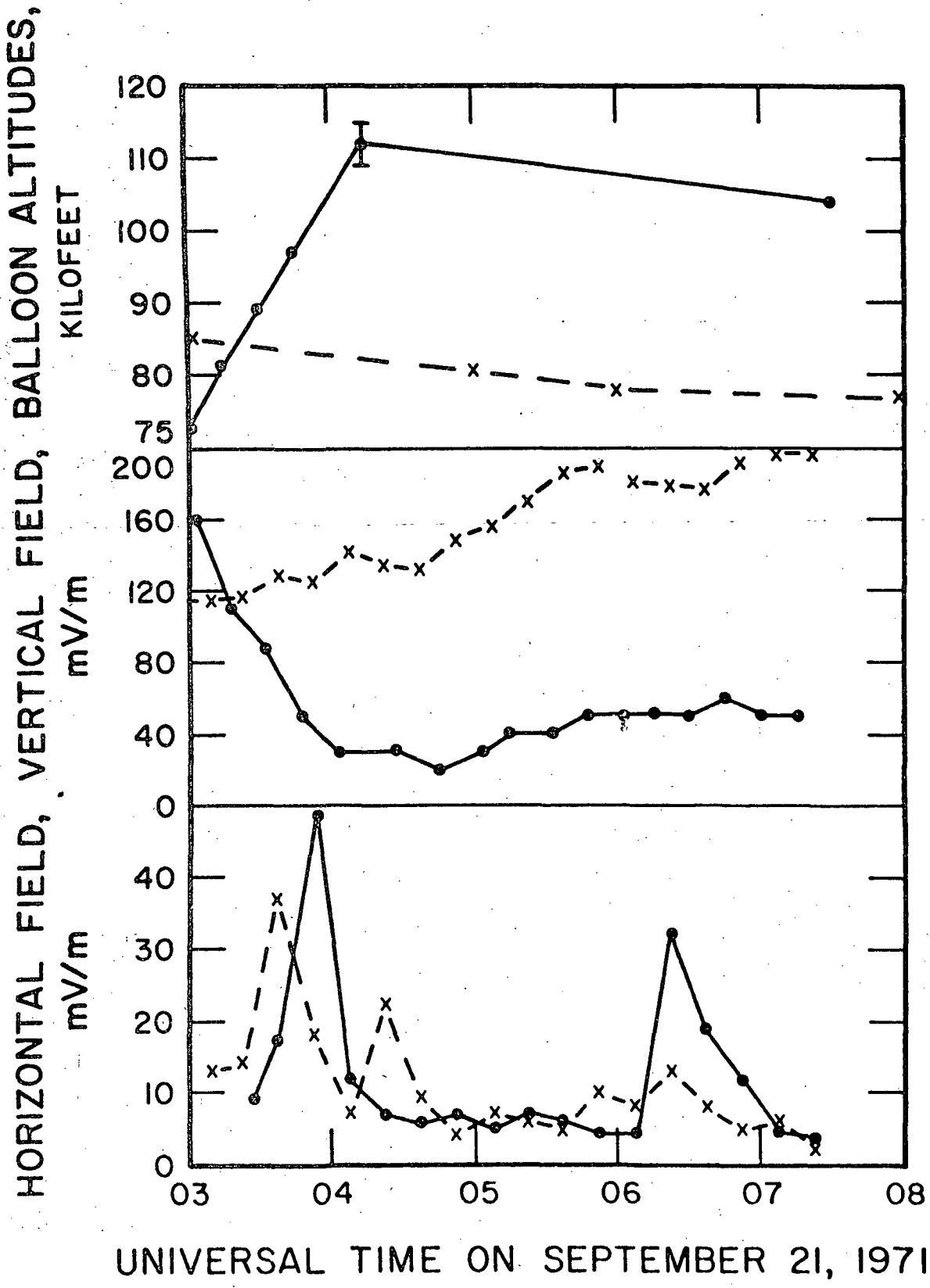
HORIZONTAL FIELD, VERTICAL FIELD, BALLOON ALTITUDES,
KILOFEET
mV/m
mV/m
120
110
100
90
80
75
200
160
120
80
40
0
40
30
20
10
0
03
04
05
06
07
08
UNIVERSAL TIME ON SEPTEMBER 21, 1971

Figure 1

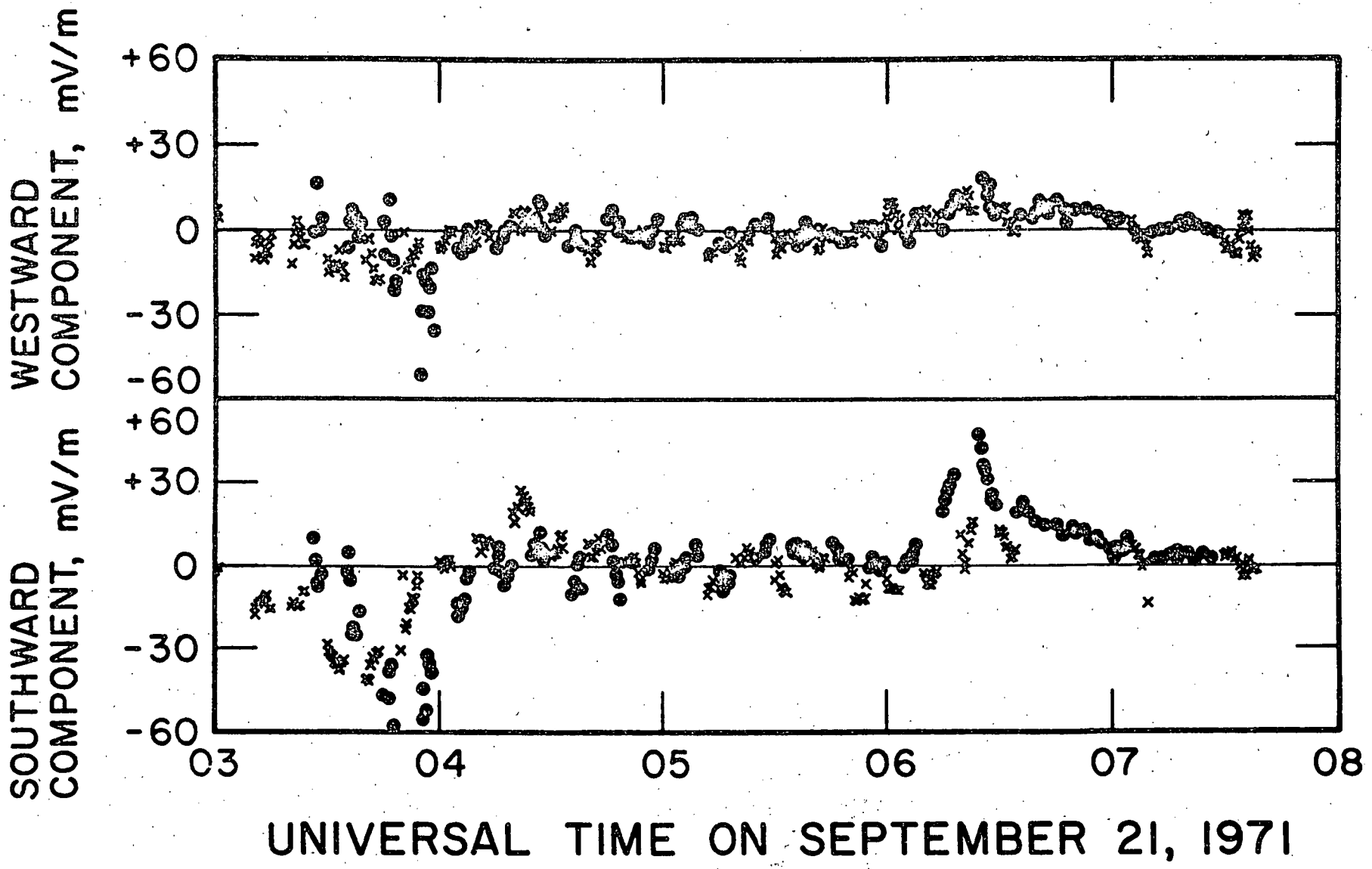
WESTWARD COMPONENT, mV/m
SOUTHWARD COMPONENT, mV/m
+60
+30
0
-30
-60
03
04
05
06
07
08
UNIVERSAL TIME ON SEPTEMBER 21, 1971

Figure 2

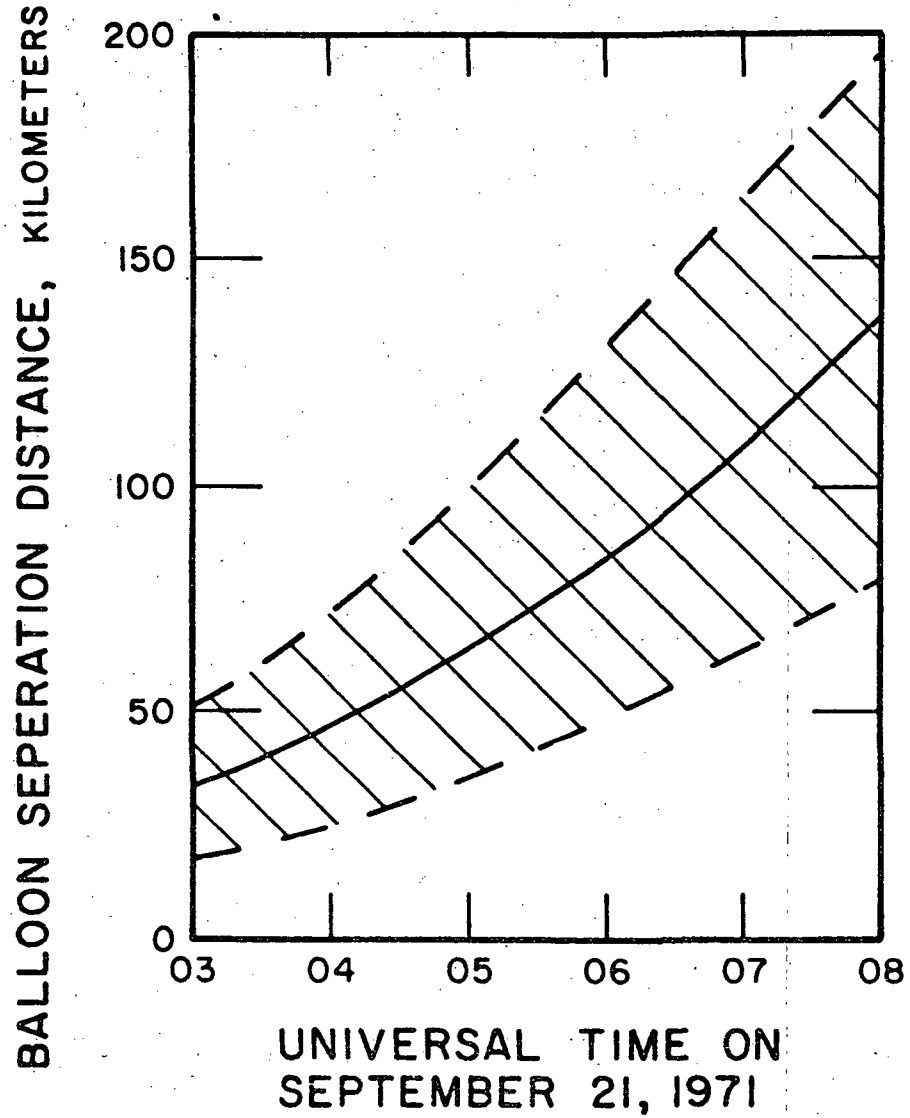
BALLOON SEPERATION DISTANCE, KILOMETERS
200
150
100
50
0
03
04
05
06
07
08
UNIVERSAL TIME ON
SEPTEMBER 21, 1971

Figure 3

SPACE SCIENCES LABORATORY

A73-32054

RELATIONS BETWEEN IONOSPHERIC ELECTRIC FIELDS AND ENERGETIC TRAPPED AND PRECIPITATING ELECTRONS

F. S. MOZER, F. H. BOGOTT
AND B. TSURUTANI

SERIES 13, ISSUE 9

FEBRUARY 1, 1972

UNIVERSITY OF CALIFORNIA, BERKELEY

Space Sciences Laboratory Series 13, Issue 9

RELATIONS BETWEEN IONOSPHERIC ELECTRIC FIELDS AND ENERGETIC TRAPPED AND PRECIPITATING ELECTRONS*

F. S. Mozer,[1] F. H. Bogott,[2] and B. Tsurutani[1]

Reproduction in whole or in part is permitted for any purpose of the United States Government

Research supported in part by the Office of Naval Research under ONR contract N00014-69-A-0200-1015 and in part by the National Aeronautics and Space Administration under contract NAS 5-10362

*Submitted for publication in the Journal of Geophysical Research

[1]Physics Department and Space Sciences Laboratory, University of California, Berkeley 94720

[2]Space Sciences Laboratory, University of California, Berkeley 94720

1 February 1972

ABSTRACT

Balloon-borne electric field and x-ray detectors have been flown from Fort Churchill and from near the foot of the magnetic field line on which the ATS-5 satellite is located, in order to obtain and compare satellite and balloon measurements of trapped and precipitating particles with balloon measurements of the ionospheric electric field. The approximately 80 hours of coordinated data show that nighttime precipitation events (1) are preceded by enhancements of the westward component of ionospheric electric field about 70% of the time, (2) cause the westward electric field strength to decrease about 70% of the time, (3) are unrelated to variations of the southward component of the ionospheric electric field. The westward electric field enhancement prior to many precipitation events occurs when the trapped electron flux is at or near the stable trapping limit. Such precipitation events are therefore interpreted as resulting from enhanced pitch angle scattering by whistler mode waves as the trapped electron flux exceeds the stable trapping limit due to the inward convection associated with the enhanced westward field. This model explains the observed diurnal dependence of the phenomenon and the poor correlation between trapped and precipitated electron intensities reported in this paper. The decrease of the westward ionospheric electric field during many precipitation events is interpreted as due to ~25 keV potential drops along magnetic field lines resulting from the increased currents flowing during precipitation. The geometry of the westward electrojet current flow is such that the westward ionospheric electric field should decrease and little or no variation should occur in the southward component during precipitation, in agreement with the experimental data.

INTRODUCTION

The first comparisons of ionospheric electric fields with precipitating auroral zone particles were based on electric field measurements performed on rockets. Aggson (1969) reported reduced electric field magnitudes in regions of auroral luminosity while Mozer and Fahleson (1970) found examples in which rockets passed through arc structures with no diminution of the fields. Correlation of more extensive balloon measurements of electric fields with the motion of auroral forms has suggested a resolution of this apparent conflict by the observation that the westward component of the ionospheric electric field was diminished in and near auroral arcs about one-third of the time (Kelley et al., 1971c). In the present paper this conclusion will be strengthened and extended by comparisons of balloon measured ionospheric electric fields with the x-rays and visible light produced by precipitating particles. Results will also be presented on typical electric field variations preceding and apparently leading to particle precipitation through comparison of such variations with the x-ray data and with energetic particle measurements made on the same magnetic field line by the energetic particle detector in the ATS-5 synchronous orbiting satellite (Bogott and Mozer, 1971).

DESCRIPTION OF THE EXPERIMENTAL DATA

Balloons equipped with electric field and x-ray detectors have been flown from Fort Churchill, Canada on April 18, 1969 and from Thompson, Canada, (near the average position of the foot of the magnetic field line on which the ATS-5 satellite measured trapped energetic electrons), on April 25, May 2 and May 5, 1970, to acquire approximately 80 hours of simultaneous measurements of ionospheric electric

fields and x-rays from precipitating particles. The electric field experiment has been described elsewhere (Mozer and Serlin, 1969; Mozer, 1971a; Mozer and Manka, 1971). The x-ray detector consisted of a three-inch diameter thallium activated sodium iodide scintillator mounted on a photomultiplier tube having a 1/16" thick lead shield around the sides. Two energy channels covering the ranges of 20-45 keV and >45 keV energy deposits were continuously monitored by logarithmic count rate meters (described in Anderson and Milton, 1964).

The 20-45 keV x-ray count rate and the perpendicular electric field components in a geomagnetic, rotating frame of reference measured during a four-hour interval of the balloon flight of May 2, 1970 are given in Figure 1, along with the 40 keV trapped electron flux measured in the ATS-5 satellite. A 400 γ negative bay in the Thompson ground magnetometer was observed to begin near 0700 UT in coincidence with the development of the positive southward component of electric field in Figure 1. The negative deviation in the horizontal component of the magnetic field became maximum near 0800 UT and the bay continued until about 0930. The peak of the 20-45 keV x-ray intensity occurring near 0750 (denoted by a dashed vertical line in Figure 1) was preceded by an enhancement of the westward electric field component near 0735, after which the x-ray curve correlated well with variations of the eastward electric field strength. There was no apparent relationship between the southward field component and the x-ray intensity. Thus, three relationships between ionospheric electric fields and precipitating particles are suggested by the event occurring near 0750 UT in Figure 1:

1. The particle precipitation is sometimes preceded by an enhancement of the westward component of the ionospheric electric field.
2. The particle precipitation sometimes "causes" the east-west component of electric field to become small.
3. The particle precipitation is not related to any variations of the southward component of the ionospheric electric field.

Figure 2 presents two and one-half hours of simultaneous particle and electric field measurements from another flight, during which a 500γ negative bay occurred between about 0900 and 1300 UT while K_p was 3+. The dashed vertical lines of this figure represent five instances of maxima in the flux of precipitated particles during which the electric field-particle correlations were similar to those summarized above. A ten-minute segment of Figure 2 is expanded in Figure 3 to illustrate that these relationships are valid on time scales as short as about one minute in the vicinity of three peaks in the x-ray flux.

During the balloon flight from Fort Churchill, good all-sky camera pictures were obtained along with the electric field and x-ray data. To study whether the correlations that are observed between ionospheric electric fields and the higher energy electrons (responsible for the >20 keV x-rays) also exist for the <20 keV particles that produce the major part of the visible auroral luminosity, the sky brightness was estimated by viewing each frame of the all-sky camera data with a photomultiplier tube. The resulting comparison of electric fields with sky brightness is given in Figure 4 for the one-hour interval

during which intense visible auroras were observed. This time interval occurred near the middle of a 300 γ, two-hour duration, negative bay. In Figure 4, five increases of sky brightness are generally preceded by enhancements of the westward electric field, are generally accompanied by decreases of the westward field component, and are not clearly related to variations of the southward field.

Detailed analysis of data of the types illustrated in Figures 1 through 4 are limited by the variability of the events, the proximity in time of one event to the next such that it is uncertain which features of the correlations belong to which events, and the limited amount of available data. For these reasons the data have been subjected only to qualitative analyses to determine the order-of-magnitude of various temporal correlations between the precipitating particles and electric fields. These analyses have been performed by two independent observers with agreement on the major conclusions described below.

In Table 1, the variations of the electric field components near times of observed increases in particle precipitation are summarized. Several conclusions may be reached from examination of the statistics presented in this table:

1. An enhancement of the westward component of the ionospheric electric field precedes observed precipitation events about 70% of the time. This precurser field enhancement could occur even more often and not always be observed since the balloon experiment measures the ionospheric field averaged over a region that may be large compared to the precipitation zone (Mozer and Serlin, 1969).
2. The westward component of the ionospheric electric field decreases during precipitation events about 70% of the time. This value is larger than the earlier 35% estimate from comparison of balloon measurements with the motion

of auroral forms (Kelley et al., 1971c) but is not inconsistent with that result since only large field decreases were counted in the earlier estimate. This decrease of the field during precipitation is associated with the precurser field enhancement in virtually every event where it occurs.

3. The 45% correlation between precipitation and all variations of the southward field component suggests that there is little or no connection between the two phenomena since such a correlation could easily occur by chance because the electric field is variable and because all types of field variations are included in the estimates.

4. Within the limited statistics of Table 1, correlations between particle precipitation and the westward component of the electric field occur only during the nighttime. The probability of obtaining the observed lack of correlation in the four daytime events by chance would be about 0.01 if the probability were 70% that the particles and westward field variations are correlated in a single event.

The relationship between the precurser westward electric field increase and precipitating particles may be examined in the opposite sense by asking what percent of westward field enhancements were followed by increased precipitation. For this study, whose results are given in Table 2, an enhancement of the westward field was defined as a 10 millivolt/meter increase of an already westward field component in less than five minutes. The small discrepancies between Tables 1 and 2 arise from uncorrected differences of interpretation by

independent analyses at different times. From Table 2, about 35% of field increases were followed by enhanced precipitation, and the probability of a daytime correlation in a given field enhancement was significantly less than that at night. The statistical relationship between the westward field precurser and precipitation increases is not significantly dependent on the sign of the southward field component, although an overwhelming percentage of both westward field enhancements and precipitation increases occurred when the southward field component was greater than zero. This is because the north-south field component was southward through most of the nights of interest as it generally is during active periods (Mozer, 1971b).

DISCUSSION

The Precurser Westward Field Enhancement

From earlier figures and in Tables 1 and 2 it has been shown that:

1. X-ray precipitation events are often preceded by enhancements of the westward component of the ionospheric electric field.
2. Precipitation events are not significantly correlated with any preceding variations of the southward component of the ionospheric electric field.

To interpret these two results, the effects of an enhanced westward field component near midnight will be considered more quantitatively. Such an enhancement causes particles to $\bar{E} \times \bar{B}$ drift inward to regions of larger magnetic field strength where their perpendicular energies are larger because the first adiabatic invariant is conserved.

This effect by itself causes a decrease in precipitation because the particle pitch angles tend toward 90^{o}. However, if the inward drift and energization occur when the trapped particle fluxes are as large as the stable trapping limit of Kennel and Petschek (1966), the resultant energization might cause the flux of electrons above some energy to increase more rapidly with decreasing radial distance than does the stable trapping flux limit, thereby causing the excess particles to be precipitated by the whistler mode instability. In this case there would be a correlation between the precurser enhancement of the westward electric field and the following particle precipitation. To test this model further, specific predictions will be compared with experimental data in the following sections.

The most obvious prediction of the above model is that enhancements of the westward field that are followed by increased x-ray intensities should occur when the trapped electron flux is near the stable trapping limit. That this expectation is generally satisfied by the experimental data may be seen in Figures 1 and 2 through comparison of the electric field and x-ray data with the differential flux of 40 keV electrons measured by the ATS-5 satellite in the equatorial plane on a magnetic field line whose foot was within about 100 km of the balloons. The dashed horizontal lines accompanying the satellite data in these figures represent the upper limit to the stably trapped flux determined experimentally from statistical analysis of ATS-5 particle data (Mozer, 1972), and they agree to within a factor of about two with the theoretical estimates of Kennel and Petschek (1966). The prominent westward electric field enhancements occurring near 0735 UT in Figure 1 and 1012, 1120 and 1140 in Figure 2 occurred while

the trapped 40 keV electron flux was near the stable limit and produced increases of the x-ray intensity, in agreement with predictions from the model.

Another satisfying feature of the present model is that it explains the obvious lack of detailed correlation in Figures 1 and 2 between the trapped particle intensities measured on the ATS-5 satellite and the precipitating electrons observed on the balloon since their relationship depends on variations of the electric field. This poor correlation is a general feature of the present data, in apparent disagreement with earlier x-ray-trapped particle comparisons (Parks and Winckler, 1969).

Since the above described precipitation model only applies or at least works best when the trapped particle fluxes are near the stable trapping limit, some other mechanism must be invoked to explain x-ray events occurring when the trapped flux is relatively small, such as near 0600 UT in Figure 1. Since this and several other events occurred while the trapped fluxes were increasing, it is likely that an injection of freshly accelerated particles took place at such times with those particles in the loss cone producing x-rays in the atmosphere while those electrons in the trapping cone produced an increase in the flux of trapped particles. Thus, it is likely that at least two different physical mechanisms are required to account for different classes of x-ray events.

The particle precipitation induced by enhancements of the westward electric field component sometimes caused the trapped flux to vary, as near 0750 UT in Figure 1, while the trapped flux was unaffected at other times such as near 1125 or 1145 UT in Figure 2.

Either situation is consistent with the present model, depending on whether the excess flux of energetic electrons produced by the inward convection was small or large. In the latter case, the reservoir of trapped particles would be filled and the excess particles precipitated without depleting the reservoir. In the former case the precipitation would deplete the reservoir as near 0750 UT in Figure 1 such that the large westward electric field present shortly thereafter was not able to refill it and no x-rays were immediately produced.

The above model of particle precipitation occurring when an increased westward electric field causes the particle flux to exceed the stable trapping limit also explains the local time dependence of the statistical observations of Tables 1 and 2 in the following way. It has been shown that the trapped energetic particle fluxes are statistically near the stable trapping limit only between local times of about 2100 to 0800 (Mozer, 1972). Thus, the precurser westward electric field enhancement of the present model is expected to produce precipitation only between such local times in agreement with the observations summarized in Tables 1 and 2.

Another prediction amenable to experimental verification concerns the hardness of the energy spectrum of precipitated particles. If the fluxes of both the 40 keV and 75 keV electrons observed on ATS-5 are near the stable limits (Mozer, 1972) then a westward electric field enhancement should produce a harder x-ray event than would occur if only the 40 keV electron fluxes are near the stable limit. The existing experimental data are not sufficient to test this important prediction but further balloon flights are planned with the goal of providing such data.

The Decrease of the Westward Ionospheric Electric Field Component During Precipitation and the Lack of any Such Correlation with the Southward Field

The correlation between the eastward electric field component and particle precipitation in Figures 1 through 4 and the statistical evidence of Table 1 require that the westward component of the ionospheric electric field tends to decrease during particle precipitation events. According to the model of the previous section, the westward electric field component near the equatorial plane on the same magnetic field line does not similarly change because it must remain enhanced to drive the inward convection causing precipitation throughout the event. These conclusions require the presence of significant parallel electric fields, at least during precipitation events. However, these parallel fields cannot influence the ionospheric north-south electric field component since this component exhibits no particular variation during the precipitation. It is the purpose of the following discussion to interpret the above observations in terms of a physical model.

Large precipitation events occur during the explosive phase of substorms at times when an enhanced westward electrojet current is flowing in the ionosphere. Correlated electric field and ground magnetic observations have shown this westward electrojet to be a Hall current driven by the southward ionospheric electric field (Mozer and Serlin, 1969). Since the precipitation causes an increase of the ionospheric Hall conductivity while the southward field does not vary, the westward electrojet current must increase during such precipitation events, as was actually observed by ground magnetometers during the events described in this paper.

The enhanced westward electrojet current most probably flows along magnetic field lines to close in the magnetosphere as illustrated in Figure 5a (Bostrom, 1964; Akasofu and Meng, 1969; Vasyliunas, 1970). Consider

$$\oint \bar{E} \cdot \overline{d\ell} = 0 \qquad (1)$$

where the line integral is performed around the loop illustrated in Figure 5a. The sum of the potential drops along the magnetic field lines plus the ionospheric potential drop are equal in magnitude to the enhanced and presumed constant potential drop perpendicular to the magnetic field in the magnetosphere. The increased current flow increases the potential drop along the magnetic field lines, and the enhanced anomalous resistivity that is associated with the increased current (Hamberger and Friedman, 1968; Kindel and Kennel, 1971) causes an even greater parallel potential drop. For both of these reasons, and to satisfy equation (1), the ionospheric potential drop, and therefore the westward electric field component in the ionosphere, must decrease.

The above ideas may be tested quantitatively on specific events. For example, the enhanced westward electric field near 0735 UT in Figure 1 caused a factor of about two increase in the westward ionospheric current according to ground magnetometer measurements, while the southward electric field that drove the Hall current remained essentially constant. Thus, the precipitation event occurring between 0740 and 0800 UT in Figure 1 must have caused the height integrated Hall conductivity in the auroral ionosphere to about double. This result is easily achieved by precipitation events of the magnitude being

considered. The factor of two increase of the westward ionospheric current caused the westward electric field to decrease by a factor of four or so. If the longitudinal extent of the diminished field region covered a distance of 1000 km, parallel potential drops of ~25 kilovolts would be needed to satisfy equation (1). The existence of such potential drops requires that wave-particle interactions produced anomalous resistivities having magnitudes that are consistent with laboratory plasma measurements (Hamberger and Friedman, 1968) and theory (Buneman, 1958; Coroniti and Kennel, 1972). Three rocket flights have yielded parallel electric field measurements having magnitudes consistent with the above ideas (Mozer and Fahleson, 1970; Kelley et al., 1971a; Kelley et al., 1971b). A satellite measurement of electrostatic waves may have detected the waves responsible for the anomalous resistivity (Kelley and Mozer, 1972).

The question of why the southward ionospheric electric field is not affected by the large parallel potential drops may be answered with reference to the curve of Figure 5b, along which the line integral of equation (1) will be evaluated. If, for example, the loop of this figure is near the eastern edge of the auroral electrojet, then the current flow and the potential drop along the two segments of magnetic field line will have the sense shown, and the sum of contributions to the integral of equation (1) from the two magnetic field line segments will be zero, to first order. Thus the presence of parallel currents and anomalous resistivity does not alter the conclusion reached in the absence of parallel electric fields that the potential drop between two magnetic field lines in a meridional plane is the same in the ionosphere as in the magnetosphere. The southward ionospheric electric field is, thus, simply related to the radial magnetospheric electric field before and

during the precipitation event and is not altered by the precipitation and changing ionospheric current.

CONCLUSIONS

In the previous sections it has been shown that:

1. At least two mechanisms for particle precipitation on auroral zone magnetic field lines are present. The first is the precipitation of freshly energized particles with a spectrum characteristic of the acceleration mechanism whenever such particles are produced with pitch angles in the loss cone. The second is the precipitation of particles due to pitch angle scattering caused by whistler mode waves whenever the trapped particle flux is near the stable trapping limit and an enhancement of the westward magnetospheric electric field causes increased inward convection near local midnight. In this case the spectrum of precipitated particles is determined by the energy spectrum of those trapped particles whose flux is near the stable trapping limit. The dependence of this second type of precipitation on both the westward electric field and the trapped particle flux explains the poor observed correlation between balloon measured x-rays and satellite measured trapped particles.
2. Enhanced particle precipitation causes an increase of the ionospheric height integrated Hall conductivity which, in turn, causes the current in the westward auroral electrojet to increase. Since the electrojet probably closes by flowing along magnetic field lines and since this flow probably causes anomalous resistivity effects parallel to the magnetic field line, potential

drops of ~25 kilovolts between the ionosphere and magnetosphere may result. The spatial geometry of these potential drops is determined by the directions of current flow and is such that the ionospheric westward electric field component must decrease while the southward field is affected less when the westward ionospheric electrojet current increases. These predicted electric field variations are consistent with experimental observations.

3. Because of the correlation between westward electric field enhancements and particle precipitation it is possible that auroral arc structures denote regions of enhanced westward electric field strength. Alternatively, if the westward field enhancement is a large scale phenomenon, arc structures may represent local regions having large pitch angle scattering because the flux of inward convecting trapped particles reaches the stable limit at these locations.

ACKNOWLEDGMENTS

We acknowledge the invaluable advice and assistance of Commander W.F. Cross and Mr. M. Evanick of the Project Skyhook program of the Office of Naval Research. This work was supported by ONR contract N00014-69-A-0200-1015 and NASA contract NAS 5-10362.

REFERENCES

Aggson, T.L., Probe measurements of electric fields in space, in Atmospheric Emissions, edited by B.M. McCormac and A. Omholt, Van Nostrand Reinhold, New York, 305, 1969

Akasofu, S.-I. and C.-I. Meng, A study of polar magnetic substorms, J. Geophys. Res., 74, 293, 1969

Anderson, K.A. and D.W. Milton, Balloon observations of x-rays in the auroral zone, 3. High time resolution studies, J. Geophys. Res., 70, 2135, 1965

Bogott, F.H. and F.S. Mozer, Equatorial proton and electron angular distribution in the loss cone and at large angles, J. Geophys. Res., 76, 6790, 1971

Bostrom, R., A model of auroral electrojets, J. Geophys. Res., 69, 4983, 1964

Buneman, O., Instability, turbulence and conductivity in current-carrying plasma, Phys. Rev. Letters, 1, 8, 1958

Coroniti, F.V., and C.F. Kennel, Polarization of the auroral electrojet, submitted to J. Geophys. Res., 1972

Hamberger, S.M. and M. Friedman, Electrical conductivity of a highly turbulent plasma, Phys. Rev. Letters, 21, 674, 1968

Kelley, M.C., and F.S. Mozer, A satellite survey of vector electric fields in the ionosphere at frequencies from 10 to 500 hertz, 1. Isotropic, high latitude, low frequency emissions, submitted to J. Geophys. Res., 1972

Kelley, M.C., F.S. Mozer and U.V. Fahleson, Electric fields in the nighttime and daytime auroral zone, J. Geophys. Res., 76 6054, 1971a

Kelley, M.C., F.S. Mozer, G. Haerendel, U.V. Fahleson and A. Kavadas, Rocket DC electric field measurements in a 1000 gamma magnetic substorm, Trans. Am. Geophys. Union, 52, 329, 1971b

Kelley, M.C., J.A. Starr and F.S. Mozer, Relationship between magnetospheric electric fields and the motion of auroral forms, J. Geophys. Res., 76, 5269, 1971c

Kennel, C.F. and H.E. Petschek, Limit on stably trapped fluxes, J. Geophys. Res., 71, 1, 1966

Kindel, J.M. and C.F. Kennel, Topside current instabilities, J. Geophys. Res., 76, 3055, 1971

Mozer, F.S., Electric field mapping in the ionosphere at the equatorial plane, Planet. Space Sci., 18, 259, 1970

Mozer, F.S., Balloon measurements of vertical and horizontal atmospheric electric fields, Pure and Appl. Geophys. 84, 32, 1971a

Mozer, F.S., Origin and effects of electric fields during isolated magnetospheric substorms, J. Geophys. Res., 76, 7595, 1971b

Mozer, F.S., Particle flux limits in the synchronous orbit, submitted to J. Geophys. Res., 1972

Mozer, F.S. and U.V. Fahleson, Parallel and perpendicular electric fields in an aurora, Planet. Space Sci., 18, 1563, 1970

Mozer, F.S. and R.H. Manka, Magnetospheric electric field properties deduced from simultaneous balloon flights, J. Geophys. Res., 76, 1697, 1971

Mozer, F.S. and R. Serlin, Magnetospheric electric field measurements with balloons, J. Geophys. Res., 74, 4739, 1969

Parks, G.K. and J.R. Winckler, Simultaneous observations of 5- to 15-second period modulated energetic electron fluxes at the synchronous altitude and the auroral zone, J. Geophys. Res., 74, 4003, 1969

Vasyliunas, V.M., Mathematical models of magnetospheric convection and its coupling to the ionosphere, in Particles and Fields in the Magnetosphere, edited by B.M. McCormac, D. Reidel Publ. Co., 60-71, 1970

Table 1. Relation of Electric Field Variations to Particle Precipitation

Local Time	Westward Field Enhancement Preceding Precipitation?		Westward Field Decrease During Precipitation?		Any Southward Field Variation Associated With Precipitation?	
	Yes	No	Yes	No	Yes	No
2100-2400	12	3	12	3	9	6
0000-0300	5	3	6	2	3	5
0300-0600	7	1	6	2	2	6
0600-0900	0	1	0	1	0	1
0900-1200	0	0	0	0	0	0
1200-1500	0	3	0	3	2	1
Total	25	11	24	11	16	19

Table 2

Relation of Particle Precipitation to Enhancements of the Westward Component of Ionospheric Electric Field

Local Time	Enhancement of Precipitation After Westward Field Increase?			
	Southward Field >0		Southward Field < 0	
	Yes	No	Yes	No
2100-2400	7	5	4	4
0000-0300	7	13	0	0
0300-0600	8	13	0	1
0600-0900	0	2	1	3
0900-1200	0	5	0	3
1200-1500	1	4	0	0
Total	23	42	5	11

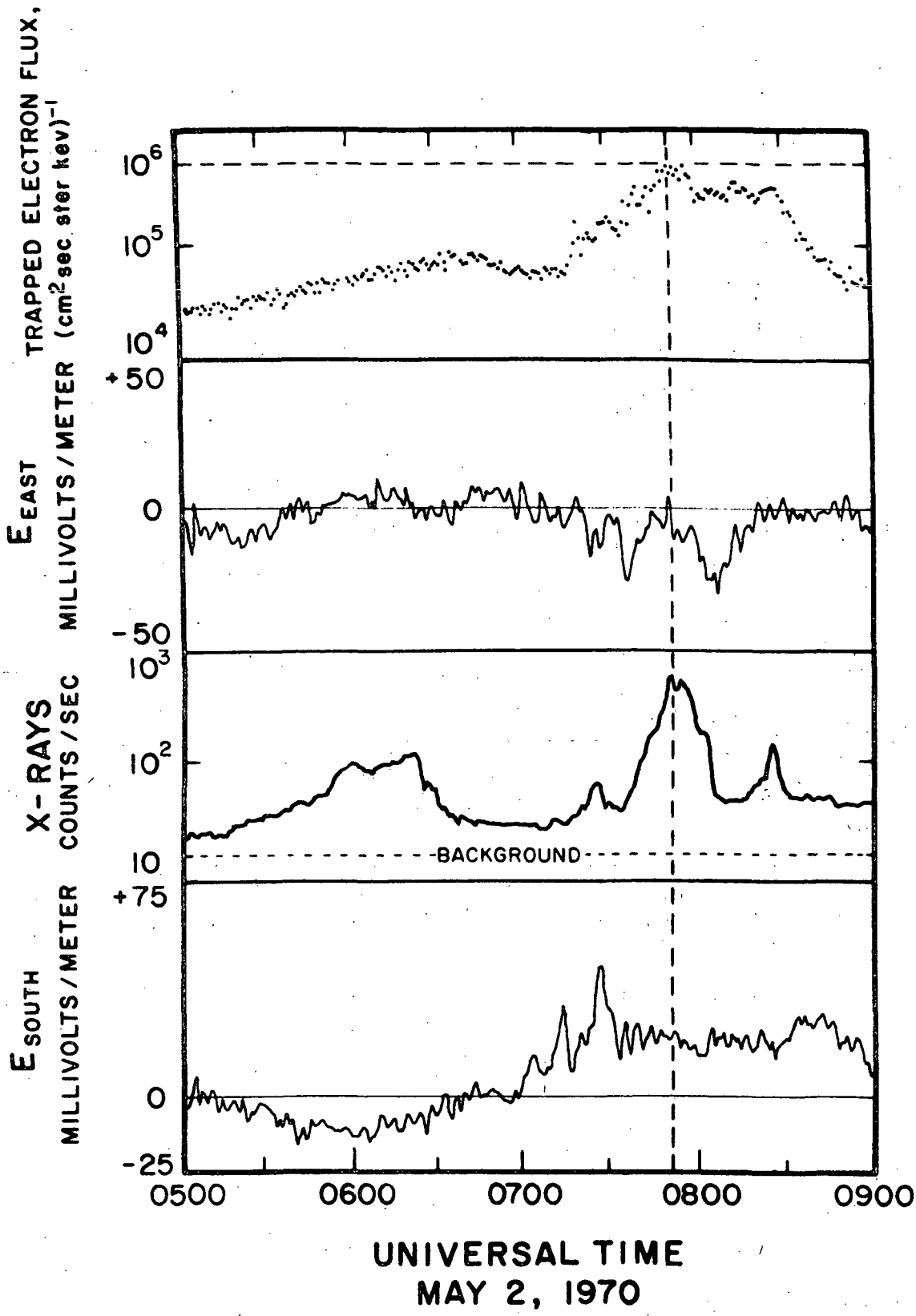

FIGURE 1: Electric field components and x-rays measured on a balloon flown from Thompson, Canada plotted with simultaneous measurements of 40 keV electrons measured in synchronous orbit on the ATS-5 satellite. The foot of the magnetic field line through the satellite was within about 100 kilometers of the balloon position during this measurement.

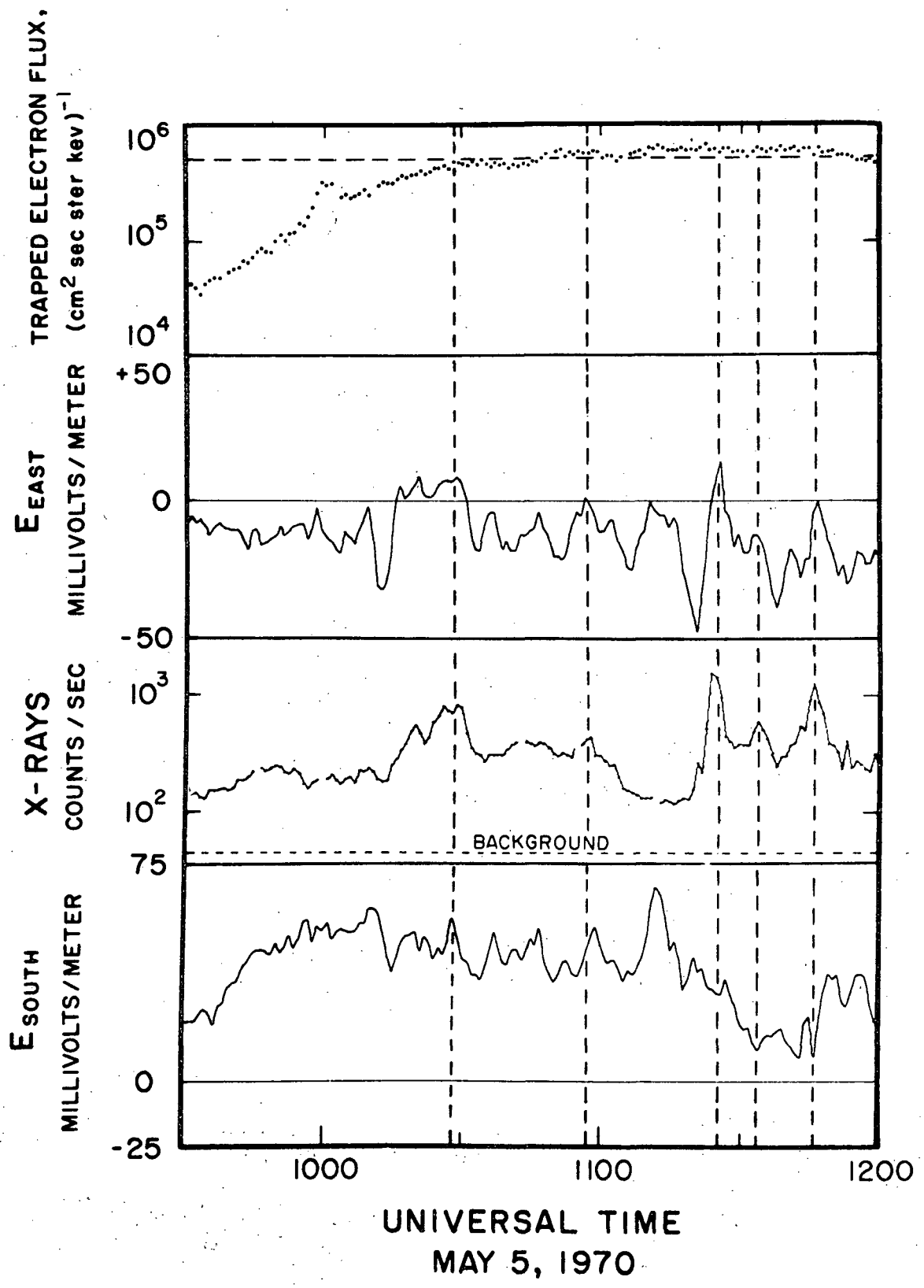

FIGURE 2: Same as Figure 1

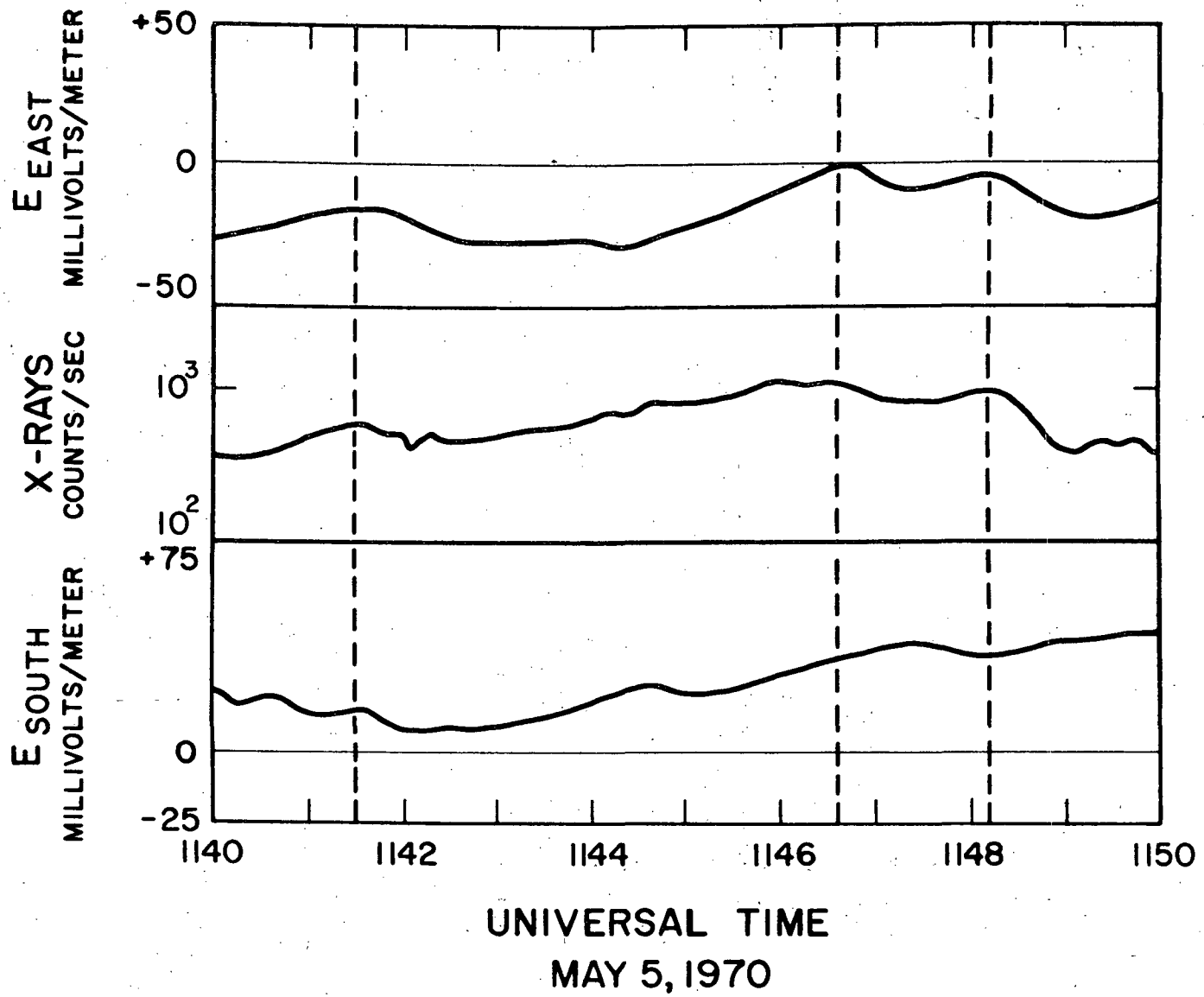

FIGURE 3: Expansion of a ten-minute time interval of the data presented in Figure 2. The random errors on each curve are a few times the widths of the lines.

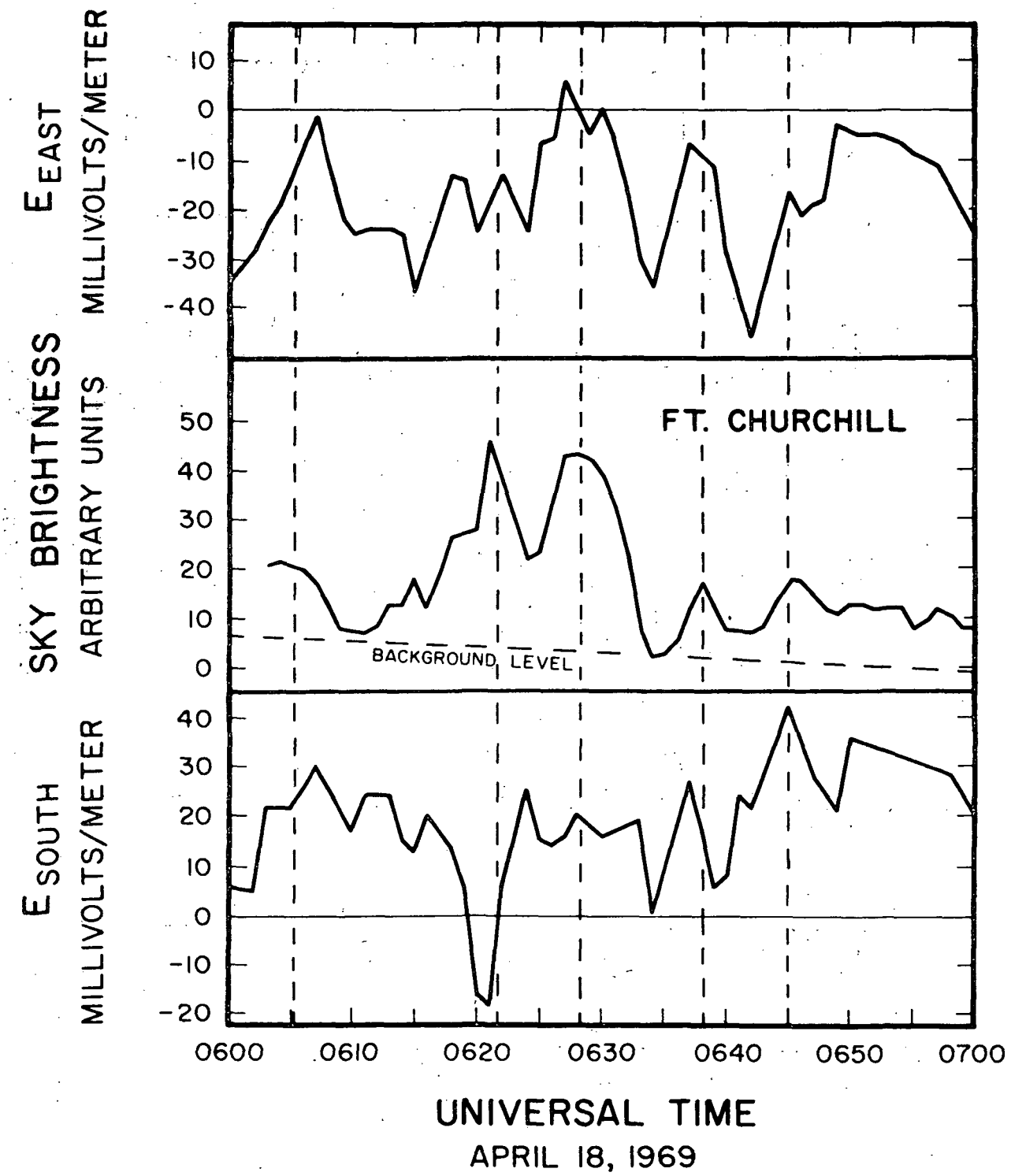

FIGURE 4: Electric field measurements obtained on a balloon flown from Fort Churchill and the sky brightness estimated from the transmission coefficient of all-sky camera negatives.

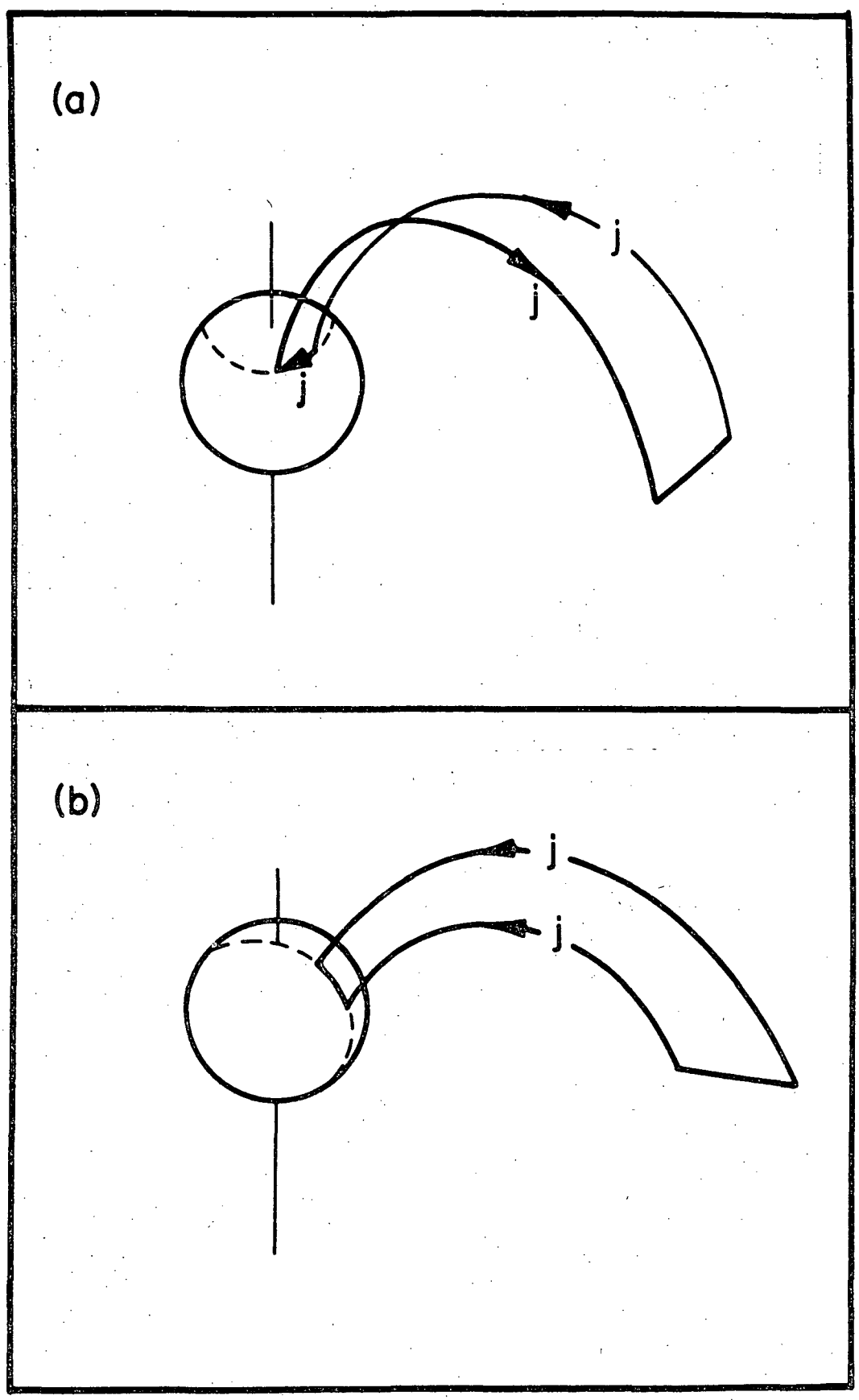

FIGURE 5: Model current patterns whose geometries allow interpretation of the electric field and particle data.

UNCLASSIFIED

Security Classification

DOCUMENT CONTROL DATA – R & D

(Security classification of title, body of abstract and indexing annotation must be entered when the overall report is classified)

1. ORIGINATING ACTIVITY (Corporate author)	2a. REPORT SECURITY CLASSIFICATION
Space Sciences Laboratory University of California Berkeley, California 94720	Unclassified
	2b. GROUP

3. REPORT TITLE

RELATIONS BETWEEN IONOSPHERIC ELECTRIC FIELD AND ENERGETIC TRAPPED AND PARTICIPATING ELECTRONS

4. DESCRIPTIVE NOTES (Type of report and inclusive dates)

Technical Report

5. AUTHOR(S) (First name, middle initial, last name)

Forrest S. Mozer, Fred H. Bogott and Bruce Tsurutani

6. REPORT DATE	7a. TOTAL NO. OF PAGES	7b. NO. OF REFS
February 1, 1972	28	23

8a. CONTRACT OR GRANT NO.	9a. ORIGINATOR'S REPORT NUMBER(S)
N00014-69-A-0200-1015	Series 13, Issue 9
b. PROJECT NO. NR 021-213	
c. NASA contract NAS 5-10362	9b. OTHER REPORT NO(S) (Any other numbers that may be assigned this report)
d.	

10. DISTRIBUTION STATEMENT

Distribution of this document is unlimited.

11. SUPPLEMENTARY NOTES	12. SPONSORING MILITARY ACTIVITY
	Nuclear Physics Branch Office of Naval Research

13. ABSTRACT

Balloon-borne electric field and x-ray detectors have been flown from Fort Churchill and from near the foot of the magnetic field line on which the ATS-5 satellite is located, in order to obtain and compare satellite and balloon measurements of trapped and precipitating particles with balloon measurements of the ionospheric electric field. The approximately 80 hours of coordinated data show that nighttime precipitation events (1) are preceded by enhancements of the westward component of ionospheric electric field about 70% of the time, (2) cause the westward electric field strength to decrease about 70% of the time, (3) are unrelated to variations of the southward component of the ionospheric electric field. The westward electric field enhancement prior to many precipitation events occurs when the trapped electron flux is at or near the stable trapping limit. Such precipitation events are therefore interpreted as resulting from enhanced pitch angle scattering by whistler mode waves as the trapped electron flux exceeds the stable trapping limit due to the inward convection associated with the enhanced westward field. This model explains the observed diurnal dependence of the phenomenon and the poor correlation between trapped and precipitated electron intensities reported in this paper. The decrease of the westward ionospheric electric field during many precipitation events is interpreted as due to ~25 keV potential drops along magnetic field lines resulting from the increased currents flowing during precipitation. The geometry of the westward electrojet current flow is such that the westward ionospheric electric field should decrease and little or no variation should occur in the southward component during precipitation, in agreement with the experimental data.

DD FORM 1 NOV 68 1473

UNCLASSIFIED

Security Classification

14. KEY WORDS	LINK A ROLE	LINK A WT	LINK B ROLE	LINK B WT	LINK C ROLE	LINK C WT
Ionospheric Electric Fields						
Energetic Trapped Electrons						
Precipitating Electrons						

Contr. Mineral. and Petrol. 33, 1–20 (1971)
© by Springer-Verlag 1971

Silica Activity and P_{total} in Igneous Rocks

J. Nicholls
Dept. of Geology, University of Calgary, Alberta, Canada
I. S. E. Carmichael
Dept. of Geology and Geophysics, University of California, Berkeley, Calif. 94720
J. C. Stormer, Jr.
Dept. of Geology, University of Georgia, Athens, Georgia 30601

Received July 16, 1971

Abstract. The variation of silica activity with temperature and pressure for a variety of silica buffers (mineral pairs) allows P_{total} to be calculated for a wide range of igneous rocks. The method also depends on evaluating $(\partial \log a_{SiO_2}/\partial P)_T$ and $(\Delta \log a_{SiO_2}/\Delta T)_P$; the former is equivalent to the partial molar volume of silica in silicate liquids, while the latter is estimated from published experiments on natural melts. Results for calc-alkaline rhyolites with phenocrysts of quartz, olivine or orthopyroxene, and iron-titanium oxides, range from 3.45 to 9.58 kilobars; a pantellerite is intermediate at 7.53 kilobars. At 1327°C, the silicate inclusions in diamond equilibrated at 63.5 kilobars, and the kimberlite crystallisation path intersected the baddeleyite-zircon reaction at 55.7 kilobars. Two trachybasalts would equilibrate with their lherzolite xenoliths at 17.0 and 21.0 kilobars at surface quenching temperatures. Potassic lavas such as orendites and ugandites at 1300°C would be in equilibrium with mantle olivine-orthropyroxene at 35.1 and 69.0 kilobars respectively. Basalts and basaltic-andesites could equilibrate (at 1100°C) with quartz at between 24.9 and 26.8 kilobars; quartz can therefore be considered a possible high pressure "xenocryst" in lavas with low Sr^{87}/Sr^{86} ratios. Andesites will equilibrate at 1300°C with the mantle at a depth of 75 kilometres; at greater depths andesite will have a basaltic precursor. In general, lavas with low silica activity will equilibrate at greater depths in the mantle than those with higher silica activities.

The Apollo 11 basalts contain minerals which suggest equilibration at 37 kilobars; the calculated quenching temperature is 1009°C, from which $\log f_{O_2}$ can be derived (−15.2) which in turn indicates approximately 0.10% Fe_2O_3 in these lavas.

Introduction

In another paper on silica activity (a_{SiO_2}) in igneous rocks (Carmichael *et al.*, 1970) we examined the variation of a_{SiO_2} with temperature for a variety of mineral pairs, each of which would buffer or define silica activity in any magma in which they occur. However, despite a vast amount of work on experimental silicate equilibria, there is no generally applicable method of extracting estimates of total pressure (P_{total}) from igneous mineral assemblages. It now seems possible, within the limitations of the thermodynamic data, to use a_{SiO_2} to estimate P_{total} for a wide variety of igneous rocks; the procedure depends on only a few, and reasonable, assumptions.

As there has been an influx of new thermochemical data in the last two or three years, we have been able to add to the reactions which define a_{SiO_2} in igneous rocks, and, as a prelude to the discussion of the effect of P_{total} on a_{SiO_2}, we first summarise the effect of temperature.

If for example, crystals of pure fayalite and ferrosilite coexist in equilibrium with a silicate liquid, then the activity of silica in that liquid is only a function of temperature at constant pressure. The variation of a_{SiO_2} can be calculated from the reaction:

$$\underset{\text{fayalite}}{Fe_2SiO_4} + \underset{\text{glass}}{SiO_2} = 2\,\underset{\text{ferrosilite}}{FeSiO_3} \tag{1}$$

which at equilibrium ($\Delta G = 0$) gives

$$\log a_{SiO_2}^{\text{liquid}} = \Delta G^0/2.303\,RT + 2 \log a_{FeSiO_3}^{\text{pyroxene}} - \log a_{Fe_2SiO_4}^{\text{olivine}}. \tag{1a}$$

For the components in their standard states (pure solids of unit activity and silica glass) at the temperature of interest and a pressure of 1 bar, the variation of $\log a_{SiO_2}^{\text{liquid}}$ with temperature can be represented by an equation of the form $A/T + B$. The two constants A and B, derived by least-squares analysis, are given in Table 1 for Eq. (1) and for the other reactions listed below. However as both fayalite and ferrosilite form solid solutions in nature, the reduced activity of the two components Fe_2SiO_4 and $FeSiO_3$ (subscripts) in their respective solid solutions (superscripts) is accounted for by the logarithm terms in Eq. (1a).

Other reactions which we will use in this paper are:

$$\underset{\text{glass}}{SiO_2} = \underset{\text{quartz}}{SiO_2} \tag{2}$$

and

$$\log a_{SiO_2}^{\text{liquid}} = \Delta G^0/2.303\,RT.$$

$$\underset{\text{forsterite}}{Mg_2SiO_4} + \underset{\text{glass}}{SiO_2} = 2\,\underset{\text{clinoenstatite}}{MgSiO_3} \tag{3}$$

and

$$\log a_{SiO_2}^{\text{liquid}} = \Delta G^0/2.303\,RT + 2 \log a_{MgSiO_3}^{\text{pyroxene}} - \log a_{Mg_2SiO_4}^{\text{olivine}}. \tag{3a}$$

$$\underset{\text{baddeleyite}}{ZrO_2} + \underset{\text{glass}}{SiO_2} = \underset{\text{zircon}}{ZrSiO_4} \tag{4}$$

and

$$\log a_{SiO_2}^{\text{liquid}} = \Delta G^0/2.303\,RT + \log a_{ZrSiO_4}^{\text{zircon}} - \log a_{ZrO_2}^{\text{baddeleyite}}. \tag{4a}$$

$$\underset{\beta\text{-nepheline}}{\tfrac{1}{2}\,NaAlSiO_4} + \underset{\text{glass}}{SiO_2} = \underset{\text{high-albite}}{\tfrac{1}{2}\,NaAlSi_3O_8} \text{ for } T < 907^\circ C, \tag{5}$$

at

$$T > 907^\circ C$$

$$\underset{\gamma\text{-nepheline}}{\tfrac{1}{2}\,NaAlSiO_4} + \underset{\text{glass}}{SiO_2} = \underset{\text{high-albite}}{\tfrac{1}{2}\,NaAlSi_3O_8} \tag{6}$$

and

$$\log a_{SiO_2}^{\text{liquid}} = \Delta G^0/2.303\,RT + \tfrac{1}{2} \log a_{NaAlSi_3O_8}^{\text{feldspar}} - \tfrac{1}{2} \log a_{NaAlSiO_4}^{\text{nepheline}}. \tag{6a}$$

$$\underset{\text{leucite}}{KAlSi_2O_6} + \underset{\text{glass}}{SiO_2} = \underset{\text{sanidine}}{KAlSi_3O_8} \tag{7}$$

and

$$\log a_{SiO_2}^{liquid} = \Delta G^0/2.303\ RT + \log a_{KAlSi_2O_6}^{feldspar} - \log a_{KAlSi_2O_6}^{leucite}. \quad (7a)$$

$$\underset{\alpha\text{-perovskite}}{CaTiO_3} + \underset{glass}{SiO_2} = \underset{sphene}{CaTiSiO_5} \quad (8)$$

and

$$\log a_{SiO_2}^{liquid} = \Delta G^0/2.303\ RT + \log a_{CaTiSiO_5}^{sphene} - \log a_{CaTiO_3}^{perovskite}. \quad (8a)$$

$$\underset{kaliophilite}{KAlSiO_4} + \underset{glass}{SiO_2} = \underset{leucite}{KAlSi_2O_6} \quad (9)$$

and

$$\log a_{SiO_2}^{liquid} = \Delta G^0/2.303\ RT + \log a_{KAlSi_2O_6}^{leucite} - \log a_{KAlSiO_4}^{kaliophilite}. \quad (9a)$$

$$\underset{magnetite}{\tfrac{2}{3}\,Fe_3O_4} + \underset{glass}{SiO_2} = \underset{fayalite}{Fe_2SiO_4} + \tfrac{1}{3}\,O_2 \quad (10)$$

and

$$\log a_{SiO_2}^{liquid} = \Delta G^0/2.303\ RT + \log a_{Fe_2SiO_4}^{olivine} + \tfrac{1}{3}\log f_{O_2} - \tfrac{2}{3}\log a_{Fe_3O_4}^{magnetite}. \quad (10a)$$

$$\underset{magnetite}{\tfrac{1}{3}\,Fe_3O_4} + \underset{glass}{SiO_2} = \underset{ferrosilite}{FeSiO_3} + \tfrac{1}{6}\,O_2 \quad (11)$$

and

$$\log a_{SiO_2}^{liquid} = \Delta G^0/2.303\ RT + \log a_{FeSiO_3}^{pyroxene} + \tfrac{1}{6}\log f_{O_2} - \tfrac{1}{3}\log a_{Fe_3O_4}^{magnetite}. \quad (11a)$$

The sources of the thermodynamic data used to calculate the A and B constants for each of the above reactions are given in Table 1. Data taken from Wones and Gilbert (1969) and Williams (1971) have been changed so that the standard state of silica is silica glass rather than quartz.

The variation of $\log a_{SiO_2}^{liquid}$ with temperature at 1 bar for the above reactions is plotted in Fig. 1, and updates the curves given previously by Carmichael *et al.* (1970). None of the conclusions suggested by them need to be modified in the light of the new data for kaliophilite, leucite and zircon. However, Williams (1970) has stated that the free energy of formation (ΔG_f^0) of enstatite should be decreased by about a kilocalorie. If this was applied equally over the temperature range shown in Fig. 1, it would depress the Fo–En curve so that it would intersect the Ab-Ne curve at about 770°C. As olivine, rather than orthopyroxene, is found with nepheline in trachytes and phonolites, it would appear that the data for nepheline are in error if William's enstatite measurements are correct.

The Effect of Pressure on a_{SiO_2}

The effect of pressure on a silica buffer can be obtained by differentiating Eqs. (1) to (9) at constant temperature and assuming for the present that the solids have unit activity. Thus

$$\left(\frac{\partial \log a_{SiO_2}^{liquid}}{\partial P}\right)_T = \frac{1}{2.303\ RT}\left(\frac{\partial \Delta G^0}{\partial P}\right)_T = \frac{\Delta V^0}{2.303\ RT}, \quad (12)$$

where ΔV^0 is the volume change of the reaction for the components in their standard states. It will be assumed that the molar volume, ΔV^0, is independent

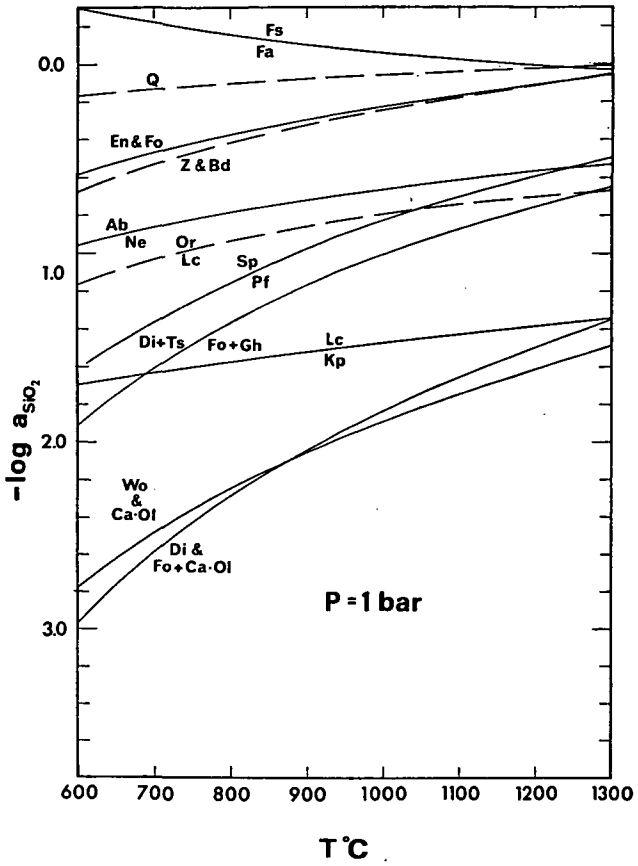

Fig. 1. Variation of log a_{SiO_2} with temperature at 1 bar for silica buffer reactions. In each case the desilicated mineral is stable at lower values of log a_{SiO_2}. All reactions are explained in the text except for $Fo + Gh + SiO_2 = Di + Ts$ which corresponds to $Mg_2SiO_4 + Ca_2Al_2SiO_7 + SiO_2 = CaMgSi_2O_6 + CaAl_2SiO_6$

of pressure; this is reasonable as the effect of temperature (800–1300°C) on increasing ΔV^0_{298} will be offset by the effect of pressure contracting ΔV^0, at least up to 10 kilobars. Thus (Eq. (12) can be integrated to give

$$(\log a^{\text{liquid}}_{SiO_2})^{P=P\text{ bars}} = (\log a^{\text{liquid}}_{SiO_2})^{P=1\text{ bar}} + \frac{\Delta V^0}{2.303\,RT}(P-1) \qquad (13)$$

where P is the pressure in bars. As $\frac{\Delta V^0}{2.303\,R}$ is a constant, values of $C = \frac{\Delta V^0}{2.303\,R}$ are given in Table 1 for each of the reactions listed above. The variation of log a_{SiO_2} with pressure at 1000°C (1273°K) for each of the reactions is plotted in Fig. 2. Note that with the exception of the kaliophilite-leucite reaction, all the slopes are negative, so that for all but the most silica-poor igneous rocks, an increase of pressure at constant T and composition promotes the presence of the more siliceous mineral of each buffer pair.

Table 1. *Coefficients A, B and C for the equation* $\log a_{SiO_2} = \Delta G^0/2.303\ RT = A/T + B + C\ (P-1)/T$ *for the listed reactions*

Eq. No.	Reaction	A	B	C	Source of Data
(1)	$Fe_2SiO_4 + SiO_2(gl) = 2FeSiO_3$	663	−0.46	−0.0406	Williams (1971), Robie and Waldbaum (1968), Kelley (1960)
(2)	$SiO_2(gl) = SiO_2(\beta - Q)$	−309	+0.183	−0.0239	Robie and Waldbaum (1968)
(3)	$Mg_2SiO_4 + SiO_2(gl) = MgSiO_3$	−1034	+0.597	−0.0424	Robie and Waldbaum (1968), Kelley (1960)
(4)	$ZrO_2 + SiO_2(gl) = ZrSiO_4$	−1228	+0.730	−0.0478	Kelley (1960), Robie and Waldbaum (1968), JANAF Tables
(5)	$\frac{1}{2}NaAlSiO_4(\beta) + SiO_2(gl) = \frac{1}{2}NaAlSi_3O_8$ ($T<907°$ C)	−871	+0.031	−0.0216	Kelley (1960), Robie and Waldbaum (1968)
(6)	$\frac{1}{2}NaAlSiO_4(\gamma) + SiO_2(gl) = \frac{1}{2}NaAlSi_3O_8$ ($T>907°$ C)	−855	+0.012	−0.0216	Robie and Waldbaum (1968), Kelley (1960)
(7)	$KAlSi_2O_6 + SiO_2(gl) = KAlSi_3O_8$	−972	−0.039	−0.0345	Robie and Waldbaum (1968); for leucite: ΔH_f^0—Kelley (1962) and Cp, Pankratz (1968)
(8)	$\alpha CaTiO_3 + SiO_2(gl) = CaTiSiO_5$	−2203	+0.905	−0.0274	Robie and Waldbaum (1968), Kelley (1960)
(9)	$KAlSiO_4(Kp) + SiO_2(gl) = KAlSi_2O_6$	−685	−0.928	+0.0064	Robie and Waldbaum (1968), and Cp—Pankratz (1968)
(10)	$^2/_3Fe_3O_4 + SiO_2(gl) = Fe_2SiO_4 + {}^1/_3O_2$	8270	−2.81	−0.0552	Wones and Gilbert (1969), Robie and Waldbaum (1968)
(11)	$^1/_3Fe_3O_4 + SiO_2(gl) = FeSiO_3 + {}^1/_6O_2$	4467	−1.63	−0.0479	Williams (1971), Robie and Waldbaum (1968)

A and B were obtained by a linear least squares analysis of calculated 1 bar data for $(\Delta G^0)/2.303$ RT.

It is also assumed that in all the solid solutions represented in Eqs. (1a) to (10a) by the logarithmic terms, the partial molar volume of each component is independent of composition, or in other words, so far as volume is concerned, the solid solutions are considered to be ideal. Thus the logarithmic activity terms in Eqs. (1a) to (10a) are assumed to be independent of pressure.

In any silicate liquid, the chemical potential of silica, is given by

$$\mu_{SiO_2}^{liquid} = \mu_{SiO_2}^0 + RT \ln a_{SiO_2}^{liquid} \tag{14}$$

where $\mu_{SiO_2}^0$ is the chemical potential of silica in the standard state, namely silica glass. If Eq. (14) is differentiated at constant temperature, re-arranged and the appropriate substitutions made, then we obtain:

$$\left(\frac{\partial \log a_{SiO_2}^{liquid}}{\partial P}\right)_T = \frac{\overline{V}_{SiO_2} - V_{SiO_2}^0}{2.303\ RT} \tag{15}$$

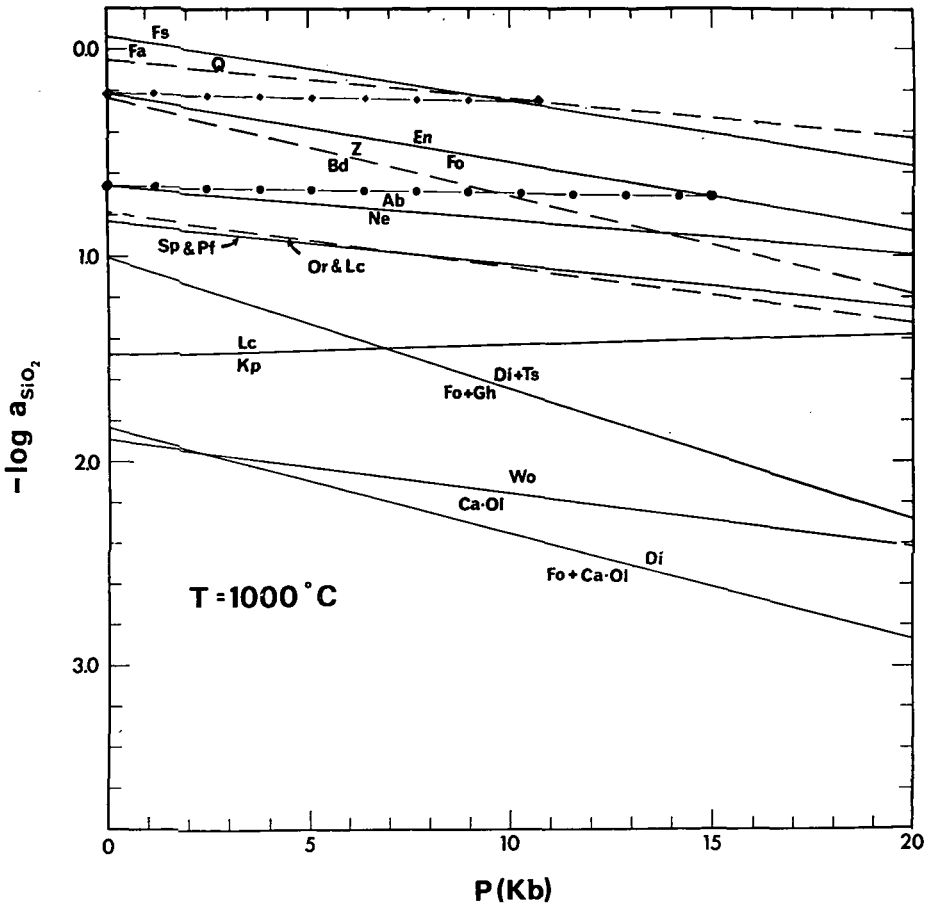

Fig. 2. The variation of $\log a_{SiO_2}$ with pressure at 1000°C for the mineral buffer reactions shown in Fig. 1. Note that all have negative slopes except for the Kp-Lc curve. The two dotted curves refer to the variation of $\log a_{SiO_2}$ as a function of pressure $(\overline{V}_{SiO_2} - V^0_{SiO_2})$ $(P-1)/2.303$ RT in the absence of a silica buffer

where V^0 is the molar volume of pure silica glass, and $\overline{V}$ is the partial molar volume of SiO_2 in the silicate liquid or magma. Again we assume that the volumes are independent of pressure, so that Eq. (15) can be integrated at constant temperature to give:

$$(\log a^{\text{liquid}}_{SiO_2})^{P=P\text{ bars}} = (\log a^{\text{liquid}}_{SiO_2})^{P=1\text{ bar}} + \frac{\overline{V}_{SiO_2} - V^0_{SiO_2}}{2.303\,RT}(P-1). \quad (16)$$

Bottinga and Weill (1970) have evaluated the partial molar volumes, $\overline{V}$, of many oxide components in liquid silicate systems for a large range of composition and temperature. Least-squares analysis of their data for $\overline{V}_{SiO_2}$ over the temperature range 1250°–1600°C gives:

$$\overline{V}_{SiO_2} = 2.573 \times 10^{-4}\,T(°K) + 26.37 \text{ c.c. mole}^{-1}$$

which with change of units (to cal. bar^{-1}) and substitution of $V^0_{SiO_2}$ gives:

$$\frac{\bar{V} - V^0}{2.303\,RT} = 1.34 \times 10^{-6} - \frac{0.0047}{T}. \quad (17)$$

By substitution of Eq. (17) into Eq. (16), we obtain:

$$(\log a^{liquid}_{SiO_2})^{P=P\ bar} = (\log a^{liquid}_{SiO_2})^{P=1\ bar} + \left[1.34 \times 10^{-6} - \frac{0.0047}{T}\right](P-1). \quad (18)$$

Two hypothetical examples of the determination of P_{total} are shown in Fig. 2. Let us suppose that a basaltic lava has a glassy groundmass which was quenched at 1000°C and 1 bar, and $\log a^{liquid}_{SiO_2}$ is -0.219 (Fig. 2). The effect of pressure on $\log a^{liquid}_{SiO_2}$ at 1000°C using Eq. (18) is shown by the upper dotted curve in Fig. 2 assuming that a silica buffer is not present. This curve intersects the Quartz curve at 10.8 kilobars, so that the hypothetical basaltic liquid, at constant temperature and constant composition, would be saturated with quartz at pressures in excess of 10.8 kilobars. As another example, assume that a phonolitic lava is quenched at 1000°C on the surface to an assemblage of glass with microlites of nepheline and albite; then $\log a^{liquid}_{SiO_2}$ would be equal to -0.629 (Fig. 2). In the absence of a silica buffer, i.e., either nepheline or albite (or both) disappears, then $\log a^{liquid}_{SiO_2}$ will vary with pressure (Eq. 18) as shown by the lower dotted line in Fig. 2. A phonolitic liquid at 1000°C would therefore be in equilibrium with forsterite and enstatite at a pressure of 15 kilobars.

Before applying these equations to actual examples with measured mineral compositions, it is necessary to digress into the relationship between the activity, a, of a component in a solid solution, and the mole fraction, X, of that component. Williams (1971) has given the following equations relating activity to composition for olivines and the calcium-poor pyroxenes.

$$\log a_{FeSiO_3} = 0.22\,(1 - X_{FeSiO_3})^2 + \log X_{FeSiO_3},$$
$$\log a_{MgSiO_3} = 0.22\,(1 - X_{MgSiO_3})^2 + \log X_{MgSiO_3},$$
$$\log a_{FeSi_{0.5}O_2} = 0.16\,(1 - X_{Fe_2SiO_4})^2 + \log X_{Fe_2SiO_4},$$
$$\log a_{MgSi_{0.5}O_2} = 0.16\,(1 - X_{Mg_2SiO_4})^2 + \log X_{Mg_2SiO_4}.$$

He indicates that these equations apply in the temperature range 900–1400°C and for pressures up to 10 kilobars. These equations contrast to the ideal mixing relationship ($\Delta H_{mix} = 0$) which for calcium-poor pyroxenes would be $X_{FeSiO_3} = a_{FeSiO_3}$ and for olivines, $a_{Mg_2SiO_4} = X^2_{Mg_2SiO_4}$, the squared term arising from an assumed random entropy of mixing on two lattice sites.

As an example of the application of William's equations, and their contrast to the ideal mixing relationship for olivine, we will use the mineral data obtained by Brown (1971) on a ugandite lava (U.111). The groundmass contains kalsilite (0.95 Kp), leucite (0.99 Lc), olivine (0.13 Fa), ilmenite and titanomagnetite (0.346 Mt). Using Buddington and Lindsley's (1964) curves, the co-existing iron-titanium oxides give an equilibration temperature of 990°C and $\log f_{O_2}$ of -11.2. Substitution of the kaliophilite-leucite data into Eq. (9a) gives a value for $\log a^{liquid}_{SiO_2}$ of -1.457 at 990°C. Substitution of the relevant mole fractions and f_{O_2} into Eq. (10a) at the same temperature gives a value of $\log a_{SiO_2}$ of -1.457

Table 2. *Values of P_{total} for quartz bearing acid lavas*

Locality and sample No.	$X_{Fe_2SiO_4}$	X_{FeSiO_3}	$T°$ C	$\log f_{O_2}$	$X_{Fe_3O_4}$	P_{total} (a = Williams) kilobars	P_{total} ($a = X$ or X^2) kilobars	P_{H_2O}[a] bars
Arran, Scotland (AC.7)	0.879	—	900	−12.9	0.442	5.62	5.44	—
Pantelleria (3112)	0.862	—	1025	−11.2	0.236	7.53	7.28	—
Mono Craters, California								
Cam. 73	0.893	—	810	−14.7	0.564	3.45	3.33	—
Cam. 99	0.893	—	790	−15.1	0.588	3.62	3.50	—
Cam. 86	—	0.629	940	−11.1	0.577	9.25	7.71	—
Cam. 93	—	0.630	960	−10.9	0.573	7.45	6.19	—
Cam. 95	—	0.664	850	−13.2	0.590	7.64	6.48	—
Lassen Peak, California								
Cal. 19	—	0.293	865	−10.9	0.844	7.83	2.61	265
Talasea, New Britain								
196	—	0.35	920	−10.5	0.768	4.94	0.30	—
279B	—	0.30	860	−11.5	0.802	3.82	−1.29	—
Taupo Region, New Zealand								
P30411	—	0.45	745	−14.6	0.783	9.58	6.77	1800
P30407	—	0.45	740	−14.6	0.783	9.58	6.77	1650
P28360	—	0.45	735	−15.2	0.752	6.12	3.32	1500
P27574	—	0.45	780	−13.6	0.755	8.91	5.99	—
P27575	—	0.447	755	−14.6	0.744	6.99	4.11	—
P27576	—	0.412	760	−14.1	0.758	8.24	4.97	—
P27580	—	0.408	755	−14.4	0.752	6.49	3.19	—
P27573	—	0.45	770	−14.0	0.752	8.55	5.66	—
P27579	—	0.45	750	−15.0	0.729	4.68	1.84	—
Average of calc-alkaline rhyolites						6.82	4.27	—

[a] P_{H_2O} has been calculated from f_{H_2O} using the tables of Burnham *et al.* (1969); f_{H_2O} was not corrected for P_{total}, which is equal to $P\Delta V_{solids}$ and is small.

for the ideal mixing assumption for olivine, and of −1.215 if the William's formulation is used. This descrepancy does not of necessity require that the William's equations are in error, but rather that the assumed ideal mixing of the titanomagnetite taken together with the ideal mixing assumption of olivine is a better way of approximating the mixing relationships of these two solid solutions; in other words the errors involved in the assumption for olivine are balanced by those for titanomagnetite. Hereafter we use the ideal mixing relationship for all solids unless the William's equations are specified for the olivine and calcium-poor pyroxene components.

The other assumptions used in the later part of the paper are as follows:

(i) The partial molar volume of any component in it's respective solid solution series is independent of composition.

(ii) A magma quenched on the surface ($P = 1$ bar) can exist as a liquid of identical composition at some depth in the crust or mantle.

(iii) The chemical potential of silica, μ_{SiO_2} is fixed at any temperature and pressure by the presence of a silica-buffer. Although the concept of the chemical potential does not require a liquid phase, we have to assume that a liquid was present in order to estimate the change of μ_{SiO_2} with pressure, Eq. (18).

(iv) Most temperatures have been estimated by using the equilibration temperatures of the coexisting iron-titanium oxides (Buddington and Lindsley, 1964); in several cases, inspired guesses have been made.

In the next two examples of calculating P_{total}, we do not have to take into account the effect of temperature on silica activity in a magma. This effect will be considered later.

Acid Lavas with Quartz Phenocrysts

Many acid lavas, particularly obsidians, contain phenocrysts of quartz together with a fayalitic olivine or an orthopyroxene, ilmenite and titanomagnetite. It is reasonable to assume that these phenocrysts crystallised at the same time, especially as they are often present in only small amounts, so that the values of temperature and oxygen fugacity (f_{O_2}) derived from the composition of the iron-titanium oxides can be assumed to apply to the whole phenocryst assemblage. By substituting $\log f_{O_2}$ and the relevant mineral data into either Eqs. (10a) or (11a), we obtain a value for $\log a_{SiO_2}^{liquid}$ at the iron-titanium oxide equilibration temperature and at P bars total pressure. This must be equal to $\log a_{SiO_2}^{liquid}$ given by Eq. (2) (Table 1) as quartz and the other phenocrysts are in equilibrium; the equations are illustrated below for a fayalite-pitchstone from Scotland (AC.7) using William's equations (p. 7) for the olivine. The mineral compositions are taken from Table 2.

$$(\log a_{SiO_2}^{liquid})^{P\text{ bars, }1173^\circ K} = \underbrace{\frac{8270}{1173} - 2.81 - \frac{0.0552}{1173}(P-1) + \log a_{Fe_2SiO_4}^{olivine} + \frac{1}{3}\log f_{O_2} - \frac{2}{3}\log a_{Fe_3O_4}}_{\text{Eq. (10a), Table 1.}} \quad (19)$$

$$= +0.0695 - \frac{0.0552}{1173}(P-1) = -\underbrace{\frac{309}{1173} + 0.183 - \frac{0.0239}{1173}(P-1)}_{\text{Eq. (2), Table 1.}}$$

$$P_{total} = 5.62 \text{ kilobars.}$$

We have tabulated in Table 2 the calculated values of P_{total} for a variety of acid lavas, the mineral data having been taken from Carmichael (1967a); Ewart *et al.* (1971) and Lowder (1970). We have given two values for P_{total} for each rock, one calculated on the ideal mixing assumption, and the other using William's equations (p. 7).

The values for P_{total} are systematically lower if the ideal mixing expression for activities is used in Eqs. (10a) and (11a), but the writers have no way of evaluating which set of data are more correct; we tend to believe the William's set here but we have no check in the rocks themselves on his activity expressions as we did in the ugandite lava (p. 7).

The data show that all the rhyolites equilibrated at less than 30 kilometres, with the one peralkaline rhyolite, a pantellerite, having an intermediate value of P_{total}. In four cases, values of P_{H_2O} are known, derived either from the occurrence of biotite or in the case of the three New Zealand rhyolites from the phenocryst assemblage of orthopyroxene, cummingtonite, and quartz (Ewart *et al.*, 1971). In all cases, P_{H_2O} is much lower than P_{total}, as has been suspected by petrologists for many years.

It is obvious from the Quartz curve in Fig. 2 that a typical acid magma precipitating quartz at a depth equivalent to an average of about 6 kilobars, will become unsaturated with quartz at lower pressure at constant temperature. Presumably this explains the resorbed or embayed quartz phenocrysts so common in acid lavas.

Many rhyolites do not contain phenocrysts of quartz, so that values of P_{total} derived from Eqs. (10a) and (11a) in conjunction with Eq. (2) will give minimum values of P_{total}. Two Icelandic rhyolites from Thingmuli have an average P_{total} of 4.19 kilobars, while a mildly peralkaline obsidian from another locality (Oraefi) indicates a minimum value of 7.58 kilobars.

Kimberlites

Nixon *et al.* (1963) have given a splendid account of the mineralogy of the Basutoland kimberlites which we use to estimate P_{total} for these rocks. A typical kimberlite contains olivine, diopside, perovskite, and ilmenite with substantial amounts of $MgTiO_3$ (giekielite). In addition, Nixon *et al.* report zircon with an outer rim of baddeleyite (ZrO_2) so that the crystallisation path must have cut the Bd-Z curve (Fig. 2) at some pressure and temperature; we have assumed a temperature of 1327°C (1600°K).

The major mineral components of a kimberlite can be represented by the following reaction

$$\underset{\beta\text{-perovskite}}{CaTiO_3} + \tfrac{1}{4}\underset{\text{fayalite}}{Fe_2SiO_4} + \tfrac{3}{4}\underset{\text{forsterite}}{Mg_2SiO_4} + \underset{\text{glass}}{SiO_2} = \tfrac{1}{2}\underset{\text{ilmenite}}{FeTiO_3} + \tfrac{1}{2}\underset{\text{giekielite}}{MgTiO_3} + \underset{\text{diopside}}{CaMgSi_2O_6}*$$

which can be recast to:

$$(\log a_{SiO_2}^{\text{liquid}})^{P\text{ bars}} = \Delta G^0/2.303\,RT + \frac{\Delta V^0}{2.303\,RT}(P-1) + \log \frac{(a_{CaMgSi_2O_6}^{\text{pyroxene}})\cdot(a_{FeTiO_3}^{\text{ilmenite}})^{\frac{1}{2}}\cdot(a_{MgTiO_3}^{\text{ilmenite}})}{(a_{\beta\text{-}CaTiO_3}^{\text{perovskite}})\cdot(a_{Fe_2SiO_4}^{\text{olivine}})^{\frac{1}{4}}\cdot(a_{Mg_2SiO_4}^{\text{olivine}})^{\frac{3}{4}}}. \quad (20)$$

Obviously the value of $\log a_{SiO_2}$ derived from Eq. (20) must be equal to that of Eq. (4a) for that point in the kimberlite crystallisation path where zircon was replaced by baddeleyite. Representative mineral data taken from Nixon *et al.* (1963) are olivine = 0.92 Fo ilmenite = 0.58 $FeTiO_3$; giekielite = 0.30 $MgTiO_3$; diopside = 0.60 $CaMgSiO_6$ and the value taken for perovskite (0.87) is the average analysis given by Smith (1970). Using the free-energy and molar volume data of Robie and Waldbaum (1968), Eq. (20), with substitution of the relevant mineral data, becomes:

$$(\log a_{SiO_2}^{\text{liquid}})^{P=P\text{ bars}} = -0.5253 - \frac{0.0338}{1600}(P-1). \quad (21)$$

* Note that this equation involves cubic β-perovskite with a molar volume of 0.79766 cal.-bar^{-1} and fayalite whose ΔG_f^0 of the solid was extrapolated to 1600°K.

Eq. (21) is set equal to Eq. (4) (assuming unit activity for both zircon and baddeleyite), the value of which (Table 1) is given below in Eq. (22).

$$\underbrace{(\log a_{SiO_2}^{liquid})^{P=P\ bars}}_{Eq.\ (21)} = -0.0375 - \frac{0.0478}{1600}(P-1). \quad (22)$$

Solution for P gives a value of 55.7 kilobars for the pressure at which baddeleyite replaces zircon at 1327°C in a kimberlite. It is now assumed that either perovskite or ilmenite disappeared at higher pressure and that the liquid at 1327°C and 55.7 kilobars was present at the stage of diamond formation (Kennedy and Nordlie, 1970); then by using the analyses of Meyer and Boyd (1969, 1970) for the olivine (0.92 Fo) and orthopyroxene (0.94 En) inclusions in diamond, a value for P_{total} can be calculated. We can state that

$$(\log a_{SiO_2}^{liquid})^{P=diamond} = (\log a_{SiO_2}^{liquid})^{P=Bd\text{-}Z\ eqlm.} + \left[1.34\times10^{-6} - \frac{0.0047}{T}\right](P - P^{Bd\text{-}Z}). \quad (23)$$

where the right hand side is obtained from Eq. (18); the value of $(\log a_{SiO_2}^{liquid})^{P=Bd\text{-}Z\ eqlm.}$ is taken from either Eq. (21) or (22) at 55.7 kilobars and equals −1.7015. Thus the right hand term of Eq. (23) becomes

$$(\log a_{SiO_2}^{liquid})^{P=diamond} = -1.7015 + \left[1.34\times10^{-6} - \frac{0.0047}{1600}\right](P - 55700). \quad (24)$$

The left-hand side of Eq. (23) is obtained from Eq. (3a) (Table 1) and if the values for the olivine and enstatite inclusions are inserted gives

$$(\log a_{SiO_2}^{liquid})^{P=diamond} = -0.0306 - \frac{0.0424}{1600}(P-1). \quad (25)$$

At equilibrium, with Eq. (24) set equal to Eq. (25), we obtain a value of 63.5 kilobars for the pressure at the stage of diamond formation. For pressures of this magnitude, mineral compressibilities, or the variation of ΔV with pressure, should be taken into account, if the information were available. Despite this, these values of P_{total} are in accord with the various speculations on kimberlite which have recently been summarised by MacGregor (1970).

The Effect of Temperature on a_{SiO_2}

One of the principal applications of the method for determining P_{total} is to lavas quenched on the earth's surface. If a silica buffer assemblage is present in the groundmass, then $\log a_{SiO_2}^{liquid}$ can be determined at the quenching temperature. However it is unlikely that a lava was ever in equilibrium with mantle material at the quenching temperature, so that knowing $\log a_{SiO_2}^{liquid}$ at one temperature, it is necessary to calculate it at some higher temperature, and then calculate the effect of pressure using Eq. (18).

The appropriate thermodynamic relationship analogous to Eq. (15) is

$$\left(\frac{\partial \log a_{SiO_2}}{\partial T}\right)_P = \frac{-\bar{H}_{SiO_2} + H^0_{SiO_2}}{2.303\,RT^2} \quad (26)$$

where $\bar{H}_{SiO_2}$ is the partial molar enthalpy of silica in the silicate liquid, and $H^0_{SiO_2}$ is the molar enthalpy of silica in the standard state (glass).

However there is no data, at least available to writers, on $\bar{H}_{SiO_2}$ in silicate liquids. So we have attempted to estimate the effect of temperature on a_{SiO_2} by using two sets of experimental results on lavas.

For an andesite, Green and Ringwood (1968) report that quartz appears on the liquidus at 1240°C (1513°K) and 18 kilobars, and in the same composition at 1330°C (1603°K) and 27 kilobars. If it is assumed that the co-precipitation of the other minerals with quartz changed the liquid composition by the same amount in each case, then by using Eq. (2) we can calculate $\log a_{SiO_2}^{liquid}$ at each temperature and pressure. Thus

$$(\log a_{SiO_2}^{liquid})^{1513°,\ 18000\ bars} = \frac{-309}{1513} + 0.183 - \frac{0.0239}{1513}(18000) = -0.3055 \quad (27)$$

and

$$(\log a_{SiO_2}^{liquid})^{1603°,\ 27000\ bars} = \frac{-309}{1603} + 0.183 - \frac{0.0239}{1603}(27000) = -0.4122. \quad (28)$$

If these values are corrected back to 1 bar using Eq. (18), in this way;

$$(\log a_{SiO_2}^{liquid})^{P=1\ bar} = (\log a_{SiO_2}^{liquid})^{P} + \left[1.34 \times 10^{-6} - \frac{0.0047}{T}\right](1-P) \quad (29)$$

we obtain -0.2738 and -0.3692 respectively. The difference between the two values, 0.0954, is taken to result from a temperature rise of 90°.

Therefore $$\frac{\Delta \log a_{SiO_2}^{liquid}}{\Delta T} = \frac{-0.0954}{90} = -10.60 \times 10^{-4} T^{-1}.$$

Similar reasoning for an olivine-tholeiite (Green and Ringwood, 1967) with a similar temperature range (110°C) gives a value of $\frac{\Delta \log a_{SiO_2}^{liquid}}{\Delta T} = -15.18 \times 10^{-4} T^{-1}$.

We follow a time honoured principle, and take the average of the two results, so that

$$(\log a_{SiO_2}^{liquid})_P^{T_2} = (\log a_{SiO_2}^{liquid})_P^{T_1} - 0.001289\,(T_2 - T_1). \quad (30)$$

We are now in a position to calculate P_{total} for any lava if we know $\log a_{SiO_2}^{liquid}$ at 1 bar and any temperature.

Trachybasalts of Southern California

In the eastern Mojave desert, there are a series of Recent lavas of trachybasalt which contain phenocrysts of olivine and pyroxene, together with a residual glass with substantial amounts of normative nepheline (Smith and Carmichael, 1969). In two of these lavas 253 and 256, olivine, titanomagnetite and ilmenite are also found as groundmass constituents; the iron-titanium oxide equilibration temperatures are given below together with the appropriate mineral data.

Sample	$X_{Fe_2SiO_4}$	T°C	$\log f_{O_2}$	$X_{Fe_2O_4}$	$\log a_{SiO_2}^{liquid}$ at 1 bar
253	0.320	980	−11.7	0.323	−0.7724
256	0.275	995	−11.4	0.320	−0.8794

Substitution of the relevant mineral compositions into Eq. (10a) gives values for $\log a_{SiO_2}$ at 1 bar for the two lavas at their respective temperatures.

In the Dish Hill cinder cone of this volcanic field there are abundant lherzolite nodules whose constituent minerals have been analysed by White (1966). Let us assume that these lavas could have been at a temperature of 1300°C, and then calculate the P_{total} at which they could have been in equilibrium with these nodules.

Using Eq. (30), we first calculate $\log a_{SiO_2}^{liquid}$ at 1300°C and 1 bar. For lava No. 253, a value of -1.1849 is obtained. Then at 1300°C, the variation of $\log a_{SiO_2}^{liquid}$ with pressure will be given by Eq. (18) (Table 1). Thus

$$(\log a_{SiO_2}^{liquid})_{1573}^{P=P\text{ bars}} = -1.1849 + \left[1.34\times10^{-6}\frac{-0.0047}{1573}\right](P-1). \qquad (31)$$

In the lherzolite nodules, $\log a_{SiO_2}^{liquid}$ is defined by the assemblage of olivine and orthopyroxene. Typical values for the composition of these minerals are 0.899 Fo and, for the orthopyroxene, 0.889 En; $\log a_{SiO_2}^{liquid}$ for the lherzolite can be calculated from Eq. (3a). Thus

$$\begin{aligned}(\log a_{SiO_2}^{liquid})^{P=P\text{ bars}} &= (\log a_{SiO_2}^{liquid})^{P=1\text{ bar}} \\ &+ \frac{\Delta V^0}{2.303\,RT}(P-1) + \log a_{Fo} - 2\log a_{En}\end{aligned} \qquad (32)$$

which from Table 1, and substituting the mineral data becomes

$$= \frac{-1034}{T} + 0.597 - \frac{0.0424}{T}(P-1) - 0.0098. \qquad (33)$$

If Eq. (33) is set equal to Eq. (31), it can be solved for P. Below we have given the values of P_{total} for each of the two lavas, firstly calculated at 1300°C, and secondly at the quenching temperature, thus assuming that the lavas have not cooled since equilibrating with the lherzolite nodules.

	1300°C	Quenching T^0C
253	44.0 kilobars	17.0 kilobars
256	47.5 kilobars	21.0 kilobars

These calculated results are not far from those obtained by Green and Hibberson (1970) who found that the near-liquidus orthopyroxenes of an alkali olivine-basalt (no normative nepheline) at 1200°C and 14 to 16 kilobars was similar in composition to it's orthopyroxene "xenocrysts".

Ugandite Lavas

These are potassic lavas from the African rift valley, whose mineral compositions (Brown, 1971) have already been noted on page 7. Log $a_{SiO_2}^{liquid}$ at 990°C and 1 bar was calculated to be -1.457 irrespective of whether Eq. (9a) or (Eq. (10a) was used. The lavas contain nodules of biotite-olivine-pyroxenite, or dunite with small amounts of biotite (Combe and Holmes, 1945). As yet orthopyroxene has

not been found either in the nodules or as xenocrysts in the lavas. However we will assume that these lavas were in equilibrium at some pressure with a generalised mantle assemblage of olivine (0.90 Fo) and orthopyroxene (0.85 En). Presumably the absence of orthopyroxene indicates that these estimates of P_{total} will be maximal, for at all lower pressures orthopyroxene of En_{85} composition will be unstable.

If Eq. (3a) is taken in conjunction with Eq. (18), then P_{total} can be obtained assuming a constant temperature of 990°C. If on the other hand the lava is considered to have cooled since leaving the mantle, then using Eq. (30) we can calculate another value for P_{total}. The results for U.111 are: 38.0 kilobars at 990°; 69.0 kilobars at 1300°C. The latter P_{total} value is not dissimilar to that calculated for kimberlite at the same temperature, which is not unsuspected, as many petrologists believe the two rock-types to be genetically connected.

Leucite Hills, Wyoming

Orendite lavas contain leucite and sanidine in the groundmass and may contain phenocrysts of olivine (ca. 0.90 Fo) or olivine with a reaction rim of phlogopite (Carmichael, 1967b). As co-existing iron-titanium oxides are absent in this suite of lavas, it is not possible to derive a temperature at which they were quenched on the surface. However as their solidus temperatures are close to, or above 1050°C, and as they often contain only small amounts of phenocrysts, it has been arbitrarily assumed that the groundmass was quenched at 1100°C. Sl is a jumillite lava from Spain, and of allied composition. Substitution of the leucite-sanidine mineral data, tabulated below, into Eq. (7a) gives $\log a_{SiO_2}^{liquid}$ at 1100°C and 1 bar, which is then substituted into Eq. (18). Although orthopyroxene phenocrysts have not been found to accompany olivine phenocrysts in the Leucite Hills lavas, we have assumed that if they did occur they would have the composition 0.85 En. Substitution of the olivine and orthopyroxene data into Eq. (3a), and its equality to the appropriate data in Eq. (18), will allow P_{total} to be calculated. A parallel calculation gives P_{total} if the lavas are assumed to have equilibrated at 1300°C with an olivine-orthopyroxene assemblage. The results are shown below.

Table 3

Sample	$X_{Leucite}$	$X_{Sandine}$	T° C	$(\log a_{SiO_2}^{liquid})^{1\ bar}$	P_{total} at 1100° C	P_{total} at 1300° C
Sl	1.000	0.903	1100	−0.7912	20.3 kilobars	37.1 kilobars
LH3-13	0.965	0.980	1100	−0.7396	18.5 kilobars	35.1 kilobars
LH-10	0.965	0.979	1100	−0.7406	18.6 kilobars	35.1 kilobars
LH-11	0.965	0.983	1100	−0.7388	18.5 kilobars	35.0 kilobars
LH-15	0.965	0.981	1100	−0.7407	18.6 kilobars	35.1 kilobars

Phonolitic Trachytes

Two kenytes from Antarctica described by Carmichael (1964) contain phenocrysts of anorthoclase enclosed by a glass with infrequent crystals of nepheline. The composition of the nepheline (0.593 Ne) suggests a temperature of about

800°C (Hamilton, 1961) and the alkali feldspar microlites have a composition of 0.464 Ab. Substitution of this mineral data into Eq. (6a) (Table 1) gives a value for $\log a_{SiO_2}^{liquid}$ at 800°C and 1 bar of −0.8340. The problem is to calculate P_{total} at which the anorthoclase phenocrysts (0.646 Ab) were in equilibrium with nepheline of groundmass composition. As nepheline did not in fact co-precipitate with the anorthoclase phenocrysts, the calculated P_{total} will be a minimum estimate, and at all higher pressures nepheline of that particular composition will be unstable. Solution of Eqs. (18) and (6a) for a kenyte (1910 — 199) gives a P_{total} value of 4.20 kilobars; the parallel calculation for 1000°C gives a value of P_{total} of 31.3 kilobars. The rather large difference between these two results for a temperature rise of 200°C, reflects the rather shallow slope of the Ab–Ne curve in Fig. 2 in comparison to the Fo–En curve.

Basic Lavas with Quartz "Xenocrysts"

Many of the basalts or basaltic-andesites associated with volcanism along the continental margins contain resorbed crystals of quartz with coronae of pyroxene grains. Examples are found in the 1851 and pre-1851 eruptions of Lassen Peak, California (Smith and Carmichael, 1968) and in Talasea, New Britain, lavas (Lowder and Carmichael, 1970), but in neither case do the Sr^{87}/Sr^{86} ratios give any indication of the incorporation of silicic material (Peterman *et al.*, 1970a, b). As the groundmass mineral compositions of these lavas are known, and assuming a quenching temperature of 1000°C, the pressure at which these lavas would be saturated with quartz can be calculated. Eq. (3a) gives a value for $\log a_{SiO_2}^{liquid}$ at 1 bar, which is inserted into Eq. (18) which in turn is equated to Eq. (2) and solved for P. The Lassen basalt gives a value of 14.3 kilobars, and the Talasea basaltic-andesite a value of 16.0 kilobars.

If a temperature of 1100°C is assumed to be the temperature at which these basalts equilibrated at depth, then the calculated values of P_{total} are 24.9 kilobars and 26.8 kilobars respectively. The so-called quartz "xenocrysts" may in fact be stable at elevated pressures, and cognate in the same way as more widely recognised high-pressure pyroxene phenocrysts in lavas (e.g., Binns *et al.*, 1970).

Basaltic Liquids and the Mantle

Many basalts show evidence either in their xenoliths or their phenocrysts of having come from the mantle, or having been in a higher pressure environment. Thus it is interesting to calculate P_{total} for these lava suites, assuming, as before, that they equilibrated with a mantle made up of olivine (0.90 Fo) and orthopyroxene (0.85 En). One example is the iron-rich tholeiitic series of Thingmuli in eastern Iceland (Carmichael, 1964). These lavas commonly have liquidus temperatures near 1100°C (Carmichael, 1967) and we shall assume, as before, that if they did equilibrate with the mantle they did so at a temperature of 1300°C. The calculations indicate that a basaltic-andesite and an olivine-tholeiite would equilibrate at 11.1 and 15.6 kilobars respectively. At their liquidus temperatures, this suite of basic lavas would become saturated with quartz over a range of 5.95 to 13.4 kilobars, and must therefore have acquired their 1 bar silica activity, or composition, at depths corresponding to lower pressures.

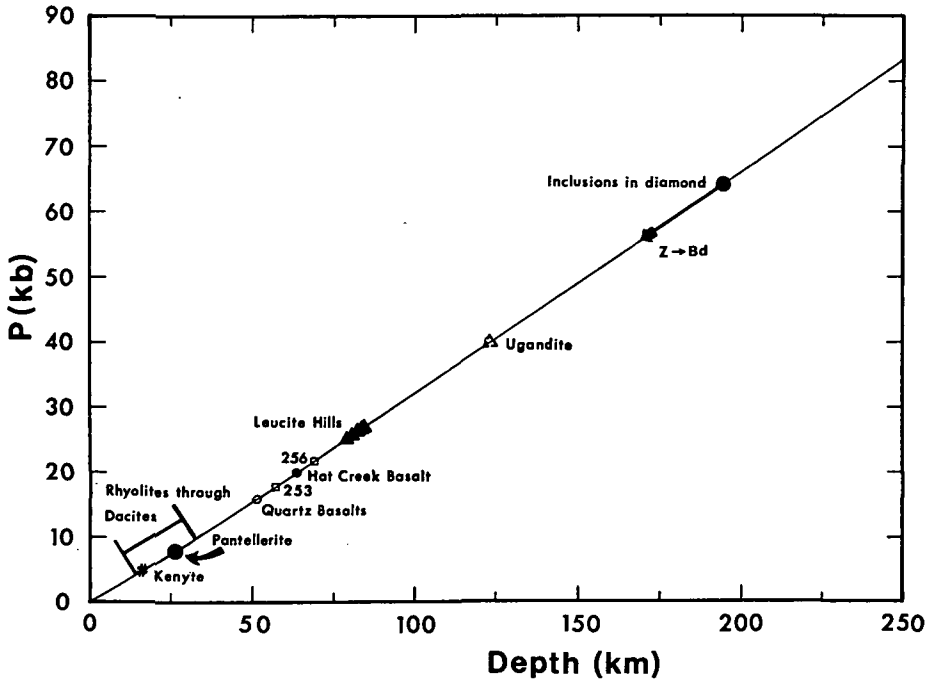

Fig. 3. The calculated values of P_{total} plotted against depth for the rock types described in the text at their quenching temperatures. 253 and 256 refer to two trachybasalts from southern California; Quartz-Basalts represents one sample from Lassen, California, and one from Talasea, New Britain; P_{total} (at 1327°C) for inclusions in diamond and Z-Bd (zircon-baddeleyite) refer to kimberlite

An olivine-bearing high-alumina basalt from the Lassen region, California, (Hat Creek) (Smith and Carmichael, 1968) would become saturated with quartz at 47.6 kilobars at it's liquidus temperature (1050°C) and at 1300°C would be in equilibrium with our generalised mantle composition at 40.2 kilobars.

In Fig. 3 we have plotted the calculated P_{total} for all the rocks described above, which can be equated to depths using Birch's (1964) depth-pressure curve. All the plotted points are derived from the actual quenching temperatures, rather than the assumed temperature of 1300°C which we have used to calculate the total pressure for equilibration with a generalised mantle composition. The general trend is for liquids of low-silica activity to equilibrate with a particular limiting reaction at greater depths than those lavas with high silica activities. We may note in passing that the calcium-content of olivine becomes diminished with increasing pressure at constant temperature (Fig. 2, lowest curve), so that as more plentiful and accurate data becomes available (e.g., Simpkin and Smith, 1966), the calcium content of olivine could be used as an indication of P_{total} in a wide variety of rocks.

Andesites and the Benioff Zone

Dickinson (1968) and Hatherton and Dickinson (1969) have shown that a correlation exists between the potassium content of andesites and basaltic-andesites

and the depth to the underlying Benioff zone. This correlation has become so widely accepted that maps are now being made of the configuration of the Benioff zone, one example being the Great Basin of western north America (Lipman *et al.*, 1971). The low velocity zone of the upper mantle lies approximately between 90 and 180 kilometres, and Hatherton and Dickinson (1969, Fig. 1) envisage this region, or it's intersection with the Benioff zone, to be the source of andesite magma or it's precursor. It is obviously informative to calculate P_{total} for an andesite lava in equilibrium with a generalised mantle composition of olivine (0.90 Fo) and orthopyroxene (0.85 En). Presumably an andesite lava (ca. 60% SiO_2) will have a value of $\log a_{SiO_2}^{liquid}$ between that defined by the Fo–En and Quartz curves in Fig. 1; we will take a value of -0.200 at 1000°C, a plausible quenching temperature for this type of lava. By using Eq. (30), we can calculate $\log a_{SiO_2}^{liquid}$ at 1300°C or 1400°C, again a reasonable estimate of the temperature at which an andesite magma could be in equilibrium with the mantle composition. The calculated values are 18.8 kilobars (1300°C) and 27.0 kilobars (1400°C) using Eq. (3a) (Table 1). Allowing for a small variation in mantle mineralogy and uncertainty of the precise value of $\log a_{SiO_2}^{liquid}$ in an andesite, an upper limit of perhaps 25 kilobars at 1300°C is reasonable. Andesites therefore equilibrate with mantle material at depths of 75 kilometres or less (Fig. 3) and at all greater depths, the andesite liquid must change in composition, or lower it's silica activity, to remain in equilibrium with the mantle.

Magmas generated at greater depths will tend to be more basaltic than andesitic, and the continued equilibration of an andesite precursor at depths between perhaps 200 kilometres and 75 kilometres may generate, by fractionation of crystalline phases which reject K_2O, the requisite increase in K_2O shown by Hatherton and Dickinson (1969) if indeed the Benioff zone is the source of the parent magma of andesite.

If magma of *andesite* composition is generated at depths greater than 75 kilometres (Green and Ringwood, 1968) then in order to maintain it's composition it will have to be segregated from the surrounding mantle. At pressures above 42.3 kilobars (1300°C) or 55.7 kilobars (1400°C), this andesite magma will become saturated with quartz. It is apparent from the density data of Bottinga and Weill (1970), that there may sufficient density contrast for quartz to sink in an andesite magma. The distribution of quartz "xenocrysts" in island arc volcanic suites with low Sr^{87}/Sr^{86} ratios could be a productive study of magma history at depth.

Lunar Basalts (Apollo 11)

Brown (1970) has provided a concise summary of the mineralogy of the lunar basalts collected by Apollo 11 and also a few preliminary comments on the Apollo 12 basalts. There are, in the Apollo 11 basalts, striking mineral incompatibilities, one for example, being the occurrence of perovskite and plagioclase, which has never been found to coexist in terrestrial lavas (Carmichael *et al.*, 1970). Other examples are the occurrence of cristobalite, perovskite and baddeleyite which are unstable at all pressures and temperatures (Figs. 1 and 2); baddeleyite and perovskite are only stable above 37 kilobars at 1000°C (Fig. 2). It seems not unlikely that these basalts are partly a mechanical mix of incompatible phases,

so that it is facile to accept the vast amount of chemical data on these basalts as indicative of a magma with the same composition as the lavas.

However silica activity can be used to give estimates of T, f_{O_2} and the rather thorny problem of the existence of an Fe_2O_3 component in these basalts. We start with the occurrence of fayalite (1.00 Fa) and pyroxferroite (0.85 Fs) in the groundmass of a lunar basalt (Brown, 1970, p. 6487). Substitution of this data into Eq. (1) at 1 bar (Table 1) gives a value for $\log a_{SiO_2}^{liquid}$ which must be equal (at 1 bar) to that defined by Eq. (2) (cristobalite has been substituted for quartz as the solid phase); the solution for T gives a value of 1009°C.

The value of $\log a_{SiO_2}$ obtained from either Eq. (1) or Eq. (2) at 1009°C is substituted in the following reaction

$$\underset{\text{iron}}{2Fe} + O_2 + \underset{\text{glass}}{SiO_2} = \underset{\text{fayalite}}{Fe_2SiO_4} \tag{34}$$

which re-arranged gives

$$\log f_{O_2} = \Delta G^0/2.303\,RT + \log a_{Fe_2SiO_4}^{olivine} - \log a_{SiO_2}^{liquid} - 2\log a_{Fe}^{iron}. \tag{35}$$

By using a value of $\Delta G^0/2.303\,RT$ at 1009°C (1282°K) taken from Eugster and Wones (1962), corrected for silica glass, and substituting $\log a_{SiO_2} = -0.0840$, $a_{Fa} = 1$, and $a_{Fe} = 1$, gives $\log f_{O_2} = -15.18$.

If a_{SiO_2}, f_{O_2}, and a_{Fa} are now substituted in the following reaction

$$Fe_3O_4 + \tfrac{3}{2}SiO_2 = \tfrac{3}{2}Fe_2SiO_4 + \tfrac{1}{2}O_2 \tag{36}$$

or

$$\log a_{Fe_3O_4}^{magnetite} = \Delta G^0/2.303\,RT + \tfrac{3}{2}\log a_{Fe_2SiO_4}^{olivine} + \tfrac{1}{2}\log f_{O_2} - \tfrac{3}{2}\log a_{SiO_2} \tag{36a}$$

a value of $a_{Fe_3O_4}$ is obtained. The value calculated is 0.0099, which is equivalent to 0.99% Fe_3O_4 in the spinel phase if ideal mixing is assumed. This in turn gives approximately 0.68% Fe_2O_3 in the spinel phase, or if the basalt contained 15% of this iron-titanium oxide, approximately 0.10% Fe_2O_3 in the rock. Most analytical chemists would shy away from reporting such small quantities of Fe_2O_3 in the presence of so much FeO (~19%), particularly with metallic iron as a component.

Conclusion

In all the calculations of P_{total} we have assumed that the composition of the lava or magma remains constant. To what extent this is true of the major components is unknown, but certainly many lavas are likely to lose water as they approach the surface and crystallise on it. It is at least possible that a magma at depth may only differ substantially from one at the surface by an increased amount of water. Experimental work on silicate systems, particularly the granite system (Tuttle and Bowen, 1958) indicates that increasing the water content of a silicate liquid increases a_{SiO_2}; in other words liquid compositions which crystallise feldspar as the initial phase when dry, crystallise quartz as the initial phase when the liquid contains water. Thus the calculated values of P_{total} for rhyolites will be *decreased* if their water component increases with depth. For basaltic magmas, increasing the water content may have the opposite effect. The data on the system diopside-forsterite-silica (Kushiro, 1969) shows that water ($P_{H_2O} = 20$ kilobars) causes the migration of the Fo–En boundary curve to higher silica contents compared to

the same boundary with dry liquids at 20 kilobars. Although the effect of water on silica activity is difficult, if not impossible, to evaluate, in principle it appears that one way a basaltic liquid of otherwise constant composition could remain in equilibrium with the mantle over a range of pressures is to increase it's water content as it migrates towards the surface.

Acknowledgements. The authors are indebted to NSF (GA-11735), NASA (NGR05-003-414) and NRC of Canada A-7372, for material support. The computation of the heat capacity data (Table 1) was enormously helped by the use of one of Professor Helgeson's programs. The last author also acknowledges the support of an NSF graduate fellowship.

References

Binns, R. A., Duggan, M. B., Wilkinson, J. F. G.: High-pressure megacrysts in alkaline lavas for north-eastern New South Wales. Am. J. Sci. **269**, 132–168 (1970).

Birch, F.: Density and composition of mantle and core. J. Geophys. Res. **69**, 4377–4388 (1964).

Bottinga, Y., Weill, D. F.: Densities of liquid silicate systems calculated from partial molar volumes of oxide components. Amer. J. Sci. **269**, 169–182 (1970).

Brown, F. H.: Volcanic petrology of Recent volcanic rocks in the Lake Rudolf region, Kenya. Unpublished Ph. D. thesis, University of California, Berkeley (1971).

Brown, G. M.: Petrology, mineralogy and genesis of lunar crystalline igneous rocks. J. Geophys. Res. **75**, 6480–6496 (1970).

Buddington, A. F., Lindsley, D. H.: Iron-titanium oxide minerals and synthetic equivalents. J. Petrol. **5**, 310–357 (1963).

Burnham, C. W., Holloway, J. R., Davis, N. F.: Thermodynamic properties of water to 1000°C and 10,000 bars. Geol. Soc. Am. Spec. Paper **132** (1969).

Carmichael, I. S. E.: Natural liquids and the phonolitic minimum. Geol. J. **4**, 55–60 (1964a).

— The petrology of Thingmuli, a Tertiary volcano in eastern Iceland. J. Petrol. **5**, 435–460 (1964b).

— The iron-titanium oxides of salic volcanic rocks and their associated ferromagnesian silicates. Contr. Mineral. and Petrol. **14**, 36–64 (1967a).

— The mineralogy and petrology of the volcanic rocks from the Leucite Hills, Wyoming. Contr. Mineral. and Petrol. **15**, 24–66 (1967b).

— The mineralogy of Thingmuli, a Tertiary volcano in eastern Iceland. Am. Mineralogist **52**, 1815–1841 (1967c).

— Nicholls, J., Smith, A. L.: Silica activity in igneous rocks. Am. Mineralogist **55**, 246–263 (1970).

Combe, A. P., Holmes, A.: The kalsilite-bearing lavas of Kabirenge and Lyakauli, southwest Uganda. Trans. Roy. Soc. Edinburgh **41**, 359–379 (1945).

Dickinson, W. R.: Circum-Pacific andesite types. J. Geophys. Res. **73**, 2261–2270 (1968).

Eugster, H. P., Wones, D. R.: Stability relations of the ferruginous biotite, annite. J. Petrol. **3**, 82–125 (1962).

Ewart, A., Carmichael, I. S. E., Brown, F. H., Green, D. C.: Voluminous low temperature rhyolitic magmas in New Zealand. Contr. Mineral. and Petrol. (in press).

Green, D. H., Hibberson, W.: Experimental duplication of conditions of precipitation of high-pressure phenocrysts in a basaltic magma. Phys. Earth Planet. Interiors **3**, 247–254 (1970).

— Ringwood, A. E.: The genesis of basaltic magmas. Contr. Mineral. and Petrol. **15**, 103–190 (1967).

Green, T. H., Ringwood, A. E.: Genesis of the calc-alkaline igneous rock suite. Contr. Mineral. and Petrol. **18**, 105–162 (1968).

Hamilton, D. L.: Nephelines as crystallization temperature indicators. J. Geol. **69**, 321–329 (1961).

Hatherton, T., Dickinson, W. R.: The relationship between andesitic volcanism and seismicity in Indonesia, the Lesser Antilles and other island arcs. J. Geophys. Res. **74**, 5301–5310 (1969).

Kelley, K. K.: High-temperature heat-content, heat-capacity, and entropy data for the elements and inorganic compounds. U.S. Bur. Mines Bull. **584** (1960).
— Heats and free-energies of formation of anhydrous silicates. U.S. Bur. Mines Rept. Invest. **5901** (1962).
Kennedy, G. C., Nordlie, B. E.: The genesis of diamond deposits. Econ. Geol. **63**, 495–503 (1968).
Kushiro, I.: The system forsterite-diopside-silica with and without water at high pressures. Am. J. Sci. **267**-A, (Schairer) 269–294 (1969).
Lipman, P. W., Prostka, H. J., Christiansen, R. L.: Cenozoic volcanism and plate-tectonic evolution of the western United States. Part I: Early and Middle Cenozoic. Trans. Roy. Soc. (London) (in press).
Lowder, G. G.: The volcanoes and caldera of Talasea, New Britain: Mineralogy. Contr. Mineral. and Petrol. **26**, 324–340 (1970).
— Carmichael, I. S. E.: The volcanoes and caldera of Talasea, New Britain: Geology and petrology. Bull. Geol. Soc. Am. **81**, 17–38 (1970).
MacGregor, I. D.: An hypothesis for the origin of kimberlite. Mineral. Soc. Amer. Spec. Pap. **3**, 51–62 (1970).
Meyer, H. O. A.: Inclusions in diamonds. Ann. Rept. Carnegie Inst. Washington Yr. Book **68**, 315–320 (1970).
— Boyd, F. R.: Mineral inclusions in diamonds. Ann. Rept. Carnegie Inst. Wash. Yr. Book **67**, 130–135 (1969).
Nixon, P. H., Knorring, O. von, Rooke, J. M.: Kimberlites and associated inclusions of Basutoland: a mineralogical and geochemical study. Am. Mineralogist **48**, 1090–1132 (1963).
Pankratz, L.: High temperature heat contents and entropies of dehydrated analcite, kaliophilite and leucite. U.S. Bur. Mines, Rept. Invest. **7201** (1968).
Peterman, Z. E., Carmichael, I. S. E., Smith, A. L.: Sr^{87}/Sr^{86} ratios of Quaternary lavas of the Cascade range, northern California. Bull. Geol. Soc. Am. **81**, 311–318 (1970a).
— Lowder, G. G., Carmichael, I. S. E.: Sr^{87}/Sr^{86} ratios of the Talasea series, New Britain, Territory of New Guinea. Bull. Geol. Soc. Amer. **81**, 39–40 (1970b).
Robie, R. A., Waldbaum, D. R.: Thermodynamic properties of minerals and related substances at 298.15°K (25.0°C) and one atmosphere (1.013 bars) pressure and higher temperatures. U.S. Geol. Surv. Bull. **1259** (1968).
Simpkin, T., Smith, J. V.: Minor element distribution in olivine. Geol. Soc. Am. Spec. Paper **203** (1966).
Smith, A. L.: Sphene, perovskite and co-existing Fe-Ti oxide minerals. Am. Mineralogist **55**, 264–269 (1970).
— Carmichael, I. S. E.: Quaternary lavas from the Southern Cascades, western U.S.A. Contr. Mineral. and Petrol. **19**, 212–238 (1968).
— — Quaternary trachybasalts from southern California. Am. Mineralogist **54**, 909–923 (1969).
Tuttle, O. F., Bowen, N. L.: Origin of granite in the light of experimental studies in the system $NaAlSi_3O_8$–$KAlSi_3O_8$–SiO_2–H_2O. Geol. Soc. Am. Mem. **74** (1958).
White, R. W.: Ultramafic inclusions in basaltic rocks from Hawaii. Contr. Mineral. and Petrol. **12**, 245–314 (1966).
Williams, R. J.: Reaction constants in the system FeO–MgO–SiO_2–O_2 at 1 atm. between 900° and 1300°C: Experimental results. Am. J. Sci. **270**, 334–360 (1971a).
— Equilibrium temperatures, pressures, and oxygen fugacities of the equilibrated chondrites. Geochim. et Cosmochim. Acta **85**, 407–411 (1971b).
Wones, D. R., Gilbert, M. C.: The fayalite-magnetite-quartz assemblage between 600°C and 800°C. Am. J. Sci. **267**-A, 480–488 (1969).

Professor Dr. I. S. E. Carmichael
Department of Geology and Geophysics
University of California
Berkely, California 94720, U.S.A.

D3

Reprinted from APPLIED OPTICS, Vol. 10, page 1904, August 1971
Copyright 1971 by the Optical Society of America and reprinted by permission of the copyright owner

Continuous Discharge Line Source for the Extreme Ultraviolet

F. Paresce, S. Kumar, and C. S. Bowyer

A continuous gaseous discharge source suitable for use between 100 Å and 1000 Å is described. The source is stable, produces little or no electromagnetic interference, and is rich in high intensity lines throughout the extreme uv. The operating characteristics of this source and its spectral output with various gases are presented.

Introduction

Because of the growing importance of the study of extreme uv radiation (xuv),[1-5] there is considerable interest in the development of high intensity radiation sources for this spectral range. A variety of sources have been proposed for these wavelengths,[6] most of which are subject to some limitations. This is especially true for sources intended for use below 500 Å. To produce radiation at these wavelengths, one usually must resort to pulsed discharge sources or magnetically constrained plasma sources, such as the duoplasmatron. A pulsed discharge source typically produces intense radio frequency background radiation. Experience has shown that to reduce this noise to tolerable levels, the entire source and all its associated circuitry must be placed inside a grounded metal cage. This obviously introduces mechanical limitations on its use.

The duoplasmatron source is mechanically rather complex and somewhat difficult to operate. For instance, the cathode must be reactivated each time it is exposed to air, a time-consuming process limiting the versatility of the device. A second drawback is that the entrance slit of the monochromator must be removed and replaced by a special source-slit combination. This operation entails a complex mounting and aligning problem for many monochromators.

An important factor to be considered in the design of a source suitable for use in any xuv calibration system is that the efficiencies of normal incidence monochromators decrease rapidly below 500 Å. Grazing incidence mounts can be employed at these wavelengths, but these typically employ rather complex movements of either the source or the detector, which introduces additional mechanical limitations. Monochromators such as the Seya-Namioka have the tremendous advantage of fixed entrance and exit slits combined with extremely simple scanning mechanisms. It is highly desirable, therefore, that the output of any xuv source be sufficiently intense that it can be used with this type of monochromator.

These considerations have led us to develop a high intensity continuous discharge source suitable for use at wavelengths below 500 Å. We note that similar motivations have prompted at least one other experimental group to develop an xuv source with many of the same characteristics as the one we describe here.[7]

Description of the Source

The source we have developed is similar in concept to the source described by Newburgh *et al.*,[8,9] but it is substantially different from that source in a number of important respects. An important feature of both of these sources is that the discharge is confined in such a manner that the negative glow of the gas discharge can be viewed directly. Most of the ionic line emissions are produced in this region and can, therefore, be observed with little or no absorption by intervening neutral gas in the positive column.

A schematic of the source is shown in Fig. 1. Both anode and cathode are constructed to allow for water cooling. The cathode is a hollow tube made of elkonite, a copper–tungsten alloy that has the advantages of a low sputtering rate and high heat conductivity and is easy to machine. The cathode has a 1-cm i.d. and a 2.5-cm o.d. The cathode tip, also of elkonite, is removable, allowing for experimentation with various types of geometries. The cathode is protected from erosion by ion bombardment by a thin quartz tube. The cathode is welded to a brass flange 8 cm in diam-

The authors are with the Astronomy Department and Space Sciences Laboratory, University of California, Berkeley, Calif. 94720.

Received 8 March 1971.

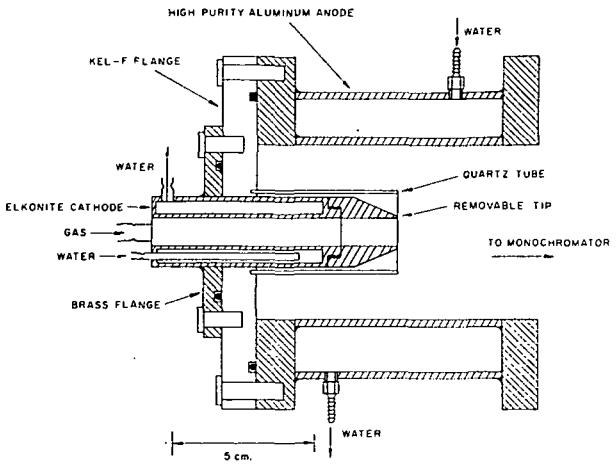

Fig. 1. Schematic diagram of the source.

eter, which is, in turn, sealed with an O-ring to a 12-cm diam Kel-F flange. This flange electrically isolates the cathode from the anode. The anode is a double-walled cylinder constructed of high purity 1100 aluminum alloy. In operation the source is buffered from the monochromator through a 5-cm long differential pumping stage.

The source is energized by a conventionally stabilized dc power supply run in series with an air-cooled ballast resistor bank of approximately 3-kΩ resistance. The discharge current can be varied between 50 mA and 800 mA at voltages between 500 V and 2000 V. To strike the discharge, up to 5000 V are required. For the highest discharge currents, water flow at a rate of 3 liters/min for the anode and of 1 liter/min for the cathode is found to provide adequate cooling.

We typically employ commercial grade gases (on the order of 0.01% impurities) with the source. The gas flow to the source is controlled by a precision needle valve assembly. Since the pressure within the source is nonuniform, it is somewhat meaningless to speak of a single source pressure. Nonetheless, the characteristics of the discharge are pressure dependent. Hence, it is necessary to specify this parameter in some manner. We chose to do this by specifying the pressure at a point in the differential pumping stage quite near the cathode tip. In normal operation the pressure at this point is between 10 Torr and 0.06 Torr. The corresponding pressure range measured at the inlet to the cathode is 50–0.2 Torr.

Spectroscopic Instrumentation

The source is mounted on a 1-m Seya-Namioka monochromator evacuated by a high speed diffusion pump. Under typical operating conditions the pressure in the monochromator varies between 5×10^{-5} Torr and 5×10^{-3} Torr, with the entrance slit 400 μ wide. The grating employed is a 1200 line/mm platinized concave grating blazed at 400 Å with a ruled area of 15 cm^2. The plate factor is approximately 6 Å/mm in the first order.

The radiation emerging from the exit slit of the monochromator is recorded by means of a channel electron multiplier (CEM) whose operating characteristics have been described elsewhere.[10] This detector is housed in an independently pumped chamber in

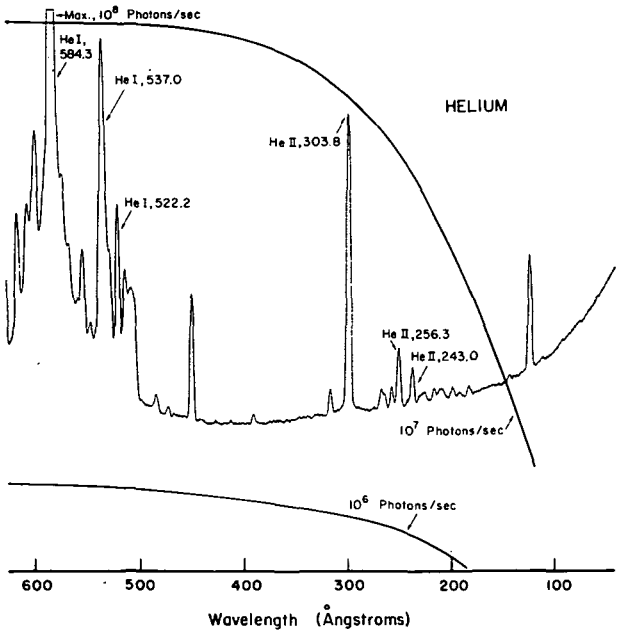

Fig. 2. Helium spectrum from the source. Operating conditions: entrance and exit slits 400 μ and 100 μ wide, respectively, discharge current 500 mA, pressure 1-mm Torr, scanning rate 50 Å/min, channel electron multiplier detector.

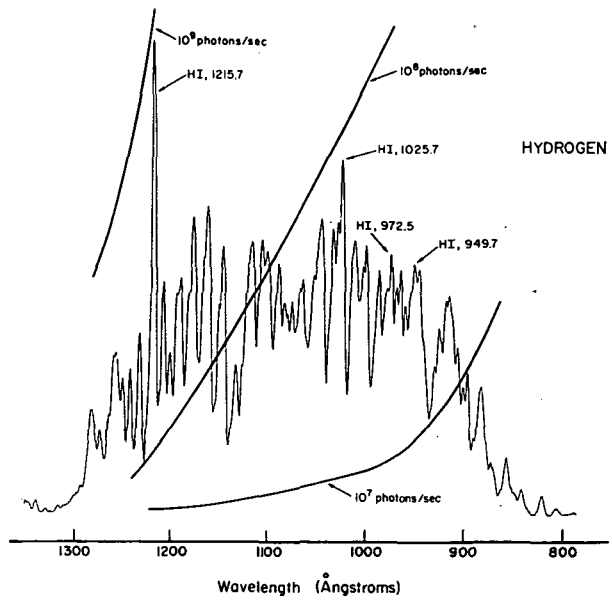

Fig. 3. Hydrogen spectrum from the source. Operating conditions: entrance and exit slits 400 μ and 100 μ wide, respectively, discharge current 500 mA, pressure 0.7 Torr, scanning rate 50 Å/min, channel electron multiplier detector.

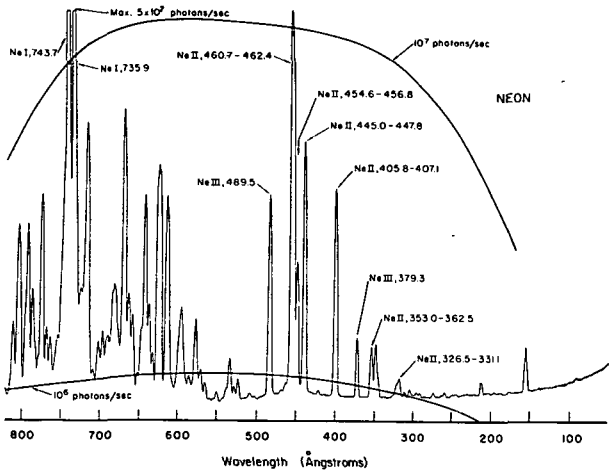

Fig. 4. Neon spectrum from the source. Operating conditions: entrance and exit slits 400 μ and 100 μ wide, respectively, discharge current 500 mA, pressure 0.8 Torr, scanning rate 50 Å/min, channel electron multiplier detector.

which the pressure is always kept below 10^{-5} Torr. The quantum efficiency of the channel electron multiplier is measured to an accuracy of $\pm 30\%$ by means of the gold photodiode technique described by Samson.[6] The output pulses of the CEM are fed to an electronic system consisting of a preamplifier, an amplifier–discriminator, and a linear ratemeter. The output of the ratemeter is fed to a conventional strip chart recorder.

Results and Discussion

Figures 2 through 5 show the output of the source with various gases. Because these spectra are recorded at relatively high speed (50 Å/min), a small distortion in the line widths and peak intensities is introduced. Intensity contours showing the photon flux at the exit slit are indicated. These contours take into account the measured wavelength sensitivity of the CEM, the distortion due to the scanning rate, and the position of the CEM with respect to the exit slit. The absolute intensity of these contour lines is known only to within $\pm 30\%$, the uncertainty in the CEM calibration.

Since no effort is made to purify the gases entering the source, many impurity lines are present in the spectra, most notably those of hydrogen, oxygen, and nitrogen. A number of unidentified lines also appear between 300 Å and 130 Å in the spectra of helium, argon, and neon. Various tests performed on these lines have shown that they are not due to discontinuities in the detector response nor to geometrical scattering processes. Tests by filter photometry show that the lines do, in fact, fall in the wavelength range from 100 Å to 300 Å. Since these lines appear to be characteristic of the gas and appear under all possible conditions of excitation, they probably originate in the reaction of the gas with some unknown impurity. At wavelengths longer than approximately 500 Å, second-order lines appear in the spectra. These are of lower intensities than the first-order lines because of the grating blaze

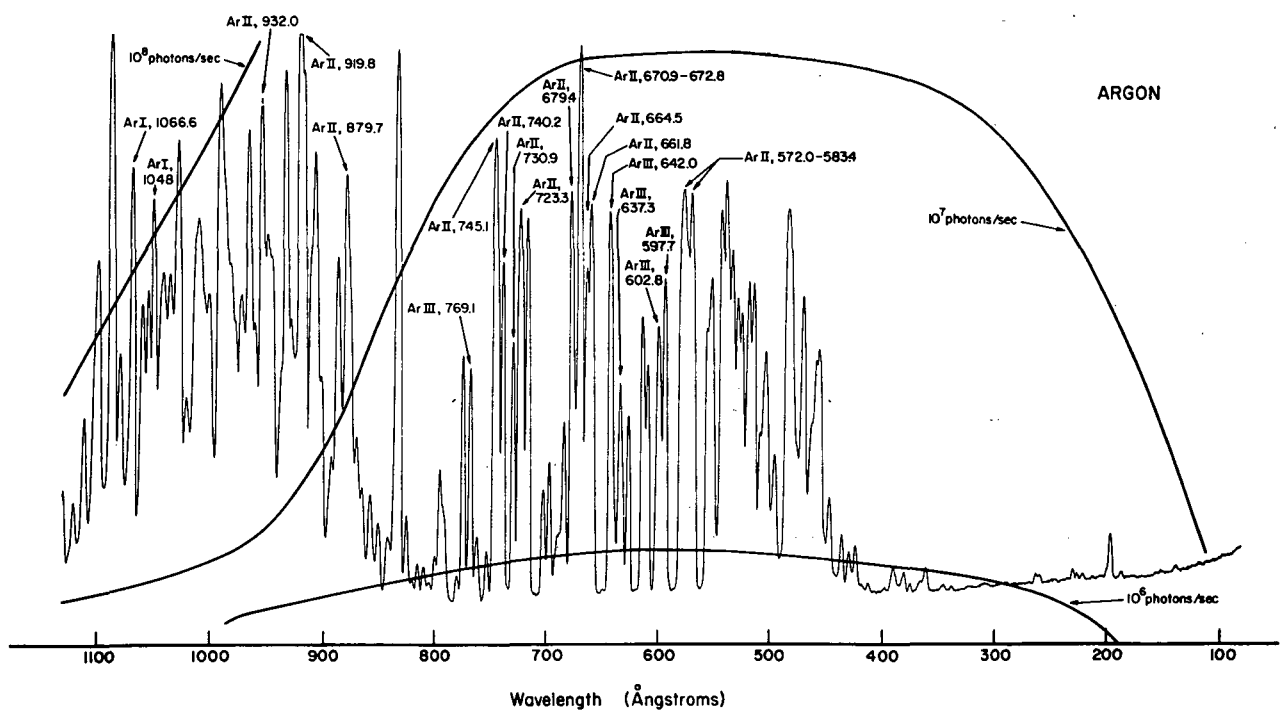

Fig. 5. Argon spectrum from the source. Operating conditions: entrance and exit slits 400 μ and 100 μ wide, respectively, discharge current 500 mA, pressure 0.7 Torr, scanning rate 50 Å/min, channel electron multiplier detector.

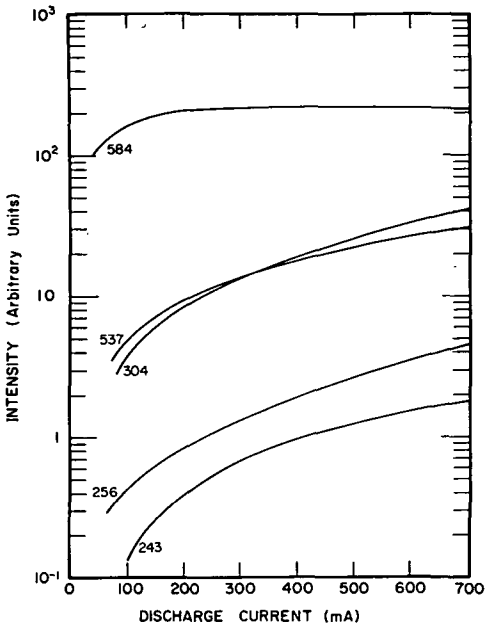

Fig. 6. Relative intensity of helium lines as a function of discharge current for a fixed pressure of 0.7 Torr.

and are easily eliminated by the use of xuv bandpass filters such as thin films of tin or indium.[10]

The radiation emitted by this source is seen to be rich in lines from neutral atoms as well as from singly and doubly ionized atoms. In this respect the source differs from typical capillary glow discharge devices and is instead more like the duoplasmatron source. In fact, a comparison with typical spectra obtained with a duoplasmatron shows that the two sources excite much the same lines. A direct comparison of the intensities of the two sources is unfortunately somewhat difficult to make because of different operating conditions among experimenters.

The output of the source is quite stable. We have made continuous runs for periods as long as 6 h and have observed no intensity changes larger than ±1%. The source also appears to be quite durable. In over 100 h of intermittent operation, we can see no indications of degradation in performance.

Parametric Studies of the Discharge

The intensity of the xuv radiation emitted by the source is found to be dependent upon both the pressure and the current in the discharge, and a number of helium lines were studied to evaluate the effects of changes in these parameters. The lines selected for this study were the He I lines at 584.3 Å and 537 Å and the He II lines at 303.8 Å and 256 Å. The results obtained are found to be generally similar to results obtained for other gases, so that the conclusions reached for helium are useful for deciding the optimum operating values for any gas.

In Fig. 6 we show the dependence of line intensity with discharge current. All line intensities are seen to increase with discharge current, although the 584-Å line quickly saturates. The ratios of 584-Å to 537-Å radiation and 304-Å to 256-Å radiation decrease with increasing discharge current toward a common value of approximately 5.

The increase in electron density and plasma temperature associated with an increase in the discharge current results in an increase of the population of excited states. This suggests that, as the discharge current is increased, a resonance line such as He 584 Å or He 304 Å will increase in intensity, saturate, then decrease slowly as an increasing fraction of the available energy is used in exciting other states. The increase in line intensities and decrease in line ratios [I (584 Å)/I (537 Å), I (304 Å)/I (256 Å), I (584 Å)/I (304 Å)] with increasing discharge currents and the slow decrease of the He I, 584-Å line at high discharge currents can all be reasonably attributed to this effect.

The behavior of the source with respect to changes in pressure is also instructive. We have plotted these data in Fig. 7. At low pressures the intensities of all lines are seen to increase with increasing pressure. The 584-Å line increases almost exponentially to a maximum value and thereafter decreases very slowly with further increase in pressure. The 537-Å line reaches a maximum at a much lower pressure and thereafter decreases slowly. Like the 584-Å line, it is not very pressure sensitive over most of the pressure range studied. The decrease of the intensity of the 304-Å line after attaining its peak value is much more precipitous. The 256-Å He II line behaves in a manner similar to the 304-Å line. It is clear that the ionic lines are extremely sensitive to pressure and that, to maximize their intensity, one must operate the source with low gas pressure and with high discharge currents.

The behavior of the line intensities as pressure is varied and is probably due to three distinct processes:

1. *Self-absorption.* This effect will become more important at higher pressures and is probably responsible for the slow decline in intensity of the 584-Å line at higher pressures.

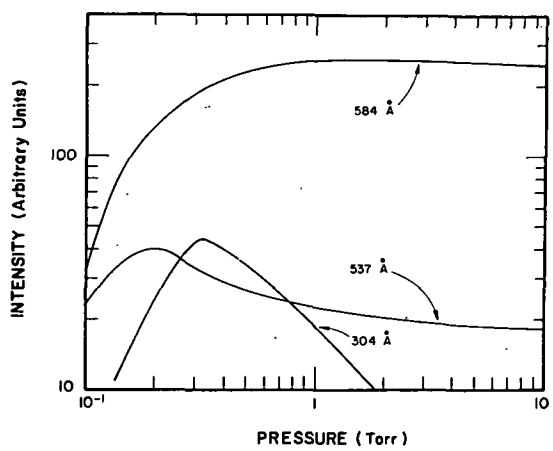

Fig. 7. Relative intensity of helium lines as a function of pressure for a fixed discharge current of 500 mA.

(2) *The decrease in the population of ionized constituents with increasing pressure.* This effect is predicted by the Saha equation and is probably primarily responsible for the rapid decrease of intensity of the 304-Å line.

(3) *Collisional de-excitation.* This phenomenon probably depopulates the excited 3^1P state through the process $He^* + He \rightarrow He_2^+ + e$ and produces the moderate decline in intensity of the 537-Å line with increasing pressure.

On the supposition that the shape of the electric field in the vicinity of the cathode would have a considerable effect on the source strength, a study was made of the effect of various tip geometries on the source intensity. This hypothesis appeared to be supported by our observation that the effect of particle bombardment on the quartz protective tube seemed to be limited to the tip of the cathode. To investigate this dependence, three types of cathode tip geometry were employed—one with the cathode cylinder wall beveled to a knife edge at the inside of the wall, one with the tip beveled to a knife edge at the outside of the wall, and the third with a simple thin-walled cylindrical geometry. The slight variations in the intensities (never exceeding 10%) are not significant enough to be clearly attributable to changes in the tip geometry. We also find that the source strength is generally insensitive to the length of the cathode.

Conclusions

The device described here possesses a number of advantages as a source of xuv radiation. It is simple and inexpensive to construct. It is easy to operate and is not a source of spurious electromagnetic radiation. The source output is very stable. A wide range of both ionic and neutral emission lines is produced with inexpensive and commonly available gases. The output spectrum is sufficiently intense that the source can be used with a Seya-Namioka monochromator at wavelengths as low as 160 Å.

This work was supported by the National Aeronautics and Space Administration under grant NGR 05-003-278. One of the authors (F. P.) was partially supported by a Fulbright Grant.

References

1. C. S. Bowyer, P. M. Livingston, and R. Price, J. Geophys Res. **66**, 2095 (1968).
2. J. M. Young, G. R. Carruthers, J. C. Holmes, C. Y. Johnson, and N. P. Patterson, Science **160**, 990 (1968).
3. F. Paresce, C. S. Bowyer, S. Kumar, and M. Lampton, Trans. Am. Geophys. Union **51**, 795 (1970).
4. C. S. Bowyer, M. J. S. Belton, M. Lampton, M. B. McElroy, W. Saslaw, and R. Poynter, "Final Report UV-Spectrometer/Photometer Science Advisory Team for 1973 Mercury/Venus Mission Design," Space Sciences Laboratory Series 11, Issue 24, 1970.
5. C. Y. Johnson, J. M. Young, and J. C. Holmes, Science **171**, 379 (1971).
6. J. A. R. Samson, in *Techniques of Vacuum Ultraviolet Spectroscopy* (Wiley, New York, 1967).
7. M. E. Levy and R. E. Huffman, Appl. Opt. **9**, 41 (1970).
8. R. G. Newburgh, L. Heroux, and H. E. Hinteregger Appl. Opt. **1**, 6 (1962).
9. R. G. Newburgh, Appl. Opt. **2**, 8 (1963).
10. C. S. Bowyer, F. Paresce, M. Lampton, and J. Mack, Planet. Space Sci. **18**, 835 (1970).

Ring Contraction in Molecular Ions of Acylated Alicyclic Amines as a Function of Ring Size

By W. J. RICHTER,* J. M. TESAREK,† and A. L. BURLINGAME

(*Space Sciences Laboratory, University of California, Berkeley, California* 94720, *U.S.A.*)

OPERATION of radical-induced ring contraction of molecular ions as a special mode of skeletal rearrangement has been proposed in a previous study of the mass spectrometric fragmentation of N-acetylmorpholine.[1] The unusual origin of the atoms involved in the formation of M–CH_3 and M–$COCH_3$ fragments was regarded as indicative of such an event. Implication of a carbon atom adjacent to nitrogen, together with a hydrogen atom from the neighbouring position, was demonstrated for the former fragment, while, for the latter, ejection of the N-acyl substituent as a single unit could be deduced. These findings were rationalized by assuming the following steps:

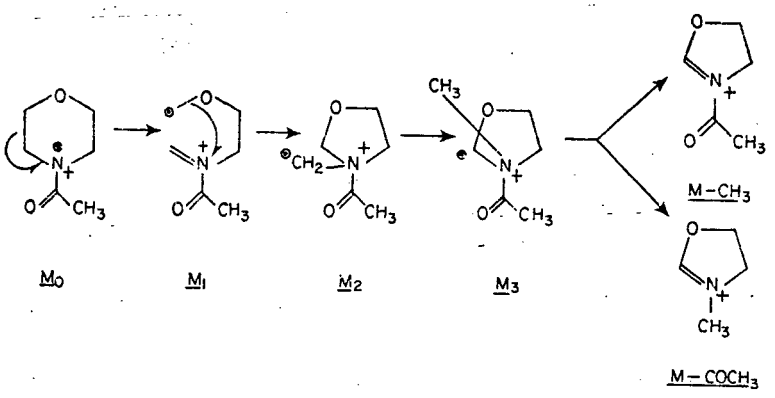

The presence of N-acyl substituents appears to be essential for operation of the process since free alicyclic amines commonly produce M–CH_3 fragments via loss of β- rather than α-carbon atoms and, furthermore, aliphatic acetamides form M–$COCH_3$ fragments via two-step elimination of α-hydrogen atoms and ketene. The selectivity with which a hydrogen atom is abstracted ($M_2 \rightarrow M_3$) from the newly generated α-position flanked by two heteroatoms (a β-position prior to ring contraction) was ascribed mainly to the fact that in this case a

* Present address: J. R. Geigy AG, Basel, Switzerland.

† Present address: Dept of Chemistry, University of North Carolina, Chapel Hill, N.C., U.S.A.

uniquely favourable type of product development control might facilitate the final step. Polar effects exerted by the oxygen donor atom might play an additional role in the preceding abstraction.

In order to delineate the general scope of ring contraction of acylated alicyclic amines in more detail, two basic modifications of the morpholine system have been examined in the present extension of this work: variation of ring size for confirmation of the underlying mechanistic rationale, and omission of the second heteroatom of the ring moiety to explore its role in effecting merely specific abstraction or in promoting final cleavage and the overall rate of the process as well. The obvious choice of model compounds to be selected in this context included N-acetylpiperidine (I), together with N-acetylpyrrolidine (II) and N-acetylhexamethyleneimine (III) as lower and higher homologues, respectively:

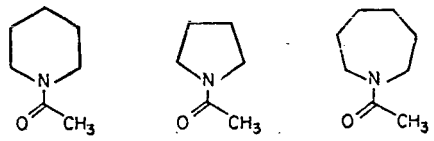

I II III

RING CONTRACTION IN N-ACETYLPIPERIDINE

Examination of this simple analogue of N-acetylmorpholine should permit one to draw conclusions as to whether and to what extent the presence of the second heteroatom in the ring moiety is responsible for its contraction, aside from effects upon specificity of hydrogen abstraction. If resonance stabilization of the product ions and product development control were to play a decisive role, ring contraction might in the absence of the oxygen atom still occur, but should be of lesser importance. Analysis for an expulsion of C–2 (C–6) instead of C–3 (C–5) as a methyl radical, and for loss of an intact acyl substituent in deuterated analogues is again used as a diagnostic tool for the recognition of comparable processes.

In addition to genesis via ring contraction (pathway *a*, loss of C–2), two other pathways for the formation of M–CH_3 fragments appear principally feasible: amine-triggered α-cleavage followed by hydrogen abstraction from an aza-allylic site, eventually leading to loss of a β-carbon atom together with an α′-hydrogen (pathway *b*, loss of C–3 or C–5), and simple cleavage within the acyl substituent eliminating a methyl radical from the N-acetyl group (pathway *c*, loss of C–8).

The mass spectrum of N-acetylpiperidine (I) displays an M–15 (M–CH_3) peak of approximately 15 per cent relative intensity, and the inspection of the spectra of several deuterium-labelled analogues (2,2-d_2-, 3,3-d_2-, 8,8,8-d_3-, 2,2,6,6-d_4-, 2,2,3,3-d_4-, 3,3,8,8,8-d_5-, and 2,2,6,6,8,8-d_7-N-acetylpiperidine) suggests the operation of all three processes. In the absence of C^{13}-labelling, accurate relative contributions cannot be readily determined due to local scrambling (posisions 2⇌6⇌8?) and complications from isotope effects of unknown magnitude and order. The scrambling effect should be eliminated or minimized in the fragmentation of 2,2,6,6,8,8,8-d_7-N-acetylpiperidine, which exhibits a split of the M–15 peak into M–16, M–17, and M–18 components, representing 42, 27, and 31 per cent group intensity, respectively. Neglecting isotope effects, ring contraction can be assumed to result in equal shifts to M–17 and M–18 (loss of C–2 or C–6), as approximately observed. Process *b* should not be subjected to primary isotope

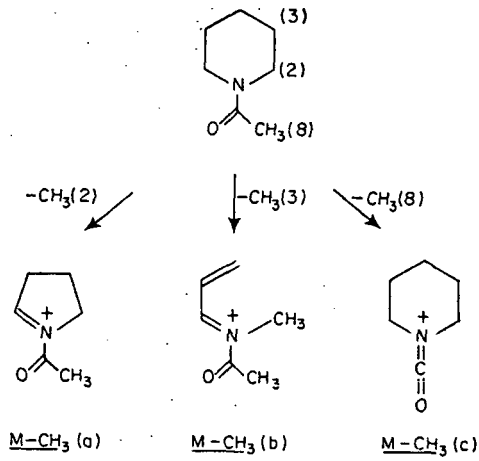

effects, due to the symmetry of the labelled positions, *i.e.* sites of abstraction, and thus exclusively produce M–CH_2D (=M–16) fragments. The products of process *c* (M–CD_3) should solely contribute to ion current at M–18. The slight preponderance of the M–18 peak over M–17 would consequently indicate a relatively minor contribution and thus lesser importance of the direct cleavage process, as opposed to a rather equal prominence of ring contraction and its alternative.

As in the case of N-acetylmorpholine, the loss of $COCH_3$ as an integral entity can likewise serve for diagnosis of intervention of ring-contracted intermediates in fragmentation of acylated alicyclic amines. Strong evidence for the expulsion of $COCH_3$ as a single unit (in addition to the common two-step loss of α-hydrogen and ketene) is provided by the spectrum of 8,8,8-d_3-N-acetylpiperidine, which exhibits shifts to M–45 (M–H–CD_2CO) and M–46 (M–$COCD_3$).

RING CONTRACTION IN LOWER AND HIGHER HOMOLOGUES

Ring contraction of molecular ions of N-acetylpyrrolidine (II) cannot be expected to represent a mode of fragmentation of major importance in view of the strained-four-membered cyclic intermediate to be traversed. The practical absence of a contraction process follows readily from the formation of the low abundance M–CH_3 fragment (2 per cent relative intensity) by means of simple cleavage of the CH_3–CO bond (loss of C–7 equivalent to process *c*). The M–43 fragment can be shown to arise[2] from a two-step loss of an α-hydrogen atom and ketene, with no contribution from its one-step/single unit alternative.

Contrary to this finding, the fragmentation of the seven-membered higher homologue of N-acetylpiperidine, N-acetylhexamethyleneimine (III), furnishes evidence of similar nature for an increased propensity toward ring contraction. Generally, it can be concluded from the data that omission of the oxygen atom as modification of the morpholine system reduces the importance of ring contraction in overall fragmentation, allowing competing processes to gain prominence. Increasing ring size, on the other hand, from six- to seven-membered systems seems to reverse this tendency substantially, lending strong support to the inference of ring contraction as a mechanistic rationale.

REFERENCES

1. Tesarek, J. M., Richter, W. J., and Burlingame, A. L. *Org. Mass. Spectrom.*, 1968, **1**, 139.
2. Duffield, A. M., and Djerassi, C. *J. Am. chem. Soc.*, 1965, **87**, 4554.

Discussion

R. T. Aplin (Dyson Perrins Laboratory, Oxford, U.K.): The *n*-butyl derivatives of both morpholine and thiomorpholine show the loss of methyl (CH_3) originating from the ring α-carbon atoms and one β-hydrogen.

Reprinted from

[redacted]

A74-15754

OMS Organic Mass Spectrometry
AN INTERNATIONAL JOURNAL

EDITOR-IN-CHIEF

PROF. ALLAN MACCOLL,
University College, 20 Gordon Street, London W.C.1

REGIONAL EDITORS

NORTH AMERICA

Prof. Robert H. Shapiro, *Department of Chemistry, University of Colorado, Boulder, Colorado* 80302

FRANCE

Dr. A. Cornu, *Commissariat a l'Énergie Atomique, Centre d'Études Nucléaires, Cedex No.* 85, *Grenoble* 38

JAPAN

Prof. Akira Tatematsu, *Faculty of Pharmacy, Meijo University, Showa-ku, Nagoya*

GERMANY

Dr. H.-Fr. Grützmacher, *Institut für Organische Chemie, der Universität,* 2 *Hamburg* 13, *Papendamm* 6

NETHERLANDS

Prof. G. Dijkstra, *Analytisch Chemisch Laboratorium der Rijksuniversiteit Utrecht, Croesestraat* 77a, *Utrecht*

AUSTRALASIA

Prof. J. S. Shannon, *Chemistry School, University of New South Wales, P.O. Box* 1, *Kensington, N.S.W.* 2033, *Australia*

USSR

Prof. N. K. Kochetkov, *N.D. Zelinsky Institute of Organic Chemistry, Academy of Sciences of the USSR, Moscow* B 334, *Leninsky prospect* 47

EDITORIAL ADVISORY BOARD

Dr. M. Barber, *A.E.I., Manchester*
Prof. H. D. Beckey, *University of Bonn*
Prof. J. H. Beynon, *Purdue University*
Prof. K. Biemann, *Massachusetts Institute of Technology*
Dr. H. Budzikiewicz, *Technische Universität, Braunschweig*
Dr. N. R. Daly, *A.W.R.E., Aldermaston*
Prof. C. Djerassi, *Stanford University*
Dr. H. W. Fehlhaber, *University of Bonn*
Prof. M. Fetizon, *University of Paris*
Dr. V. Hanus, *Czechoslovak Academy of Sciences, Prague*
Dr. W. Kelly, *Unilever Research Laboratory, Bedford*
Prof. F. W. McLafferty, *Cornell University*
Dr. A. Mandelbaum, *Technion, Haifa.*
Dr. S. Meyerson, *American Oil Company*
Prof. K. Nakanishi, *Columbia University*
Dr. R. I. Reed, *University of Glasgow*
Dr. K. D. Schuy, *Varian MAT, Germany*
Dr. D. H. Williams, *Cambridge University*

Publishing Offices: Heyden & Son Ltd., Spectrum House, Alderton Crescent, London N.W.4. (Tel. No. 01-202 5333). Published monthly. Subscriptions (including postage): (A) for libraries, university departments, research establishments and all other multiple-reader institutions; (B) for private subscribers ordering directly from the publisher certifying that the journal is for their personal use only:—

Vol. 3 1970	(A) UK Price	USA Price	German Price		(B) UK Price	USA Price	German Price
1 year	£22.15s.0d.	$ 55.00	DM220.00	1 year	£ 7.10s.0d.	$18.00	DM 72.00
2 years	£43.10s.0d.	$105.00	DM420.00	2 years	£14. 0s.0d.	$34.00	DM136.00
3 years	£64. 0s.0d.	$155.00	DM620.00	3 years	£20.10s.0d.	$50.00	DM200.00

Sets of Vols. 1 and 2 are available at £22.15s.0d., $55.00, DM220.00. (No reduced prices.)

Organic Mass Spectrometry, 1971, Vol. 5, pp. 1295 to 1306. Heyden & Son Limited. Printed in Northern Ireland

RING CONTRACTION UPON ELECTRON-IMPACT AS A FUNCTION OF RING SIZE: THE MASS SPECTROMETRIC FRAGMENTATION OF ACYLATED CYCLIC AMINES*

W. J. RICHTER,† J. M. BURSEY‡ and A. L. BURLINGAME
Department of Chemistry and Space Sciences Laboratory,
University of California, Berkeley, Ca. 94720, USA

(*Received* 28 *April* 1971; *accepted* 10 *June* 1971)

Abstract—The structural prerequisites of skeletal rearrangement by ring contraction, previously observed in N-acetylmorpholine, were explored by extending the study to N-acetylpyrrolidine, -piperidine and -hexamethyleneimine. Fragmentation via ring contraction was found to be absent in the five-membered ring, detectable in the six-membered ring, and significant in the seven-membered homologue. Ring contraction in these model compounds, i.e. in absence of oxygen as a second heteroatom in the cyclic moiety, is discussed in view of its implications and its support for an initially proposed radical-induced rearrangement mechanism.

INTRODUCTION

THE PROCLIVITY of suitable cyclic systems towards ring enlargement or ring contraction is a well-established phenomenon in solution chemistry, seemingly parallelled to some degree in mass spectrometric fragmentation. While ring expansion of simple aryl moieties to tropylium structures was revealed more than a decade ago,[1] instances of ring contraction have been reported only more recently. For example, ring contraction via carbonium ion rearrangement of highly substituted centres has been proposed[2] and experimentally supported[3] for the formation of an abundant acylium ion of mass 69 in the fragmentation of *trans*-Δ^3-10-methyl-2-octalone:

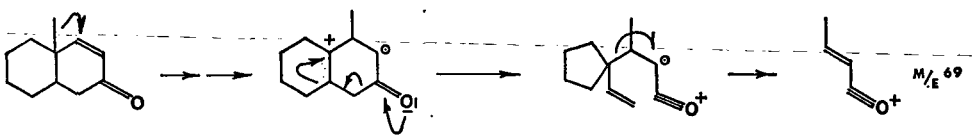

Radical-induced ring contraction of a cyclic system, as opposed to carbonium ion rearrangement, has been considered responsible[4] for the loss of an isopropyl radical from the molecular ion of $\Delta^{4(8)}$-menthene. Operation of a similar skeletal rearrangement in heterocyclic systems was subsequently proposed for the expulsion of a CH_2OH radical from 3-hydroxytetrahydropyran,[5] or more lately for the genesis of [M − CH_3] and [M − $COCH_3$] fragments from N-acetylmorpholine.[6] It was demonstrated that in the latter case expulsion of a methyl radical implicates a carbon atom adjacent to nitrogen together with a hydrogen atom from the neighbouring position, and furthermore that formation of the [M − $COCH_3$] species involves loss of the N-acetyl

* Paper taken in part from PhD Thesis, J. M. B. (J. M. Tesarek, University of California, Berkeley). Presented at the Triennial International Conference on Mass Spectrometry, Brussels, 31st August to 4th September 1970.

† To whom inquiries should be addressed. Present address: Ciba-Geigy AG, CH-4002 Basel, Switzerland.

‡ Present address: Department of Chemistry, University of North Carolina, Chapel Hill, NC 27514, USA.

substituent as a single unit rather than a two-step loss of ketene and a hydrogen atom from the ring:

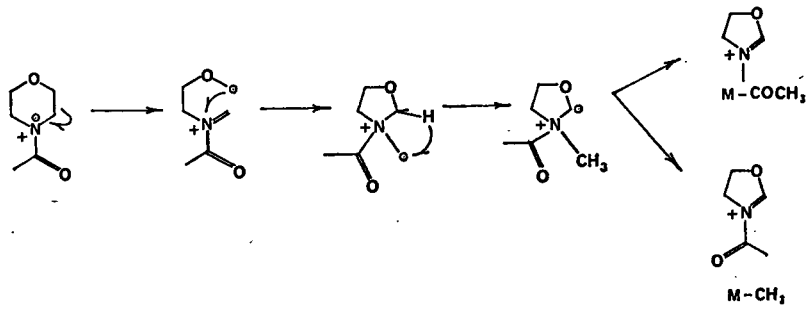

In order to determine the structural prerequisites of skeletal rearrangement by ring contraction in greater detail, two basic modifications of the morpholine moiety were explored in the present study with respect to the ease of the process: *replacement of the oxygen atom* of the ring moiety, and *variation of ring size.* The compounds selected accordingly include N-acetylpiperidine as the direct morpholine-analogue, as well as N-acetylpyrrolidine and N-acetylhexamethyleneimine as the next lower and higher homologues. As in the case of N-acetylmorpholine, analysis of the formation of [M − CH_3] and [M − $COCH_3$] fragments is employed to retrieve evidence for the operation of ring contraction in these compounds.

Ring contraction in N-acetylpiperidine

The mass spectrum of N-acetylpiperidine (I, Fig. 1) shows an [M − 15] peak (*m/e* 112) of approximately 15% relative intensity. Conceptually, two pathways other than the more complex genesis via ring contraction (loss of C-2 or C-6, process 1A) appear feasible for the formation of [M − CH_3] fragments: α-cleavage followed by hydrogen abstraction from an aza-allylic site, eventually leading to loss of a β-carbon atom (C-3 or C-5) together with hydrogen from an α′-position (process 1B), and simple cleavage effecting loss of C-8 as a methyl radical from the N-acetyl substituent (process 1C). These three processes have been investigated by means of deuterated N-acetylpiperidines.

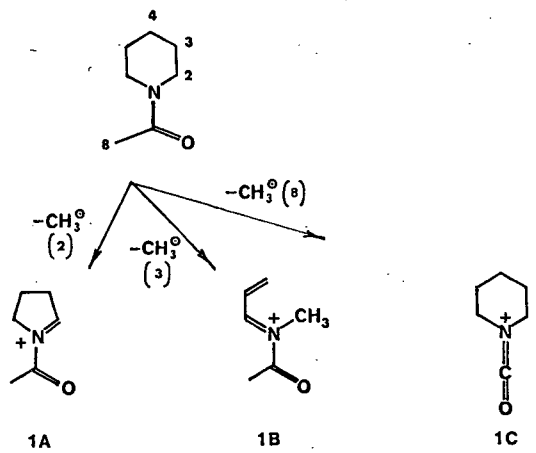

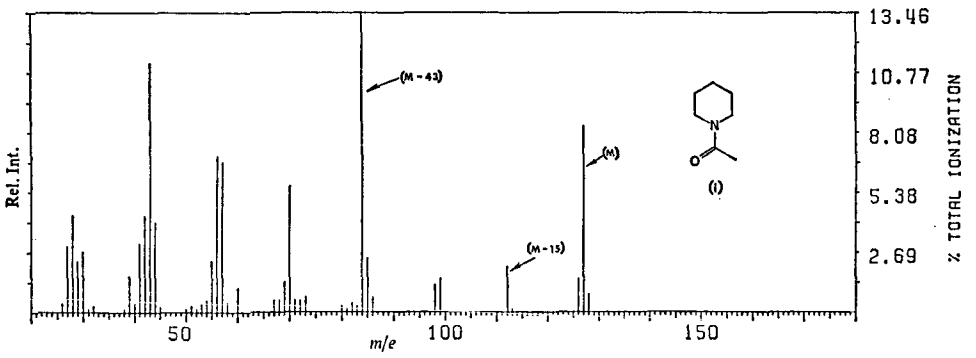

FIG. 1. Mass Spectrum of N-Acetylpiperidine (I).

The loss of a methyl group incorporating C-8 by direct cleavage (case 1C) is the chief source of [M — 15] fragments in N-acetylpyrrolidine,[7] the lower homologue of I, but has been shown to be of little importance in N-acetylmorpholine.[6] A certain prominence of such a process can be deduced for I from the labelled derivatives, in particular 8,8,8-d_3- and 3,3,8,8,8-d_5-N-acetylpiperidine (Ic and If, respectively). The observation of partial shifts to [M — 18] (loss of CD_3) constitutes compelling evidence for its occurrence (Fig. 2). Additional support for the operation of this process stems from the presence of an [M — 15] peak in the spectrum of

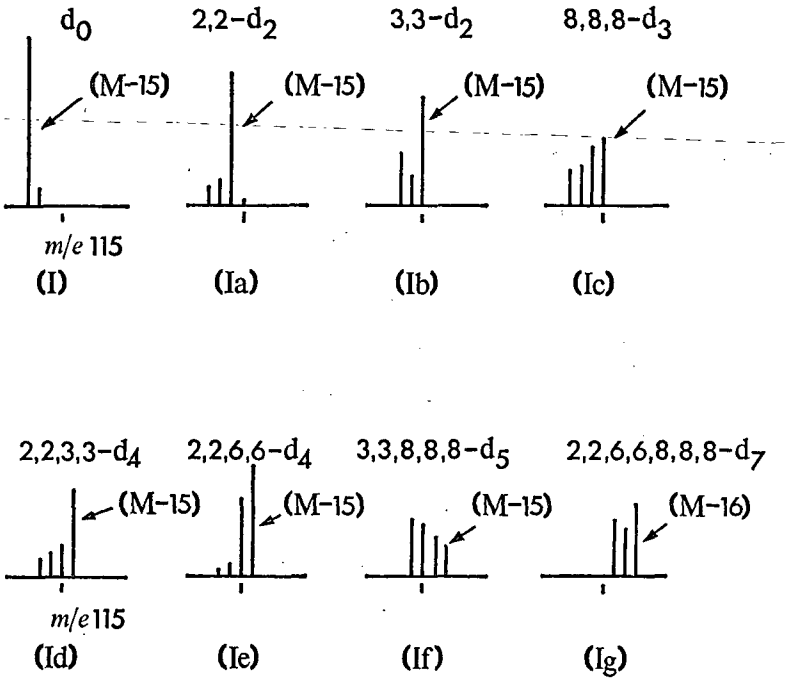

FIG. 2. Partial Mass Spectra ([M — 15] group) of Labelled Analogues (Ia to Ig) of N-Acetylpiperidine (I).

2,2,6,6-d_4-N-acetylpiperidine (Ie, Fig. 2) where contributions from other processes should be precluded.

The relative importance of amine-dominated fragmentation, as exhibited by piperidine itself (process 1B),[8] becomes readily apparent upon inspection of the spectrum of 3,3-d_2-N-acetylpiperidine (Ib, Fig. 2), where the observed [M − 17] peak should correspond to the ejection of a β-carbon atom.

Of more specific interest in the present context is the formation of an isomeric [M − CH_3] species via ring contraction of molecular ions by analogy to N-acetylmorpholine (process 1A). The actual occurrence of such a process can be inferred from a partial shift to [M − 16] in the spectrum of 3,3-d_2-N-acetylpiperidine (Ib, Fig. 2) due to the expulsion of α-carbon atoms in combination with hydrogen from a β-position. While the [M − 16] and [M − 17] peaks in this spectrum are each representative of only one competing alternative (process 1A and 1B, respectively) the portion of ion current recorded at [M − 15] is likely to include contributions from all three possible pathways: aside from the obvious contribution from direct cleavage (1C), loss of a β-carbon atom (1B) is a partial source of [M − 15] ions by virtue of the asymmetry of the label in contrast to the symmetry of the fragmentation process. The third mode of formation of [M − CH_3] fragments initiated by ring contraction (1A) can also be expected to contribute substantially to ion current at [M − 15] since the rearranged molecular species offer several equivalent choices for hydrogen abstraction:

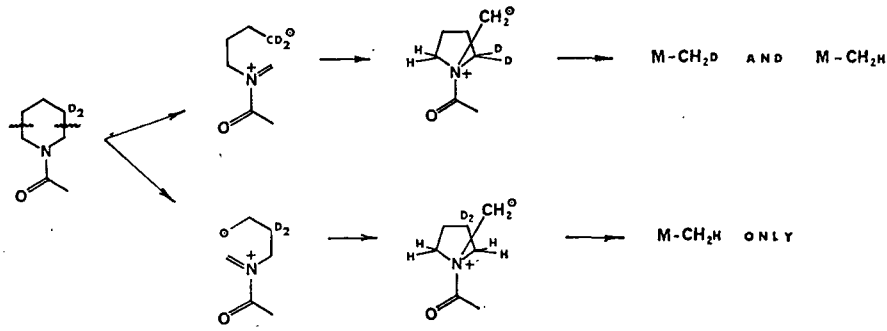

Assuming that positions adjacent to nitrogen in the two possible ring-contracted species are sites of preferential hydrogen abstraction (as in N-acetylmorpholine) the statistics of such abstraction could be expected to discriminate with a factor of three against the loss of deuterium. Operation of primary isotope effects, similar to those observed in the McLafferty rearrangement,[9] in the abstraction step would even enhance this discrimination.

In comparison to processes 1A and 1B, the importance of loss of methyl by direct cleavage (1C) appears minor, although accurate contributions cannot be readily determined, except by ^{13}C-labelling. Extensive exchange of hydrogen atoms between the acyl substituent and certain positions of the ring moiety in addition to isotope effects of unknown magnitude render assignments of relative contributions somewhat elusive. The effect of such exchange upon position 8 is clearly illustrated by the spectrum of 8,8,8-d_3-N-acetylpiperidine (Ic, Fig. 2) in which process 1C should be represented by a single peak at [M − 18] and the other two competitors 1A and 1B by a common single peak at [M − 15]. The presence of additional [M − 16] and

[M — 17] components definitely suggests loss of positional identity of the label, implicating C-8 and most likely carbon atoms adjacent to nitrogen, *e.g.* in the rearranged, cyclic molecular ions:*

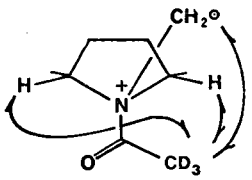

Not surprisingly, a peak group pattern closely related to that of Ic is encountered in the spectrum of 3,3,8,8,8-d_5-N-acetylpiperidine (If, Fig. 2), differing from Ic mainly in a greater weight of the [M — 18] and [M — 17] components due to process 1B. Complementary data are furnished by 2,2-d_2-N-acetylpiperidine (Ia) for which the [M — 15] component is unusually abundant. Loss of label from the ring into the acyl moiety (i.e. label distribution in the opposite direction) could explain this anomaly since under these conditions loss of methyl via 1A and 1B would not entail proportional loss of deuterium. Inspection of this peak group in the spectra of 2,2,6,6-d_4- and 2,2,3,3-d_4-N-acetylpiperidine (Fig. 2 Ie and Id, respectively) provides additional indication for an involvement of α-positions as preferential sites of exchange. Because of the apparently lesser involvement of β-positions, [M — 18] and [M — 17] peaks are of more prominence in the latter.

In order to eliminate the shortcomings of Ia to If with respect to quantitative assignments, but also to test the premise of label exchange between the indicated positions, 2,2,6,6,8,8,8-d_7-N-acetylpiperidine (Ig, Fig. 2) was prepared and analyzed. Since in this derivative the majority of the positions believed to undergo exchange are essentially saturated with label, this phenomenon should be largely suppressed and consequently errors of assignment minimized. In the spectrum of this compound, [M — 16] fragments should arise exclusively via 1B, demonstrating the true prominence of this mode of fragmentation. A comparable importance for ring contraction (1A) is borne out by the presence of [M — 17] (and [M — 18]) fragments. Statistically, a 1:1 ratio should be expected for these peaks as products of 1A, possibly enhanced in favour of [M — 17] as a result of isotopic discrimination against deuterium in the abstraction step. The slight preponderance of [M — 18] which is in fact observed would, of necessity, correspond to a relatively minor contribution of the direct-cleavage process 1C.

As in the case of N-acetylmorpholine, analysis for loss of $COCH_3$ as an integral entity in contrast to loss as ketene and hydrogen can serve as a supplementary diagnostic means for uncovering intervention of ring-contracted intermediates and products. In the case of the piperidine skeleton the presence of five contiguous carbon atoms could permit the formation of isobaric [M — 43] ions by loss of the elements of C_3H_7 instead of $COCH_3$, a possibility which can, however, be readily discounted by high-resolution analysis, showing that approximately 99% of the ion current at this mass (*m/e* 84, base peak of the spectrum) is composed of an oxygen-free species, $C_5H_{10}N$. Strong evidence for a process involving ring contraction (1D)

* Analogous exchange, but to a lesser degree, has been observed in the fragmentation of N-acetylmorpholine.[6]

derives mainly from an [M − 46] peak in the spectrum of 8,8,8-d_3-N-acetylpiperidine (Fig. 3). This portion of ion current corresponds to the ejection of the entire acyl substituent implicating C—N bond rupture as a result of rearrangement:

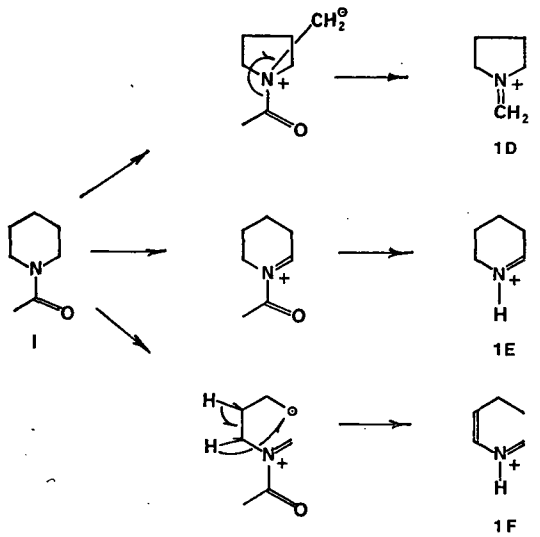

Operation of the conventional two-step elimination of ketene and an α-hydrogen from the ring (e.g. process 1E) is suggested by an [M − 45] peak in the same spectrum (loss of CD_2CO/H) and is confirmed by an [M − 44] fragment (*m/e* 87) in the spectrum of 2,2,6,6-d_4-N-acetylpiperidine (Ie, Fig. 3). That loss of a β-hydrogen atom in combination with ketene is also feasible to some extent follows from the presence of a substantial [M − 44] component (*m/e* 85) in the spectrum of 3,3-d_2-N-acetylpiperidine (Ib) as well as from a major [M − 45] component (*m/e* 89) in the spectrum of 2,2,6,6,8,8,8-d_7-N-acetylpiperidine (Ig) in which both processes 1D and 1E afford a common [M − 46] peak. One of the possible pathways compatible with this finding is included in the above scheme as process 1F.

Ring contraction in lower and higher homologues

Ring contraction in molecular ions of *N-acetylpyrrolidine* (II), the next lower homologue of I, can hardly be expected to be a process of major importance since formation of strained cyclic intermediates as well as strained products would be required. The virtual absence of such a process (2A) is readily ascertained by analysis of the positional origin of the [M − CH_3] and [M − $COCH_3$] fragments. The former is produced in an abundance of only 1 % of total ionization (Fig. 4) and was shown in a previous study[7] to arise exclusively via simple bond cleavage by loss of a methyl radical from the acetyl group (process 2C). Early evidence for this mode of formation was derived from the fact that the peak remains unshifted at *m/e* 98 in the spectrum of 7,7,7-d_3-N-acetylpyrrolidine,[7] corresponding to loss of CD_3. Complementary peak shifts are observed in the spectra of all other labelled derivatives. Process 2B, which would obviate strain both in intermediate and product, is likewise not operative, probably as a result of too low a hydrogen abstraction rate in the strained four-membered transition state required:

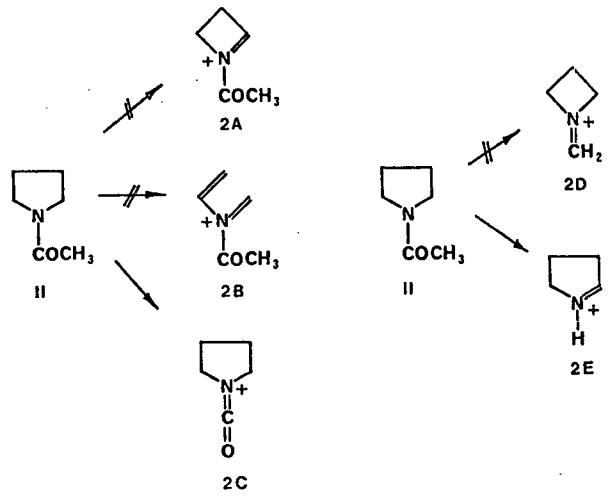

The [M — $COCH_3$] fragment, *m/e* 70, whose composition is confirmed by accurate mass measurement, is displaced to *m/e* 71 in IIc, indicating that loss of the elements C_2H_3O proceeds via the common two-step elimination of ketene and a hydrogen atom from the ring moiety[7] (process 2E), and not via expulsion of a CH_3CO radical as a result of ring contraction (process 2D). The identity of the hydrogen atom lost as

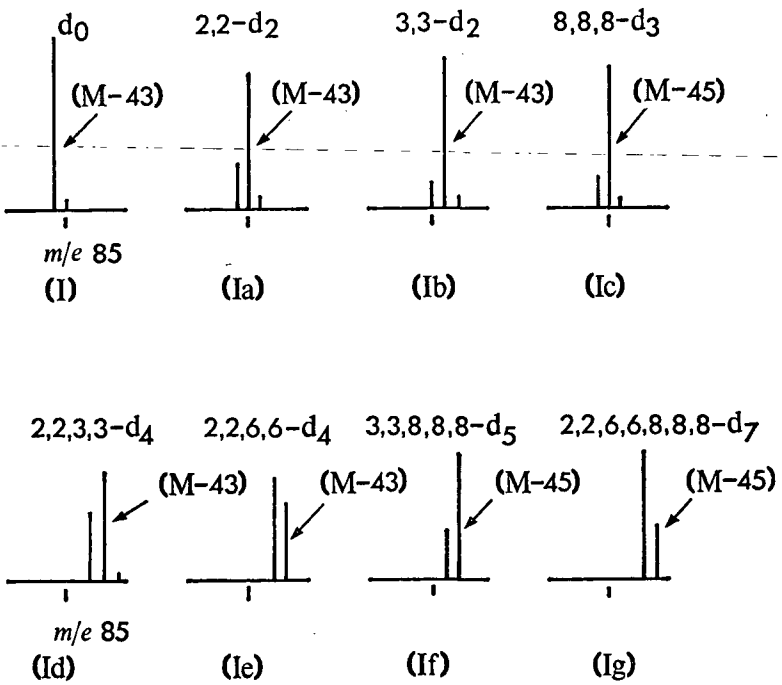

FIG. 3. Partial mass spectra ([M — 43] group) of labelled analogues (Ia to Ig) of N-Acetylpiperidine (I).

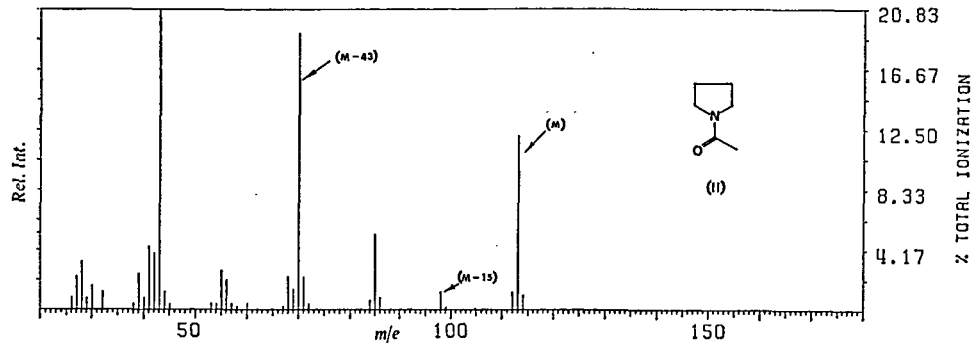

FIG. 4. Mass Spectrum of N-Acetylpyrrolidine (II).

arising from an α-position can be deduced from a shift of *m/e* 70 to 73 in the spectrum of 2,2,5,5-d_4-N-acetylpyrrolidine.[10]

As expected for an increasingly larger ring size, the seven-membered homologue of this series, *N-acetylhexamethyleneimine* (III), furnishes evidence for an enhanced propensity toward ring contraction as compared to the lower homologues I and II. Contrary to N-acetylpyrrolidine, an [M — CH_3] fragment (*m/e* 116, Fig. 5) is not only formed in high abundance (about 30% of the base peak) but stems in this case mainly from the loss of α-carbon atoms, indicative of contraction to a smaller ring (process 3A). This is evident from the spectrum of 2,2-d_2-N-acetylhexamethyleneimine (IIIa, Fig. 6) which displays a major partial shift of [M — 15] to [M — 17] (loss of CHD_2). Neglecting isotope effects, a 2:1:1 ratio would have to be expected for the peak group [M — 17]/[M — 16]/[M — 15] on grounds of asymmetry of label. Such a ratio accounts for more than 50% of the observed group intensity, leaving less than that for the entirety of competing alternatives, i.e. 3B and 3C. Ring contraction in accordance with the proposed mechanistic rationale is more explicitly reflected in the partial shift to [M — 18] in 2,2,3,3-d_4-N-acetylhexamethyleneimine (IIId) inasmuch as one site of hydrogen abstraction (C-3 or C-6) can be identified as adjacent to the carbon atom to be expelled (C-2 or C-7, respectively). Evaluation of the relative contribution of ring contraction leads in this case to a lower value (approximately 30 *vs.* 50% in IIIa), most likely due to isotope effects discriminating against [M — 18]

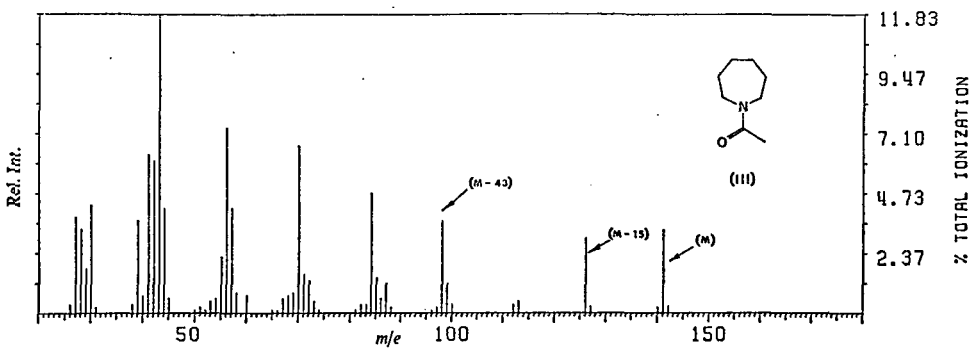

FIG. 5. Mass Spectrum of N-Acetylhexamethyleneimine (III).

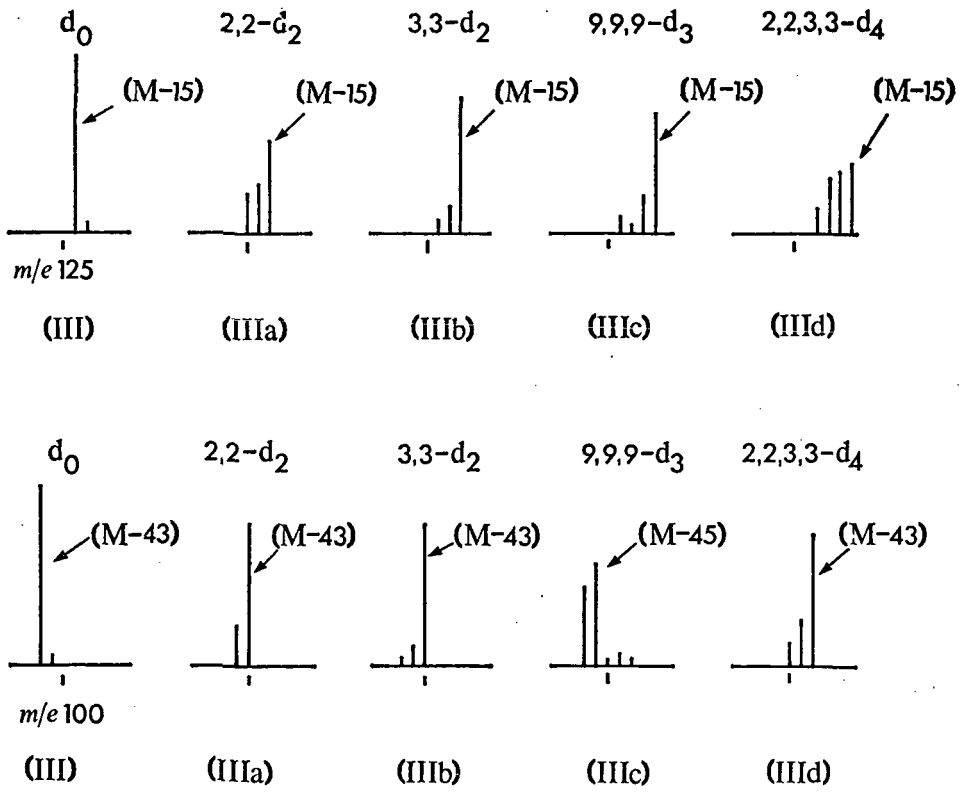

FIG. 6. Partial Mass Spectra ([M − 15] and [M − 43] group) of Labelled Analogues (IIIa to IIId) of N-Acetylhexamethyleneimine (III).

upon which the calculation is based. Approximate contributions of the losses of β-carbon atoms (C-3 and C-6, process 3B) as well as of C-9 (process 3C) can be estimated from the spectra of 3,3-d_2-N-acetylhexamethyleneimine (IIIb, Fig. 6) and of 9,9,9-d_3-N-acetylhexamethyleneimine (IIIc, Fig. 6). The observed 10% group intensity of the [M − 17] peak in the former, and of an [M − 18] peak in the latter, would indicate an approximate 20% contribution of process 3B *vs.* a 10% contribution of 3C. This last figure can be regarded as too low, since hydrogen exchange between C-9 and the ring moiety (most likely C-2 and C-7 in analogy to I) can be inferred from [M − 16] and [M − 17] contributions of decreasing intensity in IIIc, attesting to loss of label from the original position. A distinct split into [M − CH_3] and [M − CD_3] components would be expected in absence of this effect, with an intensity ratio increased in favour of the latter at the expense of the contributions of intermediate mass. Thus, a value of about 20% contribution of process 3C would appear more realistic.

The true prominence of ring contraction in III is more clearly reflected in the products of further decomposition of these ions, particularly in the ones derived from secondary loss of ketene (3A′ and 3B′), since 3C cannot undergo such a process without extensive rearrangement. The split of *m/e* 84 ([M − CH_3/CH_2CO]) into three components of almost equal intensity in the spectrum of the 2,2-d_2 compound (IIIa)

is compatible with approximately equal contributions of processes 3A′ and 3B′: the observed 1:1:1 intensity pattern can result from a superposition of a 2:1:1 peak group at [M − 59]/[M − 58]/[M − 57], as would be expected for 3A′ from the analogous pattern of 3A, and of a 1:1 peak group at [M − 58]/[M − 57], to be expected for 3B′ in analogy to 3B. The portion of ion current at [M − 15] (*m/e* 128) which exceeds a corresponding 1:1:1 ratio of the precursor ions in the same spectrum can be allotted in crude approximation to process 3C, amounting to about 20% in good agreement with the value obtained from IIIc.

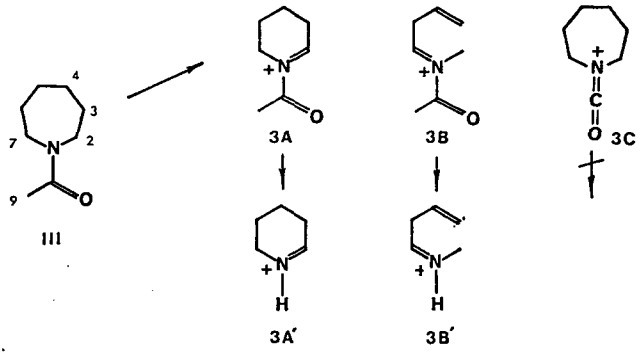

Analysis of the loss of the acyl substituent, the second criterion used for inference of ring contraction, can be applied to III only after consideration of the positional heterogeneity of the [M − 43] fragments. High-resolution analysis shows a 2:1 doublet of $C_6H_{12}N$ [M − $COCH_3$] and C_5H_8NO [M − C_3H_7] components. The substantial loss of a hydrocarbon moiety, as well as the general prominence of hydrocarbon fragments $[C_xH_y]^+$ and [M − C_xH_y] ions can be ascribed to the extended aliphatic portion of the molecule. The relative prominence of the loss of the substituent as an acetyl radical (process 3D) is borne out by a major partial shift of [M − 43] to [M − 46] (loss of $COCD_3$) in the spectrum of the 9,9,9-d_3 derivative (Fig. 6) which accounts for approximately 30% group intensity, or in consideration of the 2:1 doublet nature of the fragments for an approximate 50% contribution to the loss of C_2H_3O. This figure might again represent only a minimum value in view of the possible H/D exchange between C-9 and the ring, as observed in connection with the loss of methyl radicals. Loss of label in the course of such exchange would give rise to satellite peaks of decreasing intensity at increasing mass numbers. The comparable prominence of the [M − 45] peak in this spectrum nevertheless suggests additional operation of the common two-step loss of ketene and a ring hydrogen (process 3E).

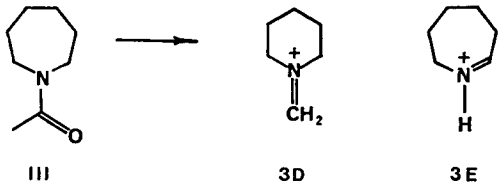

DISCUSSION

From the results of the preceding section it can be concluded that the prevalence of a ring contraction process in compounds I and III, as judged by formation of $[M - CH_3]$ and $[M - COCH_3]$ ions of highly characteristic positional origin, is dependent upon the size of the saturated heterocyclic ring. Not surprisingly, a five-membered ring (II) is too small to stabilize a contracted cyclic intermediate, so competing processes dominate its fragmentation entirely. In contrast to this, ring contraction obviously can compete favourably with other processes in a six- and particularly in a seven-membered ring (I and III, respectively). The increased importance of ring contraction in the latter is more directly reflected by the increased specific formation of the [M — 15] and [M — 43] fragments by loss of α-carbon atoms and $COCH_3$ radicals, rather than by overall contribution of the [M — 15] and [M — 43] ions to total ionization. Greater ease of ring contraction due to expansion of the cyclic skeleton is, of course, parallelled by the increased number of fragmentation pathways available to the cyclic moiety.

In the light of these results, the presence of oxygen as a second heteroatom in the ring system of N-acetylmorpholine, in which ring contraction was first found, appears favourable, though in principle not essential, to the occurrence of this process. The fact that ring contraction also operates in absence of the oxygen atom, namely in the present series of simplified analogues, lends support to the mechanistic rationale originally proposed, involving attack of a radical site at the π-system of an immonium structure[6] (M_1, pathway *a*):

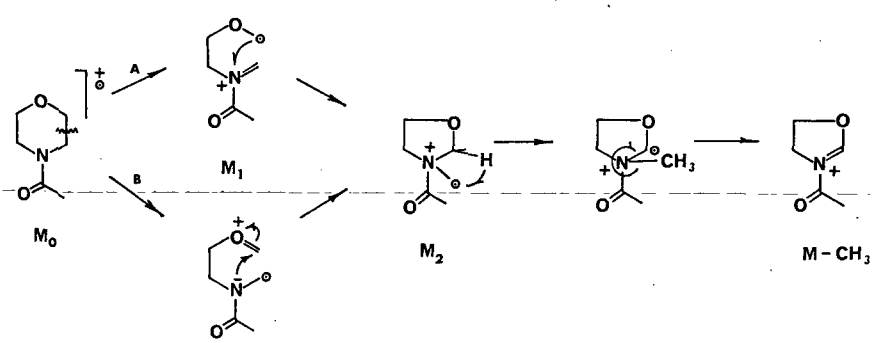

Attack of a lone pair of electrons at an oxonium structure (M_1, pathway *b*), a purely ionic alternative to the radical-induced process (*a*), would suggest that ring contraction be a definite consequence of the presence of a strong donor function (—O—) in addition to an acceptor function ($—COCH_3$) weakening the donor qualities of nitrogen. On this basis significant differences in charge distribution characteristics could account for the observed failure* of the free amine and its N-methyl derivative[6] to undergo a comparable contraction process as a result of strong charge localization at the nitrogen atom in the 'open' molecular ion M_1:

* Loss of α-carbon atoms attributable to ring contraction has been observed to very small extents in N-alkyl morpholines bearing larger alkyl substituents (e.g. n-butyl). (Dr R. T. Aplin, The Dyson Perrins Laboratory, Oxford, UK, private communication).

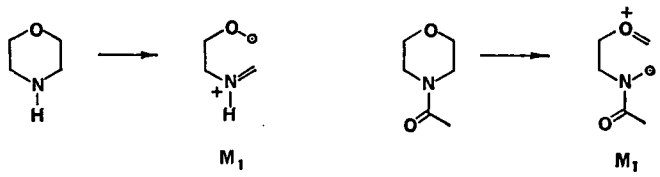

M_1 M_1

In contrast to this, the positive charge might be preferentially localized on the ether oxygen in M_1 of the N-acetyl derivative, possibly providing for a largely different fragmentation behaviour.[11] The evidence presented for occurrence of ring contraction in spite of the absence of a second donor atom in compounds I and III is obviously irreconcilable with a requirement for the presence of a second donor atom and definitely limits the role of the oxygen atom to that of a rate- and specificity-enhancing factor.

EXPERIMENTAL

High and low resolution mass spectra were obtained with a modified AEI MS-902 mass spectrometer, equipped with an all-glass inlet system. Operating conditions: inlet system 200°C, source temperature 250°C, ionizing voltage 70 V. The synthesis of the labelled N-acetylpyrrolidines, -piperidines and -hexamethyleneimines and the percentages of deuterium incorporation were reported in a preceding publication.[10]

Acknowledgements—The authors wish to acknowledge helpful discussions with Professor M. M. Bursey of the University of North Carolina, Chapel Hill, and the assistance of Dr D. H. Smith and Mr B. R. Simoneit, University of California, Berkeley, in obtaining high resolution data for the compounds investigated. Financial support was provided by the National Aeronautics and Space Administration, Grants NGL 05-003-003 and NAS 9-7889.

REFERENCES

1. P. N. Rylander, S. Meyerson and H. M. Grubb, *J. Am. Chem. Soc.* **79**, 842 (1957).
2. W. J. Richter, ref. 5 in 3. C. Djerassi, A. M. Duffield, F. Komitsky, Jr. and L. Tökes, *J. Am. Chem. Soc.* **88**, 860 (1966).
3. C. Djerassi, A. M. Duffield, F. Komitsky, Jr. and L. Tökes, *J. Am. Chem. Soc.* **88**, 860 (1966).
4. A. F. Thomas and B. Willhalm, *Helv. Chim. Acta* **47**, 475 (1964).
5. H. Budzikiewicz, C. Djerassi and D. H. Williams, *Mass Spectrometry of Organic Compounds*, Holden-Day, San Francisco, 1967, p. 257.
6. J. M. Tesarek, W. J. Richter and A. L. Burlingame, *Org. Mass Spectrom.* **1**, 139 (1968).
7. A. M. Duffield and C. Djerassi, *J. Am. Chem. Soc.* **87**, 4554 (1965).
8. A. M. Duffield, H. Budzikiewicz, D. H. Williams and C. Djerassi, *J. Am. Chem. Soc.* **87**, 810 (1965).
9. D. H. Williams, H. Budzikiewicz and C. Djerassi, *J. Am. Chem. Soc.*, **86**, 284 (1964).
10. W. J. Richter, J. M. Tesarek and A. L. Burlingame, *Org. Mass Spectrom.* **5**, 531 (1971).
11. W. Vetter, W. Meister and W. J. Richter, *Org. Mass Spectrom.* **3**, 777, (1970) and references cited therein.

INFORMATION FOR CONTRIBUTORS

General

Organic Mass Spectrometry will devote itself to the rapid publication of those papers exclusively dealing with the application of mass spectrometry to problems in organic chemistry. Intended papers should clearly add original scientific value to the field. Contributions should not have been published elsewhere and authors must agree not to communicate the same material for publication in any other journal or book. Authors are invited to submit their papers for publication to the Regional Editor where appropriate, or in all other cases to the Editor-in-Chief. From time to time review articles will be accepted, but prior consultation with one of the Editors is strongly advised. Papers may be in English, French or German. Safe receipt of contributions for publication will be acknowledged by the receiving Editor.

Manuscripts

Manuscripts should be typed in double line spacing on paper wider than 8½ inches and not deeper than 12 inches. Margins of at least 1½ inches must be left at the top, bottom and left-hand side of each page. The first page should also bear the name and full address of one author to whom the page proofs will be despatched in due course. All manuscripts should be submitted in triplicate, and in addition, a set of copies or prints of the diagrams must be attached to each copy of the manuscript. This will enable papers to be sent to two referees simultaneously and so assist rapid publication.

Abstract

Every paper for publication must be preceded by an abstract (200–250 words) setting out the essential contents. For French and German papers an English version of the abstract should also be provided.

Nomenclature

Authors should conform to nomenclature, symbols and abbreviations adopted by the Commission on the Nomenclature of Organic Chemistry of the International Union of Pure and Applied Chemistry (IUPAC).

Illustrations

Illustrations on tracing cloth, tracing paper or white card should be supplied separately from the text and must bear the names of the authors, the title and the figure number. The mass numbers for principal peaks should be indicated. Such illustrations should be carefully drawn at approximately twice the size they are required to be reproduced in the actual journal. This reduction is necessary to ensure high definition in print. Lettering must be large enough to withstand this 50% reduction and remain clearly legible. Printing area of a page is 8″ × 5¼″. Illustrations should be provided with descriptive legends which should be listed on a separate sheet.

Tables

Tables should be kept to the minimum. The same data should not be reproduced in both tabular and diagrammatic form. Essential tables should be provided with legends making them intelligible without reference to the text.

Experimental

New compounds should be indicated by underlining the name (for italics) at its first mention (excluding headings) in the Experimental Section only, and by giving analytical results in the form: (Found: C, 63·1; H, 5·4. $C_{18}H_{18}NO_4$ requires C, 63·2; H, 5·3%). Analytical results for compounds which have previously been adequately described in the literature should be given in the form: (Found: C, 62·95; H, 5·4. Calc. for $C_{18}H_{18}NO_4$: C, 63·2; H, 5·3%). The punctuation should be noted.

References

References will be cited in the text by superior numbers and listed at the end of the article. They should be in the following form:

1. R. L. Baird and A. Aboderin, *J. Am. Chem. Soc.* **86**, 252 (1964).
2. H. Budzikiewicz, C. Djerassi and D. H. Williams, *Interpretation of Mass Spectra of Organic Compounds*, Holden-Day, San Francisco, 1964.

Journal titles must be abbreviated according to the system adopted by *Chemical Abstracts*. (Supply full titles otherwise.)

Footnotes

Footnotes, as distinct from literature references, should be indicated by the following symbols:

* † ‡ § ‖ ¶

used in this sequence and commencing anew on each page; they should not be included in the numbered reference system.

Acknowledgements

These are placed at the end of the text preceding the references and should be brief.

Proofs

Page proofs, for the correction of printers' errors only, will be despatched to the author indicated on the first page of the manuscript. Any further alteration at this proof stage may have to be charged to the author and may seriously delay publication. Fifty reprints of each paper will be supplied free of charge. Additional copies can be obtained at reasonable prices.

Short Communications

Short communications will appear as a distinct section of the journal following the ordinary papers. Reprints will be available at the normal rates.

In style and presentation short communications should conform to that laid down for manuscripts, but length should be restricted to a maximum of two journal pages, i.e. approximately four pages of typed manuscript inclusive. Graphical spectral diagrams will not normally be published and if necessary details should be tabulated. Reaction schemes must be kept as simple as possible and drawn suitable for direct reproduction. The scale factor should be 1½:1, i.e. not more than 7″ (17·5 cm) wide for reduction to normal page width. Journal style should be taken into account. Editors will be responsible for refereeing and to enable as rapid publication as possible authors proofs will not be awaited before passing for press unless specifically requested, although they will be sent as a matter of course and corrections incorporated if notified in time.

Short communications should still be preceded by an abstract as for normal papers.

© Heyden & Son Ltd, 1970

All Rights Reserved. No part of this publication may be reproduced, stored in a retrieval system, or transmitted, in any form or by any means, electronic, mechanical, photocopying, recording or otherwise, without the prior permission of Heyden & Son Ltd.

HEYDEN & SON LTD.,

SPECTRUM HOUSE, ALDERTON CRESCENT, LONDON N.W.4.

D4

(*Reprinted from Nature, Vol.* 234, *No.* 5326, *pp.* 210–211, *November* 26, 1971)

Organic Analyses of Selected Areas of Surveyor III recovered on the Apollo 12 Mission

THE Apollo 12 astronauts recovered the television camera, the trenching scoop and a few smaller items from Surveyor III, which had been on the Moon for 31 months[1]. They noticed that the white surfaces of the spacecraft had become tan. The television camera remained in the Lunar Receiving Laboratory (LRL) during the quarantine period and afterwards preliminary microscopic visual examinations and extensive photography were conducted at the LRL. The camera was then shipped to Hughes Aircraft Company for detailed studies and disassembly. Whenever possible the camera was handled and examined in laminar flow clean areas. On close examination, optical interference patterns were found on the camera mirror. The effects of lunar particles on this mirror had been observed earlier[2]. We report here the organic contamination of the mirror surface and camera exterior (shroud) attributable to the spacecraft outgassing, Lunar Module (LM) descent engine blasting, possible Surveyor III engine exhaust products —although thought to be unlikely due to the spatial configuration of the spacecraft components—and unknown sources. A more detailed report of these data will be published by NASA[3].

The camera mirror and middle shroud were extracted for organic material by washing the surface with benzene or benzene and methanol (3 : 1) squirted on by a syringe and collected in a beaker. The area of the mirror which was washed with benzene was approximately 35 cm^2. The whole operation was carried out in a class 100 organic clean room. These wash solvents (redistilled nanograde purity), as well as the sample washes, were concentrated on a rotary evaporator and the total residues subjected to high resolution mass spectrometry. The mass spectrometer system consisted of a modified GEC–AEI MS-902 high resolution mass spectrometer on-line to an XDS Sigma 7 computer[4–6].

The solvent background (less than 0.1 p.p.b.) consisted of hydrocarbons, chiefly the series C_nH_{2n-6} for $n=6$ to 16, and indications of carboxylic acid fragments, $C_nH_{2n-1}O_2$ for $n=3$ to 7, and phthalates (small peak of composition $C_8H_5O_3$). The residue from the mirror wash amounted to approximately 80 μg (about 2 μg/cm^2). It consisted principally of dioctyl phthalate, hydrocarbons of the series C_nH_{2n+2} for $n=3$ to 15,

C_nH_{2n} for $n=3$ to 14, C_nH_{2n-2} to C_nH_{2n-10} for $n=5$ to 12 approximately, carboxylic acids of the series $C_nH_{2n}O_2$ for $n=1$ to 16 and 18 (palmitic and stearic acids were the major homologues of the series) and in minor amounts silicones and LM engine exhaust products. The silicone oil was substantiated by ions of compositions C_3H_9Si, $C_5H_{15}OSi_2$ and $C_7H_{21}O_2Si_3$, derived from straight chain silicones and ions of compositions $C_4H_{13}O_3Si_3$ and $C_5H_{15}O_3Si_3$, derived from cyclic silicones. The peaks attributable to LM exhaust[7,8] are NH_3, HCN, fragments CH_3NH and CH_3NCH_3, NO, and $C_2H_6N_2O$ (I).

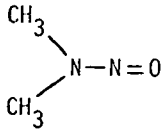

I

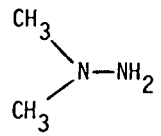

II

The nitric oxide is the major reduction product from the LM oxidizer, N_2O_4. The dimethyl oxazine (I) is a partial oxidation product of unsymmetrical dimethylhydrazine (II), the LM fuel.

The middle shroud was washed with benzene and methanol on the side toward the LM and on the side away from the LM, and the extract residues amounted to approximately 120 μg (about 5 μg/cm^2) for the sample toward the LM and approximately 200 μg (about 8.5 μg/cm^2) for the sample leeward the LM. The major constituents found for both of these samples are hydrocarbons of the series C_nH_{2n+2} for $n=2$ to 29, C_nH_{2n} for $n=2$ to 19, C_nH_{2n-2} for $n=2$ to 16, with minor amounts of C_nH_{2n-4} to C_nH_{2n-10} for approximately $n=6$ to 13, dioctyl phthalate and silicone oil. This was substantiated by the same peaks in the high resolution mass spectral data as for the mirror sample. The minor components of these samples are nitrogenous and oxygenated compounds. A group of oxygenated peaks indicate a partially depolymerized vinyl alcohol–styrene copolymer (III)[8]. The peaks of compositions $C_{13}H_{19}O_3$, $C_{11}H_{15}O_2$, $C_9H_{11}O$, and C_7H_7 (tropylium ion) fit the pyrolytic fragmentation pattern for the copolymer III. The LM descent engine products are more varied in these samples than in those from the mirror wash, but still minor. Ions fitting the compositions NH_3, HCN, probably acetonitrile and propionitrile[7,8], NO, CH_2NO, CH_3NO, C_2H_5NO (N-hydroxyaziridine[8]) and the fragment series $C_nH_{2n}NO$ for $n=3$ to 5 and $C_nH_{2n-2}NO$ for $n=5$ and 6 are found. The peaks of composition $C_2H_6N_2O$ (I), CH_4N_2O (IV), and CH_5N_2O (a protonated species of IV) are present in significant amounts. The methyl oxazine (IV) may possibly be derived from the Surveyor III engine

exhaust, because the fuel used was mainly monomethylhydrazine (V).

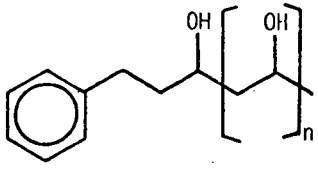

III

In summary, essentially the whole outside surface of the Surveyor III television camera was covered by lunar fines, probably from the following sources: Surveyor landing, lunar transport due to meteoroidal impacts, LM landing, and

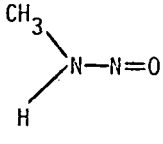

IV

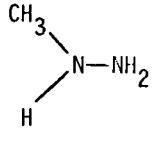

V

redistribution during return and subsequent handling. Thus the evidence for LM and possibly Surveyor III descent engine exhaust products on the shroud and mirror is not surprising. The side toward the LM was heavily sandblasted and more discoloured than the side opposite. This fact was not too well demonstrated by the organic material isolated from the shroud, except that the total ion current for the leeward sample was about double that of the sample from the side facing the LM. The same types of organic molecules were found on the mirror and both shroud samples. The sources of the various organic contaminants[9] are as follows: hydrocarbons from lubricating oils; general terrestrial contamination from exposure and bagging material; dioctyl phthalate from polyethylene bagging material (the plasticizer); carboxylic acids from decomposition of grease and general terrestrial contamination and handling; silicones from sources as lubricating oil, outgassing of electronics and plasticizer; styrene–vinyl alcohol copolymer probably from electronics insulation; and nitrogenous compounds from LM and possibly Surveyor III engine exhaust. The organic contamination levels do not seem to contribute to the discoloration of the various surfaces.

In spite of the significant amounts of terrestrial contaminants, adsorbed mainly from exposure during examination and exhibition, as well as from the bagging materials, it was still

possible to detect compounds derived from landing engine exhausts, and some compounds which may be spacecraft outgassing products. Unfortunately the LM exhaust products contaminated sample scheduled for collection by the Apollo 14 mission was not accomplished. It was accomplished by Apollo 15, and it will provide an unambiguous determination of the actual LM engine exhaust products found in the lunar environment. Such data will be of value in interpreting the findings of soft-landed spacecraft on other planets (for example, Viking on Mars). Furthermore, analyses for organic contaminants and identification of their sources, even if low in concentration, should be recognized as an important criterion for the design of optical or other active instruments for future spacecraft.

We thank Mrs E. Scott, Dr E. Gelpi and Miss P. Wszolek for technical assistance and Miss M. Petrie for high resolution mass spectrometry. This work was supported by the National Aeronautics and Space Administration.

BERND R. SIMONEIT
A. L. BURLINGAME

Space Sciences Laboratory, University of California, Berkeley, California 94720

Received September 7, 1971.

[1] Mission Evaluation Team, *Apollo 12 Mission Report*, MSC-01855, NASA-Manned Spacecraft Center, Houston, Texas (1970).
[2] Jaffe, L. D., and Rennilson, J. J., in *Surveyor Program Results*, NASA SP-184 (Washington DC, 1969).
[3] Simoneit, B. R., and Burlingame, A. L., in *Surveyor III Material Analysis Report*, NASA Special Publication (in the press).
[4] Burlingame, A. L., in *Advances in Mass Spectrometry* (edit. by Kendrick, E.), **4**, 15 (Institute of Petroleum, London, 1968).
[5] Burlingame, A. L., Smith, D. H., and Olsen, R. W., *Anal. Chem.*, **40**, 13 (1968).
[6] Burlingame, A. L., in *Recent Developments in Mass Spectroscopy* (edit. by Ogata, K., and Hayakawa, T.), 104 (University of Tokyo Press, 1970).
[7] Simoneit, B. R., Burlingame, A. L., Flory, D. A., and Smith, I. D., *Science*, **166**, 733 (1969).
[8] Flory, D. A., Simoneit, B. R., Burlingame, A. L., and Smith, I. D., *Experimental Determination of Potential Lunar Surface Organic Contamination in the Lunar Module Descent Engine Exhaust*, NASA Technical Report (in the press).
[9] Simoneit, B. R., and Flory, D. A., *Apollo 11, 12 and 13 Organic Contamination Monitoring History*, NASA Special Publication (in the press).

Printed in Great Britain by Flarepath Printers Limited, Watling Street, Colney Street, St. Albans, Herts.

SPACE SCIENCES LABORATORY

D5

SPATIAL SPARK JITTER MEASUREMENTS OF HIGHLY CHARGED NUCLEI FOR OPTICAL SPARK CHAMBERS

G. F. Smoot, A. Buffington, and L. H. Smith
Space Sciences Laboratory,
University of California, Berkeley, California

April 1972

This work was supported in full by NASA Contract NAS 9-7801 and is prepared for submittal to *Review of Scientific Instruments*.

Space Sciences Laboratory Series 13 Issue 34

UNIVERSITY OF CALIFORNIA, BERKELEY

Space Sciences Laboratory
University of California
Berkeley, California 94720

SPATIAL SPARK JITTER MEASUREMENTS OF HIGHLY CHARGED NUCLEI FOR OPTICAL SPARK CHAMBERS

G. F. Smoot, A. Buffington, and L. H. Smith
Space Sciences Laboratory,
University of California, Berkeley, California

April 1972

This work was supported in full by NASA Contract NAS 9-7801
and is prepared for submittal to *Review of Scientific Instruments*.

Space Sciences Laboratory Series 13 Issue 34

Spatial Spark Jitter Measurements of Highly Charged Nuclei for Optical Spark Chambers*

G. F. SMOOT, A. BUFFINGTON, AND L. H. SMITH
Space Sciences Laboratory, University of California, Berkeley

ABSTRACT

The spatial jitter of sparks about the paths of relativistic nuclei of various charges Z has been measured for optical spark chambers. For normal incidence the jitter measured was consistent with the $1/Z$ dependence expected from diffusion of the ionization electrons.

Many experimenters have utilized optically-viewed spark chambers filled with 90 percent neon, 10 percent helim gas mixture at STP, and with 1 cm gap spacing. Although most experiments are limited in their resolution by alignment and optical calibration uncertainties, the ultimate limit to spark chamber resolution is set by jitter in position of the sparks. The best jitter measurement reported to date is about .18 mm.[1,2] Jitter is adequately explained by diffusion of the electrons, produced by ionization, during the time interval between the incident particle's passage and the actual spark formation.[1] The mean diffusion distance for the centroid of the electrons is inversely proportional to the square root of the number of electrons. Some workers have reduced their jitter by using wider gaps,[3] by pressurizing the gas,[2] or by increasing

---

* This work was supported in full by NASA contract NAS 9-7801.

the ionization power of the incident particle.[4] Recently substantial reduction of resolution error has been achieved by the use of liquid xenon.[5] All of these methods reduce the jitter by increasing the number of electrons created. For cosmic ray nuclei experiments, and for experiments at the new heavy-ion accelerators, the large electric charge on a heavy nucleus can be expected to produce substantial reductions in spark jitter for conventional spark chamber systems. In this paper we report the results of jitter measurements on spark chamber photographs of relativistic cosmic rays with various charges. For a relativistic particle of charge Z, the number of ionization electrons produced is proportional to Z^2. Since the spark drift is inversely proportional to the square root of the number of electrons, the jitter should go as $1/Z$. We show that the spark chamber jitter is consistent with the expected $1/Z$ description, for the range $Z = 1$ through 6.

Our balloon-borne magnetic spectrometer for cosmic rays has been described previously.[6] The scintillation counters in our experiment provided unique charge identification for each event. From the 120,000 events exposed in our two balloon flights to 35 km altitude, we selected a sample of events which had unambiguous charge, nearly normal incidence (less than 0.1 radians) to our spark chambers, and a good fit to a rigidity (momentum/charge) above 5 GV/c. For these jitter measurements we accepted only events which had a spark present in every gap of the spark chambers. Figure 1 shows a typical 4-spark segment. The events selected for jitter study were measured on the Powell-Birge group's measuring microscope at the Lawrence Berkeley Laboratory. Each spark was measured four times, and the results were averaged together. Figure 2 shows the deviations of these measurements from the averages. The centering error for a single spark measurement is 1.0 micron on the film, corresponding

to 0.054 mm in the spark chambers. The least count of the microscope was one micron.

The spark locations were corrected for the sweeping of the ionization electrons (empirically determined to be 1/4 of a gap, perpendicular to the spark chamber plates) occurring between the application of a high voltage and spark formation. The four averaged sparks were least-squares fit to a straight line. The root-mean-squared spark jitter was calculated for each segment using the formula

$$\sigma_{rms} = \sqrt{\frac{\sum_{i=1}^{4} (y_i - mx_i - k)^2}{2}}$$

where m is the slope and k the intercept for the best-fit line through the sparks. Figure 3 shows the distribution of σ_{rms} observed for various charges of particles incident. It is clear from figure 3 that the heavily-ionizing particles suffer much less spark jitter than the protons.

In order to unfold the actual spark jitter from the results of figure 3, we removed the expected error from the microscope least count (0.3 microns rms), from the centering error on the four-spark average (0.56 microns rms), from the variations in electron-sweep time (0.25 microns rms), and from a 20 percent variation in spark chamber magnification over the volume of our chambers (0.3 microns rms). Figure 4 shows the resulting jitter values we have measured, as a function of the incident charge. The smooth curve shows the $1/Z$ dependence (normalized to helium) one would expect if the jitter mechanism were dominated by the statistics of electron diffusion. Our results show substantially reduced spark jitter for the more heavily ionizing particles, consistent with the simple diffusion mechanism.

We would like to thank Dr. Robert Ely of the Birge-Powell group for his assistance in getting us set up for our measurements. We also acknowledge useful conversations with Dr. Richard Muller and the support of Professor Luis W. Alvarez.

REFERENCES

1 W. A. Wenzel, "Spark Chambers," *Ann. Rev. Nucl. Sci.*, 14, 205-238 (1964).

2 W. J. Willis et al., *Nucl. Instr. Methods*, 91, 29-31 (1971).

3 P. M. Dauber, L. H. Smith, and M. A. Wahlig, *Nucl. Instr. Methods*, 84, 199-204 (1970).

4 J. Fischer, G. J. Igo, and S. B. Orbesen, *Colloque International sur L'Electronique Nuclaire*, Vol. III, pp. 5-1 - 5-3, (1968).

5 R. A. Muller, S. E. Derenzo, G. Smadja, D. B. Smith, R. G. Smits, H. Zaklad, and L. W. Alvarez, *Phys. Rev. Letters*, 27, 532 (1971).

6 L. H. Smith, A. Buffington, M. A. Wahlig, and P. Dauber, *Rev. Sci. Instr.*, 43, 1-11 (1970).

FIGURE CAPTIONS

Fig. 1. Photograph of a typical four-spark segment. This particular segment is from a beryllium nucleus track.

Fig. 3. The smooth curves are the best fits to the expected shape for pure Gaussian jitter of the sparks.

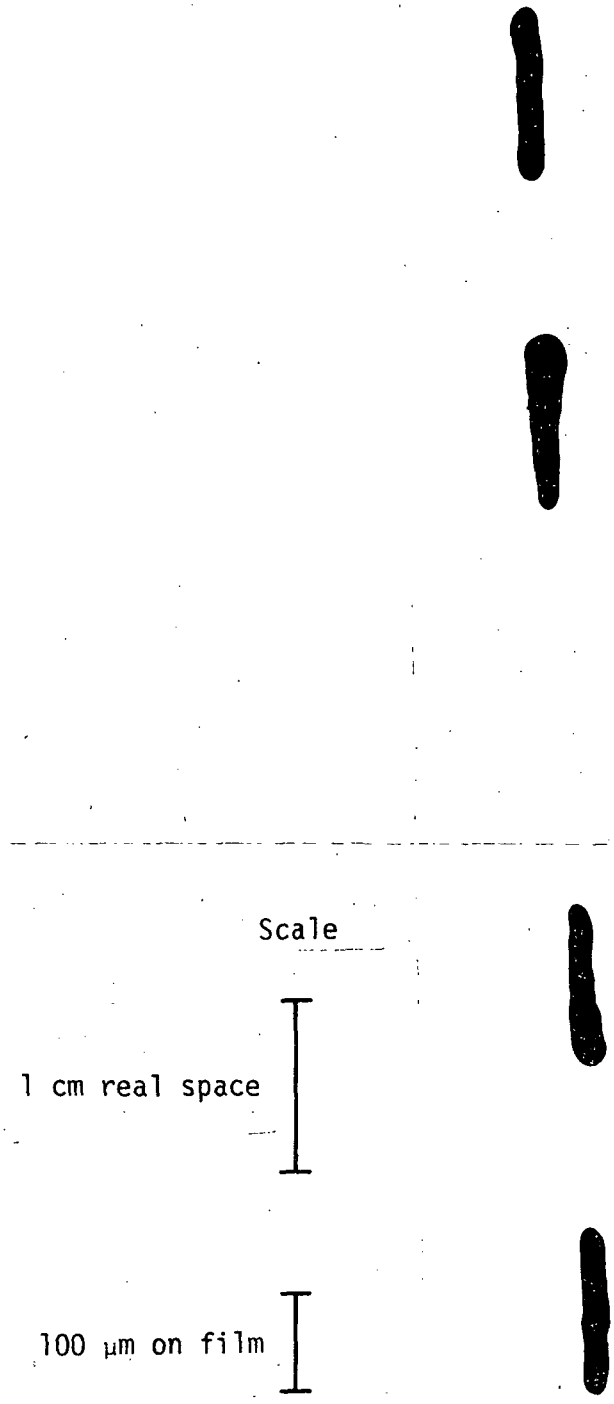

Figure 1

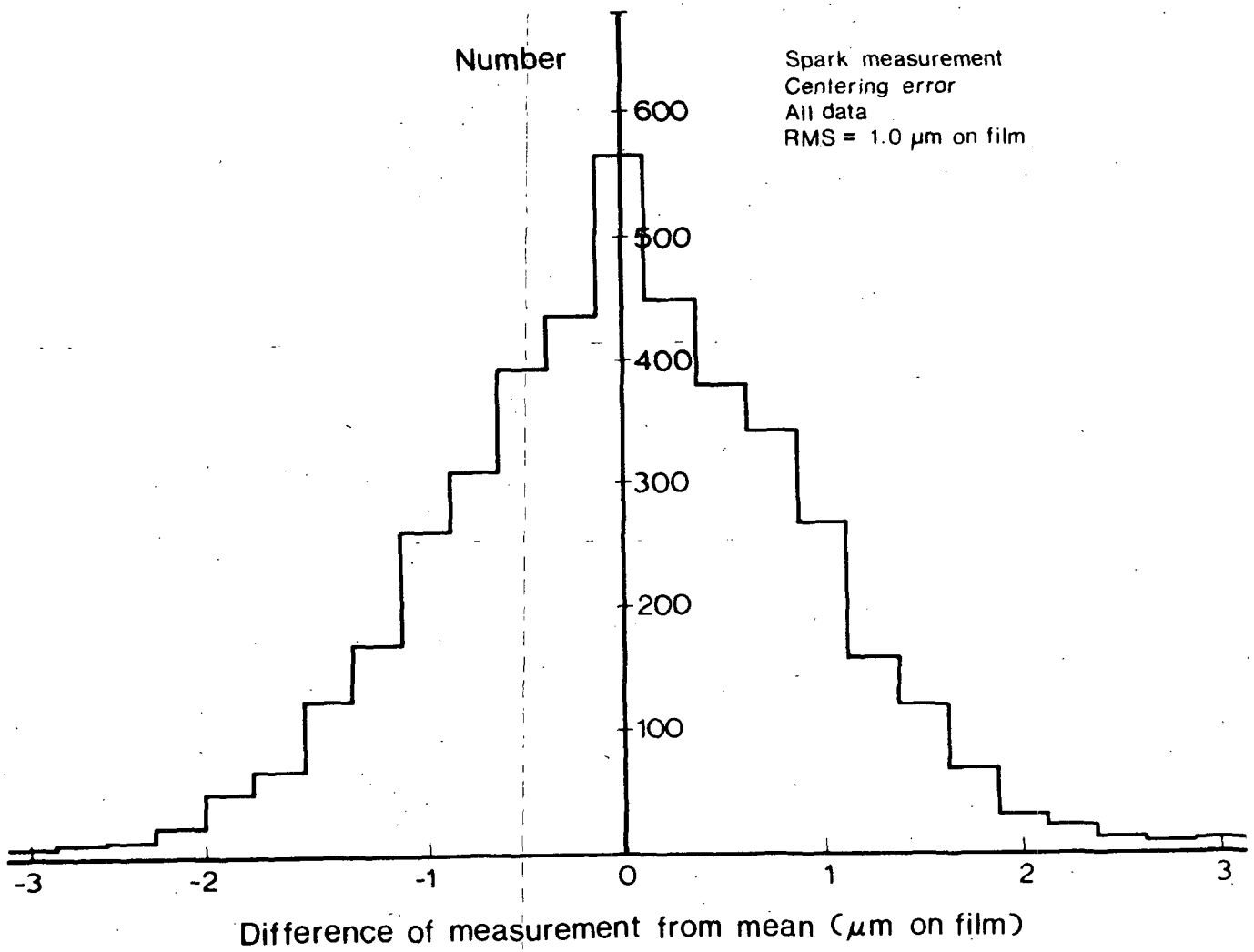
Number
Spark measurement
Centering error
All data
RMS = 1.0 μm on film
600
500
400
300
200
100
-3
-2
-1
0
1
2
3
Difference of measurement from mean (μm on film)

Figure 2

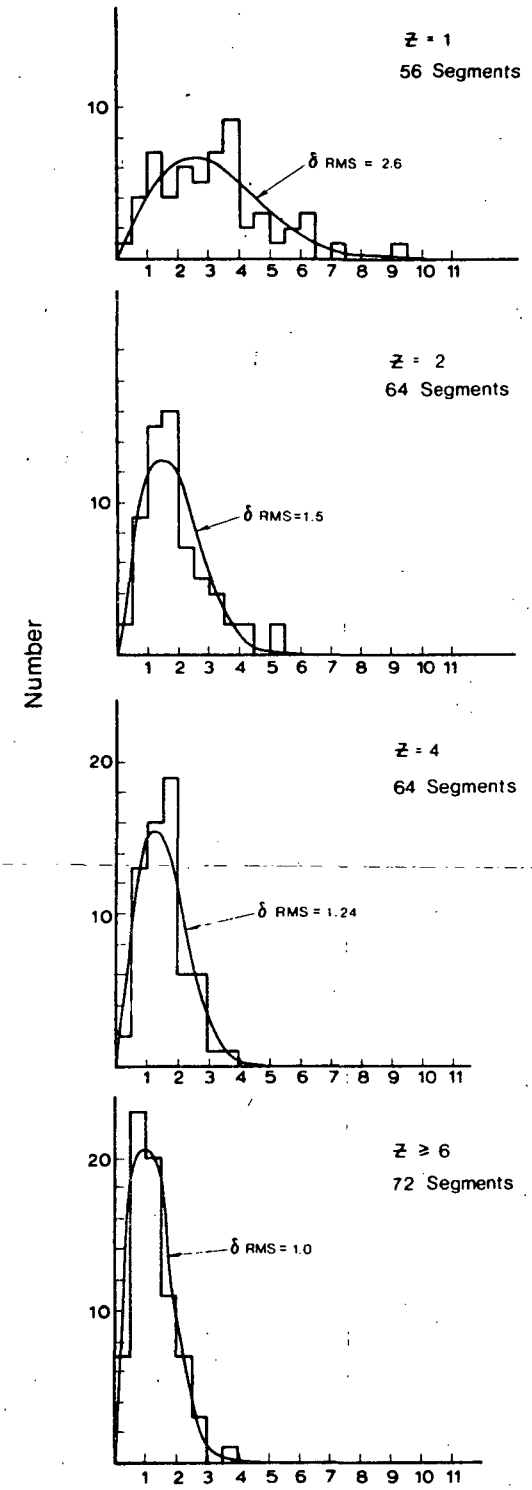
Z = 1
56 Segments
δ RMS = 2.6
Z = 2
64 Segments
δ RMS=1.5
Z = 4
64 Segments
δ RMS = 1.24
Z ≥ 6
72 Segments
δ RMS = 1.0
Number
10
20
1 2 3 4 5 6 7 8 9 10 11
Root mean squared spark deviation (μm on film)

Figure 3

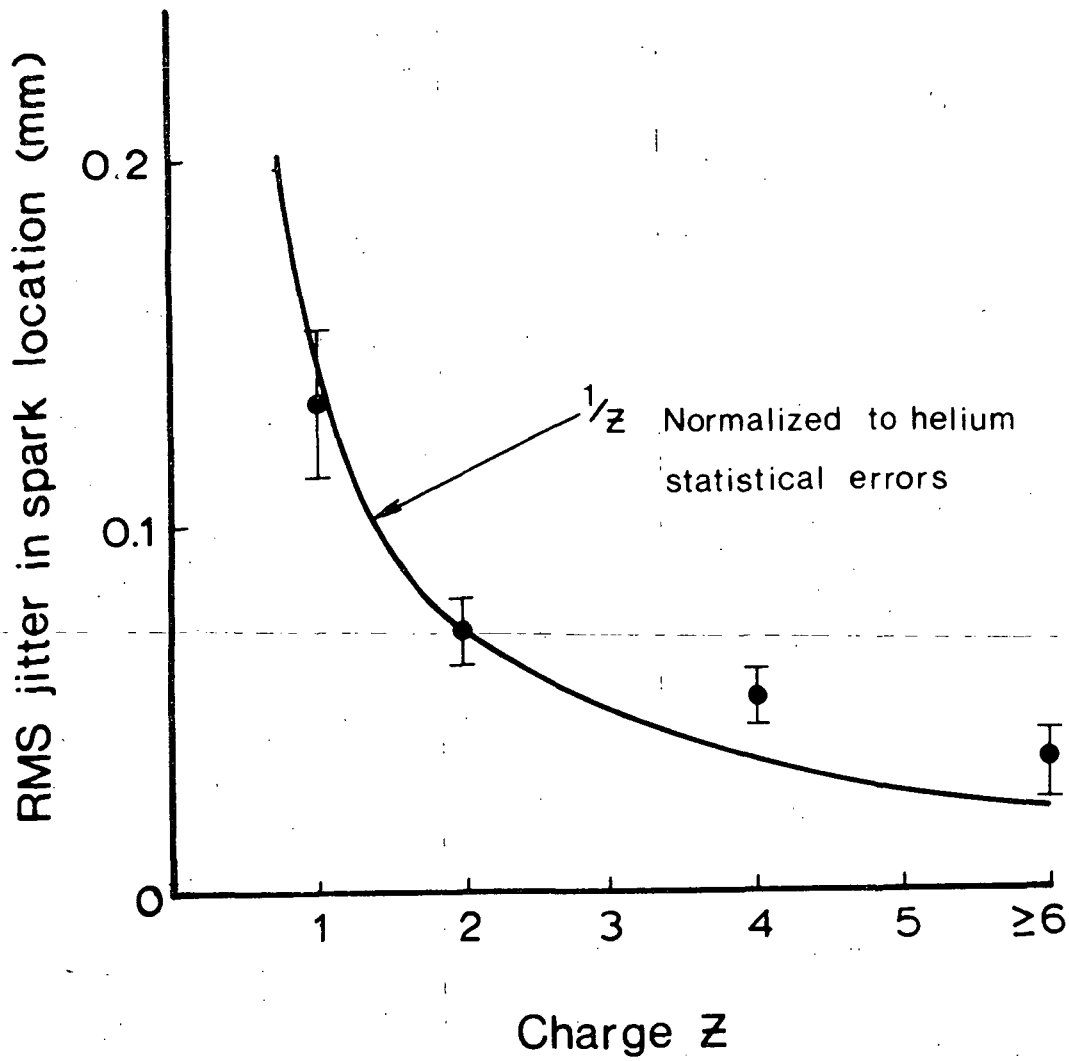
RMS jitter in spark location (mm)
0.2
0.1
0
1
2
3
4
5
≥6
Charge Z
1/Z
Normalized to helium
statistical errors

Figure 4

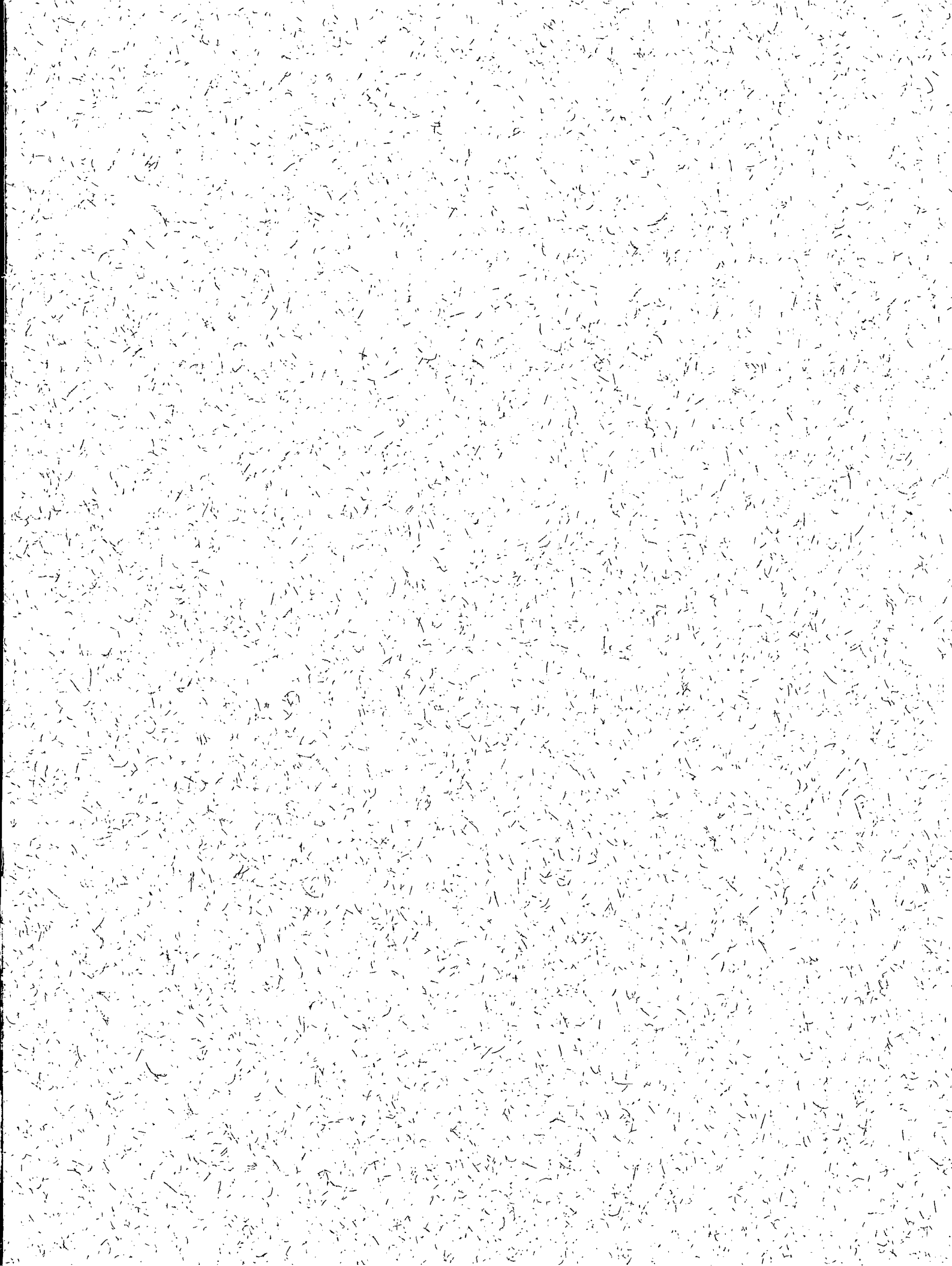

A72-42409

THE ONSET OF MAGNETOSPHERIC SUBSTORMS

B. Tsurutani

Physics Department and Space Sciences Laboratory
University of California, Berkeley 94720

and

F. Bogott

Space Sciences Laboratory
University of California, Berkeley 94720

February 16, 1971

ABSTRACT

An examination of the onset of magnetospheric substorms is made using ATS-5 energetic particles, conjugate balloon x-rays and electric fields, all sky camera photographs, and auroral zone magnetograms. It is shown that plasma injection to ATS distances, conjugate 1-10 keV auroral particle precipitation, energetic >40 keV electron precipitation, and enhancements of westward magnetospheric electric field component all occur with the start of slowly developing negative magnetic bays. No trapped or precipitating energetic particle features are seen with later sharp negative magnetic bay onsets.

INTRODUCTION

Simultaneous balloon x-ray and electric field measurements were made from the approximate northern terminus of the field line which passes through the ATS-5 synchronous orbit satellite. Two isolated substorms which occurred during relatively quiet days (ΣK_p = 18, 19) are examined using these data and additional ground based information. The start of midnight meridian negative magnetic bays, the enhancement of energetic >5 keV plasma at ATS, the precipitation of energetic >40 keV electrons, and the additional enhancements of magnetospheric westward electric fields are found to be interrelated, and occur within 10 minutes of each other. Ground based all-sky camera data and riometer absorption data gave additional information of auroral bulge propagation properties.

DESCRIPTION OF THE EXPERIMENT

A joint balloon x-ray and electric field experiment was conducted by the University of California, Berkeley group, from Thompson, Manitoba, Canada, the foot of the magnetic field line of the ATS-5 satellite. Experimental payloads were balloon borne to altitudes of 11-12 g/cm^{-2} on April 25, 1970 and May 5, 1970 and to 7 g/cm^{-2} on May 2, 1970. Each payload contained a collimated 3-inch diameter NaI(Tl) Harshaw integral x-ray detector with an upward look angle of 2π steradians. Two x-ray energy channels, 25-45 keV and >45 keV, were continuously monitored by logarithmic count rate meters (previously described in the literature by Anderson and Milton, 1964). The other part of the payload consisted of a set of orthogonal electric field sensors which can indirectly measure horizontal electric fields at ionospheric (100 km) heights (Mozer and Serlin, 1969). The ATS-5 energetic particle data consisted of

40, 70 and 120 keV electrons; 60, 120 and 165 keV protons, and energetic flux of >5 keV particles. The particle detectors have previously been described (Bogott and Mozer, 1971).

For ground based information of substorm activity, magnetograms from Churchill, Great Whale River, Meanook and Thompson were used to determine the magnetic bay events (Table 1). All-sky camera and riometer data from Churchill added additional information of auroral activity at geomagnetic latitudes (L = 8.0) above Thompson (L = 6.6).

RESULTS

In order to better understand the physical significance of slow bay onsets, two isolated slowly developing negative bays have been selected and examined using all available data. One event occurred on May 2, 1970, the other on May 5, 1970.

In Figure 1, a slowly developing negative bay is detected at Thompson, a midnight sector station, at ~0700 UT on May 2. Later, large sharp negative bays of 250 gamma magnitude are detected eastward of Thompson at Great Whale River at ~0745 UT, and northward of Thompson at Churchill at ~0742 UT coincident with a sharp riometer absorption event also detected at that station. At the time of the start of the slowly decreasing bay onset, ~0700 UT, westward and southward ionospheric electric fields are further enhanced by 5-15 millivolts/meter and 10-25 millivolts/meter respectively, together with enhanced energetic >40 keV electron precipitation over Thompson.

Sharp enhancements of energetic (>5 keV) plasma fluxes are detected at ATS at 0700 UT, at the time of the start of the slowly developing negative bay (Figure 2). Energetic electron and proton flux enhancements are observed to occur at approximately 0710 UT, delayed

about 10 minutes from the start of the plasma injection. No striking features in either the plasma data or in the energetic particle data are observed at the time of the sharp negative bay onsets, 0742 or 0745 UT.

The physical significance of the later sharp negative bay onset detected at Churchill at ~0742 UT is examined. Churchill all-sky photographs (Figure 3) indicate auroral activity in the southwest horizon at or prior to 0720 UT (The exact time of the auroral breakup and the start of the expansion is unknown because Thompson all-sky camera data were not available). Motion of these auroral forms in a northeastern direction is observed (expansion of the auroral bulge, Akasofu, 1965) with auroral light producing particle precipitation first reaching the Churchill zenith at 0742 UT corresponding to the time of the sharp negative bay onset and the sharp riometer absorption increase. An auroral bulge propagation velocity of 0.2-0.4 km/sec is calculated and is well within the typical bulge expansion speeds reported by Akasofu et al. (1966). It has been previously shown by Akasofu et al (1971) in analysis of substorm negative bay developments from a meridian chain of observatories, that bays occurring at high latitudes are delayed in time and are sharp in nature due to features of the propagation of the auroral bulge Barcus (1965) has shown that riometer absorption events during auroral breakups at $L = 8$ of ≤ 25 keV electrons occurring in overhead passing auroral forms. Thus the correlation of riometer absorption, overhead passage of auroral forms, and sharp negative bay onsets are what one would expect, from the results of prior literature.

Figure 4 illustrates another example of an isolated substorm on May 5. The start of the auroral midnight sector negative bay at Meanook is detected at ~0900 UT. Auroral zone ground stations eastward of Meanook, Thompson and Great Whale River detect slowly developing negative bays without any apparent sharp negative onsets. High latitude

stations, Churchill and Baker Lake (not shown) detected sharp negative onsets at 1025 UT and 1035 UT, respectively, roughly 1½ hours past the start of the auroral zone midnight sector bay onset. Again, the sharp negative Churchill bay is coincident with an increase in riometer absorption at that station, similar to the previous example. However, Churchill all-sky data were not available for this event to show the propagation of the auroral bulge.

It is noted that the start of the slow bay onset at ~0900 UT was related with the southward turning of the interplanetary magnetic field (IMF) at either 0830 UT or 0900 UT; in either case within 30 minutes of the southward turning of the IMF, consistent with the observations of Tsurutani and Meng (1971) and Foster et al. (1971). The IMF remained southward throughout the development of the bay, and the later northward turning of the IMF at 1110 UT was roughly coincident with the start of the recovery phase of the bay. Westward and southward ionospheric electric field enhancements of 5-10 millivolts/meter and precipitation of energetic >40 keV electrons are observed at 0900 UT, the same time as the start of the slow bay onset at Meanook.

As in the previous example on May 2, the energetic (>5 keV) plasma injection is detected at the time of the start of the midnight sector magnetic bay, 0900-0920 UT. The plasma injection is gradual with the low energy (~1 keV) particles being injected first, ~0900 UT, and the more energetic particles later in time (DeForest, private communication). This is indicated by the increase of >40 keV electrons at ~0930 UT. There are no outstanding energetic particle features or plasma features at the time of the Churchill and Baker Lake sharp negative bays, 1025 UT and 1035 UT respectively.

CONCLUSION AND DISCUSSION

Both substorm examples showed features which were strikingly consistent: the start of the slowly developing magnetic bays in the midnight sector auroral zone was accompanied by westward ionospheric electric field enhancements, the precipitation of energetic (>40 keV) electrons, and the injection of energetic plasma at ATS-5 distances, indicating the onset of the substorm. The later sharp negative bay onsets seen eastward and northward of local midnight were found to be unrelated to any plasma features or energetic electron or proton features observed by ATS-5; in one example, May 2, the sharp onset was clearly seen to be due to the auroral bulge propagation with a finite velocity of 0.2-0.4 km/sec. In the other example, May 5, no remarkable sharp bay onset in the auroral zone was observed eastward of local midnight although the bay was clearly identified as being related with a substorm. It is therefore noted that sharp bay onsets are not necessary for the identification of substorms. Our results indicate that midnight sector auroral zone magnetic bays are associated with magnetospheric substorms (Parks and Winckler, 1968) independent of the nature of the bay onset. The morphology of the substorms examined agreed with the model presented by Akasofu (1965).

The detection of the energetic plasma injection at the onset of the substorm and the simultaneous enhanced electric fields may indicate that the substorm particles are simply inward convected plasma sheet particles (Chase, 1969). The delayed appearance of the energetic >40 keV particles from the appearance of the lower energy auroral particles could be explained by the energy versus distance configuration of the inner edge of the quiet time plasma sheet (Schield and Frank, 1970), assuming that

ATS lies earthward of this sheet. Larger magnitude magnetospheric westward electric fields would be associated with faster inward convection, and subsequently less time dispersion of the injection of the energetic particles from the auroral plasma.

ACKNOWLEDGMENTS

The authors would like to thank Professor K. A. Anderson and Professor F. S. Mozer for their support and helpful suggestions during the study. Appreciation is extended to Professor S-I. Akasofu and Dr. C-I. Meng for the critical readings of the manuscript and subsequent suggestions. The ATS-5 magnetic B_z component was supplied by Mr. T. Skillman of GSFC. Interplanetary magnetic field θ (solar magnetospheric coordinates) data were kindly supplied by Dr. D. H. Fairfield of GSFC.

This work was supported by the National Aeronautics & Space Administration under grant NGL-05-003-017 and contract NAS5-10362 and by the Atmospheric Sciences Section of the National Science Foundation under grant GA-26582.

REFERENCES

Akasofu, S-I., Dynamic morphology of auroras, Space Sci. Rev., 4, 498, 1965

Akasofu, S-I., D. S. Kimball, and C-I. Meng, Dynamics of the aurora-V, Poleward motions, J. Atmosp. and Terr. Physics, 28, 497, 1966

Akasofu, S-I., Wilson, C. R., Snyder, L. and Perreault, P. D., Results from a meridian chain of observatories in the Alaskan sector (I), Planetary Space Science 19, 477, 1971.

Anderson, K. A., and D. W. Milton, Balloon observations of x-rays in the auroral zone, 3. High time resolution studies, J. Geophys. Res., 69, 4457, 1964

Barcus, J. R., Balloon observations on the relationship of energetic electrons to visual aurora and auroral absorption, J. Geophys. Res., 70, 2135, 1965

Bogott, F. H., and F. S. Mozer, Equatorial proton and electron angular distributions in the loss cone and at large angles, J. Geophys. Res., 76, 6790, 1971

Chase, L. M., Evidence that the plasma sheet is the source of auroral electrons, J. Geophys. Res., 74, 348, 1969

DeForest, S. E., and C. E. McIlwain, Plasma clouds in the magnetosphere, J. Geophys. Res., 76, 3587, 1971

Foster, J. C., D. H. Fairfield, K. W. Ogilvie, and T. J. Rosenberg, Relationship of interplanetary parameters and occurrence of magnetospheric substorms, J. Geophys. Res., 76, 6971, 1971

Mozer, F. S., and R. Serlin, Magnetospheric electric field measurements with balloons, J. Geophys. Res., 74, 4739, 1969

Mozer, F. S., and R. H. Manka, Magnetospheric electric field properties deduced from simultaneous balloon flights, J. Geophys. Res., 76, 1697, 1971

Parks, G. K., and J. R. Winckler, Acceleration of energetic electrons observed at the synchronous altitude during magnetospheric substorms, J. Geophys. Res., 73, 5786, 1968

Schield, M. A., and L. A. Frank, Electron observations between the inner edge of the plasma sheet and the plasmasphere, J. Geophys. Res., 75, 5401, 1970

Tsurutani, B, and C-I. Meng, Interplanetary magnetic field variation and substorm activity, submitted to J. Geophys. Res., 1971

FIGURE CAPTIONS

1. The first sign of a slowly developing negative bay at Thompson (the approximate auroral oval local midnight station), x-ray precipitation over Thompson and enhancements of the westward and southward Thompson ionospheric electric fields, at ~0700 UT. A later sharp negative bay at 0745 UT is detected eastward of Thompson at Great Whale River, and another sharp bay onset is detected northward of Thompson at Churchill at 0742 UT coincident with a sharp riometer absorption event also detected at that station.
2. ATS-5 satellite substorm energetic > 5 keV plasma flux increases at ~ 0700 UT. Flux increases of 40 keV and 75 keV electrons and of 60 keV protons occur at ~ 0710 UT, slightly delayed from the plasma injection.
3. The expansion of the auroral bulge first reaches the Churchill zenith at 0742 UT. This is the same time as that of the sharp bay onset and the riometer absorption at Churchill (Figure 1).
4. The start of the local midnight sector negative bay at Meanook, energetic electron precipitation over Thompson, and enhancements of Thompson westward and southward ionospheric electric fields at ~ 0900 UT. No later sharp negative bays are detected at the auroral zone stations eastward of Meanook, at Thompson or Great Whale River. However, a later sharp negative bay onset is detected at Churchill at 1025 UT, coincident with riometer absorption at that station.
5. Enhancements of energetic plasma flux > 5 keV at ATS-5 at 0900 UT. Flux increases of 40 keV and 75 keV electrons and 60 keV protons occur at ~ 0930 UT, delayed from the plasma injection.

Table 1. Ground Magnetic Observatories

Magnetic Observatory	Geomagnetic Latitude	Geomagnetic Longitude
Meanook	61.8°	301.0°
Thompson	65.5°	319.0°
Great Whale River	66.6°	347.4°
Fort Churchill	68.7°	322.8°

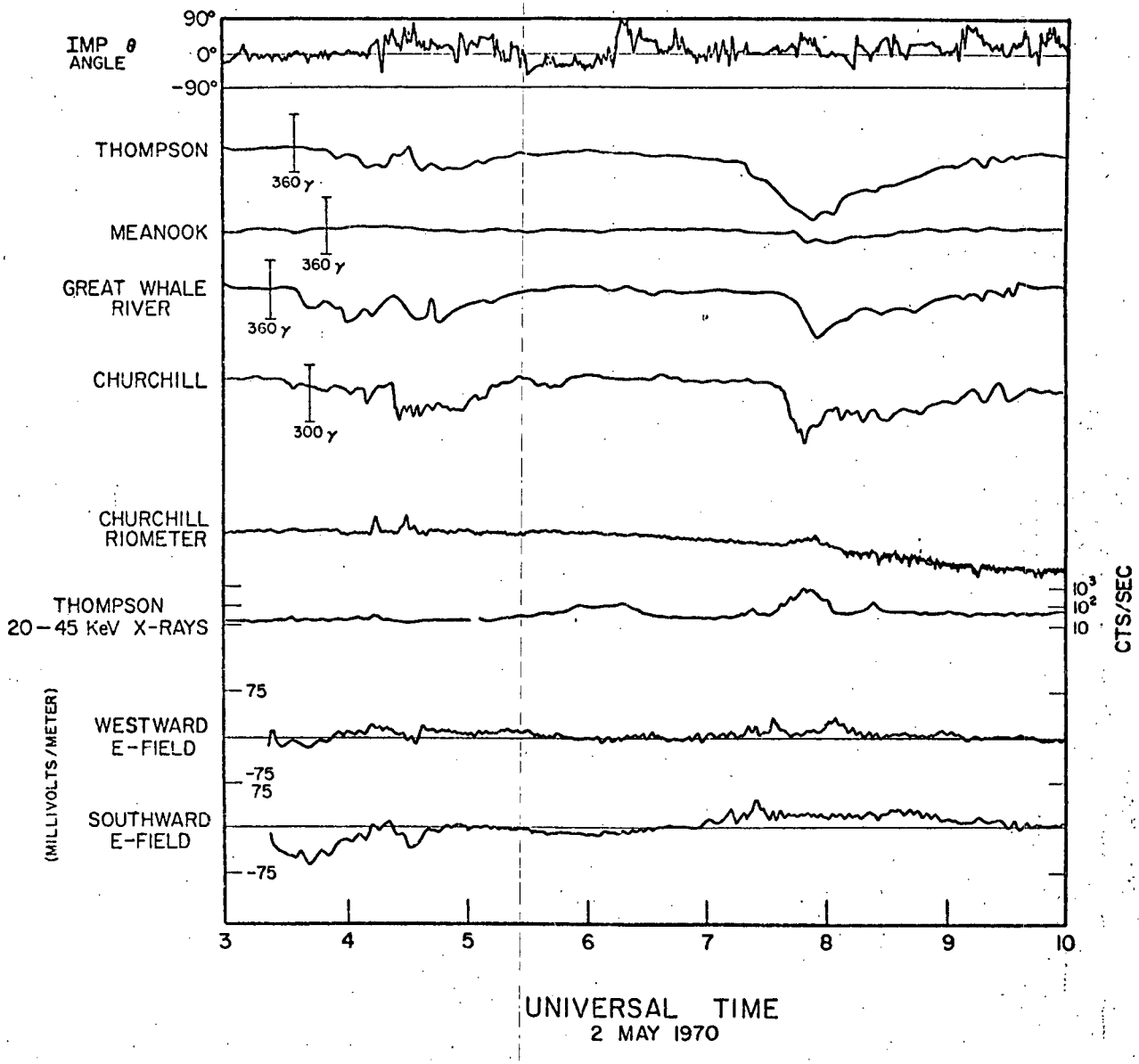
IMP θ ANGLE
90°
0°
-90°
THOMPSON
360γ
MEANOOK
360γ
GREAT WHALE RIVER
360γ
CHURCHILL
300γ
CHURCHILL RIOMETER
THOMPSON 20-45 KeV X-RAYS
10³
10²
10
CTS/SEC
(MILLIVOLTS/METER)
75
WESTWARD E-FIELD
-75
75
SOUTHWARD E-FIELD
-75
3
4
5
6
7
8
9
10
UNIVERSAL TIME
2 MAY 1970

Figure 1

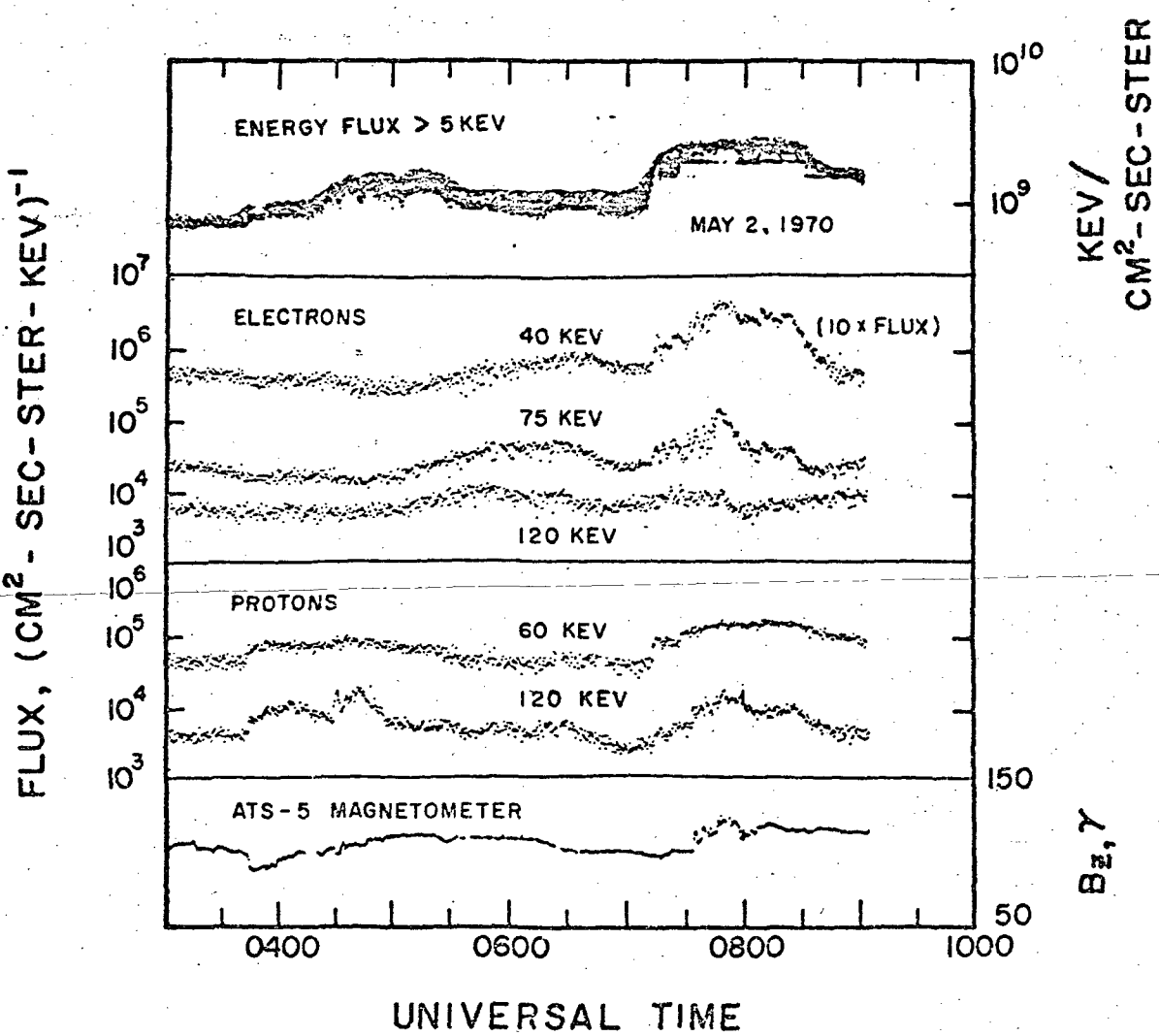
ENERGY FLUX > 5 KEV
MAY 2, 1970
ELECTRONS
40 KEV
(10 x FLUX)
75 KEV
120 KEV
PROTONS
60 KEV
120 KEV
ATS-5 MAGNETOMETER
FLUX, (CM2 - SEC - STER - KEV)-1
KEV / CM2 - SEC - STER
Bz, γ
0400
0600
0800
1000
UNIVERSAL TIME

Figure 2

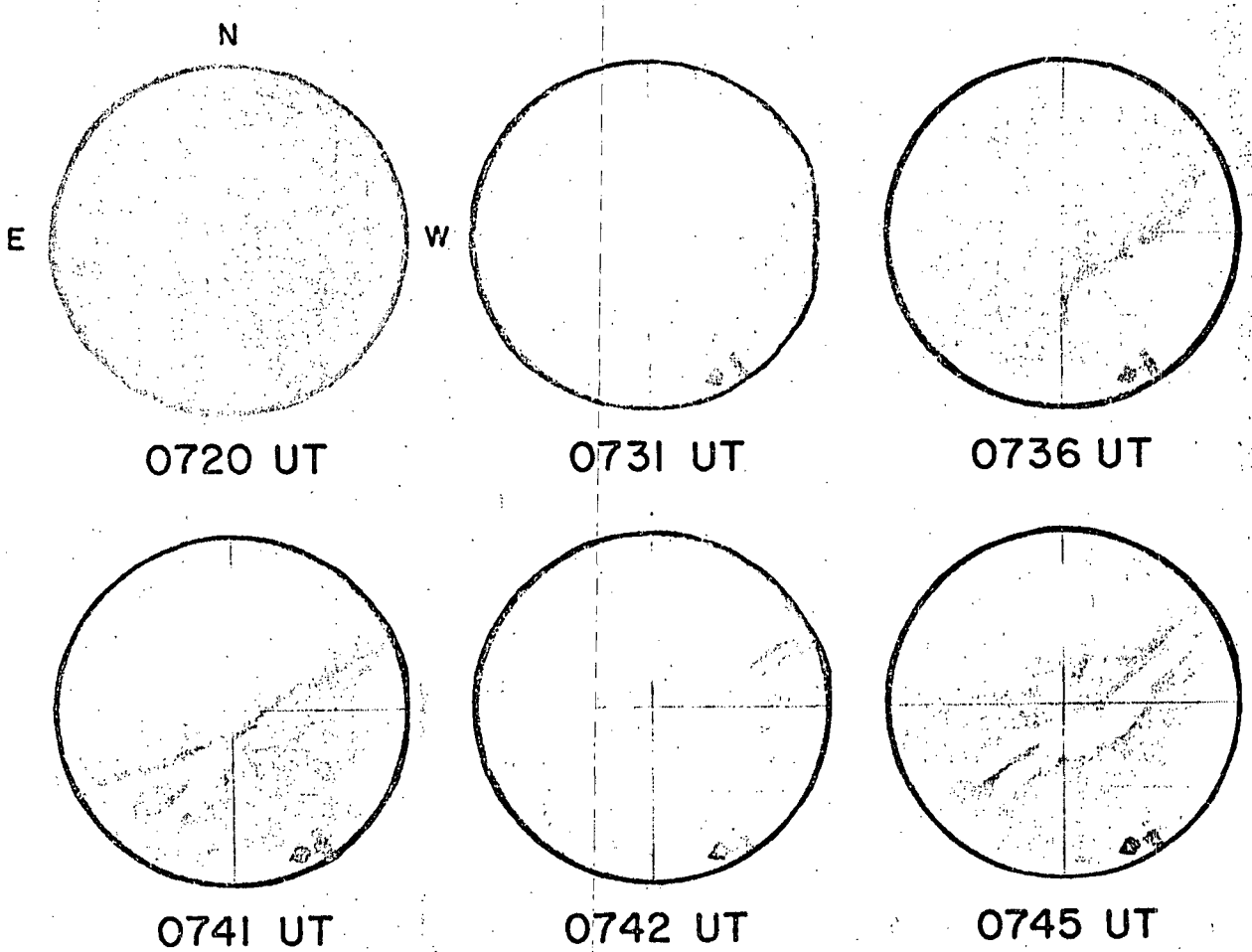
CHURCHILL ALL-SKY
MAY 2, 1970
N
E
W
0720 UT
0731 UT
0736 UT
0741 UT
0742 UT
0745 UT

Figure 3

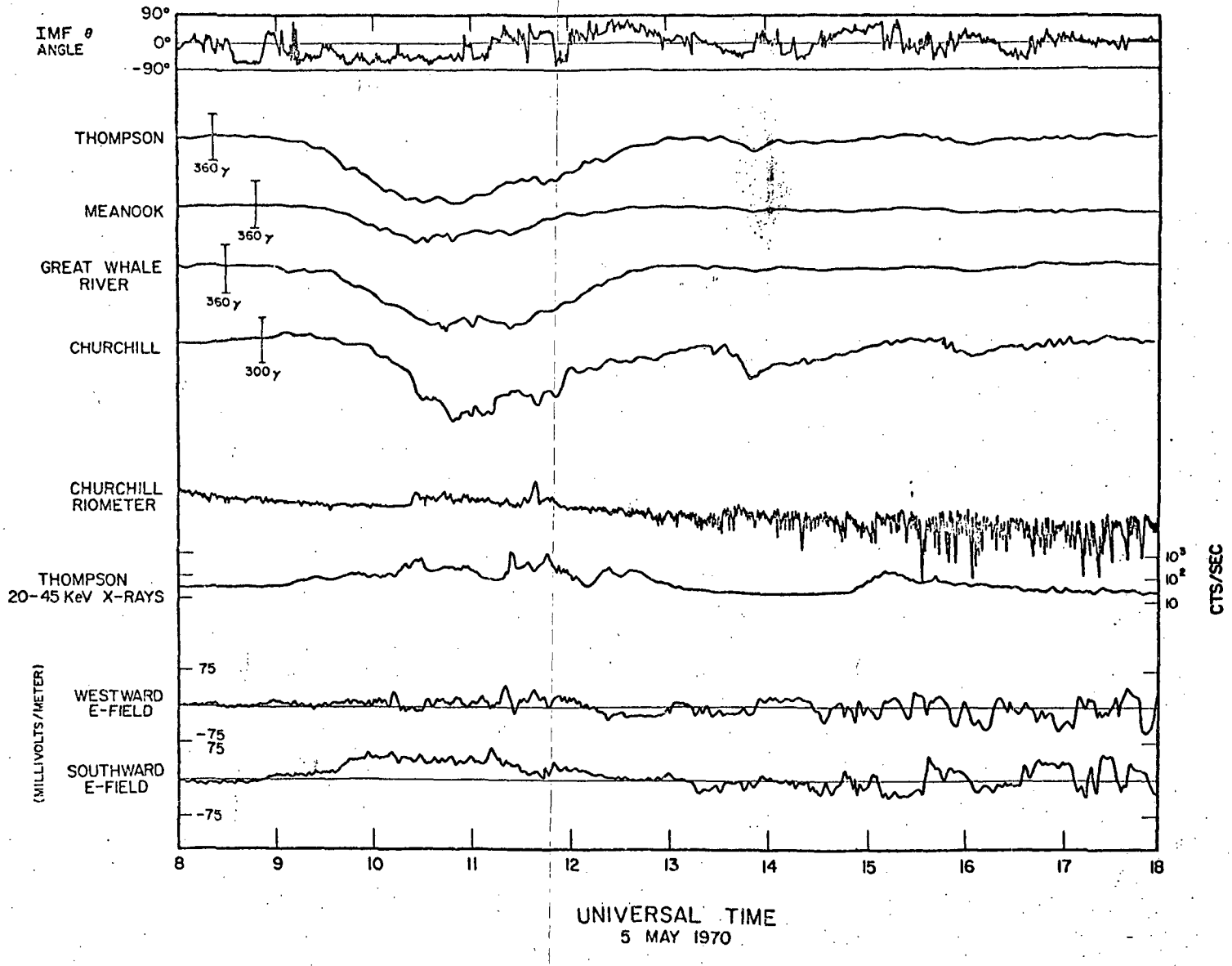
IMF θ ANGLE
90°
0°
-90°
THOMPSON
360γ
MEANOOK
360γ
GREAT WHALE RIVER
360γ
CHURCHILL
300γ
CHURCHILL RIOMETER
THOMPSON 20-45 KeV X-RAYS
10^3
10^2
10
CTS/SEC
(MILLIVOLTS/METER)
75
WESTWARD E-FIELD
-75
75
SOUTHWARD E-FIELD
-75
8
9
10
11
12
13
14
15
16
17
18
UNIVERSAL TIME
5 MAY 1970

Figure 4

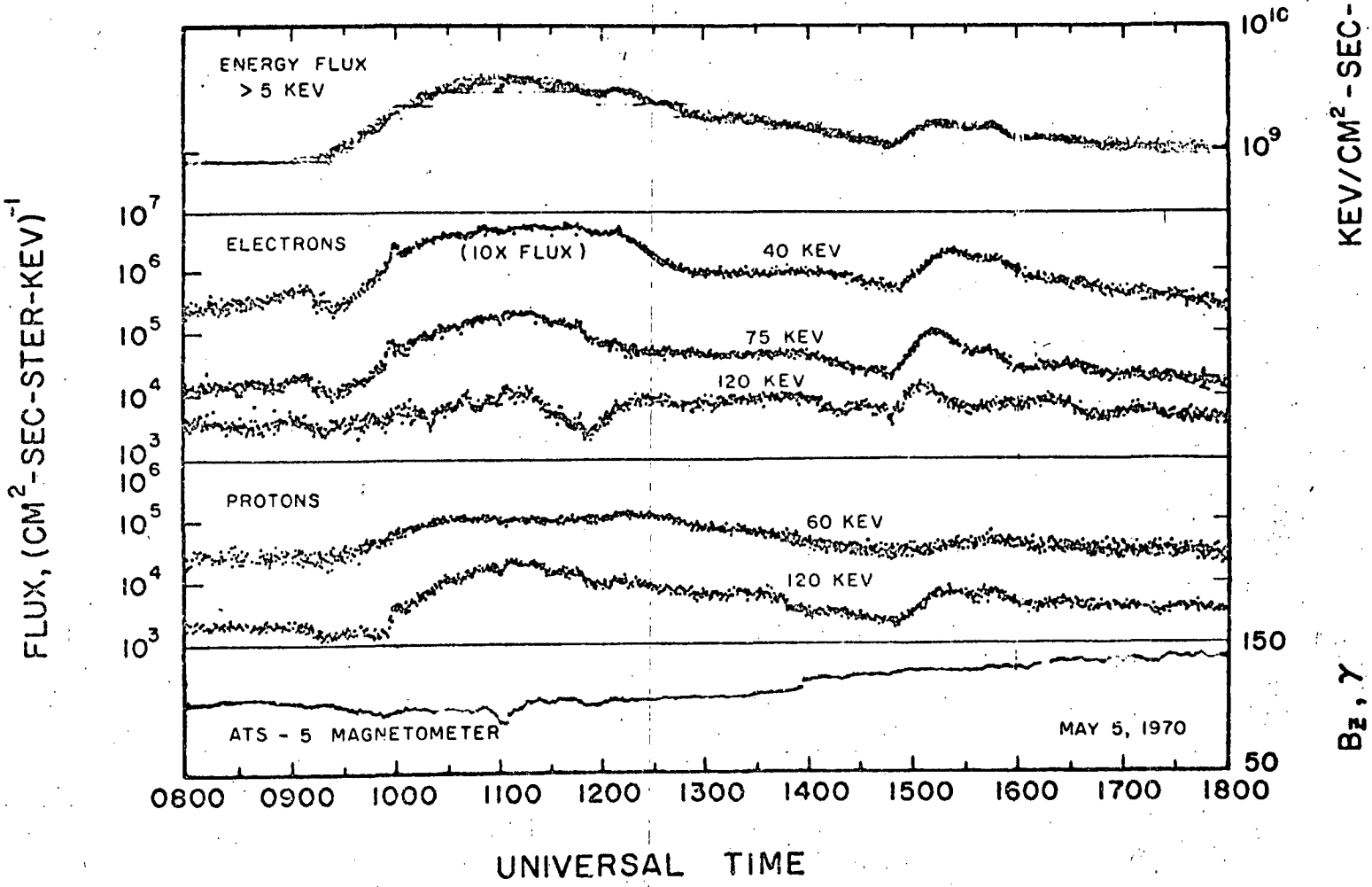
ENERGY FLUX
> 5 KEV
ELECTRONS
(10X FLUX)
40 KEV
75 KEV
120 KEV
PROTONS
60 KEV
120 KEV
ATS - 5 MAGNETOMETER
MAY 5, 1970
FLUX, (CM²-SEC-STER-KEV)⁻¹
KEV/CM²-SEC-STER
Bz, γ
UNIVERSAL TIME
0800 0900 1000 1100 1200 1300 1400 1500 1600 1700 1800

Figure 5